



Università degli Studi di Ferrara

DOTTORATO DI RICERCA IN
"SCIENZE DELLA TERRA"

CICLO XXVIII

COORDINATORE Prof. Coltorti Massimo

RECENT TECTONIC ACTIVITY OF THE CENTRAL
SECTOR OF THE FERRARA ARC EMPHASIZED BY A
MULTIDISCIPLINARY APPROACH

Settore Scientifico Disciplinare GEO/03

Dottoranda

Dott.ssa Mantovani Ambra

Mantovani Ambra

Tutore

Prof. Caputo Riccardo

Caputo Riccardo



Anni 2013/2015

*“Look up at the stars and not down at your feet.
Try to make sense of what you see,
and wonder about what makes the universe exist.
Be curious.”*

Stephen Hawking

Contents

I	Introduction	25
1	Motivation and research purposes	27
2	The Po Plain: an evolving foredeep basin	35
2.1	Geodynamic and stratigraphic evolution of Northern Italy	35
2.2	The buried structures of the Po Plain	41
2.3	Recent tectonic evolution of the Ferrara Arc: evidences and implications . .	45
2.3.1	Seismological and geodynamic evidences	45
2.3.2	Geomorphological evidences	50
3	The western Ferrara Province	55
3.1	Hydrographic and morphological evolution	55
3.2	Stratigraphic architecture of the Pliocene- Quaternary succession	58
II	Applied methods and data collections	65
4	Geotechnical methods and data collection	67
4.1	Static cone penetration tests	68
4.1.1	Equipment and procedures	68
4.1.2	Soil profile interpretation	69
4.2	Soil liquefaction	77
4.2.1	Liquefaction phenomena	77

4.2.2	Soils susceptibility to liquefaction and ground failure	78
4.2.3	Semi-empirical procedures for the evaluation of liquefaction potential during earthquakes	81
4.2.4	Liquefaction Potential Index (LPI) and Liquefaction Severity Number (LSN)	92
4.3	Data collection and processing	97
4.3.1	Geognostic database of the Sant'Agostino Municipality	97
4.3.2	Qualitative and quantitative assessment of susceptibility to liquefaction	99
5	Geophysical methods and data collection	101
5.1	Seismic ambient noise: nature and composition	102
5.1.1	Noise-based techniques	104
5.2	SPAC-ESAC methodologies: analytical procedure and application	104
5.2.1	Frequency-slowness analysis	107
5.3	Horizontal-to-Vertical Spectral Ratio (HVSR or H/V)	108
5.3.1	The theoretical basis of the H/V method	108
5.3.2	Applications of the H/V	113
5.4	Data collection and processing	114
5.4.1	ESAC surveys: array configuration, measurements and processing .	114
5.4.2	HVSR surveys: measurements and data processing	119
5.4.3	Interpretation and inversion of the H/V curves	127
III	Applications	133
6	Case studies	135
6.1	Geophysical pseudo-2D sections	135
6.1.1	Cento-Bondeno profile	136
6.2	Tectonic deformation <i>versus</i> site effects	144
6.2.1	The May 2012 Emilia earthquakes imaged by geodetic approaches	144
6.2.2	Major geomorphic effects: liquefaction and local subsidence	150

6.3	Seismic Microzoning of the Sant'Agostino Municipality	156
6.3.1	Subsoil model and amplification estimation	156
6.3.2	Cartographic maps	159
6.3.3	Stratigraphic architecture and depositional evolution	174
6.4	Quantitative assessment of liquefaction potential	176
6.4.1	The May 20, 2012 Emilia earthquake: liquefaction-induced deformations	176
6.4.2	Test sites	184
6.4.3	Site specific acceleration	187
6.4.4	Evaluating the liquefaction potential	189
6.4.5	Comparison of LPI and LSN values	191
IV	Summary	195
7	Conclusions	197
7.1	Geophysical pseudo-2D sections	197
7.2	Tectonic deformation <i>versus</i> site effects	199
7.3	Seismic microzoning of the Sant'Agostino Municipality	199
7.4	Quantitative assessment of liquefaction potential	201
7.5	Improvements and future works	202
V	References	205

List of Figures

2.1	Satellite image of the Po Plain.	36
2.2	Tectonic setting of Apennines-Tyrrhenian domain. 1) main thrusts, 2) normal faults, 3) buried tectonic lines, 4) fold axes, 5) volcanic centers, 6a) new-formed oceanic crust, 6b) deep basins in the African-Adriatic domain and 7) African and Adriatic foreland (modified from Margheriti <i>et al.</i> , 2003).	38
2.3	Po Plain and northern Adriatic Sea: the four buried structural arcs and main tectonic features (from Costa, 2003).	41
2.4	a) Location of two seismic lines that cross the central-eastern sectors of the Po Plain. b) Interpreted seismic lines (from Boccaletti <i>et al.</i> , 2004).	44
2.5	Historical seismicity of the Regione Emilia-Romagna, from 1000 a.C. to 2006 (from Carannante <i>et al.</i> , 2015).	46
2.6	Instrumental seismicity of the Emilia-Romagna Region between 1983 to May 2012 (data from ISIDe, http://iside.rm.ingv.it/).	46
2.7	May-June 2012 Emilia seismic sequence (earthquakes location from Massa <i>et al.</i> , 2013).	47
2.8	A) Vent fractures with ejected sandy material. B) Sandy material covering the courtyard of a settled and shifted house. C) Surface ruptures. D) Evidence of a penetration of a clayey cap layer by a sandy material (from Caputo and Papathanassiou, 2012).	49
2.9	a) Velocity field in northern Italy expressed with respect to a non moving Adriatic microplate defined by sites located in the Po Plain. b) Velocity profile 1a-1b (see map), along Bologna and Venezia (from Devoti <i>et al.</i> , 2011).	50

2.10	a) Deformation pattern of the May 2012 seismic sequence (from Bignami <i>et al.</i> , 2012). b) Schematic representation in map view and cross-section of the effects that slip on a generic blind, low-angle thrust fault may have on geomorphic/sedimentary processes (from Burrato <i>et al.</i> , 2003).	52
2.11	Drainage network evolution in the central part of the southern Po Plain north of Bologna (from Burrato <i>et al.</i> , 2012). The modern drainage pattern is reproduced in the background of all of the panels. The basemap of the lower-right panel is from Bigi <i>et al.</i> (1992).	53
3.1	Geomorphological map of the eastern sector of the Po Plain (from Castiglioni <i>et al.</i> , 1999).	56
3.2	Geomorphological sketch map of the western Ferrara Province showing the complex hydrographic drainage developed in historical times as a consequence of tectonic activity, climatic changes and human interventions. Letters indicate distinct branches of the Po, Reno and Panaro rivers referred to in the text. Legend: 1) palaeo- and active levees associated with a morphological relief; 2) palaeo-channels entrenched in the alluvial plain; 3) flooding areas characterized by sandy deposits; 4) surface evidence of liquefaction phenomena caused by the May 20, 2012 event; 5) major breaches and associated fan deposits (from Caputo <i>et al.</i> , 2015).	57
3.3	a) Trace of a geological profile that runs between Cento and Occhiobello. The basemap of the figure is from Bigi <i>et al.</i> (1992). b) Reconstruction of the geological and structural configuration of the subsurface along the profile (from Martelli and Romani, 2013).	60
3.4	Basal isobathes of the Upper Emiliano-Romagnolo Synthem (from Boccaletti <i>et al.</i> , 2004).	61
3.5	Synoptic view of the Quaternary stratigraphic units of the Po Plain subsurface (from Molinari <i>et al.</i> , 2007).	63
4.1	The Begemann (1965) soil profiling chart.	70

4.2	The Schmertmann (1978) soil profiling chart.	71
4.3	The Douglas and Olsen (1981) soil profiling chart.	72
4.4	The Robertson <i>et al.</i> (1986) soil profiling chart.	73
4.5	The Robertson (1990) soil profiling chart.	74
4.6	Contours of soil behaviour type index I_c (dashed lines), on normalized SBTn Q_{tn} - F_R chart (from Robertson, 2009).	76
4.7	Limits in the gradation curves separating liquefiable and non-liquefiable soils (Tsuchida, 1970).	79
4.8	Schematic illustration of procedure to calculate maximum shear stress, τ_{max} , and stress reduction coefficient, r_d (after Seed and Idriss, 1971).	84
4.9	Cyclic resistance ratio (CRR) for clean sands vs normalized and dimension- less tip resistance q_{c1N} based on CPT (Robertson and Campanella, after 1996 update).	86
4.10	Curves relating the CRR to q_{c1N} for clean sands with $M = 7.5$ and $\sigma'_{v0} = 1$ atm (from Idriss and Boulanger, 2004, 2006).	90
4.11	Comparison of field case histories for cohesionless soils with high fines content and curve proposed by Robertson and Wride (1998) for soils with $I_c = 2.59$ (apparent FC=35%) (from Idriss and Boulanger, 2004; 2006). . . .	91
4.12	a) Curves for estimating the postliquefaction volumetric strain of clean sands (modified from Ishihara and Yoshimine, 1992). b) Relationship between postliquefaction volumetric strain and equivalent clean sand normalized CPT tip resistance for different values of the factor of safety F_s (Zhang <i>et al.</i> , 2002). . . .	96
4.13	Example of the organization of the numerical data in an excel sheet.	99

5.1	a) Model of an elastic layer over a half-space. Poisson's ratio (ν) were determined from V_S as follows: $\nu=0.499$ for $V_S < 150$ m/sec; $\nu=0.499-1.16 \cdot 10^{-4}$ for $V_S \geq 150$ m/sec. b) Particle motion of three types of fundamental Reyleigh waves for the above described models. c) Three types of H/V ratio of fundamental Rayleigh waves. Downward arrows show trough periods: type 1, $V_{S1} = 250$ m/sec; type 2, $V_{S1} = 200$ m/sec; type 3, $V_{S1} = 50$ m/sec (from Konno and Ohmachi, 1998).	110
5.2	Simplified structure of a sedimentary basin (Nakamura, 2000).	111
5.3	a) H/V of Rayleigh waves for two layered ground, with different impedance contrasts. b) Group velocity of Rayleigh waves. c) Relationship between characteristics of Rayleigh wave and impedance ratio (from Nakamura, 2000).	113
5.4	Tectonic sketch map of the Ferrara Arc (red lines; Pieri and Groppi, 1981) showing the location of the investigated profile (black line).	114
5.5	Particular of the array configuration for the acquisition of the experimental data.	115
5.6	Location of the measured sites (yellow triangles) along the Cento-Bondeno profile (black line). In transparency is shown the DSM from LIDAR survey. A simplified outline of the main thrusts (red lines) of the buried Northern Apennines is also reported (from Pieri and Groppi, 1981).	116
5.7	Fundamental mode dispersion curves calculated from the array surveys performed along the Cento-Bondeno profile.	118
5.8	The 1D velocity profiles obtained by the array surveys performed along the Cento-Bondeno profile.	119
5.9	a) Seismograph and b) seismometer employed for the single-station noise measurements.	120
5.10	Location of the measured sites (blue squares) along the Cento-Bondeno profile (black line). In transparency is shown the DSM from LIDAR survey. A simplified outline of the main thrusts (red lines) of the buried Northern Apennines is also reported (from Pieri and Groppi, 1981).	121

5.11	Location of the HVSR measurements performed for the seismic microzoning study of the Sant'Agostino Municipality. In transparency is shown the DSM from LIDAR survey.	123
5.12	Example of HVSR processing (site 2 along the Cento-Bondeno profile) with Grilla software (www.tromino.eu). a) HVSR curve. b) amplitude spectra of the three ground motion components. c) HVSR pattern as a function of time with transient removal and d) HVSR as a function of the azimuth (i.e. directional analysis).	126
5.13	Example of H/V inversion (site 39 along the Cento-Bondeno profile) with OpenHVSR routine (Bignardi <i>et al.</i> , 2015 submitted to <i>Computers & Geosciences</i>). a) Starting subsoil blocky layered model. b) Final subsoil blocky layered model. c) Best match between experimental and inverted data for the frequency band 0.5-5.0 Hz. d) Comparison between the smooth Vs model obtained by the ESAC survey and the best one from H/V subsoil blocky layered inversion.	131
6.1	a) Shear-wave velocity section along the Cento-Bondeno profile. 1D velocity profiles from b) ESAC and c) Re.Mi. surveys. d) Location of the measured sites superimposed on the Structural Model of Italy (Bigi <i>et al.</i> , 1992) . . .	138
6.2	Smoothed HVSR profile obtained by gridding each average HVSR curve, between 0.5 and 5 Hz. Relative amplitudes are color-coded (see colorbar). Some examples of the HVSR curves are also shown.	140
6.3	a) Map showing the basal limit of the Complex Aquifer A2 (from Martelli Luca - RER, personal communication) and the traces of the two available geological sections, oriented NW-SE and SW-NE; b) NW-SE section (portion of the C-C' geological profile from RER & ENI-AGIP, 1998). The red star represents the projection onto the section of the depth of the resonant interface for site 39 (see Fig. 6.4).	141

6.4	a) Vs profiles obtained by the inversion of the HVSR curves, in the frequency range 0.5-5 Hz. b) Particular of the c) geological profile made by Martelli and Romani (2013) (orange line in Fig. 6.3).	143
6.5	DInSAR results applied to a) Canadian RADARSAT-1 satellite data and b) European COSMO-SkyMed-1 satellite data. a) The paired images are dated May 12 and June 5, 2012 and thus document the deformation associated with both mainshocks (May 20 and 29). Note the distinct (though partially overlapping) effects of the two principal morphogenic earthquakes. b) The paired images are dated May 19 and May 23, 2012 and thus document the deformation associated only with the first mainshock (May 20). The High Precision Levelling (HPL) lines discussed later are also shown (from Caputo <i>et al.</i> , 2015).	146
6.6	The first order levelling network belonging to the “Consorzio Pianura di Ferrara”, Ferrara Province, which was re-measured following the 2012 seismic sequence. Small dots represent the benchmarks of the Consortium, the hexagons represent the labelled benchmarks discriminating the levelling lines, while the triangle is the reference benchmark belonging to the Italian First Order Levelling Network, re-surveyed in 2005 by the IGM (Istituto Geografico Militare) (from Caputo <i>et al.</i> , 2015).	147
6.7	Vertical movements measured along the three levelling lines closest to Ferrara (i.e. farthest from the epicentre), with a mean E–W orientation and showing remarkable stability. The error bar at each benchmark calculated on the basis of the standard deviations of the differences in elevation (pre- to post-earthquake) is smaller than the symbol size. Capital letters refer to the benchmarks labelled in Fig. 6.6. HPL: high-precision levelling; RS1: RADARSAT-1; CSK: COSMO-SkyMed (from Caputo <i>et al.</i> , 2015).	148

- 6.8 Vertical movements measured along the three levelling lines closest to the epicentral area with a mean ESE–WNW orientation showing a uniform behaviour of the single levelling lines, albeit variable from north to south. The error bar at each benchmark calculated on the basis of the standard deviations of the differences in elevation (pre- to post-earthquake) is smaller than the symbol size. Capital letters refer to the benchmarks labelled in Fig. 6.6. HPL: high-precision levelling; RS1: RADARSAT-1; CSK: COSMO-SkyMed (from Caputo *et al.*, 2015). 149
- 6.9 Vertical movements measured along the two levelling lines running perpendicular to the May 20 fault strike. Profile G–F–C (a) well reproduces the satellite results, while profile H–D–B shows some marked differences with strongly subsided benchmarks. The error bar at each benchmark calculated on the basis of the standard deviations of the differences in elevation (pre- to post-earthquake) is smaller than the symbol size. Capital letters refer to the benchmarks labelled in Fig. 6.6. HPL: high-precision levelling; RS1: RADARSAT-1; CSK: COSMO-SkyMed (from Caputo *et al.*, 2015). 151
- 6.10 Geomorphological features observed in Mirabello the area. a) Google Earth frame of the cemetery area showing the distribution of secondary co-seismic effects, such as sand ejection points (blue dots), ground deformation sites (red squares), drill cores (black stars), ground ruptures (yellow arrows) and sliding direction due to lateral spreading (white arrows). The yellow star indicates the location of benchmark 78020 characterized by 11.4 cm of subsidence. b) Ground ruptures observed on top of the abandoned levee (see (a) for location). c) Effects of the lateral spreading on the lateral wall of the cemetery (see (a) for location). d) Example of ground deformation associated with shallow liquefaction (see (a) for location).78080, which was apparently uplifted ca. 8 cm relative to the ground surface, thus coming out off its case. 153

6.11	Geomorphological features observed in the San Carlo area. a) Digital elevation model clearly showing the two levees of the palaeo-Reno River. Red lines represent the major ground ruptures observed after the May 20 event (Caputo and Papathanassiou, 2012) generally associated with lateral spreading phenomena (white arrows). Blue dots are sand ejection points while black ones are penetration tests providing information about the shallow subsoil. Yellow stars are benchmarks of the HPL line. b) The foundation of the lamp post installed in the center of the roundabout at the northern entrance to San Carlo where diffuse liquefaction has occurred (c) (see (a) for locations). d) The southern wall of the cemetery built on the slope of the palaeolevee and affected by lateral spreading contributing to the subsidence of benchmark 78090. e) Example of a water well located close to benchmark.	155
6.12	a) Locations of array and single-station noise measurements carried out by the Geological Survey of the Regione Emilia-Romagna. b) Location of array and single-station noise measurements suggesting the occurrence of an impedance contrast (i.e. bedrock) at depth lesser than 100 m. c) Bottom isobaths of AES and (d) AES6 (from Martelli and Romani, 2013).	157
6.13	Bedrock depth estimation (blue line) through the comparison between H/V curves, Vs profile obtained by array surveys and stratigraphic constraints. CH: locations of crosshole investigations performed at Medolla and Mirandola (Modena Province) (from Martelli and Romani, 2013).	158
6.14	Map showing an approximate bedrock depth. A1: bedrock depth greater than 100 ± 20 m; A2: bedrock depth lower than 100 m (from Martelli and Romani, 2013).	159
6.15	Surveys Map of the Sant'Agostino Municipality.	160
6.16	Geological Map of the Sant'Agostino Municipality.	163
6.17	Geological-Technical Map of the Sant'Agostino Municipality.	166
6.18	Homogeneous Microzones in Seismic Perspective (MOPS) Map of the Sant'Agostino Municipality.	168

6.19	Amplification Factors and Liquefaction Hazard Map of the Sant'Agostino Municipality.	170
6.20	Shear-wave velocity (V_{s30}) Map of the Sant'Agostino Municipality.	172
6.21	Natural resonance frequencies Map of the Sant'Agostino Municipality.	173
6.22	a) Trace of a geological profile across San Carlo area. b) Reconstructed geological section based on penetrometric tests and drill cores (from Papathanassiou <i>et al.</i> , 2015).	175
6.23	Epicentral area showing the liquefaction manifestations observed during post-event field surveys (Caputo and Papathanassiou, 2012; Papathanassiou <i>et al.</i> , 2012; Di Manna <i>et al.</i> , 2012; Emergeo Working Group, 2013). The stars indicate the instrumental epicenters of the May 20 ($M_w = 6.1$) and May 29 ($M_w = 6.0$) events (Pondrelli <i>et al.</i> , 2012; Massa <i>et al.</i> , 2013), the hexagons represent the corresponding macroseismic epicenters (Galli <i>et al.</i> , 2012), while the square is the surface projection of the slip plane centroid (Ganas <i>et al.</i> , 2012; Cesca <i>et al.</i> , 2013; Pezzo <i>et al.</i> , 2013). Continuous and dashed gray-scale contours represent the slip planes proposed by Ganas <i>et al.</i> (2012) and Pezzo <i>et al.</i> (2013), respectively. The triangle represents the Mirandola seismographic station (MRN) belonging to the national network, while the rhombs are the boreholes for the aquifers monitoring. The two black boxes indicate the investigated areas represented in Figs. 6.32 and 6.33.	177
6.24	Examples of damages produced by the May 20, 2012 earthquake. a) Broken pipelines. b) Paved roads. c) Buildings with cracking due to differential settlement. d) Lateral spreading (from Papathanassiou <i>et al.</i> , 2015).	178
6.25	Examples of large-diameter water wells which locally enhanced the sand ejection during shaking and liquefaction of the sandy aquifer bodies (from Papathanassiou <i>et al.</i> , 2015).	179
6.26	Examples of ground loss due to liquefaction and consequent settlement of the buildings (from Papathanassiou <i>et al.</i> , 2015).	180

6.27	Examples of ground ruptures induced by lateral spreading phenomena occurring on top of an abandoned levee between San Carlo and Sant’Agostino. Fractures are several meters-long, arranged in complex overlapping and overstepping sets, characterized by horizontal opening up to 20 cm, sometimes by vertical displacements of 10–15 cm and locally by sand ejection (from Papathanassiou <i>et al.</i> , 2015).	181
6.28	Example of an incipient buckling process affecting the top layer(s) and due to differential horizontal movements triggered by lateral spreading phenomena (from Papathanassiou <i>et al.</i> , 2015).	182
6.29	Examples of bulging phenomena caused by the failed attempt of sand ejection due to the presence of a strong cap layer (from Papathanassiou <i>et al.</i> , 2015).	183
6.30	Representative sections across San Carlo (a) and Mirandola (b) areas based on penetrometric tests and cores. Note the strong lateral lithological variations occurring in the shallow subsoil and the different distribution of the sandy bodies in the two investigated areas. Legend: 1) silt and silt-clay (alluvial plain deposits from Apennine rivers); 2) silt-sand (proximal levee deposits); 3) major sandy bodies (channel deposits); 4) clay (marsh deposits) with peat lenses (a); 5) medium-coarse sand (alluvial plain deposits of Po River). A0 and A1 indicate the semi-confined and the first confined aquifers, respectively (Rapti-Caputo and Martinelli, 2009; Molinari <i>et al.</i> , 2007). . .	187
6.31	The PGA calculated as a function of the focal distance based on the GMPE proposed by Bindi <i>et al.</i> (2011); dashed curves are the $\pm \sigma$. Rhombs and triangles represent represent the test sites of the eastern and western epicentral areas, respectively. The circles indicate the PGA value measured during the May 20 main shock at the several stations belonging to the Italian seismographic network (itaca.mi.ingv.it). The record at the Mirandola station (MRN), which is the only one in the seismic near-field, is in perfect agreement with the predicted value.	189

6.32	The LPI values calculated for the two investigated epicentral areas of Mirandola (a) and Sant’Agostino (b). See Fig. 6.23 for locations.	192
6.33	The LSN values calculated for the two investigated epicentral areas of Mirandola (a) and Sant’Agostino (b). See Fig. 6.23 for locations.	192
6.34	Cumulative distribution of the LSN (a) and LPI (b) within the investigated areas. Squares and triangles correspond to penetration tests drilled in ‘non-liquefied’ and ‘liquefied’ zones, respectively, as observed in the field after the earthquake. The vertical dashed lines represent the different thresholds discussed in the text.	193
6.35	Correlation between LPI and LSN values for all the investigated sites. The dashed lines indicate the threshold criteria proposed by the different authors as discussed in the text. The four gray scale areas tentatively separate LPI–LSN conditions associated with liquefaction evidence observed on ground surface: class-I: ‘almost no’, class-II: ‘few’, class-III: ‘likely’ and class-IV: ‘very likely’.	194

List of Tables

4.1	Soil behavior type index (I_c) for the SBT zones of the normalized Q_{tn} - F_R chart (from Robertson, 2009).	76
4.2	Convention for the identification of the geognostic surveys archived in the database.	98
5.1	Noise sources and related frequency range according to Gutenberg (1958), Asten (1978) and Asten and Henstridge (1984).	102
5.2	Detailed information about the ESAC and ReMi measurements performed along the Cento-Bondeno profile.	117
5.3	Detailed information about the HVSR measurements performed along the Cento-Bondeno profile.	122
5.4	Detailed information about the HVSR measurements performed for the seismic microzoning study of the Sant' Agostino Municipality.	125
6.1	LPI and LSN calculated for the selected boreholes. W corresponds to Mirandola area, while E refers to San Carlo and Sant' Agostino villages. The test code, according to the Emilia-Romagna archival standards (http://ambiente.regione.emilia-romagna.it/geologia/cartografia/webgis-banchedati/), is reported in the second column. Water table is in meters below ground surface. Peak ground acceleration (PGA) as percentage of gravity. Test sites drilled within 'liquefied' (Y) and 'not-liquefied' (N) zones are indicated.	186

Part I

Introduction

Chapter 1

Motivation and research purposes

The investigated area by this research project is the central-eastern sector of the Po Plain, which is a large alluvial plain representing the foredeep of two opposite-verging fold-and-thrust belts, the Northern Apennines and the Southern Alps. In particular, the attention was focused on the shallowest portion (down to few hundreds of meters) of the Ferrara Arc, which is one of the three major arcs of blind, north-verging thrusts and folds forming the external front of the Northern Apennines. Despite its flat appearance, hydrocarbon exploration (Pieri and Groppi, 1981) revealed that the external thrusts of the Apennines are buried underneath a variably thick Pliocene-Quaternary sequence of clastic materials.

As common for other large and tectonically active continental foredeep basins, the Po Plain is characterized by blind faulting. The issue of blind faulting became widely debated in the Earth sciences community in 1989, when a series of 'hidden earthquakes' hit central and southern California, USA, between 1983 and 1987, and following the October 17, 1989, Loma Prieta, California, earthquake (M_W 6.9) (Burrato *et al.*, 2012). As stated by Stein and Yeats (1989), "*...large earthquakes can take place not only on faults that cut the Earth's surface, but also on 'blind' faults under folded terrain*".

Several authors have supported the hypothesis that the tectonic activity of the frontal part of the Northern Apennines ceased in Early Pleistocene (Argnani and Frugoni, 1997; Bertotti *et al.*, 1998; Argnani *et al.*, 2003; Picotti *et al.*, 2008); while other studies have suggested that some of the anticlinal structures buried in the Po Plain are still tectonically active, on the basis of geomorphological and cinematic indicators (Burrato *et al.*, 2003;

Boccaletti *et al.*, 2004; 2011; Scrocca *et al.*, 2007).

This debate found a practical example on May 20 and 29, 2012 when two moderate earthquakes ($M_W = 6.1$ and 5.9 ; Pondrelli *et al.*, 2012) hit a wide area of the eastern sector of the Po Plain, causing 27 casualties, thousands of injuries, severe damages to historical centers and industrial areas.

The Emilia seismic sequence had a relevant social, cultural, emotional and economical impact but, from the scientific point of view, represented an important case study. This research has been realized in the frame of the PhD Spinner Project EGEST (“Effetti geologici superficiali del terremoto emiliano 2012: studi finalizzati al miglioramento della sicurezza e sostenibilità dello sviluppo territoriale”; coord. R. Caputo), promoted by the Regione Emilia-Romagna in the following months after the earthquakes, and of the Seismic Microzoning Project of the Sant’Agostino Municipality (western Ferrara Province). The major aim of this Ph.D. project was the application of different geological, geotechnical and geophysical strategies in order to emphasize the recent tectonic evolution of this sector of the buried Northern Apennines and improve the knowledge of such properties for the shallow subsoil, as they play a key role in controlling the coseismic effects of the earthquakes.

A relevant coseismic effect due to the reactivation of reverse blind faults, as in the case of the Po Plain, is the bending of the topographic surface and the consequent uplift of the broader epicentral area. The occurrence of active tectonic structures responsible for the local uplifts and even for the complex interactions with the hydrographic network have influenced not only the distribution of the sediments on the surface, but also in the subsoil (down to some tens of meters), thus producing important stratigraphic variations and therefore also changes in the geophysical properties of the materials. These are particularly evident in the deeper geology (Pieri and Groppi, 1981; Boccaletti *et al.*, 2004; 2011; Ghielmi *et al.*, 2010), but they could be also recognized within the shallow deposits (RER & ENI-AGIP, 1998; Molinari *et al.*, 2007; Calabrese *et al.*, 2012).

The Po Plain, as other alluvial plains, are among the most densely populated areas worldwide, because of the combination of morphological, hydrological and geological factors that make them advantageous for human settlements. Considering the wide exposure

of the Po Plain and its seismogenic potential, it is clear that the seismic hazard is particularly high. Therefore, determining the space distribution of the uplift rate together with the location of active faults is of utmost concern not only for reconstructing the recent tectonic evolution of the region, but also to help understanding where active faults are located.

The assessment of the base seismic hazard is not sufficient for the definition of the seismic action in similar seismotectonic contexts, as it provides an evaluation of ground shaking for rock or stiff soil conditions (i.e. seismic bedrock) that can be subject to considerable modifications due to local effects, in terms of peak values, duration and frequency content, showing different values over short distances. Moreover, the near-surface geological conditions in the upper tens of meters at soft sites are one of the dominant factors in controlling the occurrence of coseismic effects and consequently the earthquake damage patterns (Boatwright *et al.*, 1991; Caserta *et al.*, 1999; Margheriti *et al.*, 2000), as it was observed for the May 2012 Emilia seismic sequence (Bordoni *et al.*, 2012).

Therefore, the undeniable need of a careful and reliable assessment of site amplification phenomena led to develop many techniques to identify the main characteristics of site response in case of soft deposits. The approaches based on numerical simulation (see Panza *et al.*, 2001 for a review) coupled with dedicated geophysical and geotechnical surveys (penetrometric tests, cross-hole, boreholes, etc.), suffer severe limitations in urbanized areas because of their cost and environmental impact. Other techniques consist in directly measuring the site response from earthquake recordings. Although this is the best approach because it provides an unbiased experimental estimation of the site transfer amplification factor, its application is restricted to areas with relatively high rates of seismicity and hence of seismic records (Bonney-Claudet *et al.*, 2006). In general, within the several geophysical methods applied for the assessment of the site effects, it has been widely accepted that the shear-wave velocity (V_s) profile can be a good parameter for their quantitative evaluations (Okada, 1986; Ohori *et al.*, 2002). However, getting the in situ V_s through direct surveys (e.g. active seismic methods) can be too expensive to carry out over wide areas. Thus, the application of non-invasive and indirect techniques to assess or supplement the shear-wave velocity measurements is particularly attractive.

Since the pioneer work by Kanai *et al.* (1954), methods exploiting the seismic ambient noise have been studied and became very popular as a tool to estimate seismic site responses because its measurement is much easier than earthquake observations and is suitable for inference of spatial variability of seismic site responses (i.e. microzoning). Nowadays, two noise-based techniques are largely used to determine site response parameters: the horizontal to vertical Fourier amplitude spectral ratio (HVSR or H/V) and the more advanced array techniques (e.g. ReMi, SPAC, ESAC). The HVSR strategy was first proposed in 1970 by Nogoshi and Igarashi, but it became popular after Nakamura's (1989) contribution. Notwithstanding the lack of theoretical agreement about the interpretation of this ratio, the frequency corresponding to the maximum value of the H/V function (f_0) was shown to have a strict correspondence with the local resonance frequency of the sedimentary cover (f_r) (see Bonnefoy-Claudet *et al.*, 2006; Lunedei and Albarello, 2010; Albarello and Lunedei, 2011; Tuan *et al.*, 2011). This evidence is particularly important because it means that the f_r is directly linked to the thickness of the sedimentary cover. Accordingly, in case some information about the local shear-wave velocity profile is available, the H/V curves represent an effective exploratory tool for seismic microzoning studies and geological surveys, allowing to obtain the depth of the resonant interface(s). The various array strategies consist in recording the seismic noise by means of an array of sensors. These methods exploit the dispersive properties of the surface waves for the calculation of the dispersion. Relevant information concerning phase velocities of waves propagating across the array are obtained from average cross-spectral matrixes relative to sensor pairs. Afterwards, the Vs profile is obtained from the inversion of the dispersion curve.

For microzoning purposes, such measurements were generally carried out in a sparse way, in order to cover the entire territory. The idea was to perform several investigations along alignments in order to reconstruct reliable pseudo-2D sections, several kilometers-long, so emphasizing the possible occurrence of lateral shear wave velocity (and amplitude) variations, which will likely reflect the stratigraphic changes and hence evidences of a recent tectonic evolution. Additionally, through the inversion of HVSR curves, the following step consisted in retrieving the depth of the major impedance contrast(s) and 'follow' these

surfaces along the entire investigated transects.

The most common geotechnical investigations especially in the professional activity, are the cone penetration tests, which are low-cost indirect surveys that could achieve continuous measurements of some geotechnical parameters of the soil (i.e. tip resistance q_c , lateral friction f_s and, wherever possible, the water pressure u_2). The repeatability of such measurements, the opportunity to investigate a huge volume of soil and, as mentioned above, the continuous measurements of parameters that highlight the stratigraphic features, make these tests ideal tools for the identification of lithological variations and for the reconstruction of the stratigraphic profile (Lo Presti *et al.*, 2009). Additionally, coupled with a reliable analysis of the seismic hazard, these surveys provide the basic ingredients for the computation of the susceptibility to liquefaction of a soil.

The issues previously described were investigated through the application of the above described methodologies, thus concretising in four case studies briefly described in the following.

Geophysical pseudo-2D sections. A set of geophysical surveys were carried out across some major tectonic structures of the eastern Po Plain, belonging to the central sector of the Ferrara Arc. The investigations included several passive seismic measurements carried out along a profile running from Cento to Bondeno (western Ferrara Province), ca. 27 km-long and oriented SSW-NNE, i.e. almost perpendicular to the regional trend of the buried structures of the Ferrara Arc. Were applied the ESAC strategy (Aki, 1957; 1964) to obtain several 1D shear-wave velocity profiles, subsequently assembled to reconstruct pseudo-2D velocity sections providing information about the shallow subsurface (100-150 m depth), and the HVSR technique (Nakamura, 1989) to infer the resonant frequency(ies) of the investigated sites. Based on a constrained inversion between the Vs profiles and the HVSR curves, the depth of the major impedance contrast(s) were also estimated.

Tectonic deformation versus site effects. As a consequence of the May 2012 Emilia seismic sequence, ground deformations were induced at different scales involving areas from a few meters to several hundred meters in size; they caused horizontal movements up to several centimeters (i.e. lateral spreading), and both positive and negative vertical movements,

the latter generally much more frequent and locally exceeding some tens of centimeters. These effects on the earth's surface occurred with a jeopardized pattern, thus influencing both terrestrial (i.e. High Precision Levelling) and satellite-based techniques (i.e. DInSAR), albeit in different ways. The comparison of the results of both geodetic techniques substantially agree, although there were some noticeable local discrepancies along the village of Sant'Agostino-San Carlo-Mirabello (western Ferrara Province), for which were documented spectacular and locally very intense liquefaction. Through the analysis of the distribution of the surface manifestations, geomorphological features and geognostic surveys, it was also possible to document how local site effects (i.e. liquefaction) can strongly influence the local elevations even completely reversing the large-scale tectonic signal.

Seismic Microzoning of the Sant'Agostino Municipality. A significant part of my Ph.D. was carried out in the frame of a dedicated research project financed by the Municipality of Sant'Agostino (western Ferrara Province), aimed to the realization of the Seismic Microzoning study for the whole territory. Following the seismic sequence of May 2012, with the Ordinance 70/2012 the President of the Regione Emilia-Romagna predisposed the realization of seismic microzoning studies, limited to the urbanized areas, for the most damaged municipalities, including Sant'Agostino. Thus, all the activities were carried out in a complementary and synergistic way with the Geological Survey of the Regione Emilia-Romagna, in order to provide to the local Administration a refined survey of the entire territory. The major outcomes of the microzoning study were represented by a series of maps where the areas subject to possible coseismic effects (e.g. liquefaction, site fundamental resonance frequency and amplification, etc.) in case of future seismic events were clearly delimited.

Quantitative assessment of liquefaction potential. The existing post-earthquake reports and the availability of geotechnical data provided by in-situ tests allowed to compute liquefaction potential parameters for two test areas, Mirandola (northern Modena Province) and Sant'Agostino (western Ferrara Province). In particular, the Liquefaction Potential Index (LPI, Iwasaki *et al.*, 1978) and the Liquefaction Severity Number (LSN, Tonkin and Taylor, 2013) were evaluated and then correlated by considering liquefaction phenomena ei-

ther observed on site or not.

As a final comment, in geological and seismotectonic conditions similar to those characterizing the 2012 Emilia epicentral area, where the seismic bedrock is buried beneath a thick sedimentary cover and the hydrocarbon exploration provide important information about the deeper geology, the application of a multidisciplinary approach based on the techniques above mentioned, allows the geological, geotechnical and geophysical characterization of the shallow subsurface, therefore indirectly contributing to a better mitigation of the seismic risk.

Chapter 2

The Po Plain: an evolving foredeep basin

2.1 Geodynamic and stratigraphic evolution of Northern Italy

The Po Plain represents the widest flat area of Italy, extending for over 400 km in an approximately E-W direction from the western Alps to the Adriatic Sea, and it corresponds to the drainage basin of the Po River. The morphological boundaries of the plain are represented by the contact between the Quaternary alluvium outcropping in the plain, the Southern Alps to the north and the exposed portion of the Northern Apennines to the south (Fig. 2.1).

The Southern Alps are a post-collisional chain formed by the overlapping of south-verging Permian-Mesozoic and Tertiary sedimentary succession, thrust and folded since the Eocene to Pliocene-Quaternary (Castellarin, 2001). The Northern Apennines are a fold and thrust belt with northeastward convexity and vergence (Barchi *et al.*, 2001), developed mainly in Neogene times in the framework of the collision between the European continental margins (Sardinia-Corsica block) and the Adriatic microplate (e.g. Alvarez, 1972; Reutter *et al.*, 1980).

Given the lack of exposed structures, the structural setting of the Po Plain was imaged for the first time during the past decades by a dense grid of reflection seismic profiles in the frame of hydrocarbon and water resources explorations (AGIP Mineraria, 1959; Aquater, 1976; 1978; Aquater-ENEL, 1981). Following the results of these researches several authors



Figure 2.1: Satellite image of the Po Plain.

focused their attention on this area, contributing with their studies to a more detailed reconstruction of the structural characteristics of the basin and of the sedimentary cover (Rizzini and Dondi, 1979; Pieri and Groppi, 1975; 1981; Bartolini *et al.*, 1982; Pieri, 1983; Castellarin and Vai, 1986; Boccaletti *et al.*, 1987; 1990; 2004; 2011; Bigi *et al.*, 1992 ; Doglioni, 1993; RER & ENI-AGIP, 1998; Amorosi *et al.*, 1999; Castiglioni and Pellegrini, 2001; Molinari *et al.*, 2007; Amorosi, 2008; Fantoni and Franciosi, 2008; 2010; Amorosi *et al.*, 2014). By the synthesis of these studies it is possible to define the Po Plain as a foredeep basin originated since the Cretaceous for the progressive migration of the African plate toward the European one, following the subduction of the interposed Adria microplate (Channell *et al.*, 1979; Pieri and Groppi, 1981).

The present tectonic configuration (Fig. 2.2) is the result of a series of main tectonic phases listed below (Abbate *et al.*, 1986; Boccaletti *et al.*, 1990; Dalla *et al.*, 1992; Treves, 1992; Frepoli and Amato, 1997; Centamore *et al.*, 2002; Rosenbaum and Lister, 2005; Carminati *et al.*, 2012):

- the rifting phase, with the opening of the Ligurian-Piedmont Ocean, since Late

Triassic-Liassic;

- the oceanic convergence phase, with the closure of the Ligurian-Piedmont Ocean due to the eastward movement of the Iberian block, since Late Cretaceous;

- the Africa-Europe continental collision (Early Eocene to Late Oligocene) during which the Apennines tectogenesis began (ensialic phase);

- the opening of the Balearic and Tyrrhenian Basins, started with the rifting in an E-W direction of the continental lithosphere of the Corsica-Tuscany block from Late Oligocene, has driven the east-northeast shifting of the Apennines thrust-belt-foredeep system that progressively incorporated more external sectors of the foreland (Late Oligocene- Early Miocene to Late Pliocene);

- the late and post-orogenic phase (from Late Pliocene onward) during which the evolution of the foredeep was driven by a thrust system evolving in a piggy-back mode towards the foreland to the northeast.

Since Middle Pliocene, the migration of the flexural margin of the foredeep was locked by the previously formed opposite verging Southern Alps structures, thus favoring the development of out-of-sequence thrusts.

The evolution of the Po Basin is strictly connected with the activation of the Mesozoic carbonate basement (Centamore *et al.*, 1986; Dondi & D'Andrea, 1986; Cresta *et al.*, 1989; Passeri, 1984) overthrusts and/or developing of new-formed thrusts in the overlying sequence (Boccaletti *et al.*, 1987).

Starting from the Late Oligocene, the formation of the Apennines chain led to the development of deep and subsiding foredeep basins, wherein thick turbidites sequences and low sea deposits were accumulated in marginal basins of modest size (M cycle, Ricci Lucchi *et al.*, 1982). Therefore, the Po Basin becomes an active continental margin related to the development of two synorogenic molassic basins: the oldest linked to the formation of the Alps and a younger one (post-Messinian) related to the Apennines domain (Astori *et al.*, 2002). Since the end of Miocene, the progressive shift of the Apennines thrust belt caused flexural collapses in the Po foreland and therefore the development of a strongly subsiding basin, the Po-Adriatic molassic foredeep (Cremonini and Ricci Lucchi, 1982; Gasperi *et al.*,

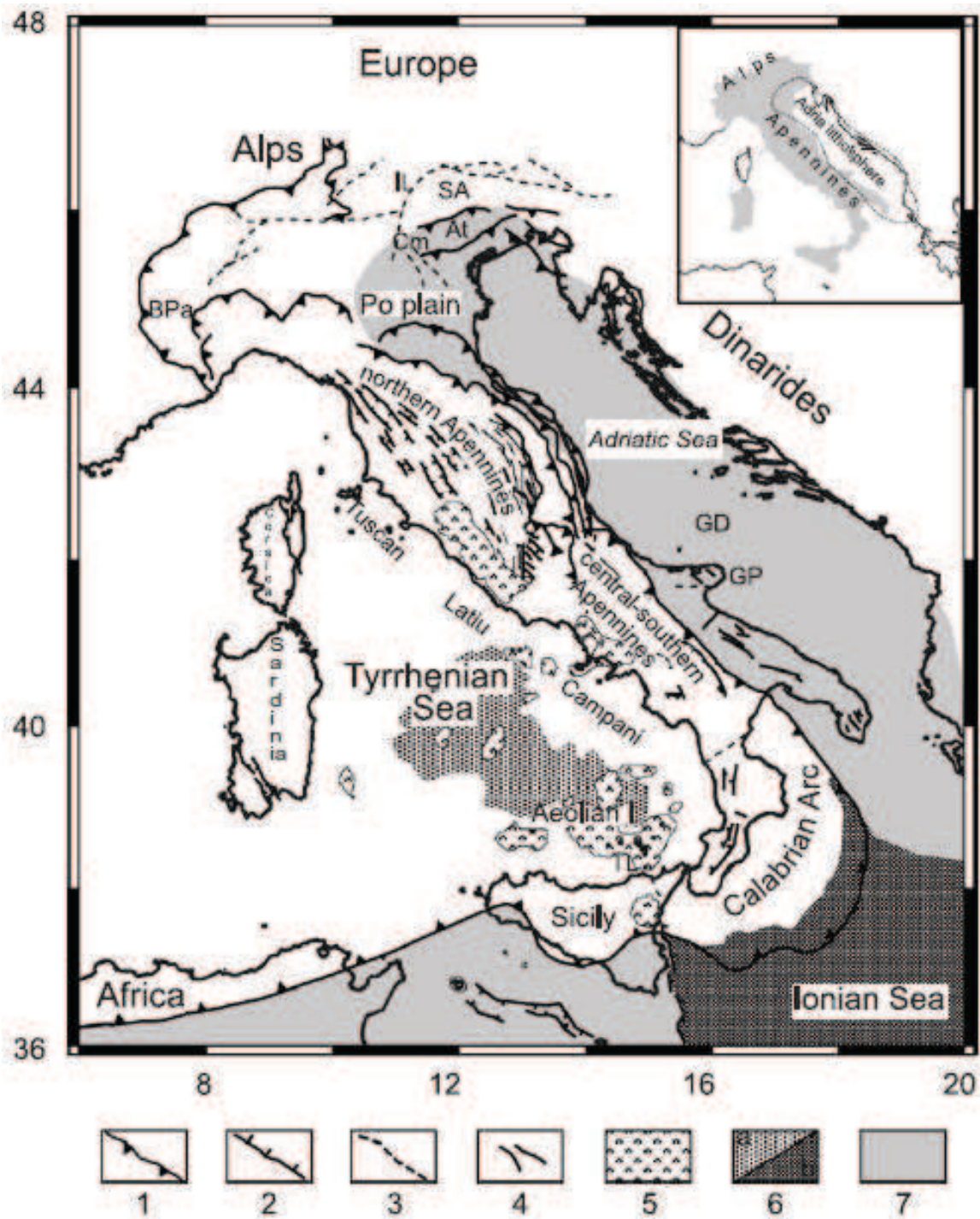


Figure 2.2: Tectonic setting of Apennines-Tyrrhenian domain. 1) main thrusts, 2) normal faults, 3) buried tectonic lines, 4) fold axes, 5) volcanic centers, 6a) new-formed oceanic crust, 6b) deep basins in the African-Adriatic domain and 7) African and Adriatic foreland (modified from Margheriti *et al.*, 2003).

1984; Castellarin *et al.*, 1985). This deformative phase caused the emersion of the Apennines chain and for the first time a fluvial drainage system start feeding the foredeep basin (Ricci Lucchi *et al.*, 1982). Between the Late Messinian and Early Pliocene, a complex

sedimentary cycle (M-P1 cycle, Ricci Lucchi *et al.*, 1982) related to the gradual drying of the Mediterranean ended (Gelati *et al.*, 1989; Butler *et al.*, 1985; Vai, 1997 ; Cavazza and Wezel, 2003). This led to a generalized “regression” phenomenon in the basinal area that favoured the deposition of evaporitic sediments (Dondi *et al.*, 1982; Roveri *et al.*, 2001) in the marginal sector, whereas in the central part of the basin the turbiditic sedimentation continued (Castellarin *et al.*, 1985). After the end of the Messinian salinity crisis, the rapid rise of the sea level restored marine environments above the areas which were previously emerged. Predominantly pelitic deposition affected these sectors, while in the deepest ones prevailing arenaceous-pelitic turbidites (Dondi and D’Andrea, 1986). Since Lower Pliocene (3.9-3.6 Ma), the migration of the deformation front to NE and the subsequent activation of the buried thrust and folds arcs below the Po Plain (P2 cycle, Ricci Lucchi *et al.*, 1982) led to a substantial modification in the geometry of the foreland basin. The distribution of different facies (e.g. sand and conglomerates in the intra-apenninic area and turbidites in the N-NE sector of the basin) denotes that, from Pliocene onwards, there was not a continuous fore-deep but several depocenters delimited to the north by the Emilia and Ferrara Arcs (Dondi *et al.*, 1982; Dondi and D’Andrea, 1986). The transition between Pliocene and Pleistocene is marked by an unconformity (1.73 Ma) that can be considered as the base of the Quaternary Marine cycle (Qm, Ricci Lucchi *et al.*, 1982).

At the end of Lower Pleistocene (1.1 Ma), the continuous uplift of the Apennines chain, starting from the western portion of the basin, promoted the marine regression and thus the development of shallower environments (cartographic unit 4; ; Boccaletti *et al.*, 2004). Starting from the early Middle Pleistocene (0.8-0.65 Ma) an unconformity highlighted a new uplift phase: the deposition of coastal sands (cartographic unit 3; Boccaletti *et al.*, 2004) along the entire apenninic margin thus ending the Lower Pleistocene Marine cycle (Qm, Ricci Lucchi *et al.*, 1982). Moreover, the persisting uplift phase led to the definitive development of continental environments marked by the deposition of the Emiliano-Romagnolo Supersynthem (RER & ENI-AGIP, 1998; Qc cycle, Ricci Lucchi *et al.*, 1982). In the sheets of the Geological Map of Italy (scale 1:50.000) of the Po Plain, made by the Regione Emilia-Romagna, the Emiliano-Romagnolo Supersynthem is divided into two syn-

tems: the Lower (AEI; 0.65-0.45 Ma) and Upper Emiliano-Romagnolo Synthems (AES; 0.45 Ma-Holocene). The former consists of Po fluvio-deltaic facies (i.e. silty clay with sand intercalations), while the latter of floodplain fluvial facies of Apennines origin (Boccaletti *et al.*, 2004). The discordance that separates the continental deposits from the marine ones is generally marked by an angular unconformity, as well as the discontinuity between AES and AEI Synthems. In addition, also the AES deposits may lie directly above marine ones and this configuration represents the most recent angular unconformity (0.45 Ma; Boccaletti *et al.*, 2004). The AES Synthem consists of a series of different depositional cycles, referred to as subsynthems, whose limits are placed in correspondence of the base of the “transgressive” marine deposits. The ‘transgressive’ basal portion of each subsynthem lies above the fluvio-deltaic sandy sediments of the underlying cycle and is characterized by the presence of fine material (e.g. floodplain, marsh and coastal plain clays) with subordinated sandy intercalations. In contrast, the ‘regressive’ portion consists of alluvial plain deposits (e.g. fine sediments of overflowing river) where channel sands are subordinated in the form of isolated lenticular bodies. On the top of each cycle channel sands become abundant, thus forming laterally wider bodies (RER & ENI-AGIP, 1998; ISPRA, 2009). Starting from the bottom of the AES Synthem it is possible to distinguish at least two depositional cycles that, due to the lack of information, were grouped together (Upper Undifferentiated Emiliano-Romagnolo Synthem - AESind, Middle Pleistocene; RER & ENI-AGIP, 1998; ISPRA, 2009). Above the latter, can be identified three most recent subsynthems that were correlated with just as many depositional cycles (RER & ENI-AGIP, 1998; ISPRA, 2009), respectively named:

- AES6 (Bazzano Subsynthem, Middle Pleistocene);
- AES7 (Villa Verrucchio Subsynthem, Late Pleistocene);
- AES8 (Ravenna Subsynthem, Late Pleistocene-Holocene).

Locally, overlying the AES8 Subsynthem, it is possible to find out the presence of a few meters-thick unit (up to 10 m in correspondence of fluvial ridges) named Unità di Modena (AES8a), mainly characterized by floods river deposits (ISPRA, 2009). Historical and archaeological data suggest that this unit began its deposition since IV-VI century A.D. (Bondean, 1986; Ciabatti and Veggiani, 1990; Montevicchi and Novara, 2000; Veggiani, 1987).

In summary, the architecture of the Po Plain filling is characterized by a generally “re-
gressive” trend, interrupted by lesser fluctuations, evidenced by the transition from offshore
Pliocene deposits, to marine-marginal and then to alluvial Quaternary sediments (Ricci Luc-
chi, 1986).

2.2 The buried structures of the Po Plain

The most impressive features of the Po Plain are buried beneath a thick syntectonic succes-
sion, deposited in the Neogene-Quaternary foredeep. This configuration is the result of the
combination of fast subsidence-sedimentary rates and conversely low tectonic ones, which
promoted the deposition of a thick clastic succession, sealing the external fronts of North-
ern Apennines. Indeed, the real Northern Apennines front is located in the central-southern
portion of the Po Plain and is represented by four major arcs, consisting of blind thrusts and
folds: from west to east are distinguished the Monferrato Arc, the Emilia Arc, the Ferrara
Arc and the Adriatic Arc (Costa, 2003; Fig. 2.3).

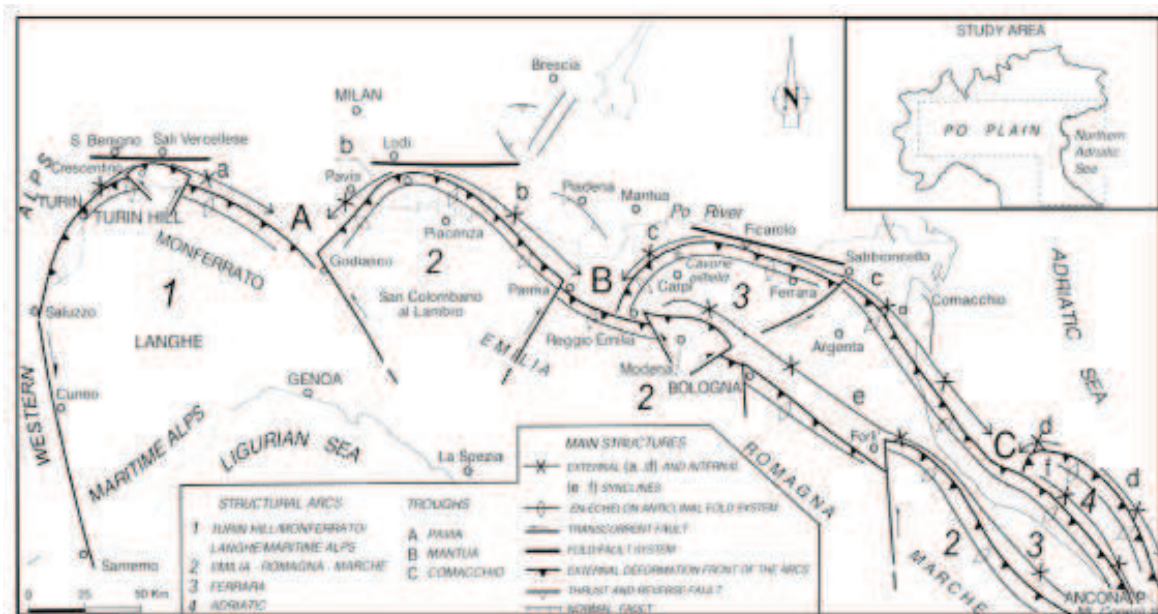


Figure 2.3: Po Plain and northern Adriatic Sea: the four buried structural arcs and main tectonic features (from Costa, 2003).

The arcs have a similar structure and asymmetry. The western side strikes NE-SW
to NNE-SSW and is characterized by NW-verging, compressive, low-angle frontal struc-

tures; conversely, the eastern side strikes WNW-ESE to NW-SE and is characterized by NE-verging, compressive, high-angle frontal structures (Costa, 2003).

The Ferrara Arc, running from Reggio Emilia to the Adriatic Sea and Marche coast, consists of Messinian-Quaternary autochthonous and parautochthonous terrigenous deposits overlying Mesozoic to Paleogene carbonate units (Pieri and Groppi, 1981; Nardon *et al.*, 1991).

The outer border of this arc is marked by a set of structural highs originated by fold-fault system arranged roughly en-echelon (e.g. Bagnolo, Cavone, Casaglia, Argenta; Pieri and Groppi, 1981); while the inner and outer portions of the arc are depressed and covered by a thicker Pliocene-Quaternary sequence. The arc started to develop in Early Pliocene (Costa, 2003) with widespread uplift of the external margin and the formation of the above-mentioned structural highs. Activity is still ongoing, as evidenced by the May 2012 Emilia seismic sequence. As a consequence, the syntectonic Early Pliocene deposits are reduced or absent in correspondence of the tectonically uplifted areas (Pieri and Groppi, 1981).

For better understanding the present-day subsurface configuration two geological sections are reported and discussed in the following. Their location is shown in Fig. 2.4a and they are based on the interpretation of seismic reflection profiles (Boccaletti *et al.*, 2004).

The geological section B-B' (Fig. 2.4b) extends from Modena to Mirandola. It highlights the presence of two major buried tectonic structures: the southern one coincides with the eastern extremity of the Emilia Arc, while the northern is part of the Ferrara Folds. These structures are set on the Miocene turbidites units (M in Fig. 2.4b). Below the city of Modena, between 2 and 6 km-depth, exist a series of thrusts and reverse faults. Moving to the north, it is possible to recognize the presence of a broad depression, known as Carpi-Cento basin (Serva, 1990), filled by a few kilometres-thick post-Messinian deposits where the Miocene turbidites generate an asymmetric syncline. Regarding the Ferrara Arc, the compressive tectonic led to the development of a structural high associated with a fault-propagation-fold (Mirandola anticline) whose three-dimensional geometry is controlled by synthetic and antithetic faults.

The geological section C-C' (Fig. 2.4b), running between Bologna and the Po River,

highlights the progressive thinning of the Miocene turbidites moving toward the Ferrara Folds. In this area the Meso-Cenozoic carbonate succession is tectonically uplifted almost to the ground surface as well as the Triassic sequence and the underlying crustal basement, which lies less than 10 km-depth. These profiles emphasize that the main overthrusts cutting the Triassic and the Meso-Cenozoic sequences clearly propagate into the Miocene turbidites; in addition, these structures are connected at depth with compressive structures affecting the carbonate sequence and the basement (Boccaletti *et al.*, 2004; 2011).

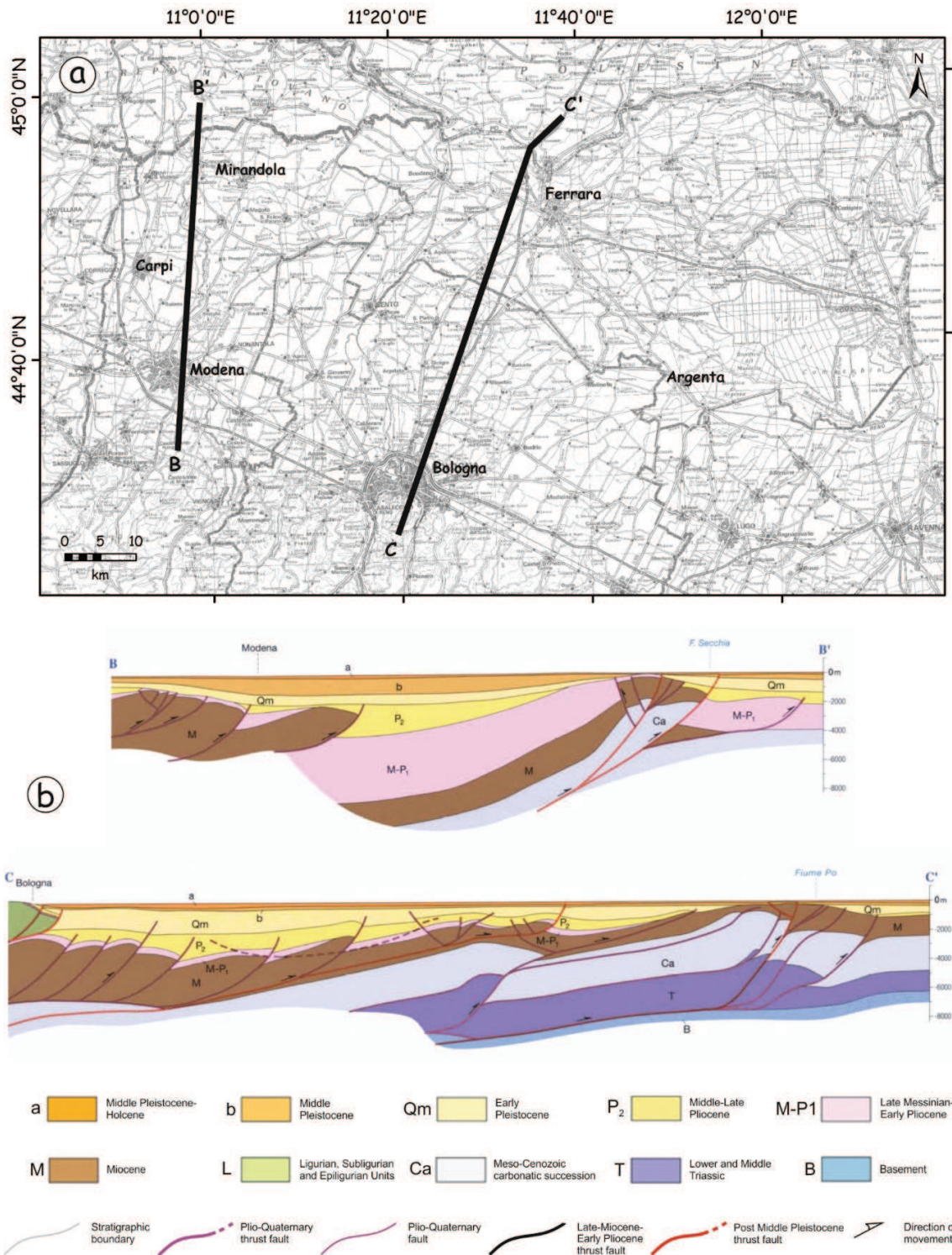


Figure 2.4: a) Location of two seismic lines that cross the central-eastern sectors of the Po Plain. b) Interpreted seismic lines (from Boccaletti *et al.*, 2004).

2.3 Recent tectonic evolution of the Ferrara Arc: evidences and implications

2.3.1 Seismological and geodynamic evidences

As mentioned before, the developing of the Northern Apennines mainly began during Late Oligocene and the process is still active, as highlighted by young and evolving morphologies (e.g. evidences of uplift and subsidence), structural analysis, geophysical studies and seismological evidences.

According to the latest version of the Italian seismic catalogue (Rovida *et al.*, 2011), the Ferrara Arc has a centuries-old seismic history (Fig. 2.5). Several events are reported for the city of Ferrara, as the March 20, 1234 ($M_W = 5.1$, $I_0 = 7.0$; Fig. 2.5, #3) and the February 22, 1346 earthquakes ($M_W = 4.9$, $I_0 = 6.5$; Fig. 2.5, #1) The most relevant historically known local event is the so-called 1570 Ferrara earthquake ($M_W = 5.4$, $I_0 = 7.5$; Fig. 2.5, #4): this event was characterized by a complex seismic sequence that started on November 17, 1570 with four strong shocks, went on with closely spaced aftershocks up to early 1572 and then have gradually run out over the following couple of years (Guidoboni *et al.*, 2007). Few years after, on March 17, 1574 a moderate earthquake affected the western portion of the Ferrara Arc, near Finale Emilia ($M_W = 4.7$, $I_0 = 6.0$; Fig. 2.5, #2). On March 19, 1624 a moderate earthquake ($M_W = 5.4$) struck the southeast sector of the Ferrara Arc, reaching a maximum intensity of 8-9 MCS close to the town of Argenta (Guidoboni *et al.*, 2007). Two similarly-sized earthquakes occurred in 1796 ($M_W = 5.6$, $I_0 = 7.0$) and 1909 ($M_W = 5.5$; $I_0 = 6.5$). In Fig. 2.6 the epicenters of the recorded earthquakes in the Emilia Romagna Region, in the time span 1983-May 2012 (ISIDe, <http://iside.rm.ingv.it/>), are shown. The overall framework of the instrumental seismicity shows that most of the available data are represented by low magnitude ($M \leq 3$) events prevalently located on the exposed sector of the Northern Apennines chain, in the first 10 km and between 20 and 60 km-depth. The only exceptions are represented by two areas located in the central-western sector of the Ferrara Arc, near Reggio Emilia and between Mirandola and Bondeno, where the seismic energy released in the selected time-span is higher relative to the surroundings areas.

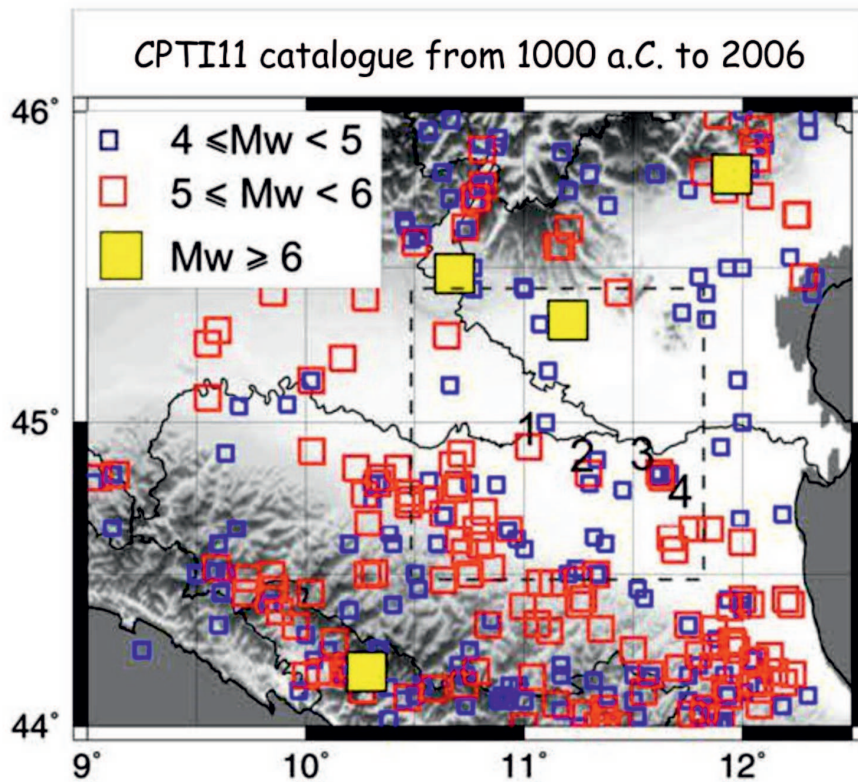


Figure 2.5: Historical seismicity of the Regione Emilia-Romagna, from 1000 a.C. to 2006 (from Carannante *et al.*, 2015).

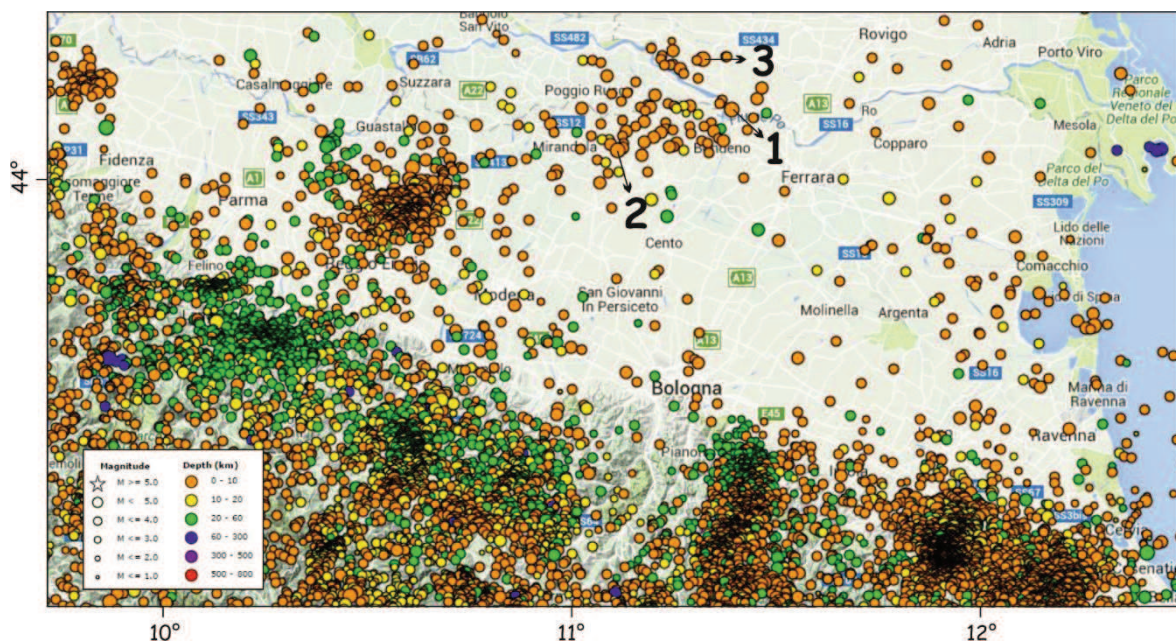


Figure 2.6: Instrumental seismicity of the Emilia-Romagna Region between 1983 to May 2012 (data from ISIDE, <http://iside.rm.ingv.it/>).

The most recent evidence of the activity of Ferrara Folds is represented by the May 2012 Emilia seismic sequence, when two such structures WSW of Ferrara were reactivated. On May 20 and 29, 2012 two moderate earthquakes ($M_W = 6.1$ and 5.9 , respectively; Pondrelli *et al.*, 2012; Fig. 2.7), followed by a noticeable aftershock sequence (Saraò and Peruzza, 2012; Scognamiglio *et al.*, 2012) hit the central-eastern sector of the Po Plain. In particular, the two major structures involved in the process are characterized by left-stepping, largely overlapping geometry and were associated with mainly dip-slip reverse faulting, as highlighted by the fault plane solutions of the main and aftershocks (Pondrelli *et al.*, 2012; Scognamiglio *et al.*, 2012).

From 1983 until May 2012, this area was affected by only three low-moderate earthquakes: the December 6, 1986 Polesine earthquake ($M_L = 4.1$, Fig. 2.6, #1; ISIDE), the May 8, 1987 Mantova earthquake ($M_L = 4.0$, Fig. 2.6, #2; ISIDE) and the July 17, 2011 Ferrara earthquake ($M_L = 4.7$, Fig. 2.6, #3; ISIDE).

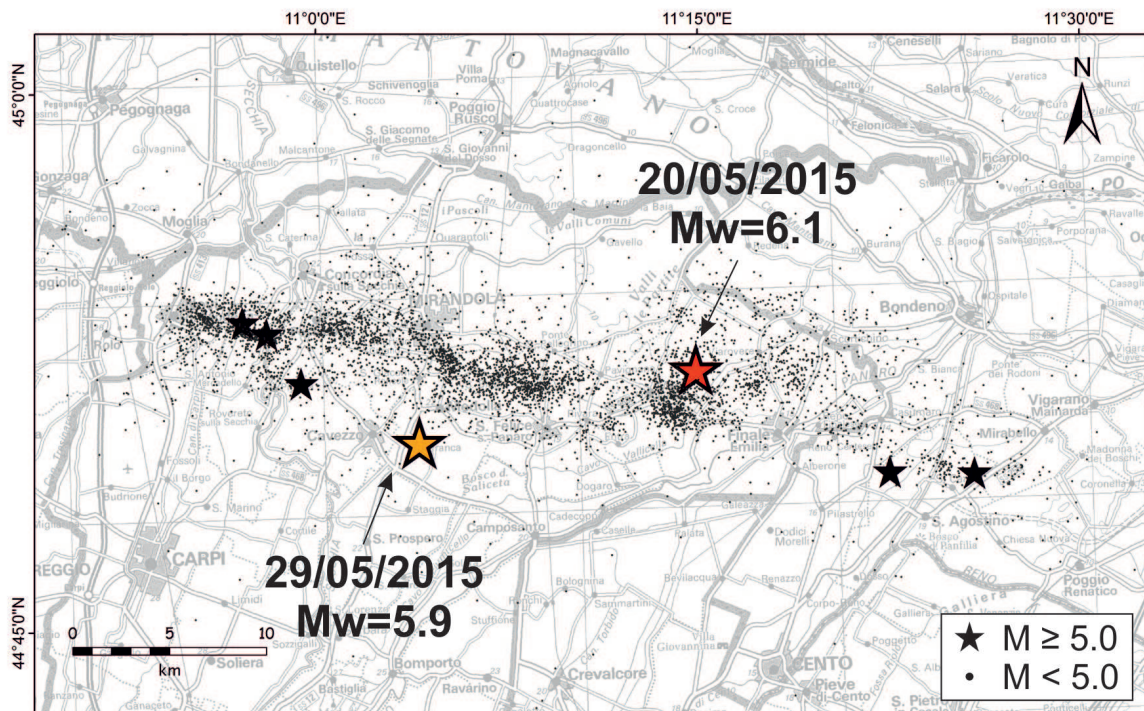


Figure 2.7: May-June 2012 Emilia seismic sequence (earthquakes location from Massa *et al.*, 2013).

A peculiar coseismic effect observed in concomitance with the May 2012 Emilia seismic sequence was the amplification of the ground motion (Bordoni *et al.*, 2012). As reported by Stucchi *et al.* (2011), one of the possible causes is the soil condition of the Po alluvial basin. Luzi *et al.* (2013) demonstrated that the structure of the Po Plain can ‘trap’ the incoming direct wavefield and convert the body waves into surface waves, thus producing relevant ground shaking (Massa and Augliera, 2013).

In Italy, other noticeable examples of site amplification in alluvial basins are the Gubbio, Città di Castello, L’Aquila and Fucino basins (Bordoni *et al.*, 2003, Bindi *et al.*, 2009; Cara *et al.*, 2001; Milana *et al.*, 2011). This behavior was observed and simulated for other important alluvial basins worldwide, such as for Los Angeles Basin (Hanks, 1975; Joyner, 2000; Somerville *et al.*, 2004), Osaka Basin (Kagawa *et al.*, 2004) and Kanto Basin beneath the city of Tokyo (Hisada *et al.*, 1993; Sato *et al.*, 1999).

Aside the ground motion amplification effects, the first shock triggered extensive liquefaction-induced ground effects at the surface, and caused severe structural damage to unreinforced masonry and precast industrial buildings within the broader epicentral area.

These effects were particularly diffuse and severe for Sant’Agostino, San Carlo and Mirabello villages (Fig. 2.8A-D), in the western Ferrara Province, which are built along an abandoned reach of the Reno River. This sector of the Po Plain is characterized by the presence of paleo riverbeds, out-flow channels and fans of the major Apennines streams crossing the area during the Holocene (Castiglioni *et al.*, 1999). Their occurrence mostly controlled the distribution of the observed liquefaction phenomena. Therefore, taking into account the age and type of the deposits, the susceptibility to liquefaction of the geological units within the investigated area is considered high following the criteria suggested by Youd and Perkins (1978).

Similar scenarios have been generated in comparable alluvial settings for example in concomitance of the 1990 Luzon Philippines, the 2007 Niigaten Chuetsu-oki Japan and the 2010 Darfield New Zealand (Wotherspoon *et al.*, 2012) earthquakes, showing that this type of geological and geomorphological settings is favorable to earthquake-induced surface ruptures and liquefaction phenomena.



Figure 2.8: A) Vent fractures with ejected sandy material. B) Sandy material covering the courtyard of a settled and shifted house. C) Surface ruptures. D) Evidence of a penetration of a clayey cap layer by a sandy material (from Caputo and Papathanassiou, 2012) .

Ongoing deformation in the Po Plain is also highlighted by GPS measurements (Serpelloni *et al.*, 2005; Devoti *et al.*, 2011). In Fig. 2.9a the velocity field in northern Italy is shown, highlighting a N-NE directed convergence between the Southern Alps and the Northern Apennines. In particular, the north-eastern thrust front (profile 1a-1b, Fig. 2.9b) is affected by a shortening trend of about 2 mm/y (Devoti *et al.*, 2011).

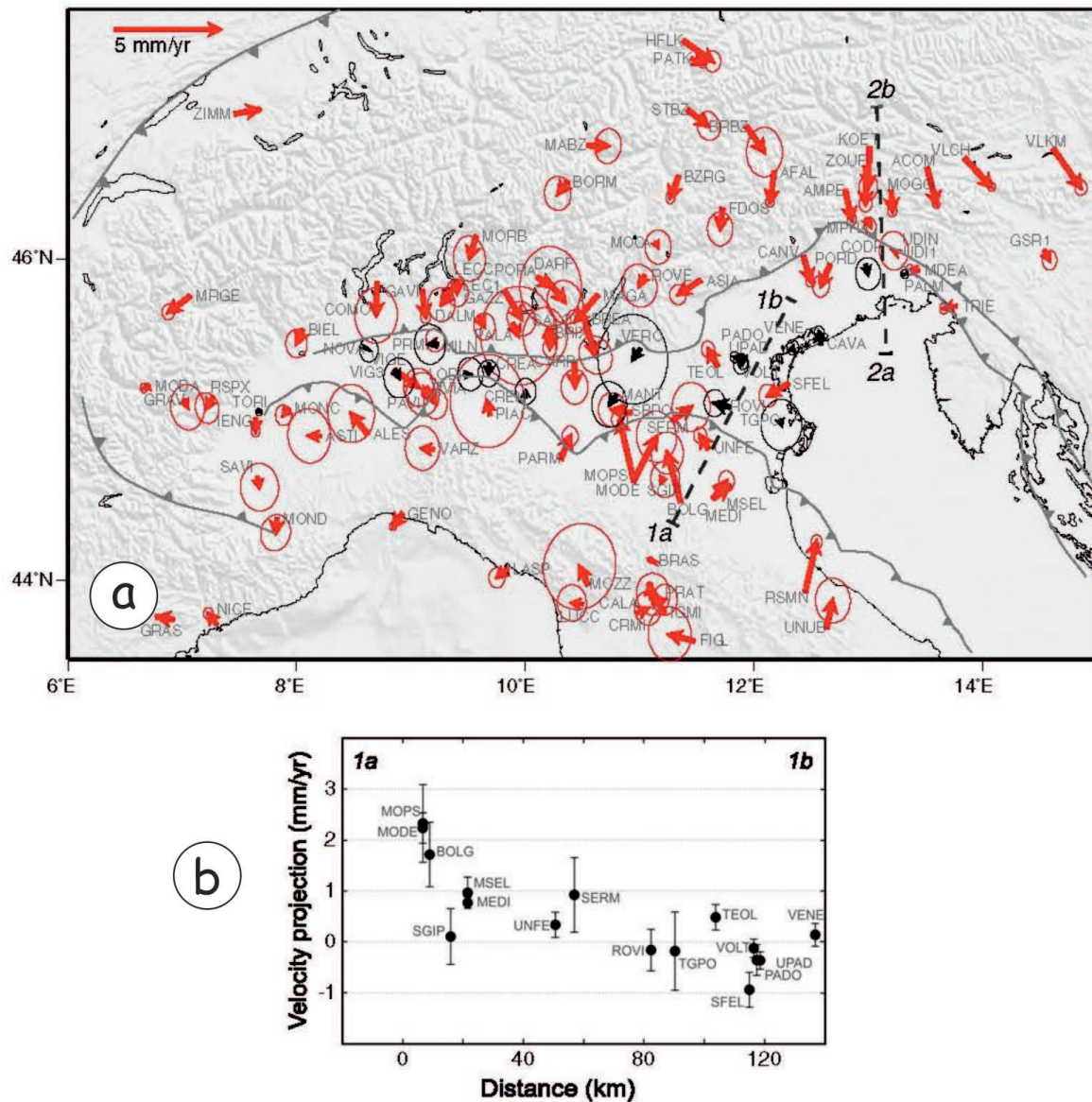


Figure 2.9: a) Velocity field in northern Italy expressed with respect to a non moving Adriatic microplate defined by sites located in the Po Plain. b) Velocity profile 1a-1b (see map), along Bologna and Venezia (from Devoti *et al.*, 2011).

2.3.2 Geomorphological evidences

The bending of the topographic surface and the consequent uplift of the broader epicentral area are among the major coseismic effects due to the reactivation of reverse blind faults as, for example, in the case of the Northern Apennines underlying the Po Plain (Burrato *et al.*, 2003). As a consequence of the geometry and kinematics of these seismogenic sources, the rock volume above the rupture is affected by a typical bending process, known as fault-

propagation folding, which led the uplift of the epicentral area and, therefore, to the deformation of the topographic surface (Bignami *et al.*, 2012; Salvi *et al.*, 2012).

In the case of the main shocks of the May 2012 sequence this phenomenon was observed in correspondence of the two epicentral areas; (Bignami *et al.*, 2012; Salvi *et al.*, 2012; Tizzani *et al.*, 2013; Caputo *et al.*, 2015). In Fig. 2.10a is reported the map of the uplift distribution, obtained by a satellite technology of differential interferometry (DInSAR; Bignami *et al.*, 2012). The overall deformation pattern, showing a maximum uplift of about 200 mm, is the result of the combination of the individual models associated with the two mainshocks: the eastern sector of the deformation field is associated with the May 20 event, while the western one to the May 29 earthquake. Another interesting observation is that the uplifted sector is surrounded by an area characterized by minor subsidence, which peaked at ca. 10 mm between Carpi and Cento (Bignami *et al.*, 2012). This pattern is in good agreement with the expected kinematics of reverse buried faults (Vannoli *et al.*, 2004).

As summarized in Fig. 2.10b, several geological, geomorphic and landscape features are particularly sensitive to the effects induced by the slip on a blind thrust (e.g. topography, thickness and shape of the growth strata, erosional/depositional behavior of the drainage network, geometry of erosional and/or depositional surfaces). Among these, the drainage network is particularly sensitive to vertical deformation and therefore useful for analyzing flat areas, where few or no landforms constrain the location of active faults (Holbrook and Schumm, 1999; Schumm *et al.*, 2000). In particular, the uplifted area is affected by erosion, lack of drainage and antecedence phenomena, while the subsiding area is characterized by attraction of drainage and deposition (Fig. 2.10b). River diversions are the most clear indicators that the stream is approaching a rising anticline or entering a syncline. The evolution of sedimentation and topography and of the geometry of geomorphic features is controlled by the growth of the anticline and of the syncline, which may or may not have a perceptible morphologic expression depending on the ratio between tectonic and sedimentation rates.

More specifically, if the rate of vertical tectonic displacement is higher than the sedimentation rate, the anticline will have a morphological expression and will be subjected to erosion, while the syncline will be represented by a depressed area that may be filled up

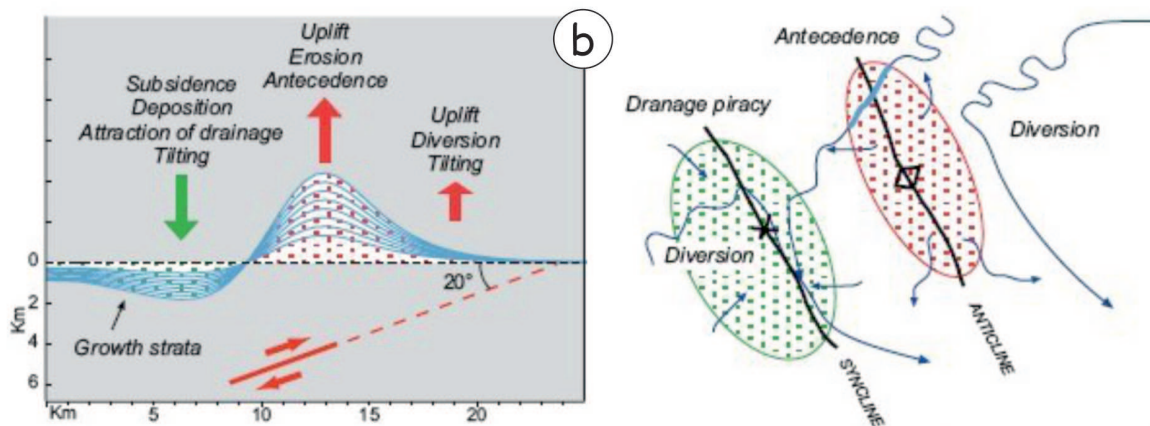
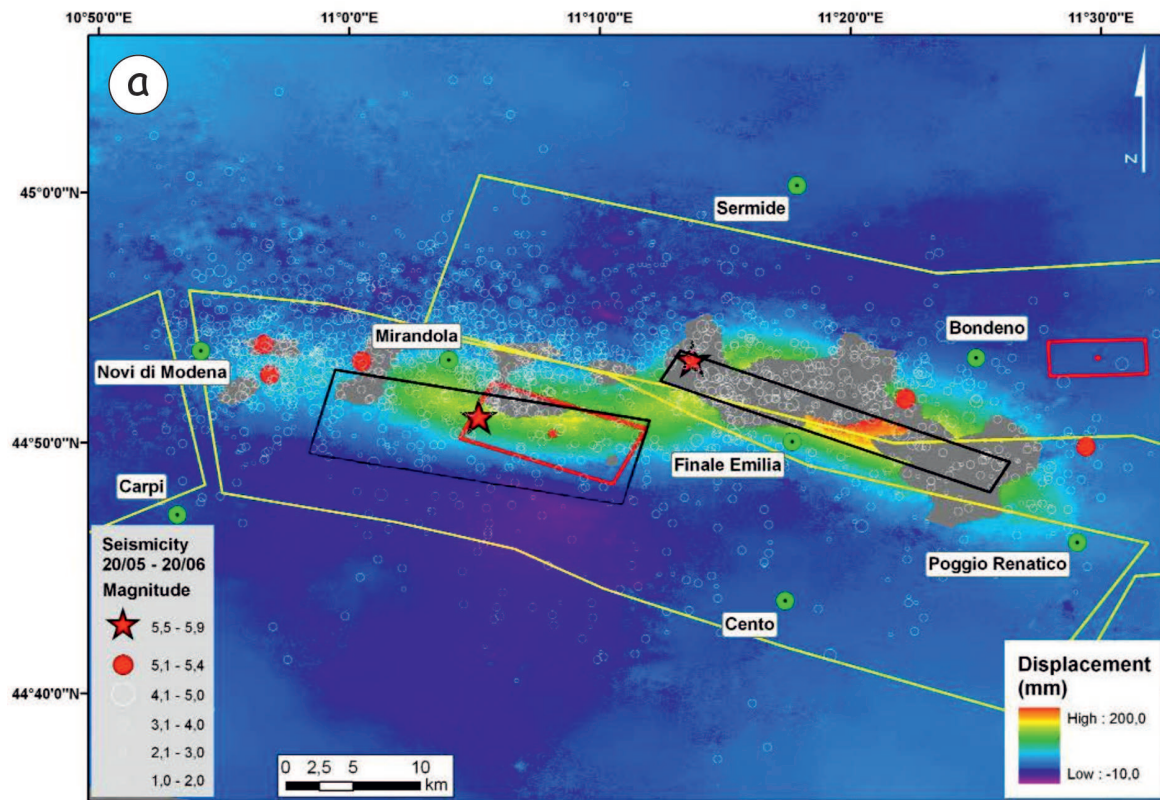


Figure 2.10: a) Deformation pattern of the May 2012 seismic sequence (from Bignami *et al.*, 2012). b) Schematic representation in map view and cross-section of the effects that slip on a generic blind, low-angle thrust fault may have on geomorphic/sedimentary processes (from Burrato *et al.*, 2003).

with sediments. The evolution of the tectonic topography created by the growth and lateral propagation of the anticline is controlled by linear and areal surface processes that tend to create a smoothed steady-state morphology (Champel *et al.*, 2002). Burrato *et al.* (2003) carried out several morphological analyses on the drainage network of the Po Plain. In selected cases, they demonstrated the concomitance of 1) the location of a drainage anomaly,

2) the existence of a buried anticline, and 3) the occurrence of significant past seismicity, thus supporting a causative link among these factors. In 2012, Burrato *et al.* recognized that the Holocene evolution of the drainage network in the central sector of the Po Plain has followed a consistent pattern through time, highlighting areas of relatively slight subsidence and uplift that spatially correspond to the buried anticline-syncline pairs of the Northern Apennines front (Fig. 2.11).

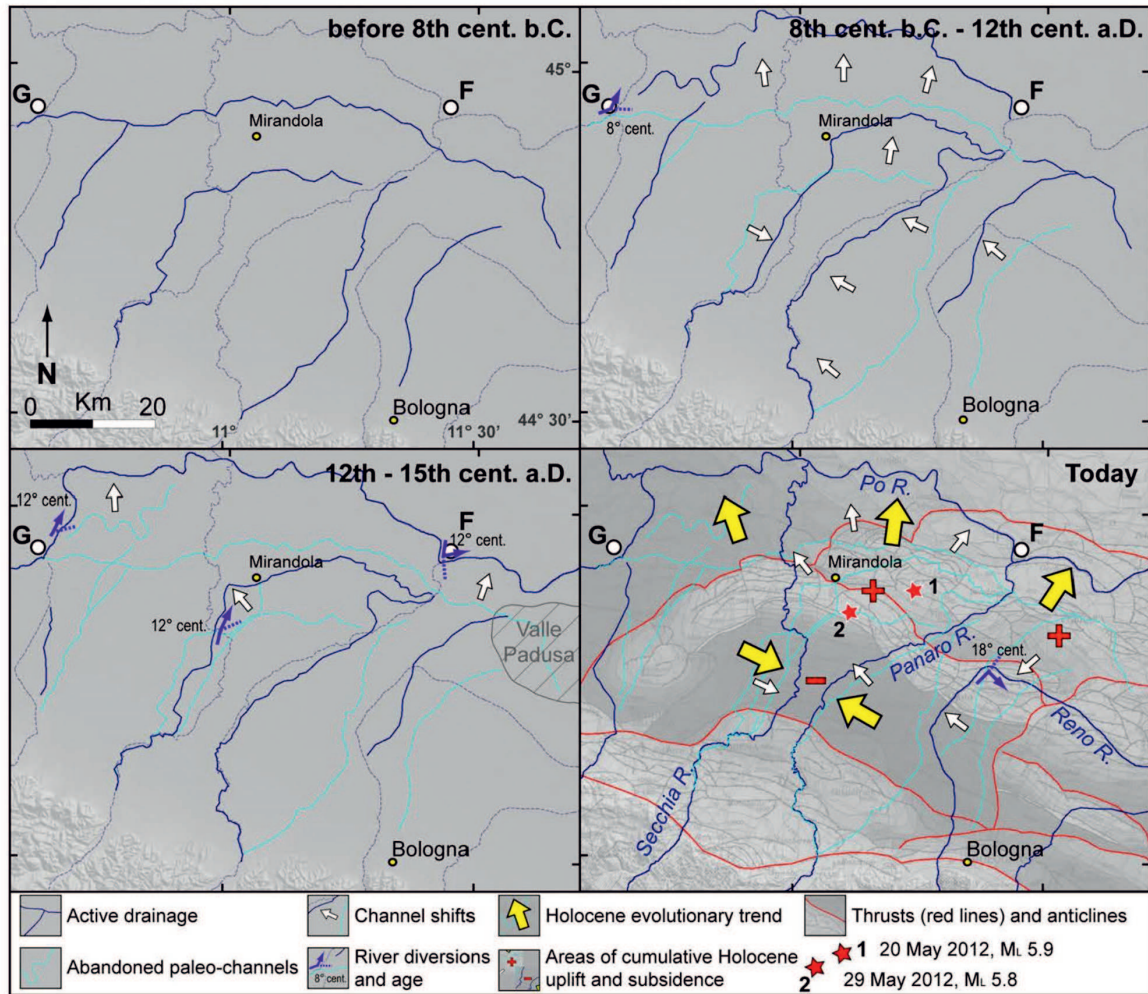


Figure 2.11: Drainage network evolution in the central part of the southern Po Plain north of Bologna (from Burrato *et al.*, 2012). The modern drainage pattern is reproduced in the background of all of the panels. The basemap of the lower-right panel is from Bigi *et al.* (1992).

Chapter 3

The western Ferrara Province

3.1 Hydrographic and morphological evolution

The present-day morphological arrangement of the western Ferrara Plain is the direct result of competition among high deposition rates, tectonic activity and differential compaction, as well as the latest Pleistocene-Holocene climatic variations. These natural phenomena basically caused differential vertical movements which governed the recent hydrographic evolution and caused highly variable (both lateral and vertical) sedimentary distribution in the shallow subsoil. As a consequence, the alluvial plain was crossed by only a few water-courses at any time, although at present it is characterized by many abandoned river channels and widespread flood deposits (Castiglioni *et al.*, 1999; Fig. 3.1). All these sedimentary bodies generally represent distinct morphological features that stand out altimetrically from the otherwise flat territory. Their topographic evidence (up to several metres) is commonly proportional to the importance of the channel and to their age. However, in the last two millennia, human activities have also played a role in the evolution of the territory.

The western Ferrara Province consists of a gently ENE dipping topographic surface ranging between 20 m a.s.l. close to Cento village to ca. 4 m east of Ferrara. The mean slope is about 0.5‰, but the gradient can be as high as 5‰ where local topographic ‘anomalies’ are associated with active or abandoned levees or fluvial breaches (Caputo *et al.*, 2015).

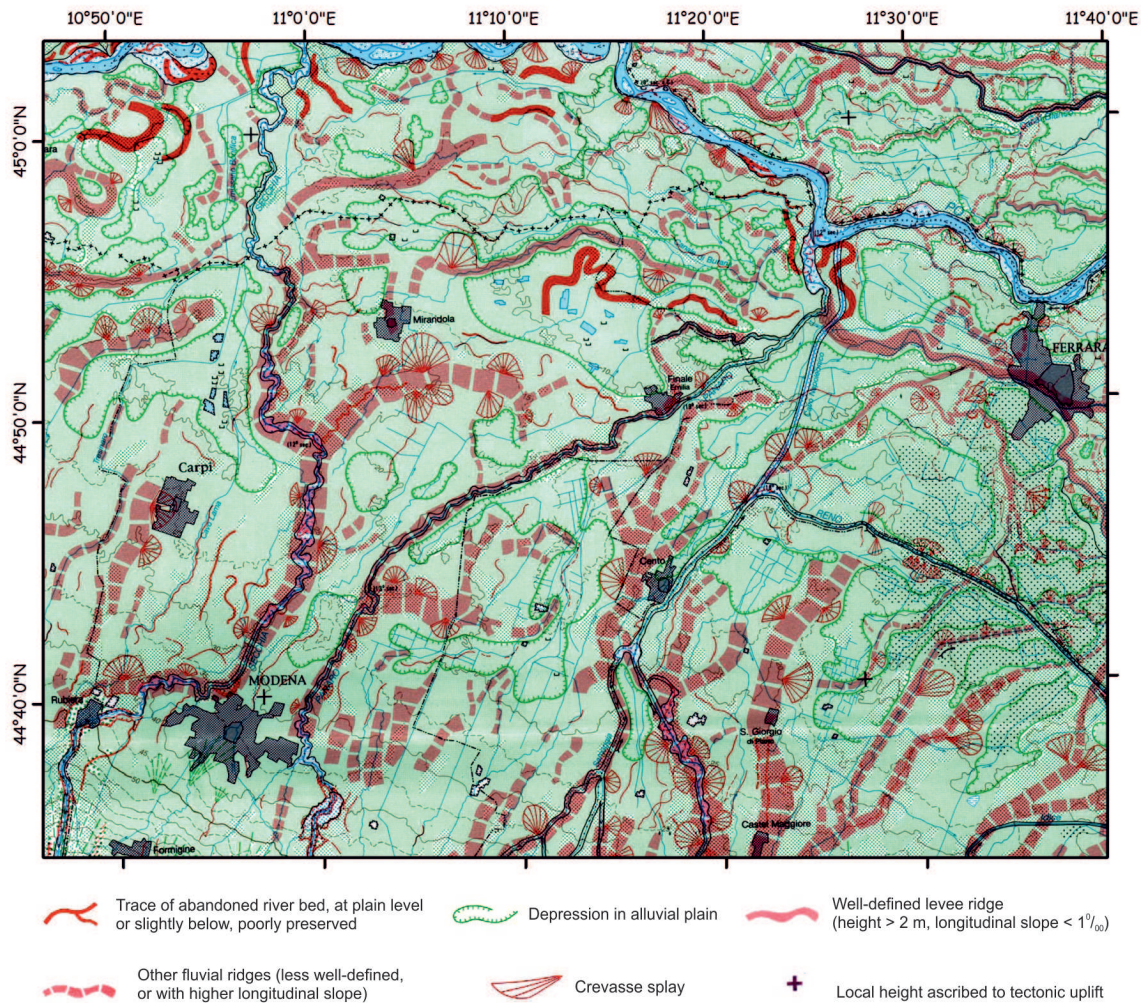


Figure 3.1: Geomorphological map of the eastern sector of the Po Plain (from Castiglioni *et al.*, 1999).

About 2500 years ago, the lowest sector of the Po River flowed across the present-day Ficarolo, Bondeno, Ferrara and Cona, forming the so-called Po di Ferrara (*a* in Fig. 3.2). In the same period, characterized by a generally warm climate, the Reno River flowed across the present-day San Pietro and Poggio Renatico (*b* in Fig. 3.2). In the 6th-8th century A.D., the climate was particularly wet and the abundant precipitation caused hydrographic instability. During this period, The Po di Ferrara splits into the Volano and Primaro branches (*c* and *d* in Fig. 3.2, respectively), while the Reno River shifted westwards along a new course across Galliera (*e* in Fig. 3.2) and a few centuries later further west close to Pieve di Cento. The restored warm conditions in the 9th-11th centuries favoured the expansion of farming within the plain, although in the 11th century the whole area suffered a critical hydrographic rearrangement due to several disastrous floods near Ficarolo which diverted the

Po River (Po Grande) north of Ferrara (*f* in Fig. 3.2). This strong territorial reorganization was likely caused by the reactivation of the Casaglia blind thrust and consequent growth of the associated fault-propagation anticline.

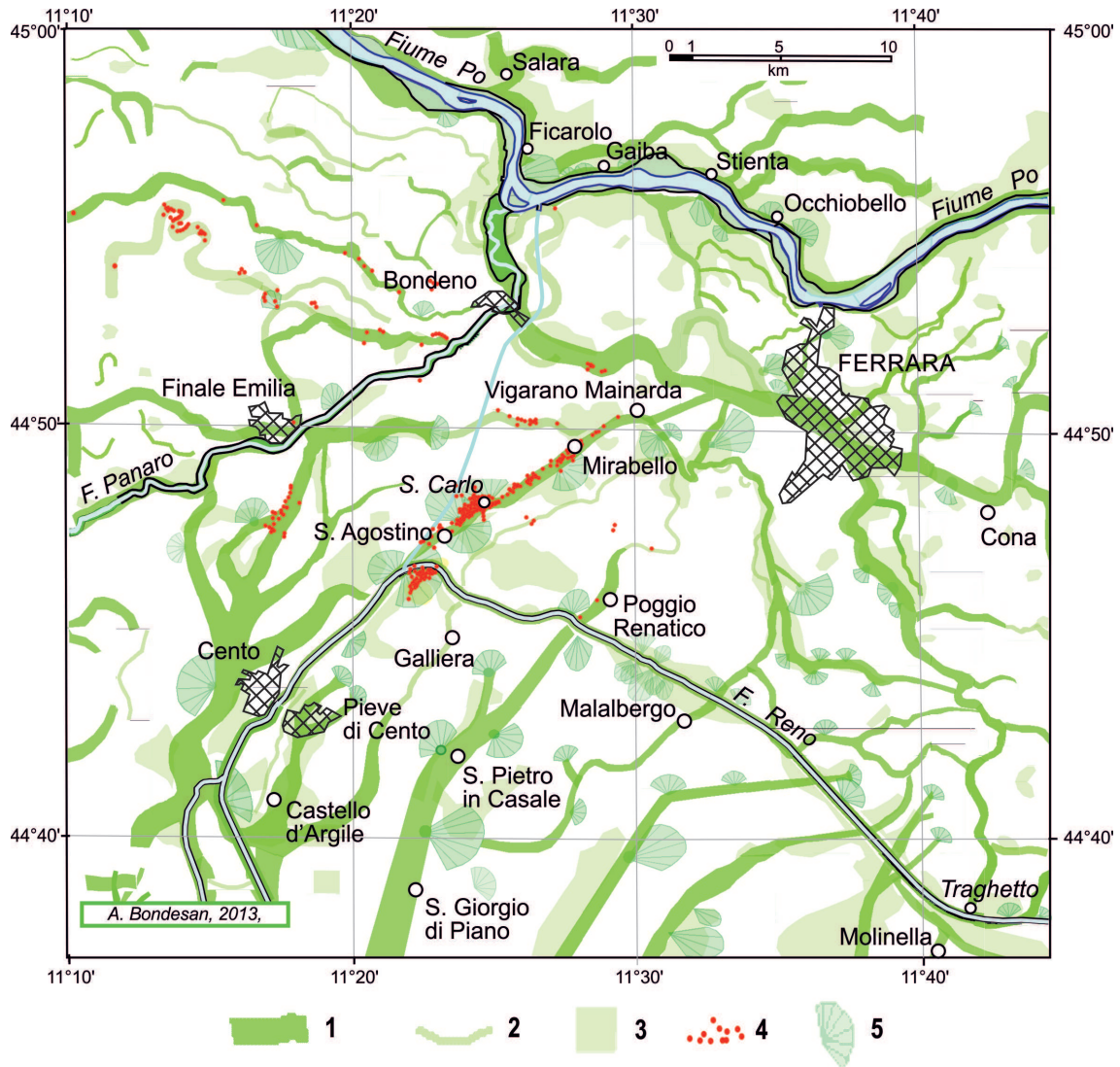


Figure 3.2: Geomorphological sketch map of the western Ferrara Province showing the complex hydrographic drainage developed in historical times as a consequence of tectonic activity, climatic changes and human interventions. Letters indicate distinct branches of the Po, Reno and Panaro rivers referred to in the text. Legend: 1) palaeo- and active levees associated with a morphological relief; 2) palaeo-channels entrenched in the alluvial plain; 3) flooding areas characterized by sandy deposits; 4) surface evidence of liquefaction phenomena caused by the May 20, 2012 event; 5) major breaches and associated fan deposits (from Caputo *et al.*, 2015).

In the following centuries, the water discharge of the southern branches of the Po River progressively decreased, inducing a gradual infill of the channels which was further worsened by the inflow of the Panaro River near Bondeno (*g* in Fig. 3.2). In the same period,

the Reno River began to split into several channels (*h*, *i*, *l* and *m* in Fig. 3.2), distributing water and sediments in a broad area north of Cento (Bondesan *et al.*, 1992). Following the disastrous floods in 1451 and 1457 (Frizzi, 1848), the Reno River was artificially channelled between Cento and Pieve (*n* in Fig. 3.2) and it soon started to rapidly prograde (several kilometres in just a few years) toward Sant'Agostino and Vigarano Mainarda (*o* in Fig. 3.2), where it was left to freely flood and fill the area between Ferrara and Poggio Renatico. In 1526, this branch of the Reno River was connected to the Po di Ferrara by means of a channel dug east of Vigarano (*p* in Fig. 3.2). This intervention drastically accelerated the infilling of the old Po channel causing as many as 40 floods in just 16 years and widespread swamping of the area around the town (Bottoni, 1873). As a consequence, this artificial connection was cut in the 17th century and the Reno River was diverted south-eastwards (*q* in Fig. 3.2) to induce land reclamation by sedimentary infilling (Roversi, 1989). At that time, the worsening climatic conditions (i.e. increased precipitation, water discharge and sediment transport) necessitated progressive artificial elevation of the levees for many rivers crossing the area and a hydraulic management plan. For example, in order to drain the swamp area created SW of Ferrara, the Cavo Benedettino (*r* in Fig. 3.2) was excavated from 1724 to 1742, with partial exploitation of older river channels and in 1771-1775 the Reno River was diverted south-eastwards near Sant'Agostino Franceschini, 1983) (*s* in Fig. 3.2). In the meantime, the Panaro River between Finale Emilia and Bondeno flowed along two courses, a natural branch and a partially artificial channel (*g* and *t* in Fig. 3.2, respectively), of which the former was abandoned at the end of the 19th century.

3.2 Stratigraphic architecture of the Pliocene-Quaternary succession

The studies conducted by RER & ENI-AGIP (1998) and Boccaletti *et al.* (2004, 2011) revealed that the Pliocene-Quaternary succession is greatly deformed and confirmed that the transitions between marine-continental sedimentation are the result of important tectonic phases followed by periods of strong subsidence. Therefore, the strongly variable thickness

of the Pliocene-Quaternary succession (from several hundred to a few tens meters thick in correspondence of the buried anticlines; RER & ENI-AGIP, 1998; Boccaletti *et al.*, 2004; 2011) and its deformation reflect the influence of the complex evolution of the buried faults.

A geological section (Fig. 3.3b) running in an NE-SW direction between the villages of Cento and Occhiobello (Fig. 3.3a), clearly highlights how the development of anticline-syncline pairs has deformed the overlying alluvial sequence, particularly influencing the depth of the basal limits of the Lower and Undifferentiated Emiliano-Romagnolo Synthem (AEI and AESind, respectively). Another example is represented by the Carpi-Cento basin (Fig. 3.3a), where the alluvial sequence is more than 300 m thick, while in correspondence of the Casaglia anticline, between Diamantina and Occhiobello, is reduced to about 100 m thick. It is important to note that the tectonic deformation fades toward the ground surface, thus to the youngest deposits. Additionally, due the occurrence of growing anticlines in the subsurface, the stratigraphic sequence may be not only 'condensed' but also incomplete, as in the case of the Casaglia anticline where the Lower-Middle Pleistocene marine deposits lies directly above the Upper Miocene marls.

The great number of subsurface data collected during hydrocarbon explorations and water research allowed the mapping of the principal Quaternary unconformities: the most recent surface, mappable at the regional scale, is the base Upper Emiliano-Romagnolo Synthem (AES). The trend of this surface (Fig. 3.4; Boccaletti *et al.*, 2004) was mainly derived from Table 1 of RER & ENI-AGIP (1998) and is characterized by the presence of uplifted and depressed areas. The AES base surface is very shallow at the top of the Ferrara Arc (less than 50 m), while it is deeper in the footwall of the thrust fronts (Boccaletti *et al.*, 2011). The observation that the structural highs are located above the top of the buried structures of the Ferrara Arc suggests their Late-Pleistocene tectonic activity.

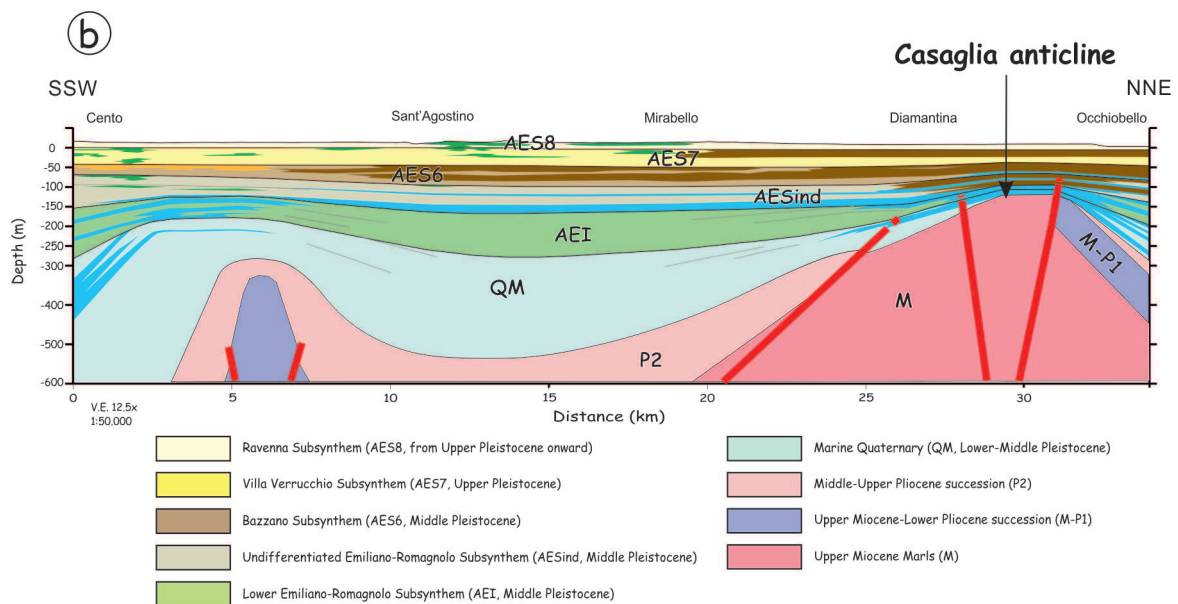
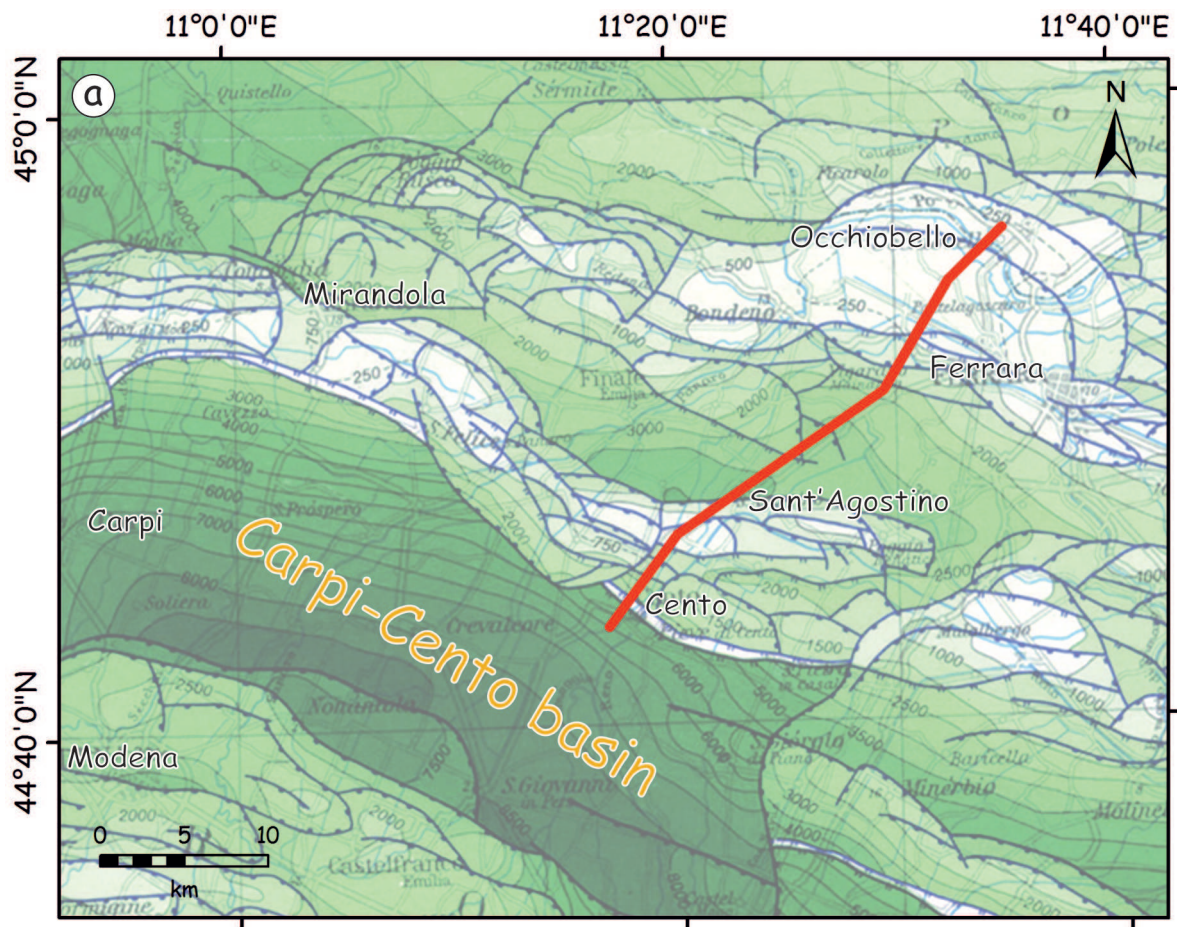


Figure 3.3: a) Trace of a geological profile that runs between Cento and Occhiobello. The basemap of the figure is from Bigi *et al.* (1992). b) Reconstruction of the geological and structural configuration of the subsurface along the profile (from Martelli and Romani, 2013).

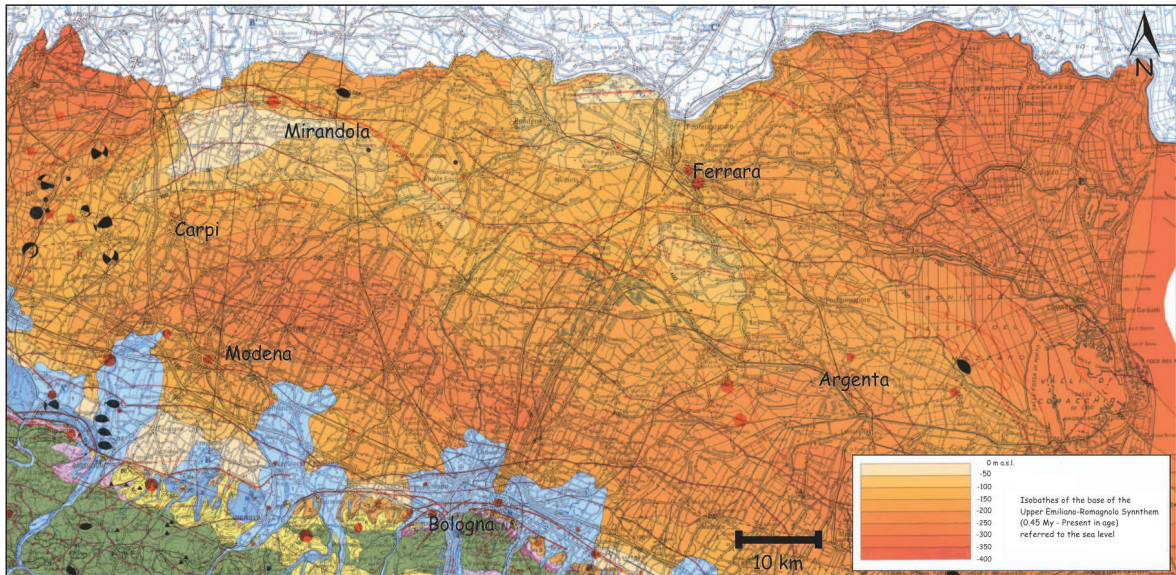


Figure 3.4: Basal isobathes of the Upper Emilian-Romagnolo Synthem (from Boccaletti *et al.*, 2004).

Most of the Northern Italy aquifers are within the Pliocene-Quaternary succession, therefore the Po Basin represents a valuable reservoir, particularly interesting for many researchers who have investigated and reconstructed its stratigraphic features (Ori, 1993; Amorosi and Farina, 1995; Vittori and Ventura, 1995; Bertotti *et al.*, 1998; RER & ENI-AGIP, 1998; Amorosi *et al.*, 2004; Amorosi and Colalongo, 2005; Scardia *et al.*, 2006; Molinari *et al.*, 2007; Amorosi, 2008).

In 1998, RER & ENI-AGIP recognized three Aquifers Groups, defined as Hydrostratigraphic Units, separated by permeability barriers, informally named A, B and C starting from the surface. The Group C (3 to 0.65 Ma) is represented by marine and deltaic depositional systems, while coastal and alluvial plain ones characterize the Aquifers Groups B (0.65 to 0.45-0.35 Ma) and A (0.45-0.35 Ma to present).

Molinari *et al.* (2007) studied in detail the shallowest Aquifer Group (A) due to its high vulnerability to anthropogenic activities and to the indiscriminate water resources exploitation. The main goal of this study was the detailed reconstruction of the water reservoirs of the Ferrara Province, so updating the knowledge about their sedimentary and tectonic evolution. In addition, this study revealed the great influence of the tectonic activity of the buried structures (i.e. the Ferrara Arc) on the distribution and thickness of the A Aquifer Group sediments. The authors distinguished five Aquifers Complexes (i.e. Hydrostratigraphic Units)

named, from the bottom, as i) A4, ii) A3, iii) A2 (subdivided in A2-I/A2-II), iv) A1 (subdivided in A1-I/A1-II) and the v) A0 freatic aquifer.

The trend of the A4 top surface is strongly influenced by the geometry of the deeper tectonic structures: in fact, this limit lies between 90 and 100 m b.s.l. above structural high, while in the eastern sector where the tectonic structures dip toward E-NE it reaches 260 to 280 m depth (Molinari *et al.*, 2007).

The same evidences are valid for the A3 top surface: in fact, over structural high this limit lies between 70 and 90 m, whereas in correspondence of the structural depressions it reaches 220-230 m depth. The deltaic sandy deposits of both complexes are distributed in the same areas, thus reflecting a substantial interruption in the paleogeographical evolution of the basin (Molinari *et al.*, 2007).

The A2-II Complex consists of marine sands and its top surface progressively lowers eastwards from 110 to 190 m b.s.l.. The A2-I sandy deposits have the greatest spatial extension: the top base ranges from 40 m b.s.l. in the northwestern sector of the province to 130 m depth in the eastern one. In addition, a series of undulations mainly oriented SW-NE, suggest a possible tectonic influence of the buried arcs. The analysis of the isopaches map relative to those of the oldest aquifers suggested an eastward migration of the fluvio-deltaic system (Molinari *et al.*, 2007).

The A1-II Complex is distinct into two principal bodies: the western one of continental origin and the eastern one represented by marine sediments. A part from the nature, the main difference is that the top of the eastern sandy body is located at greater depth (ca. 80-90 m b.s.l.). The western body mainly lies within the structural depression developing between the Poggio Renatico-Spinazzino and Casaglia structural highs. This evidence demonstrates how the fluvial and/or distributor channel deposits were preferably accumulated in the most subsiding areas. The A1-I Complex is constituted by Po River sandy deposits, whose top surface lies at about 50-60 m b.s.l. in the eastern sector of the Ferrara Province and it reaches 5 to 10 m depth in the western one. Also in this case, the evolution of the fluvio-deltaic depocenter seems to reflect the geometry of the growing anticlines.

Summarizing, the Hydrostratigraphic Units are composed of at least one or more

coarsening upward sequences. The base of each sequence is represented by a low permeability layer, serving as aquiclude between the different units. Within every Aquifer Group are distinct several Aquifer Complexes, constituted by coarsening upward depositional sequences as mentioned above.

Due the correspondence between the Aquifers Complexes and the Stratigraphic Units defined in the Geological Map of Italy (CARG Project), the A Aquifer is developed in the Upper Emiliano-Romagnolo Synthem (AES), the B Aquifer in the Lower Emiliano-Romagnolo Synthem (AEI) and the C Aquifer in the marine Quaternary deposits (Fig. 3.5; Molinari *et al.*, 2007).

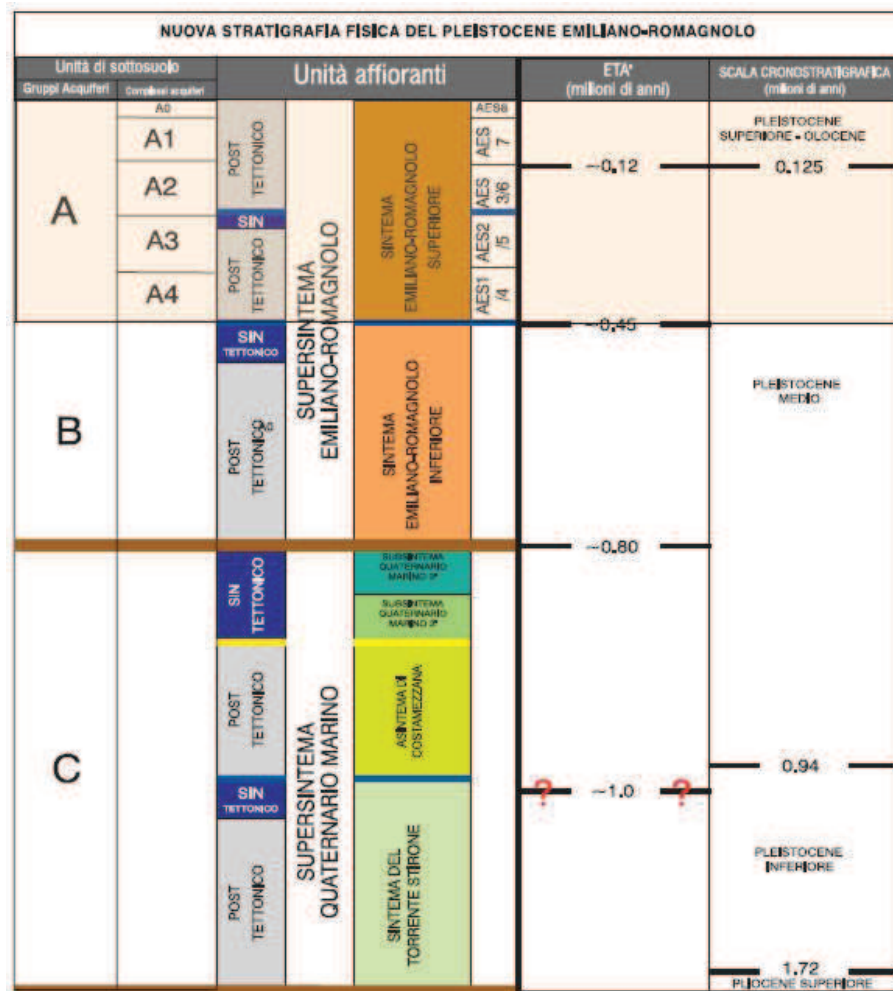


Figure 3.5: Synoptic view of the Quaternary stratigraphic units of the Po Plain subsurface (from Molinari *et al.*, 2007).

Part II

Applied methods and data collections

Chapter 4

Geotechnical methods and data collection

The aim of the geotechnical methods is to provide useful information about the characteristics of a soil in terms of lithostratigraphy, geometric relations of the lithotechnic units, physical-mechanical properties and groundwater conditions, that are fundamental in order to reconstruct a plausible geological and geotechnical subsoil model. A series of different in-situ and laboratory tests allow the collection of such information. Among the several types of geotechnical surveys, the cone penetrometer test is increasingly becoming a preferred in-situ test for site characterization due to its high standardization degree, fast execution and moderate cost over traditional methods of investigation, such as drilling (Lunne *et al.*, 1997; Mayne, 2007; Shuttle and Cuning, 2007). The numerical values are used as input for geotechnical and engineering purposes, like the assessment of the liquefaction susceptibility of a soil and its lithological profile (Eslami and Fellenius, 2004).

For the aims of this research project, the (numerical) information of such surveys were exploited i) for documenting how the occurrence of site effects (in terms of liquefaction) can strongly influence the large-scale tectonic signal (see Section 6.2), ii) in the frame of the analyses performed for the Seismic Microzoning study of the Sant'Agostino Municipality (see Section 6.3) and iii) for the quantitative assessment of the liquefaction potential for two prone areas considering the May 20, 2012 Emilia earthquake (see Section 6.4).

A detailed discussion about the i) different types of penetrometric surveys and soil profile interpretations, ii) semi-empirical procedures for the evaluation of the liquefaction potential, iii) data collection and processing is reported in the following sections.

4.1 Static cone penetration tests

4.1.1 Equipment and procedures

The CPT is performed by exploiting the mechanical or electrical static penetrometer, which acts over a cone placed at one end of a system of rods, pushed into the ground with steady velocity (ca. 2 cm/s). The measured parameters are the cone resistance (q_c) and the sleeve friction (f_s). In case of soft soils (e.g. from clay to coarse sand), the test can be pushed to 40 m depth and over. The measuring of the resistances are carried out on the surface, thus errors related to the equipment weight and to the deformability of the rods system must be taken into account; moreover, any deviation from the vertical of the rods system leads to erroneous assessment of the reached depth (Cestari, 2009). An evolution of the mechanical penetrometer is represented by the electrical one (CPTe). In this case, the tip resistance of and sleeve friction are independently measured by sensors installed on the tip of the penetrometer, which transmit an electrical signal to a control unit located on the ground surface. Additionally, the rods are equipped with clinometric sensors which allow to correct eventual deviation from the vertical. The measuring frequency of q_c and f_s is greater (from 2 to 5 cm) and the data, digitally acquired, can be visualized during the execution of the survey. The possible limitations are the major costs of the equipment and the potential malfunctioning of the electronic components (e.g. sensibility to temperature variations, instrument calibration, etc.) (Cestari, 2009).

The cone resistance (q_c) is defined as the ratio between the measured axial strength (Q_c) acting on the cone and the total area of the cone base (A_C); while, the sleeve friction (f_s) is calculated by the ratio between the friction strength (Q_s) acting on the sleeve and the lateral area of the sleeve. When the electrical penetrometer is equipped with a porous element (i.e. filter) it is referred to as piezocone; thus, the cone resistance (q_c), the friction sleeve (f_s) and additionally pore pressure (u) can be measured. In this case it is necessary to define the following parameters:

- the cone area factor (a) as the ratio between the net (A_N) and total area (A_C) of the cone;

- the penetration pore pressure (u) measured during the penetration;
- the generated pore pressure (Δu) as the difference between the penetration pore pressure (u) and the hydrostatic pressure (u_0);
- the total corrected cone resistance (q_t) defined as $q_c + u(1-a)$.

The Seismic Cone Penetration Test (SCPTu) combines the previous techniques, thus contributing to a further evolution of the methodology. Besides the above described parameters, such survey allows to measure the in-situ shear wave velocity profile. The penetrometer is equipped with geophones that record the seismic waves generated by artificial sources: based on the receivers-seismic source configuration can be carried out downhole or cross-hole surveys (Cestari, 2009).

4.1.2 Soil profile interpretation

One of the major applications of the penetrometric tests is the determination of soil stratigraphy and the identification of soil type (Robertson, 2010). As the cone penetrometer progressed (i.e. from mechanical, electrical to piezocone) the reliability of the soil type also improved (Fellenius *et al.*, 2000). However, site investigation based on CPT only has a drawback because the sampling is not allowed or particularly limited; so traditional soil classification using the Unified Soil Classification System (USCS) cannot be performed. Therefore, many scientists focused their attention in developing methods for soil classification (Ku *et al.*, 2010).

In 1965, Begemann proposed a soil classification based on the observation that coarse-grained soils generally are characterized by high values of cone resistance and friction sleeve, than do fine-grained soils, therefore the soil type is not a strict function of either parameter but a combination of them. In Fig. 4.1 the Begemann soil profiling chart is shown: the soil type is a function of the ratio between the friction sleeve f_s and the cone resistance q_c (i.e. the friction ratio, R_f), indicated by the slope of the fan out lines. This chart, by deriving from tests carried out in Holland with a mechanical cone, is site-specific (i.e. directly applicable only to the specific geological sites where it was developed), but at any rate it has important general qualitative value.

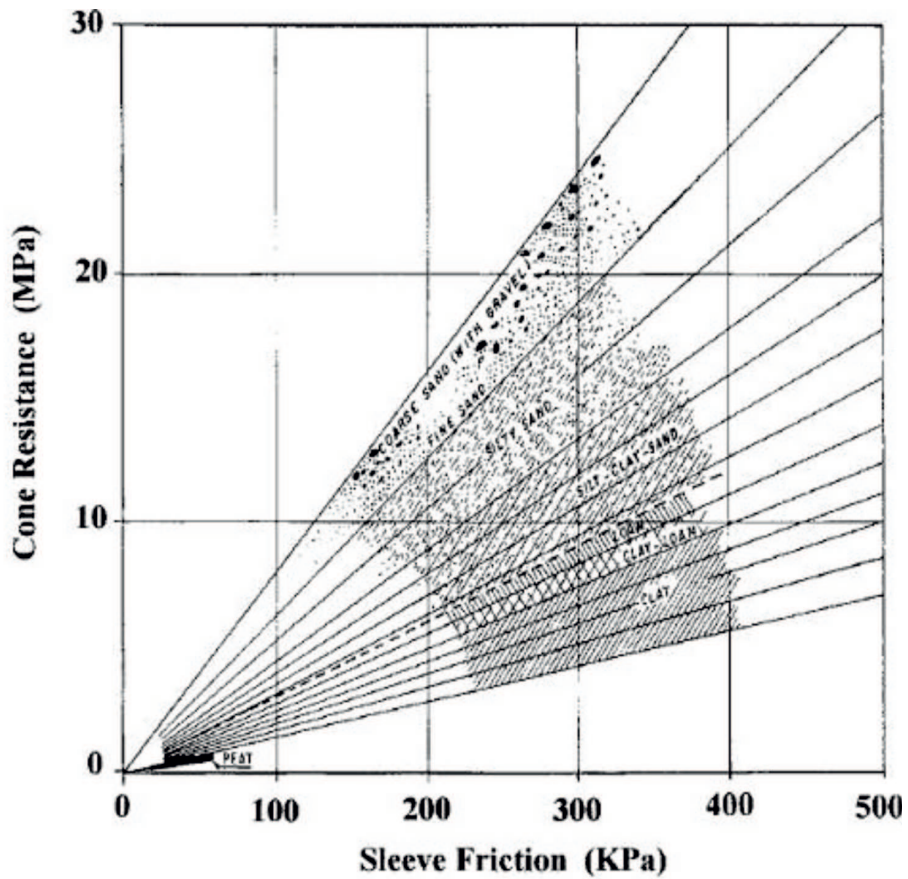


Figure 4.1: The Begemann (1965) soil profiling chart.

The friction ratios identify the soil types as follows:

- coarse sand with gravel through fine sand 1.2% - 1.6%
- silty sand 1.6% - 2.2%
- silty sandy clayey soils 2.2% - 3.2%
- clay and loam, and loam soils 3.2% - 4.1%
- clay 4.1% - 7.0%
- peat > 7%

Schmertmann (1978) proposed the profiling chart shown in Fig. 4.2. The chart, based on mechanical cone data carried out in Florida, incorporates Begemann's CPT data and indicates zones of common soil type. Are also defined the boundaries for loose/dense

sand and consistency of clays and silts, which are imposed by definition. The soil type is defined as a function of the ratio between the cone resistance q_c (logarithmic scale) and the friction ratio R_f . The main differences with the Begemann's chart concern the limit between the various lithologies and the non-linear relation between q_c and f_s .

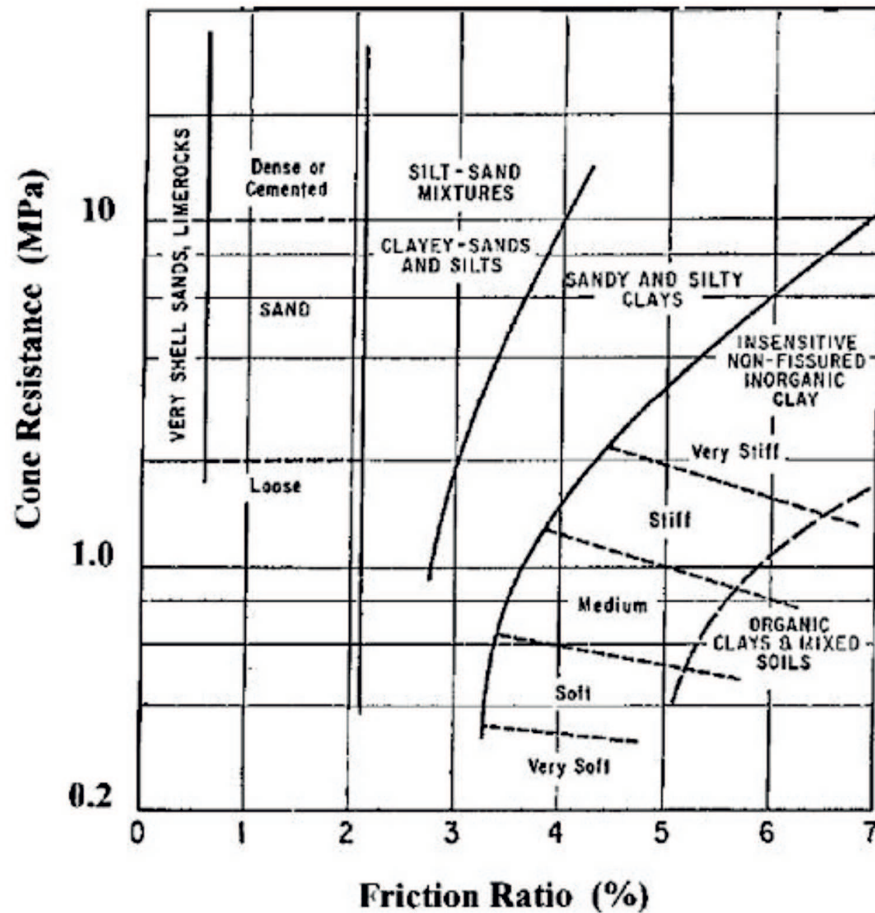


Figure 4.2: The Schmertmann (1978) soil profiling chart.

Douglas and Olsen (1981) were the first to propose a soil profiling chart calibrated on the electrical cone penetrometer, based on the ratio between R_f and q_c . Their chart (Fig. 4.3) appends the classification for the UCSCS to the soil type system. It defines several zones using three upward curving lines representing the increasing content of coarse-grained soil and four lines with equal friction sleeve; in this way, sensitive or 'metastable' soil can be distinguished.

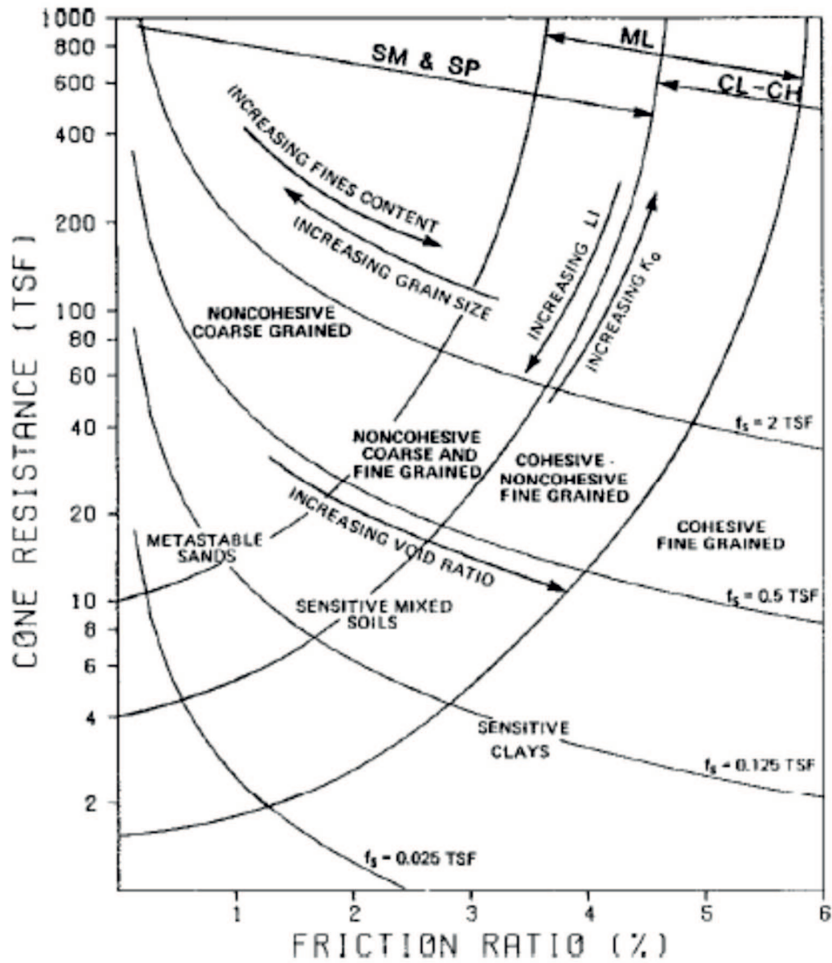


Figure 4.3: The Douglas and Olsen (1981) soil profiling chart.

Robertson *et al.* (1986) and Campanella and Robertson (1988) were the first to present a chart based on the piezocone with the cone resistance corrected for the pore pressure (q_t). Even if the chart (Fig. 4.4) is shown in terms of the corrected cone resistance q_t , it can be used equally well with uncorrected cone resistance, q_c , since the difference between q_c and q_t is small, except in soft fine grained soils that produce high penetration pore pressures.

Robertson *et al.* (1986) and Robertson (1990) stressed that the CPT-based charts were predictive of Soil Behaviour Type (SBT), since the cone responds to the in-situ mechanical behavior of the soil and not directly to soil classification criteria based on grain-size distribution and soil plasticity (e.g. Unified Soil Classification System, USCS).

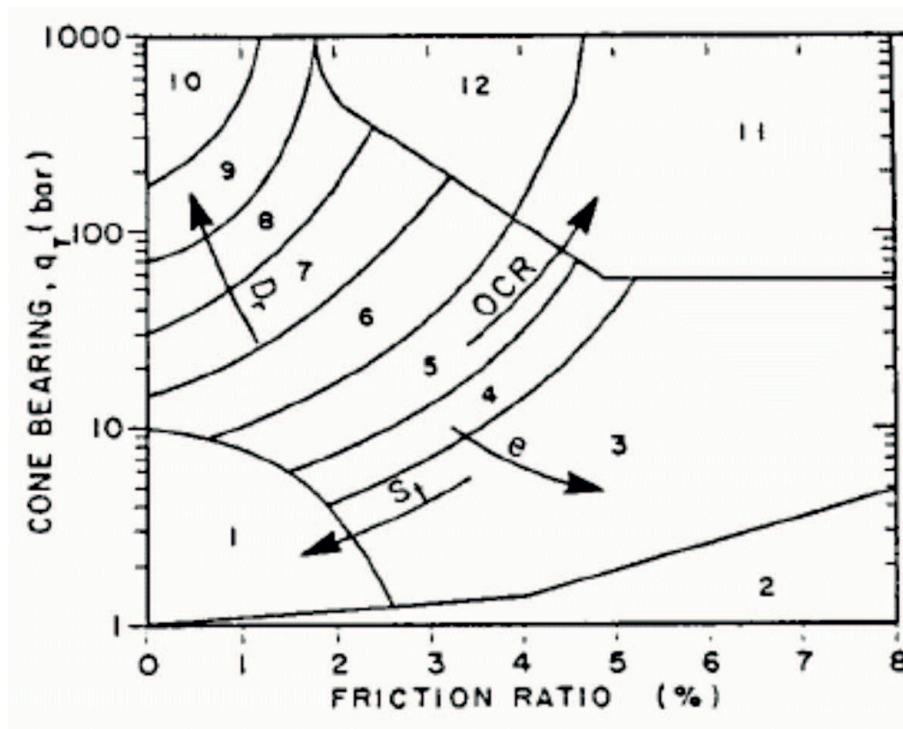


Figure 4.4: The Robertson *et al.* (1986) soil profiling chart.

In the chart are distinguished 12 SBT, as follows:

- | | |
|--------------------------------|--|
| 1. sensitive fine-grained soil | 7. silty sand to sandy silt |
| 2. organic soil | 8. sand to silty sand |
| 3. clay | 9. sand |
| 4. silty clay to clay | 10. sand to gravelly sand |
| 5. clayey silt to silty clay | 11. very stiff fine-grained soil |
| 6. sandy silt to clayey silt | 12. overconsolidated or cemented sand to clayey sand |

An important limitation is not to take into account the depth of the measurements (i.e. the total and effective geostatic stress), which can lead to erroneous evaluation of the soil type; in fact the soil resistance, even within the same type of soil, tends to increase with depth due to the overburden (Cestari, 2009).

Therefore, Robertson (1990) proposed a refinement of the Robertson *et al.* (1986) chart profiling shown in Fig. 4.5, plotting the normalized cone resistance (Q_{t1}) against the normalized friction ratio (F_r).

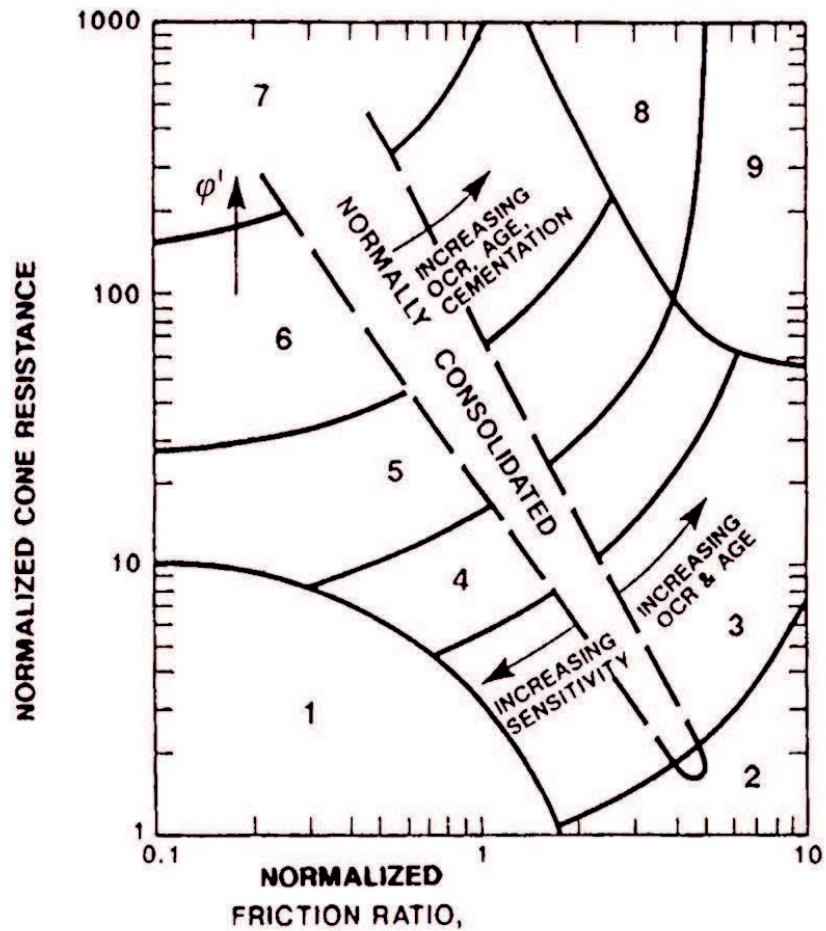


Figure 4.5: The Robertson (1990) soil profiling chart.

The normalized cone resistance is defined as follows:

$$Q_{tn} = (q_t - \sigma_{v0}) / \sigma'_v \quad (4.1)$$

where q_t = cone resistance corrected for pore water pressure;

σ_v = total overburden stress;

σ'_v = effective overburden stress;

$(q_t - \sigma_v)$ = net cone resistance.

The normalized friction factor is defined as the friction sleeve over the net cone resistance, as follows:

$$R_f = f_s / (q_t - \sigma'_v) \quad (4.2)$$

In the chart are distinguished 9 SBT, as follows:

- | | |
|--|--|
| 1. sensitive, fine-grained soils | 6. sand (silty sand to clean sand) |
| 2. organic soil and peat | 7. sand to gravelly sand |
| 3. clay (clay to silty clay) | 8. sand - clayey sand to 'very stiff' sand |
| 4. silt mixtures (silty clay to clayey silt) | 9. very stiff, fine-grained, overconsolidated or cemented soil |
| 5. sand mixtures (sandy silt to silty sand) | |

The normalization was proposed to compensate for the cone resistance dependency on the overburden stress and, therefore, when performing deep CPTu (i.e. deeper than about 30 m) a profiling chart developed for shallow surveys is not recommended. In general, the normalized charts provide more reliable identification of Soil Behavior Type (SBTn) than the non-normalized (SBT). Since 1990 other charts were developed, based on either non-normalized or normalized parameters (e.g. Jefferies and Davies, 1991; Olsen and Mitchell, 1995; Eslami and Fellenius, 1997).

Jefferies and Davies (1993) identified that a soil behavior type index (I_c) could represent the SBTn zone in the Q_{tn} - F_r chart (Fig. 4.5), where I_c is essentially the radius of concentric circles that define the boundaries of soil type. Robertson *et al.* (1998) modified the definition of I_c to apply to the Robertson (1990) Q_{tn} - F_r chart (Fig. 4.5), as defined by:

$$I_c = \sqrt{(3.47 - \log Q_{tn})^2 + (\log F_r + 1.22)^2} \quad (4.3)$$

$$Q_{tn} = \left(\frac{q_t - \sigma_{v0}}{P_a} \right) \cdot \left(\frac{P_q}{\sigma'_{v0}} \right)^n \quad (4.4)$$

$$n = 0.381 \cdot I_c + 0.05 \cdot \left(\frac{\sigma'_{v0}}{P_a} \right) - 0.15 \leq 1 \quad (4.5)$$

$$F_R = \left(\frac{f_s}{q_t - \sigma_{v0}} \right) \cdot 100(\%) \quad (4.6)$$

The I_c contours, which are shown in Fig. 4.6 on the Robertson (1990) Q_{tn} - F_R chart, can be used to approximate the SBT boundaries (see Table 4.1; Robertson, 2009).

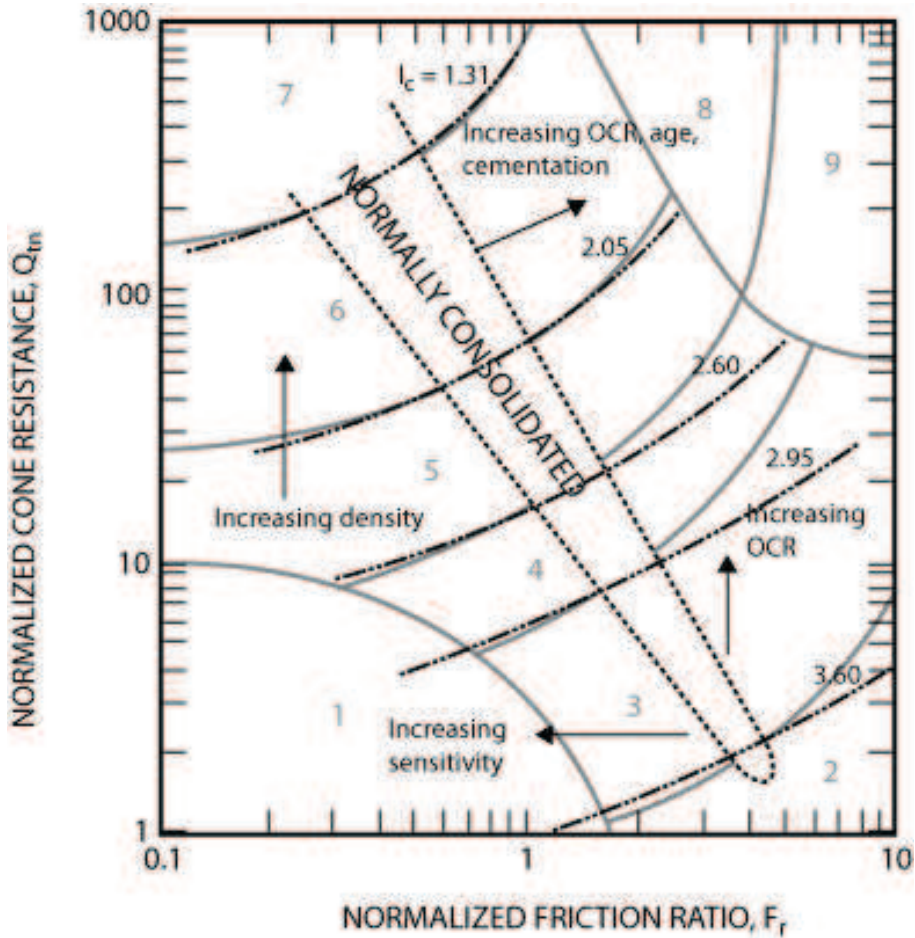


Figure 4.6: Contours of soil behaviour type index I_c (dashed lines), on normalized SBTn Q_{tn} - F_R chart (from Robertson, 2009).

I_c	SBT zone (Robertson, 1990)
$I_c < 1.31$	7
$1.31 < I_c < 2.05$	6
$2.05 < I_c < 2.60$	5
$2.60 < I_c < 2.95$	4
$2.95 < I_c < 3.60$	3
$I_c > 3.60$	2

Table 4.1: Soil behavior type index (I_c) for the SBT zones of the normalized Q_{tn} - F_R chart (from Robertson, 2009).

4.2 Soil liquefaction

4.2.1 Liquefaction phenomena

One of the most dramatic causes of damage to structures during earthquakes is the occurrence of liquefaction in saturated sand deposits (Idriss and Boulanger, 2008): this phenomena can be defined as the transformation of a granular material (i.e. silty sands to gravelly sands) from a solid to a liquefied state as a consequence of increased pore-water pressure and reduced effective stress (Marcuson, 1978).

The liquefaction phenomenon of soil deposits can be described as the reduction of shear strength due to pore pressure buildup in the soil skeleton. The shear strength of cohesionless soil, τ , depends mainly on the angle of internal friction and the effective stress acting on the soil skeleton, as follows:

$$\tau = \sigma' \tan \varphi \quad (4.7)$$

$$\sigma' = \sigma - u \quad (4.8)$$

where τ = shear stress;

σ' = effective vertical stress;

σ = total vertical stress;

u = pore pressure;

φ = angle of internal friction.

Liquefaction results from the tendency of soils to decrease in volume when subjected to shearing stresses. When loose saturated soils are subject to earthquake cyclic 'loading', the soil grains tend to rearrange into a more dense packing as the water is forced out. If the water drainage is impeded, the pore pressure in the soil increases progressively with the shear load. When the pore pressure equals the total stress, thereby reducing the effective stress to zero, sands will, at least temporarily, completely lose their stiffness and shear strength ('initial

liquefaction' state). At the onset of initial liquefaction, loose sands will undergo unlimited deformations or flow without mobilizing significant resistance to deformation (Martin *et al.*, 1975; Seed and Idriss, 1982). As a result, structures supported above or within the liquefied deposit undergo significant settlements and tilting: water flows upward to the surface creating sand boils, while buried pipelines and tanks may become buoyant and float to the surface. This phenomenon is referred to as "liquefaction" and is obviously a condition to be avoided in any type of major construction.

4.2.2 Soils susceptibility to liquefaction and ground failure

A study of local site geology is essential part for characterized the nature and possible extent of soils that are susceptible to liquefaction. The extent or degree of liquefaction depends on the distribution of cohesionless sediments (gravels, sands, and very low-plasticity silts) within the deposit and requires a sufficiently high water table for the sediments to be largely saturated. The most susceptible sediments are fills and alluvial, fluvial, marine, deltaic, and wind-blown deposits (Idriss and Boulanger, 2008). Since liquefaction is associated with the tendency of soil grains to rearrange when subjected to cyclic loading, anything that prevents this 'adjustment' will increase the soil resistance to liquefaction. Grain-size, particle cementation, soil fabric and aging are important factors that can hinder particle rearrangement (Seed, 1979). The type of soil most susceptible to liquefaction is one in which the resistance to deformation is mobilized by friction between particles. If other factors such as grain shape, uniformity coefficient and relative density are equal, the frictional resistance of cohesionless soil decreases as the grain size of soils becomes smaller. Tsuchida (1970) summarized the results of sieve analysis performed on a number of alluvial soils that were known to have liquefied or not during earthquakes. He proposed ranges of grain size curves separating liquefiable and non-liquefiable soils (Fig. 4.7). The area within the two inner curves in the figure represents sands and silty sands, the soils with the lowest resistance to liquefaction. A soil with a gradation curve falling in the zones between the outer and inner curves is less likely to liquefy. The space between the two curves farthest to the left reflects the influence of fines in decreasing the tendency of sands to densify during seismic shearing.

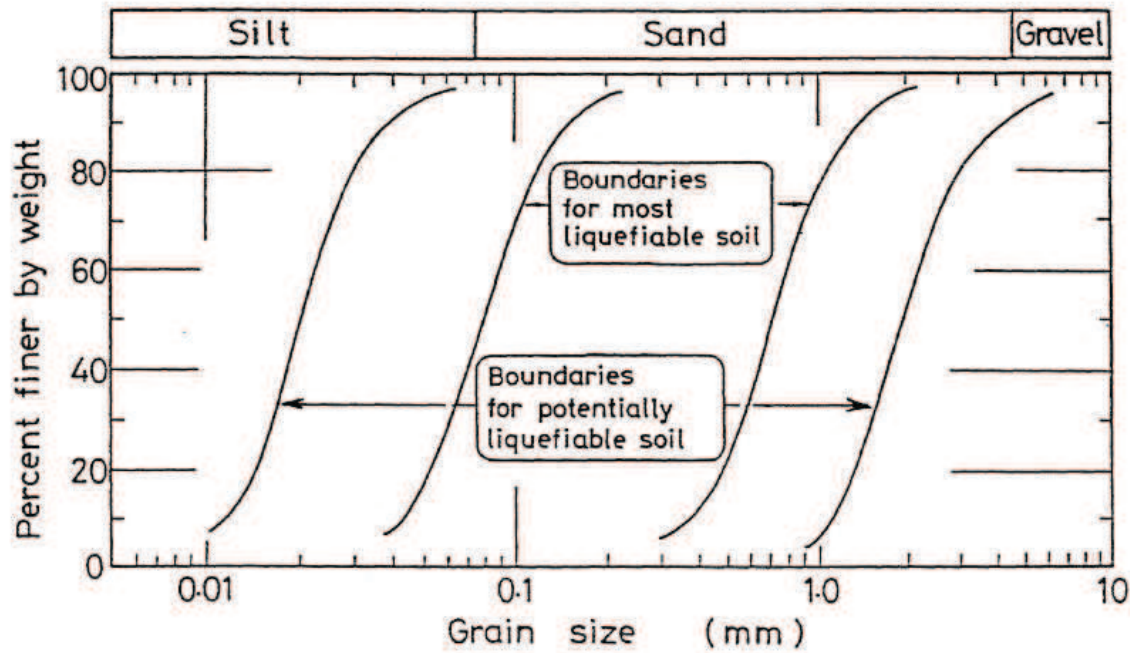


Figure 4.7: Limits in the gradation curves separating liquefiable and non-liquefiable soils (Tsuchida, 1970).

Fines with cohesion and cementation tend to make sand particles more difficult to liquefy or to seek denser arrangements. However, non-plastic fines such as rock flour, silt and tailing slimes may not have as much of this restraining effect. Ishihara (1985) stated that clay- or silt-size materials having a low plasticity index value will exhibit physical characteristics resembling those of cohesionless soils, and thus have a high degree of potential for liquefaction. Walker and Steward (1989), based on their extensive dynamic tests on silts, have also concluded that non-plastic and low plasticity silts, despite having their grain size distribution curves outside of Tsuchida's boundaries for soils susceptible to liquefaction, have a potential for liquefaction similar to that of sands and that increased plasticity will reduce the level of pore pressure response in silts.

In addition, sediments are most susceptible to liquefaction when they are recently deposited getting more resistant as they become older. Youd and Hoose (1977) stated that alluvial deposits older than late Pleistocene (10,000-130,000 years) are unlikely to liquefy except under severe earthquake loading conditions, while late Holocene deposits (1,000 years or less) are most likely to liquefy, and earlier Holocene (1,000-10,000 years) deposits are moderately liquefiable.

Surface evidence has most commonly been associated with liquefaction occurring at depths of less than about 15-20 m. This is related to the fact that the shallower deposits are typically the youngest and therefore most susceptible to liquefaction. Liquefaction at greater depths beneath level ground surfaces may not be manifested at the ground surface and thus may go undetected (Idriss and Boulanger, 2008).

Liquefaction will not occur in dry soils. Only settlement, as a result of densification during shaking, may be of some concern. Available laboratory test results (Sherif et al., 1977) show that liquefaction resistance for soils increases as the degree of saturation decreases, and that sand samples with low degree of saturation can become liquefied only under severe and long duration of earthquake shaking.

In order to induce extensive damage at level ground surface from liquefaction, the liquefied soil layer must be thick enough so that the resulting uplift pressure and amount of water expelled from the liquefied layer can result in ground rupture such as sand boiling and fissuring (Ishihara, 1985; Dobry, 1989). If the liquefied sand layer is thin and buried within a soil profile, the presence of a non-liquefiable surface layer may prevent the effects of the at-depth liquefaction from reaching the surface. A first attempt to establish a threshold value for the thickness of a non-liquefiable surface layer to avoid ground damage due to liquefaction, based on just three case histories, was proposed by Ishihara (1985).

Seismic strain history can significantly affect the resistance of soils to liquefaction, as it was demonstrated from laboratory test results that prior (Finn *et al.*, 1970; Seed *et al.*, 1977; Singh *et al.*, 1980). Low levels of prior seismic strain history can significantly increase soil resistance to pore pressure buildup during subsequent cyclic loading: the increased resistance may result from uniform densification of the soil or from better interlocking of the particles in the original structure. Large strains, however, associated with large pore pressure generation and conditions of full liquefaction can develop weak zones in the soil due to uneven densification and redistribution of water content (National Research Council, 1985; Whitman, 1985), and thus lower the resistance of the soil to pore pressure generation during subsequent cyclic loading.

The National Research Council (1985) lists eight types of failure commonly associated with soil liquefaction during earthquakes:

- sand boils, which usually result in subsidence and relatively minor damage;
- flow failures of slopes involving very large down-slope movements of a soil mass;
- lateral spreads resulting from the lateral displacements of gently sloping ground;
- ground oscillation where liquefaction of a soil deposit beneath a level site leads to back and forth movements of intact blocks of surface soils;
- loss of bearing capacity causing foundation failures;
- buoyant rise of buried structures such as tanks;
- ground settlement, often associated with some other failure mechanism;
- failure of retaining walls due to increased lateral loads from liquefied backfill soil or loss of support from liquefied foundation soils.

4.2.3 Semi-empirical procedures for the evaluation of liquefaction potential during earthquakes

In common geotechnical and engineering practices, the prevailing approach for the evaluation of liquefaction potential is based on simplified methods.

Seed and Idriss (1971) proposed a methodology named “Simplified Procedure” for evaluating liquefaction potential of soils. Since then the procedure has become the most widely used method for liquefaction hazard assessments. The Simplified Procedure was developed from empirical evaluations of field observations as well as field and laboratory test data. The database of field evidences collected for this procedure were mostly surface evidences such as ground fissures, sand boils or lateral spreads which indicate that liquefaction occurred in a specific area. Calculation, or estimation, of two variables is required for evaluating the liquefaction resistance of soils: (1) the seismic demand on a soil layer, expressed in terms of Cyclic Stress Ratio (CSR) and (2) the capacity of the soil to resist liquefaction, expressed in terms of Cyclic Resistance Ratio (CRR).

The simplified methods consist of two different approaches, known as deterministic and probabilistic. In the first case the limit state curve, expressing the soil resistance in terms

of CSR, is determined by drawing a curve that discriminates the cases of observed liquefaction or not, so almost entirely "visual", without any probabilistic processing of the data. Afterwards, the possible occurrence of liquefaction phenomena is predicted by calculating the factor of safety (F_s ; Seed and Idriss, 1971), defined as the ratio between CRR and CSR, and assessing whether this parameter is less (liquefaction) or greater than 1 (no liquefaction) (Facciorusso, 2008).

The probabilistic approach, instead, is based on the simultaneous analysis of the influence of several parameters which can favour the occurrence of liquefaction, thus deriving countless liquefaction resistance curves, each corresponding to a different probability of liquefaction (PL) (Facciorusso, 2008).

The development of liquefaction correlations from case histories has progressed over the years through the effort of many researchers, particularly in the time-consuming investigations of individual case histories. The first CPT liquefaction correlations based directly on case histories were published by Zhou (1980), using observations from the 1978 Tangshan earthquake. The evolution of CPT procedures since then includes notable correlations by Shibata and Teparaksa (1988), Stark and Olson (1995), Suzuki *et al.* (1995; 1997), Robertson and Wride (1997; 1998), and Olsen (1997). A 1996-1997 workshop by the National Center for Earthquake Engineering Research (NCEER, 1997) and the National Science Foundation (NSF) provided a timely summary of most of the extant SPT-, CPT-, and V_s -based correlations and analytical procedures (Youd *et al.*, 2001). The next few years gave the opportunity to improve the knowledge due to the occurrence of several large earthquakes: in particular, Seed *et al.* (2001; 2003), Moss (2003), and Moss *et al.* (2006) and Idriss and Boulanger (2004; 2008) proposed valuable compilations of those new data and associated revisions to the liquefaction procedures and correlations. Information for each case history was compiled by identifying the combination of the earthquake-induced CSR and in-situ penetration resistance that best represents the critical zone for each site. In compiling the case histories into a common data set, it is necessary to adopt some standard reference condition to which each case history can be adjusted. This was done by adopting the reference condition of an $M = 7.5$ earthquake and an effective overburden stress of $\sigma'_{v0} = 1$ atm.

In the frame of this research project (i.e. Seismic Microzoning of Sant'Agostino Municipality and quantitative assessment of LPI and LSN indexes for two liquefaction prone areas considering the May 20, 2012 Emilia earthquake) and in order to evaluate the factor of safety followed the Idriss and Boulanger (2008) stress-based approach. Additionally, in order to take into account the fines content in the absence of site-specific laboratory test data, the Robertson and Wride (1998) approach was applied. Both approaches were followed since Facciorusso *et al.* (2013) showed that the Idriss and Boulanger (2008) method provides the most reliable results, in terms of consistency with the effects observed after the May 20, 2012 earthquake and in order to maintain the consistency with the procedure followed by Tonkin and Taylor (2013) for the development of LSN methodology. In the following there is a brief description of the two above mentioned methods.

If the soil column above a depth z can be approximated as a rigid body (Fig. 4.8), the maximum shear stress at the base of the column can be computed as follows:

$$(\tau_{max})_r = \frac{\gamma z}{g} a_{max} = \sigma_{v0} \frac{a_{max}}{g} \quad (4.9)$$

where a_{max} = maximum horizontal acceleration at the ground surface;

γ = average unit weight of the soil above depth z ;

g = gravity acceleration;

σ_{v0} = total vertical stress at depth z .

In reality, the soil column behaves as a deformable body (Fig. 4.8), and hence the maximum shear stress will differ from the value for a rigid body with the same maximum ground surface acceleration. The maximum shear stress for a deformable body can be determined from dynamic site response analysis, and the results compare to the rigid body case as follows:

$$(\tau_{max})_d = r_d (\tau_{max})_r \quad (4.10)$$

where r_d = shear stress reduction coefficient (accounts for the flexibility of the soil column; i.e. $r_d = 1$ corresponds to a rigid body behaviour).

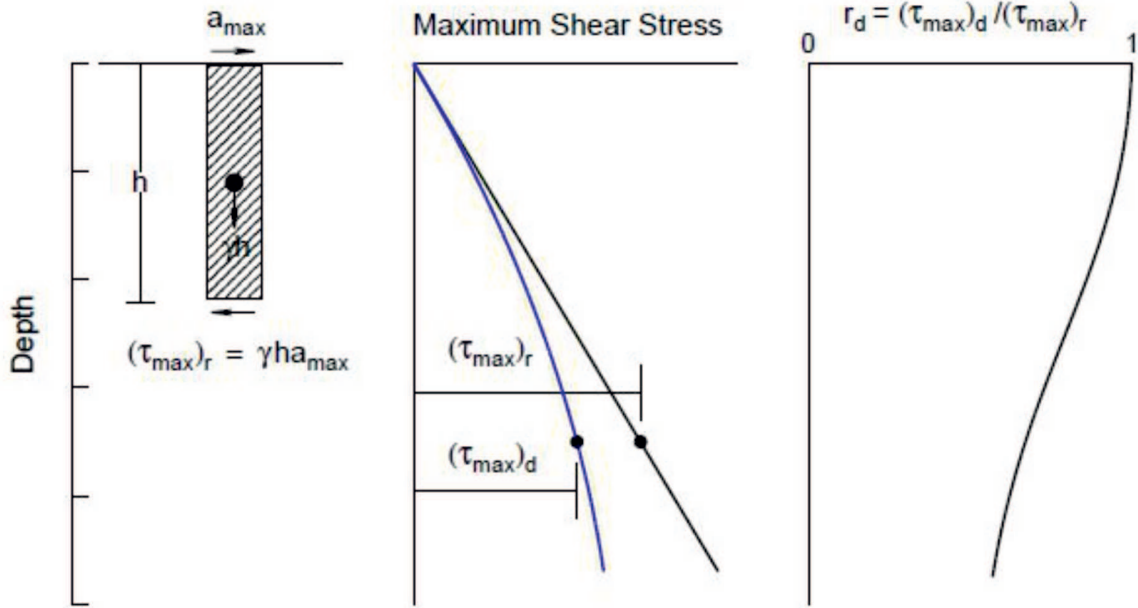


Figure 4.8: Schematic illustration of procedure to calculate maximum shear stress, τ_{\max} , and stress reduction coefficient, r_d (after Seed and Idriss, 1971).

For the estimation of the vertical overburden stress (i.e. σ_{vo}/σ'_{vo}), the knowledge of the soil weight unit (γ) is necessary. It was estimated following the correlation proposed by Robertson and Cabal (2010):

$$\frac{\gamma}{\gamma_w} = 0.27 \cdot \log(R_f) + 0.36 \cdot \log\left(\frac{q_t}{P_a}\right) + 1.236 \quad (4.11)$$

where γ_w = unit weight of water;

R_f = friction ratio;

q_t = corrected cone resistance;

P_a = atmospheric pressure.

The earthquake-induced cyclic stress time series involves numerous cycles at different strengths, with the damaging effects of the irregular time series depending on the number of cycles and the stress magnitudes for each cycle. An irregular time series can be approximated by a uniform cycles stress time series with an equivalent number of uniform cycles that depends on the uniform cyclic stress amplitude.

Seed and Idriss (1971) proposed to represent earthquake-induced cyclic stresses by using a representative value (or equivalent uniform value) equal to 65% of the peak cyclic

stress. The corresponding earthquake-induced CSR is therefore computed as follows:

$$CSR = 0.65 \frac{\tau_{max}}{\sigma'_{v0}} = 0.65 \frac{\sigma'_{v0}}{\sigma'_{v0}} \frac{a_{max}}{g} r_d \quad (4.12)$$

where σ'_{v0} = effective vertical stress at depth z .

In order to estimate cyclic liquefaction resistance of sand, Robertson and Campanella (1985) developed one of the first liquefaction chart based on the corrected cone resistance (q_{c1}). Although cone penetration resistance is often just corrected for overburden stress (q_{c1}), truly normalized (i.e. dimensionless) cone penetration resistance corrected for the overburden stress q_{c1N} can be given by:

$$q_{c1N} = \frac{q_{c1}}{P_a} = C_Q \cdot \left(\frac{q_c}{P_a} \right) = \left(\frac{P_a}{\sigma'_{v0}} \right)^n \cdot \left(\frac{q_c}{P_a} \right) \quad (4.13)$$

where q_c = measured cone resistance;

C_Q = correction for the overburden stress (a maximum value of 2 is generally applied to CPT at shallow depth; Robertson and Wride, 1998);

n = exponent typically equal to 0.5 for clean sand (Robertson and Wride, 1998);

P_a = atmospheric pressure (0.1 MPa).

The chart of Robertson and Campanella (1985), revised and updated in the frame of the NCEER workshop (1996-1997), is shown in Fig. 4.9 (q_{c1N} -CRR relation). Field observation data used to upgrade the chart are based on the following conditions: Holocene age, clean sand deposits (fine content $FC \leq 5\%$), level or gently sloping ground, magnitude $M_W = 7.5$ earthquakes, 'liquefiable' depth range from 1 to 15 m and representative average q_c values for the layer that was considered to have experienced cyclic liquefaction.

It is particularly important to take into account that, for the same CRR, CPT penetration resistance in silty sands is smaller because of the greater compressibility and decreased permeability of silty sands. As a consequence, Robertson and Fear (1995) recommended operating an average correction on the tip resistance depending on the 'apparent fines content', in order to report the normalized tip resistance of silty sand to the normalized tip resistance of equivalent clean sand.

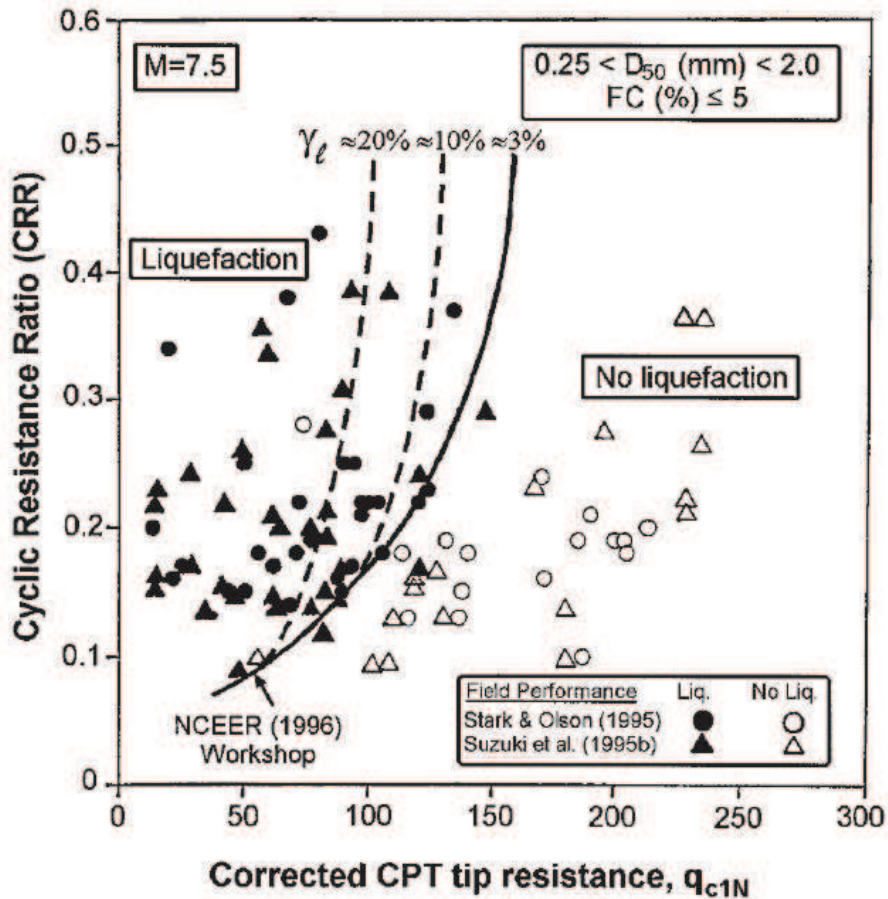


Figure 4.9: Cyclic resistance ratio (CRR) for clean sands vs normalized and dimensionless tip resistance q_{c1N} based on CPT (Robertson and Campanella, after 1996 update).

Robertson and Wride (1998) proposed an equation to obtain the equivalent clean sand normalized CPT penetration resistance ($q_{c1N,cs}$), which is a function of both the measured penetration resistance (q_{c1N}) and the grain characteristics, as follows:

$$q_{c1N,cs} = K_c \cdot q_{c1N} \quad (4.14)$$

where K_c is a correction factor being a function of the grain characteristics of the soil (later defined).

The unknown grain-size characteristics of in-situ soils, such as fines content, can be initially estimated directly from CPT data using, for example, the soil behavior charts proposed in Figure 4.6 (Robertson, 2010 modified from Robertson, 1990 and Robertson and Wride, 1998), where soil type in $Q_{tn} - F_R$ plane are subdivided by I_c curves. Along the normally consolidated region in Fig. 4.6, SBT index increases with increasing of fines

content and soil plasticity. In order to determine an estimation of the apparent fines content, the following simplified relationships were suggested:

- $I_c < 1.26$ apparent fines content $FC (\%) = 0$;
- $1.26 \leq I_c \leq 3.5$ apparent fines content $FC (\%) = 1.75 \cdot I_c^{3.25} - 3.7$;
- $I_c > 3.5$ apparent fines content $FC (\%) = 100$.

The recommended relationship between I_c and the correction factor K_c is defined as:

- $I_c \leq 1.64$ $K_c = 1.0$ (for clean sand);
- $I_c > 1.64$ $K_c = -0.403 \cdot I_c^4 + 5.58 \cdot I_c^3 - 21.63 \cdot I_c^2 + 33.75 \cdot I_c - 17.88$.

Robertson and Wride (1998) suggested that it was reasonable to assume that soil with $I_c > 2.6$, falling into the clayey silt to clay regions of the CPT soil behavior chart, are non-liquefiable. Conversely, soils that fall in the lower left region of such chart (i.e. $I_c > 2.6$ and $F_R \leq 1.0\%$) can be very sensitive and, hence, possibly susceptible to both cyclic and flow liquefaction.

The shear stress reduction coefficient (r_d) is considered as originally evaluated by Seed *et al.* (1971), with an average value of:

$$\begin{cases} r_d = 1.0 - 0.00765 \cdot z & z < 9.15m \\ r_d = 1.174 - 0.0267 \cdot z & 9.15 \leq z < 23m \end{cases} \quad (4.15)$$

The Cyclic Resistance Ratio (CRR) can be thus defined for an earthquake of magnitude (M) equal to 7.5, as follows:

$$50 \leq q_{c1N,cs} < 160 \quad CRR = 93 \left(\frac{q_{c1N,cs}}{1000} \right)^3 + 0.08 \quad (4.16)$$

$$q_{c1N,cs} < 50 \quad CRR = 0.833 \left(\frac{q_{c1N,cs}}{1000} \right)^3 + 0.05 \quad (4.17)$$

The CPT-based liquefaction correlation and some case histories were re-evaluated also by Idriss and Boulanger (2003), using data collected by Shibata and Teparaska (1988), Kayen *et al.* (1998), Boulanger *et al.* (1995; 1997), Stark and Olson (1995), Suzuki *et al.* (1997) and Moss (2003). This re-evaluation incorporated adjustments and parameters re-

vision: the cyclic stress ratio was improved to reflect the number of equivalent cycles that occurred up to the time when liquefaction was triggered, in order to consider that the stronger is the motion, the earlier liquefaction occurs. All CRR and q_{c1N} values were re-calculated using the revised r_d and MSF for cyclic stress conditions and C_N for the cone resistance; a stress correction factor, K_σ , was also introduced. Information for each case history was compiled by identifying the combination of the earthquake-induced CSR and in-situ penetration resistance that best represents the critical zone for each site. In compiling the case histories into a common data set, it is necessary to adopt some standard reference condition to which each case history can be adjusted. This was done by adopting the reference condition of an $M = 7.5$ earthquake and an effective overburden stress of $\sigma'_{v0} = 1$ atm.

The earthquake-induced CSR at each site was then adjusted to the equivalent CSR for the reference values of $M = 7.5$ and $\sigma'_{v0} = 1$ atm, as follows:

$$CSR_{M_w=7.5;\sigma'_{v0}=1} = CSR_{M,\sigma'_{v0}} = \frac{1}{MSF} \cdot \frac{1}{K_\sigma} \quad (4.18)$$

$$CSR_{M_w=7.5;\sigma'_{v0}=1} = 0.65 \left(\frac{a_{max}}{g} \right) \left(\frac{\sigma'_{v0}}{\sigma'_{v0}} \right) r_d \frac{1}{MSF} \cdot \frac{1}{K_\sigma} \quad (4.19)$$

Indeed, normalized tip resistance was established with the following formulation:

$$q_{c1N} = \frac{q_{c1}}{P_a} = C_N \frac{q_c}{P_a} \quad (4.20)$$

Thus, the tip resistance was normalized introducing a factor C_N , both theoretically and experimentally determined. Boulanger (2003) proposed a linear exponential trend for this normalization factor, expressed as:

$$C_N = \left(\frac{P_a}{\sigma'_{v0}} \right)^m = \left(\frac{P_a}{\sigma'_{v0}} \right)^{1.338 - 0.249 \cdot (q_{c1N})^{0.264}} \quad (4.21)$$

Stress reduction coefficient (r_d), originally proposed by Seed and Idriss (1971), accounts for flexibility of the ground. Golesorkhi (1989) evaluated the variations of r_d with earthquake magnitude and later Idriss (1999) derived the following relationship:

$$r_d = \exp[\alpha(z) + \beta(z) \cdot M] \quad (4.22)$$

$$\alpha(z) = -1.012 - 1.126 \cdot \text{sen} \left(\frac{z}{11.73} + 5.133 \right) \quad (4.23)$$

$$\beta(z) = -0.106 - 0.118 \cdot \text{sen} \left(\frac{z}{11.28} + 5.142 \right) \quad (4.24)$$

where M = moment magnitude.

The magnitude scale factor (MSF) used by Idriss and Boulanger (2008) was developed by Idriss (1999), who derived the following relationship:

$$MSF = 6.9 \cdot \exp \left(-\frac{M}{4} \right) - 0.058 \leq 1.8 \quad (4.25)$$

Lastly, for the CSR determination was introduced the effect of the overburden stress for cyclic stress behavior (Boulanger, 2003; Boulanger and Idriss, 2004) through a K_σ factor defined as follows:

$$K_\sigma = 1 - C_\sigma \cdot \ln \left(\frac{\sigma'_{v0}}{P_a} \right) \leq 1 \quad (4.26)$$

where C_σ can be expressed in terms of the overburden corrected penetration resistances (q_{c1N}) as:

$$C_\sigma = \frac{1}{37.3 - 8.27 \cdot (q_{c1N})^{0.264}} \leq 0.3 \quad (4.27)$$

The CRR- q_{c1N} relation revised by Idriss and Boulanger (2004, 2006) is computed as:

$$CRR_{M=7.5} = \exp \left[\frac{q_{c1N}}{540} + \left(\frac{q_{c1N}}{67} \right)^2 - \left(\frac{q_{c1N}}{80} \right)^3 + \left(\frac{q_{c1N}}{114} \right)^4 - 3 \right] \quad (4.28)$$

In Fig. 4.10, a comparison between this CRR- q_{c1N} relation (eq. 4.28) and those proposed by Shibata and Teparaksa (1988), Robertson and Wride (1997), Suzuki *et al.* (1997), and the 5% probability curve by Moss (2003) is shown. The derived relation (Eq. 4.28) is

comparable to the curve proposed by Suzuki *et al.* (1997) for clean sands. It is more conservative than the corresponding curves by Robertson and Wride (1997) and by Seed *et al.* (2003) for almost the entire range of q_{c1N} . The curve proposed by Shibata and Teparaksa (1988) is less conservative than the derived relation except for q_{c1N} greater than about 165.

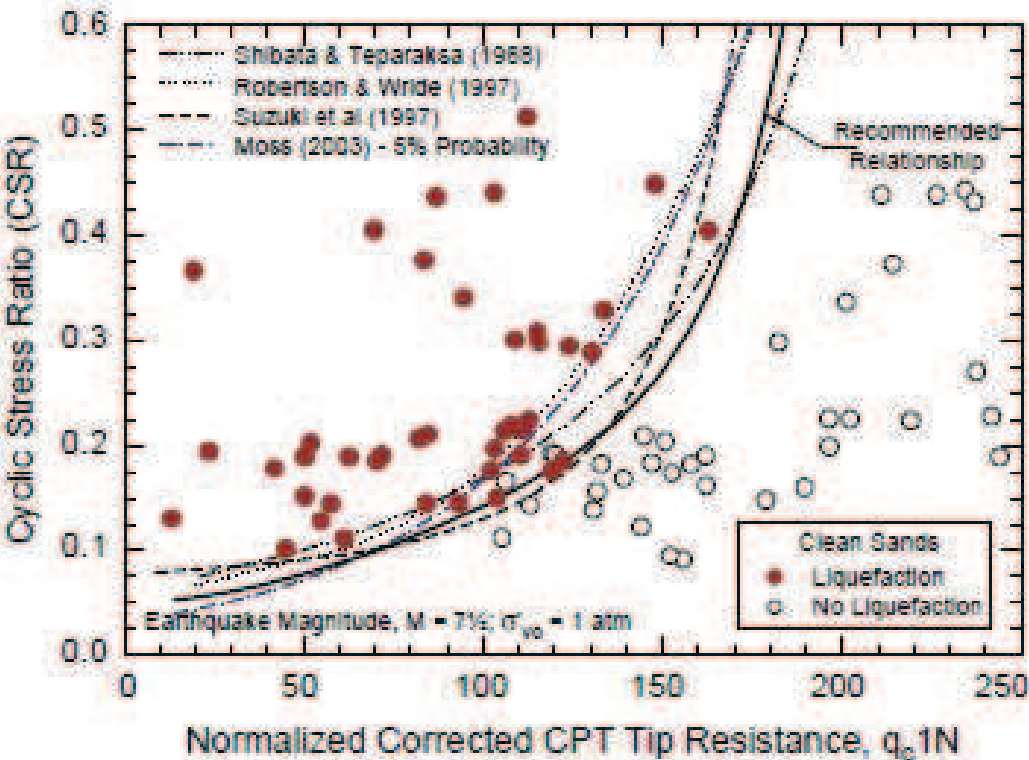


Figure 4.10: Curves relating the CRR to q_{c1N} for clean sands with $M = 7.5$ and $\sigma'_{vo} = 1$ atm (from Idriss and Boulanger, 2004, 2006).

The CPT-based approach can be modified to account for the effects of non-plastic fines content on the liquefaction resistance. Robertson and Wride (1998) and Suzuki *et al.* (1997) suggested the use of the ‘soil behavior type index’, I_c (Jefferies and Davies, 1993), which is a function of the tip resistance (q_c) and sleeve friction ratio (R_f), to estimate the values of CRR for cohesionless soils with high fines content. The overburden corrected cone tip resistance value for clean sand ($q_{c1N,cs}$), with fine content (FC) equal to 35%, can be computed as (Idriss and Boulanger, 2008):

$$q_{c1N,cs} = q_{c1N} + \Delta q_{c1N} \tag{4.29}$$

$$\Delta q_{c1N} = \left(5.4 + \frac{q_{c1N}}{16}\right) \cdot \exp \left[1.63 + \frac{9.7}{FC+0.01} - \left(\frac{15.7}{FC+0.01}\right)^2\right] \quad (4.30)$$

The derived relation between CRR and penetration resistances for clean sands can be expressed as follows (Idriss and Boulanger, 2008):

$$CRR_{M=7.5} = \exp \left[\frac{q_{c1N,cs}}{540} + \left(\frac{q_{c1N,cs}}{67}\right)^2 - \left(\frac{q_{c1N,cs}}{80}\right)^3 + \left(\frac{q_{c1N,cs}}{114}\right)^4 - 3 \right] \quad (4.31)$$

The curve recommended by Robertson and Wride (1998) relating CRR- q_{c1N} at $I_c=2.59$ (defined by these authors as corresponding to an ‘apparent’ fines content $FC = 35\%$) is presented in Fig. 4.11. Also shown in this figure are the CPT-based data points for the cases examined by Moss (2003) for cohesionless soils with $FC=35\%$. As can be seen in Fig. 4.11, the curve recommended by Robertson and Wride (1997) is unconservative in relation to these newer case history data points.

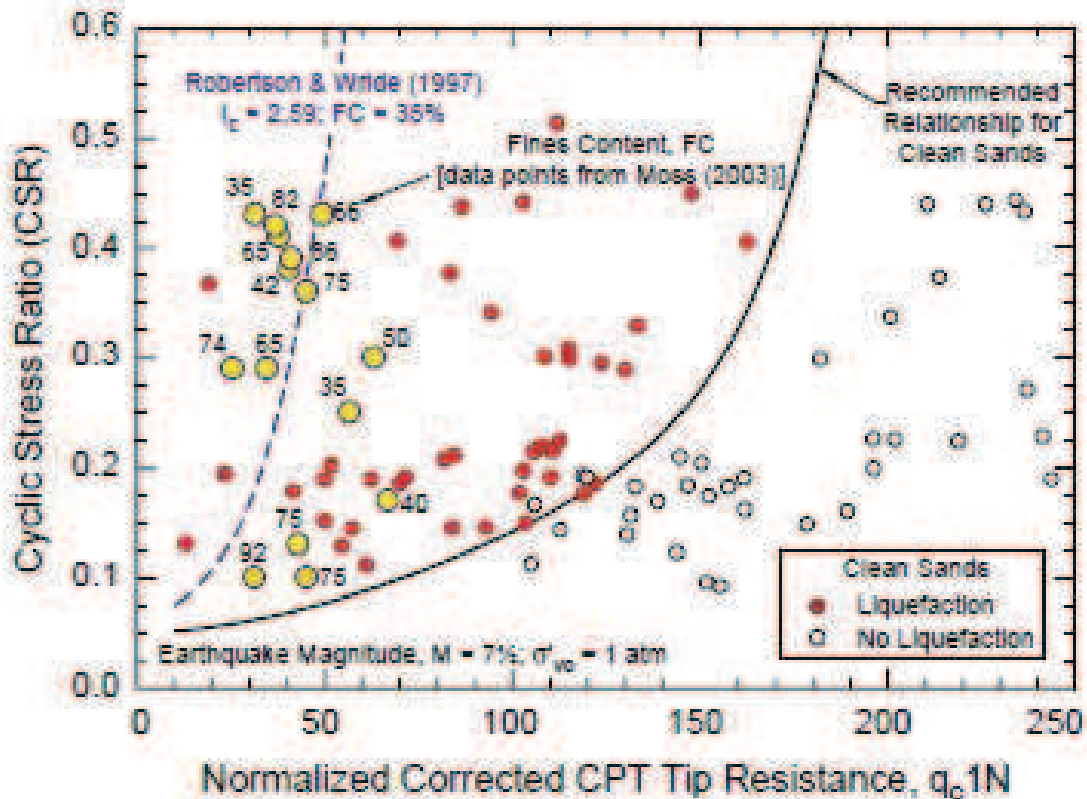


Figure 4.11: Comparison of field case histories for cohesionless soils with high fines content and curve proposed by Robertson and Wride (1998) for soils with $I_c=2.59$ (apparent $FC=35\%$) (from Idriss and Boulanger, 2004; 2006).

4.2.4 Liquefaction Potential Index (LPI) and Liquefaction Severity Number (LSN)

Liquefaction Potential Index (LPI) is a parameter firstly developed by Iwasaki *et al.* (1978) to characterize the potential for surface manifestations of liquefaction, by weighting factors of safety and thickness of potentially liquefiable layers according to depth. It assumes that the severity of liquefaction is proportional to:

- cumulative thickness of the liquefiable layers;
- proximity of liquefied layers to the surface;
- amount by which the factor of safety (F_s ; i.e. the ratio between CRR and CSR) is less than 1.0.

Iwakaski *et al.* (1978) defined LPI as follows:

$$LPI = \int_0^h F(z) \cdot w(z) \cdot dz \quad (4.32)$$

where $F = 1 - F_s$, for $F_s \leq 1$;

$F = 0$, for $F_s > 1$;

$w(z) = 10 - 0.5 \cdot z$

$z =$ depth [m] from the surface.

In the formulation of Iwasaki *et al.* (1978), F_s was determined using a standard penetration test (SPT)-based simplified method established by the Japan Road Association (1980). The integration depth (h) is commonly limited to 20 m. Iwasaki *et al.* (1978) discriminated some threshold LPI values for evaluation of the severity of liquefaction-induced damages observed during earthquakes, on the basis of field observations at liquefaction sites in Japan. According to the threshold values proposed by Iwasaki *et al.* (1978) the liquefaction potential should be characterized as ‘low’ at sites where $0 < LPI < 5$, ‘high’ where LPI is in the range 5–15 and ‘very high’ above 15 (hereafter ‘Iwasaki criterion’).

An important confirmation of the Iwasaki criterion was provided by Toprak and Holzer (2003) which computed LPI values from CPTs instead of SPTs at sites with surface manifestations of liquefaction during the 1989 Loma Prieta, California, earthquake. In

their calculations, they used the Iwasaki *et al.* (1978) LPI formulation, but the factor of safety was calculated using the CPT-based method by Robertson and Wride (1998), which employs the simplified procedure proposed by Seed and Idriss (1971). Toprak and Holzer (2003) concluded that sand boils likely occur where $LPI \geq 5$ and lateral spreading phenomena will occur where $LPI \geq 12$. They also suggested that these findings were consistent with the Iwasaki criterion, a conclusion subsequently supported by findings of further studies by Holzer *et al.* (2005; 2006a; b).

Sonmez (2003) developed a modified scale by adding a threshold value of 1.2 instead of 1 for the calculation of F_s and introduced two new categories of liquefaction failure potential by distinguishing $LPI = 0$ as 'non liquefiable', 0 to 2 as 'low', 2 to 5 as 'moderate', 5 to 15 as 'high' and >15 as 'very high'. Afterwards, Sonmez and Gokceoglu (2005) performed some modifications on the finding of Sonmez (2003), concluding that the use of a probability-based factor for variable F_s was more realistic. By taking into account an equation proposed by Lee *et al.* (2004), Sonmez and Gokceoglu (2005) suggested a procedure for evaluating a variant of LPI, known as the Liquefaction Severity Index (L_s). In addition, they introduced a classification where for $L_s = 0$ a site is considered as 'non-liquefied', 0 to 15 the severity is considered as 'very low', 15 to 35 as 'low', 35 to 65 as 'moderate', 65 to 85 as high and > 85 as 'very high'.

Lee *et al.* (2004), based on their study following the 1999 Chi-Chi, Taiwan, earthquake, reported that when the CPT-based method by Robertson and Wride (1998) was used to determine the factor of safety, the calculated LPI values did not match either the Iwasaki criterion or the results by Toprak and Holzer (2003). Almost 50% of liquefied cases had an $LPI > 15$ with only 10% of liquefied cases having an $LPI < 5$. To the contrary, 85% of non-liquefied cases had an $LPI > 5$, and 30% of non-liquefied cases even had an $LPI > 15$. Therefore, Lee *et al.* (2004) suggested that if the Robertson and Wride (1998) method is used to determine F_s , the two threshold values of the Iwasaki criterion, 5 and 15, should be modified to 13 and 21, respectively. Accordingly, liquefaction risk is high for sites with $LPI > 21$ and low for sites with $LPI < 13$.

Lenz and Baise (2007) computed LPI values for the East Bay of the San Francisco

California Bay Area, using both CPTs and SPTs. They found that CPT-based LPI characterization results in higher hazard in the same study area than those derived from the SPT. They suggested that the bias could be caused by either misclassification of soil type in the CPT or a bias in the CPT-based simplified procedure for liquefaction potential. They attributed the latter to the finding by Juang *et al.* (2002) that soils with an equal F_s value, determined with different simplified methods, may not have the same liquefaction potential due to the different degrees of model bias associated with these methods. They also noticed that CPTs provide a more reliable and consistent measure of liquefaction potential, as it has a much higher degree of repeatability than SPT (Jefferies and Davies, 1993), and it also provides a continuous profile, while SPTs do not.

Papathanassiou (2008) proposed an LPI-based probabilistic approach for the evaluation of liquefaction-surface evidences and, by taking into account a cut-off value of 50% probability. He used the SPT-procedure from Youd *et al.* (2001) to compute LPI from several tests performed after the 1999 Chi Chi (Taiwan), 1999 Kocaeli (Turkey) and 2003 Lefkada (Greece) earthquakes. The median LPI values for cases of high liquefaction severity, medium liquefaction severity, and no-failure were 38, 24, and 14, respectively. Accordingly, Papathanassiou (2008) suggested threshold LPI values of 19 and 32 as opposed to 5 and 15 per the Iwasaki criterion and he also defined a threshold value of $LPI = 14$ for discriminating the cases of liquefaction surface manifestation from the non-liquefaction ones. This classification took also into account the susceptibility to liquefaction criteria proposed by Seed *et al.* (2003) for the classification of the soil layers. The fact that Papathanassiou (2008) followed the recently published susceptibility criteria, and considered silty soils for the computation of LPI, are the main reasons for this higher threshold value of $LPI = 14$. Moreover, Maurer *et al.* (2014) concluded that this high LPI value might be explained by the fact that Papathanassiou (2008) analyzed soils with high fines content.

Juang *et al.* (2008) computed LPI with the concept of probability of surface manifestation of liquefaction (P_G) and recommended the following classification of risk for surface manifestation of liquefaction; ‘extremely low’ when $P_G < 0.1$, ‘low’ for $0.1 < P_G < 0.3$, ‘medium’ when $0.3 < P_G < 0.7$, ‘high’ when $0.7 < P_G < 0.9$ and ‘extremely high’ for $P_G >$

0.9. He concluded that the two threshold values (5 and 15) assumed in the Iwasaki criterion are likely not universally applicable and that the LPI scale should be rigorously re-calibrated anytime a component model of the LPI procedure is modified. Moreover, this discrepancy between the existing calibrations proposed by several authors as briefly reviewed above may be also due to different types of considered liquefiable layers (e.g. clean sand or silty sands and sandy silts). Furthermore, Maurer *et al.* (2014) pointed out the importance of having consistency in the way threshold LPI values are determined and how the LPI values are computed to assess liquefaction hazard.

The LSN is a new parameter developed by Tonkin and Taylor (2013) to reflect damaging effects of shallow liquefaction and should be considered as a probabilistic measure indicating risk assessment. The LSN could be considered as an extension of the philosophy at the basis of the LPI and represents an alternative method for assessing the response of structures to liquefaction. The LSN rating represents the intensity of liquefaction by using volumetric densification strain as a proxy (e_v), with depth weighting by a hyperbolic ($1/z$) rather than a linear reduction (van Ballegooy *et al.*, 2012). According to Tonkin and Taylor (2013), the LSN is higher for liquefiable soils closer to the ground surface in comparison to liquefiable layers at depth.

The equation that should be used for computing the LSN is:

$$LSN = 1000 \cdot \int_0^h \frac{e_v}{z} dz \quad (4.33)$$

where z is the depth from the surface to the layer of interest in meters and e_v is the volumetric densification strain in the subject layer induced by the earthquake loading, estimated following the approach proposed by Zhang *et al.* (2002).

As in Eq. 4.33, the integration depth is commonly posed equal to 20 m because the contribution of the underlying layers would be negligible.

Nagase and Ishihara (1988) and Ishihara and Yoshimine (1992), mainly based on laboratory tests, established a family of curves (Fig. 4.12a), from which the volumetric strain resulting from the dissipation of pore-water pressures was correlated with the relative density (D_r) and the factor of safety against liquefaction (F_s) for clean sands. As the relative

density D_r cannot be measured directly from the CPT, several empirical correlations between D_r and cone resistance (q_c) have been proposed (e.g. Jamiokowsky *et al.*, 1985; Tatsuoka *et al.*, 1990). In order to exploit the curves shown in Fig. 4.12a for the estimation of the postliquefaction volumetric strains of silty sands using the CPT, some modifications for take into account the grain characteristics or fines content must be made. Zhang *et al.* (2002) suggested to use the equivalent clean sand normalized CPT penetration resistance ($q_{c1N,cs}$), defined by Robertson and Wride (2008). This parameter can thus be treated as the cone tip resistance for a clean sand and used directly to estimate the postliquefaction volumetric strain at certain values of the factor of safety (Fs). The correlations between $q_{c1N,cs}$ and postliquefaction volumetric strain (ϵ_v) for different Fs were developed on the basis of the curves of Ishihara and Yoshimine (1992) and are shown in Fig. 4.12b.

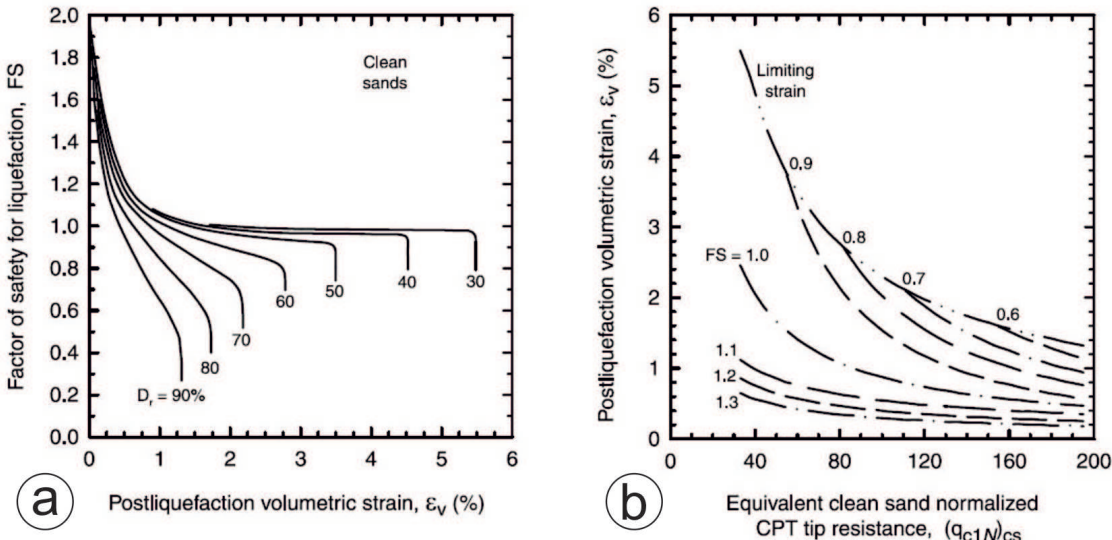


Figure 4.12: a) Curves for estimating the postliquefaction volumetric strain of clean sands (modified from Ishihara and Yoshimine, 1992). b) Relationship between postliquefaction volumetric strain and equivalent clean sand normalized CPT tip resistance for different values of the factor of safety Fs (Zhang *et al.*, 2002).

Based on the observed land damages caused by Christchurch 2010–2011 earthquakes (Tonkin and Taylor, 2010a; b; 2013; Cubrinovski *et al.*, 2011; Orense *et al.*, 2011; Wotherpoon *et al.*, 2012; O’Rourke *et al.*, 2014) and the results provided by thousands of CPTs performed in the epicentral area, Tonkin and Taylor (2013) developed a first classification of LSN associating ‘little-to-no expression of liquefaction’ to $0 < LSN < 10$, ‘minor expression of liquefaction and sand boils’ to $10 < LSN < 20$, ‘moderate-to-severe expression of lique-

faction and likely settlement' when $20 < \text{LSN} < 30$ and 'major expression of liquefaction, damage to ground surface and severe settlement of structures' when $30 < \text{LSN} < 40$. Finally for LSN values greater than 50, 'severe damage and widespread evidence of liquefaction at the surface' is reported.

4.3 Data collection and processing

4.3.1 Geognostic database of the Sant'Agostino Municipality

The first phase of this work consisted in the collection, georeferencing and archiving of all the geognostic and geophysical data that can provide information (stratigraphic, lithological, geomechanical, hydrogeological) on the shallow subsoil, say up to some tens of meters depth. Starting from the preexisting information stored in the database managed by the Regione Emilia-Romagna, it was subsequently conducted a systematic research in the archives of several professional geologists which worked in the broader area. The most important added value of this effort was the reconstruction and the upgrade of the geotechnical and geophysical archive of the municipality, which had been almost completely destroyed due to the collapse of the Sant'Agostino town hall. Thanks to the new data collection I performed, more than three hundred new survey sites and associated metadata have been added, thus enabling also the Regione Emilia-Romagna to upgrade its database. At present about 700 sites (including penetration tests, water wells and geophysical surveys) are available, that is more than twice existing before this investigation.

All these data are now included and available in the database managed by the Regione Emilia-Romagna through accessing to the dedicated website

(<http://geo.regione.emilia-romagna.it/geocatalogo/>).

Each survey is uniquely identified by a 10-digit code, composed as follows:

- the first six-digits identify the section of the Regional Technical Map in which the survey is located;
- a letter identifying the type of survey (prefix in Table 4.2);
- a three-digit progressive number identifier of a survey within a section of the Re-

gional Technical Map (progressive in Table 4.2).

Prefix	
B	seismic cone penetration test
C	mechanical cone penetration test
E	electrical cone penetration test
F	cross-hole
J	MASW
N	array noise measurement
P	drill-core and water well
R	single-station noise measurement
U	piezo-cone penetration test

Progressive	
001-399	penetrometric test and drill-core
400-499	continuos drill-core
500-599	penetrometric test and drill-core made by the Regione Emilia-Romagna
600-899	water well

Table 4.2: Convention for the identification of the geognostic surveys archived in the database.

The second phase of the work consisted in the digitalization of the available penetration tests (more than four hundred), in order to exploit their numerical content for microzon- ing purposes, i.e. for the quantitative analysis of the liquefaction hazard.

The measured parameters of each penetrometric test (i.e. q_c , f_s and, only for CPTu and SCPTu, also u_2) were converted from the raster to a digital format.

The digitization procedure was methodologically different, according to the original format of the data:

1. if the data were already in numerical format (.xls, .txt, .csv), they were simply copied and pasted;
2. if the data were available in raster format (.pdf, .jpg), an optical character reader and a utility (Engauge Digitizer) specifically developed for digitization purpose were used.

Afterwards, the numerical data were organized in excel sheets (Fig. 4.13).

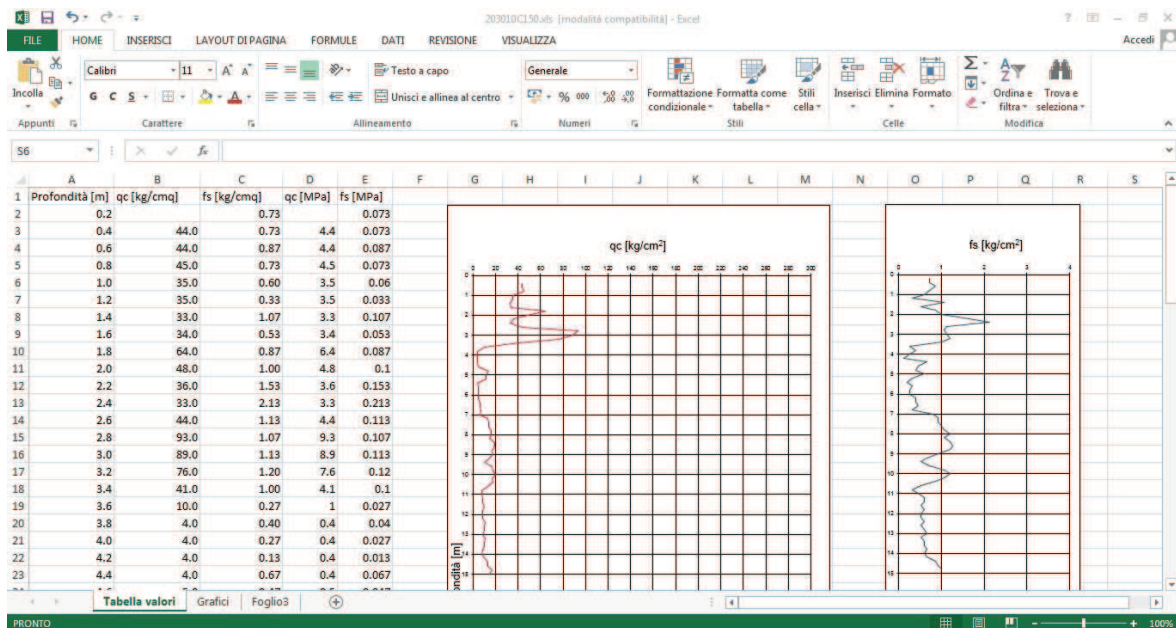


Figure 4.13: Example of the organization of the numerical data in an excel sheet.

4.3.2 Qualitative and quantitative assessment of susceptibility to liquefaction

As widely discussed in the previous paragraph, liquefaction occurs due to the shaking generated by moderate to strong earthquakes ($M_W > 5.0$), especially in floodplain and coastal areas that are often characterized by loose granular sediments and shallow aquifer. This phenomena is the result of the combined effect of triggering factors (characteristics of the earthquake in terms of magnitude and local acceleration) and the predisposing ones (subsoil conditions and geomorphological framework): in the case of the Sant’Agostino Municipality, liquefaction has been one of major causes of damage and collapse of buildings due to the concomitance of these factors.

Therefore, in order to recognize and define the possible areas subject to liquefaction hazard, the available data were analyzed.

All the penetration tests were preliminarily examined from a semi-quantitative point of view for detecting the presence of liquefiable horizons. In particular, in accordance with the Geological Survey of the Regione Emilia-Romagna the surveys have been classified on the basis of the thickness and depth of the liquefiable layer(s) as follows:

- L1: saturated liquefiable layer(s) in the first 5 m b.g.s. (at least 30-40 cm thick);

- L2: saturated liquefiable layer(s) between 5 to 10 m b.g.s. (at least 1 m thick);
- L3: saturated liquefiable layer(s) between 10 to 15 m b.g.s. (at least 2 m thick);
- L4: saturated liquefiable layer(s) between 15 to 20 m b.g.s. (at least 2 m thick).

Subsequently, a quantitative assessment of the liquefaction hazard was performed by calculating the Liquefaction Potential Index, LPI (Iwasaki *et al.*, 1978), through a dedicated software, CLiq (v.1.7.5.27). The input parameters for the calculation are a) the magnitude M_{Wmax} , deduced from the seismogenic zonation ZS9 (Meletti and Valensise, 2004), equal to 6.14 for the Municipality of Sant'Agostino, b) the acceleration a_{gmax_s} ($PGA * F_{APGA}$), computed by the Regione Emilia-Romagna following the regional guidelines (DAL 2007) and c) the water's depth, conventionally assumed equal to 1 m for interfluvial areas and 3 m in correspondence of the palaeo levees. The calculation was performed for both electrical penetration tests and mechanical ones, despite the high degree of uncertainty in the measurement of the sleeve friction characteristic of the latter type of investigation (Lo Presti *et al.*, 2009) and that the methods for the evaluation of the liquefaction hazard were developed for piezocone cone penetration tests.

The entire data and results collection is available under request.

Chapter 5

Geophysical methods and data collection

The aim of the geophysical methods is the investigation of the physical properties of the subsoil (e.g. electrical resistivity, density, elastic constants, magnetic susceptibility, etc.). Such methods are based on active or passive strategies.

The active methods (GPR, geoelectric, seismic and electromagnetism surveys) consisted on the direct or indirect perturbation of a field strength related to the investigated parameter(s). On the contrary, the passive methods (seismic ambient noise, magnetic, thermic and gravimetric investigations) do not require artificial sources of energy, but they basically exploited the natural radiation or the ambient noise recorded at the ground surface.

An attractive feature of some geophysical surveys is not to be invasive and therefore, for their execution, the drilling of boreholes is not required. Such investigations are carried out from the ground surface, thus their implementation is easier and cheaper than other methods (Lai *et al.*, 2000).

For the purpose of this research project were applied two passive methods based on the seismic ambient noise (i.e. Extended Spatial Auto-Correlation - ESAC and Horizontal-to-Vertical Spectral Ratio - HVSR), in order to reconstruct pseudo-2D sections along two transects, several kilometers-long, crossing the central sector of the Ferrara Arc, emphasizing the possible occurrence of lateral shear wave velocity (and amplitude) variations, which will likely reflect the stratigraphic changes (see Section 6.1).

A detailed description of the theoretical basis of the employed techniques, data collection and processing is reported in the following sections.

5.1 Seismic ambient noise: nature and composition

The seismic ambient noise (hereafter ‘noise’) is a set of small amplitude oscillations (10^{-4} - 10^{-2} mm) of the ground surface characterized by a wide frequency content (0.05-100 Hz), partially below human sensing (Okada, 2003).

The origin of these oscillations may be natural such as wind, oceanic waves and meteorological conditions or artificial as well as road traffic and industrial activities. Classifying all noise sources is not an easy task. Gutenberg (1958) established a list of different types of sources according to their frequency. Asten (1978) and Asten and Henstridge (1984) reached the same conclusions in a noise review (see Table 5.1).

Sources	Gutenberg (1958)	Asten (1978) - Asten and Henstridge (1984)
oceanic waves	0.05-0.1 Hz	0.5-1.2 Hz
meteorological perturbations	0.1-0.25 Hz	0.16-0.5 Hz
oceanic hurricanes	0.3-1 Hz	—
local meteorological conditions	1.4-5 Hz	—
volcanic tremor	2-10 Hz	—
anthropogenic activities	1-100 Hz	1.4-30 Hz

Table 5.1: Noise sources and related frequency range according to Gutenberg (1958), Asten (1978) and Asten and Henstridge (1984).

These analyses show that noise has basically two different origins, natural and artificial, that are characterized by distinct frequency content. In particular, the difference among long-period ($T > 1$ s) and short-period ($T < 1$ s) noise corresponds to the traditional distinction between ‘microseisms’ and ‘microtremors’, from natural and artificial origin, respectively. However, depending on the geology, the 1 s boundary between the two domains may be shifted to longer periods. Accordingly to Seo (1997), in deep basin there could be energy enough to excite the microtremor at frequencies lower than 1 Hz; in addition, in urban context, artificial noise may be more energetic than the natural one, even at intermediate periods (up to a few seconds). Significant daily amplitude variations (with a factor of 3 to 4 between day and night) clearly indicate microtremors, as suggested by Seo (1997).

The artificial noise is dominated by frequency higher than 1 Hz and is obviously characterized by diurnal variation in both amplitude and period (Yamanaka *et al.*, 1993; Kanai

and Tanaka, 1961). On the contrary, the natural noise is predominantly characterized by frequencies lower than 1 Hz with relative amplitude and periodical variations related to the cyclicity of each source (Longuet-Higgins, 1950; Haubrich *et al.*, 1963; Akamatsu *et al.*, 1992; Friedrich *et al.*, 1998). As an example, the temporal variations of noise characterized by these low frequencies have a good relationship with the changes of the atmospheric pressure. The noise energy increases with lower atmospheric pressure reaching a maximum soon after the minimum in atmospheric pressure and viceversa (Sakaji, 1998).

Achieving the composition of the noise wave field is not an easy task and many issues are still open and widely debated (Bonney-Claudet *et al.*, 2004; Bonney-Claudet and Bard, 2006). Several scientists investigated this phenomena in order to define:

- the ratio of body waves to surface waves (Douze, 1964; 1967; Toksöz and Lacoss, 1968; Li *et al.*, 1984; Horike, 1985; Yamanaka *et al.*, 1994);
- the ratio of Love to Rayleigh waves (Chouet *et al.*, 1998; Ohmachi and Umezono, 1998; Yamamoto *et al.*, 2000; Arai *et al.*, 1996; Cornou, 2002; Okada, 2003);
- the ratio of fundamental Rayleigh mode to higher modes (Tokimatsu, 1997; Stephenson, 2003).

From the synthesis of the above mentioned papers and additional numerical simulations (Bonney-Claudet *et al.*, 2004; Bonney-Claudet and Bard, 2006) it can be emphasized that:

- at lower frequency (below 1 Hz), noise seems to be mainly represented by fundamental Rayleigh waves, while there is no general agreement for higher frequencies;
- the relative proportion of Love waves is significant (at least 40% or more);
- higher modes of Rayleigh waves can exist in the noise wave field and soil stratification plays an important role in the excitation of higher modes.

Notwithstanding this phenomena have been observed since the end of the 19th century (Bertelli, 1872), studying Earth noise has become popular when Brune and Oliver (1959) published the curve of high and low seismic background displacement based on a world-wide survey of station noise.

5.1.1 Noise-based techniques

Starting from the 1950s, diffusion of seismology and equipment technical improvement allowed significant advances in the understanding of noise phenomena. As above described, several authors investigated the origin and the nature of noise as well as the possible noise-based techniques and applications.

One of the most important are the array techniques (wave time delay measurements between coupled stations). These methods are linked with the property of surface waves dispersion and allow to obtain the shear-wave velocity profile. There are two main array techniques: the frequency-wave number analysis (f-k; Capon *et al.*, 1967; Capon, 1969; Lacoss *et al.*, 1969) and the spatial autocorrelation analysis (SPAC; Aki, 1957; 1964).

Other techniques, based on single-station noise recordings, are the site reference and the horizontal-to-vertical spectral ratios.

5.2 SPAC-ESAC methodologies: analytical procedure and application

The pioneristic studies of Aki (1957; 1964) demonstrated that the phase velocities in sedimentary layers can be determined using a statistical analysis of seismic ambient noise. He assumed that noise represents the sum of waves propagating without attenuation in a horizontal plane in different directions with different powers, but with the same phase velocity for a given frequency and also that these waves are statistically independent. He proposed the Spatial Auto-Correlation method (SPAC) which consists in the acquisition of seismic ambient noise through an array of equidistant stations forming pairs at varying azimuth, in order to estimate the phase velocity from surface wave observations without considering their direction of propagation. This is possible because we assume that the dispersive wave field propagates along a free surface and that it is stationary and stochastic in space and time.

Considering a stochastic wavefield (Aki, 1957) formed by the superposition of many directions in the horizontal plane, all of them propagating with the same constant phase velocity. The ground motion at two locations on the surface (x, y) and $[x + r \cos(\lambda), y + r$

$\sin(\lambda)]$ may be written as:

$$u(x, y, t) \quad (5.1)$$

and

$$u[x + r\cos(\lambda), y + r\sin(\lambda), t] \quad (5.2)$$

where $u(x, y, t)$ is the velocity observed at point (x, y) at time t , r is the inter-station distance and λ is the azimuth.

The spatial autocorrelation function $\phi(r, \lambda, t)$ can therefore be defined as:

$$\phi(r, \lambda, t) = \langle u(x, y, t)u[x + r\cos(\lambda), y + r\sin(\lambda), t] \rangle \quad (5.3)$$

where $\langle \rangle$ denotes the mean value of $u(t)$ over the time domain.

The azimuthal average of the spatial autocorrelation function can be written as:

$$\phi(r) = \frac{1}{2\pi} \int_{2\pi}^0 \phi(r, \lambda) d\lambda \quad (5.4)$$

Aki (1957) showed also that the azimuthal average of the spatial autocorrelation function $\phi(r)$ and the power spectral density $\phi(\omega)$ of the wavefield u , where ω is the angular frequency, are related as follows:

$$\phi(r) = \frac{1}{\pi} \int_0^\infty \phi(\omega) J_0 \frac{\omega}{c(\omega)} d\omega \quad (5.5)$$

where $c(\omega)$ is the frequency-dependent phase velocity and J_0 is the zero-order Bessel function.

Applying a bandpass filter to the signals, the spectral density becomes:

$$\Phi(r) = P(\omega_0) \delta(\omega - \omega_0) \quad (5.6)$$

where $P(\omega_0)$ is the power spectral density at the frequency ω_0 and $\delta(\omega)$ is the Dirac function.

The spatial autocorrelation function can be written as:

$$\Phi(r) \equiv \phi(r, \omega_0) = P(\omega_0) J_0 \frac{\omega_0}{c(\omega_0)} r \quad (5.7)$$

By fitting the azimuthally averaged spatial correlation function obtained from measured data to the Bessel function it is possible to calculate $c(\omega_0)$.

Beyond the clear advantages compared to active methods, the SPAC one (fixed value of r), presents an inconvenience due to its circle array developed to ensure the isotropic nature of the acquired signal, which may prevent its use in urban areas. Recently, Okada (2003) and Ohori *et al.* (2002) demonstrated that it's possible to use simpler arrays (with geophones placed along T, L or X profile); in fact, since $c(\omega_0)$ is a function of frequency, better results are achieved by fitting the spatial-correlation function at each frequency to a Bessel function, which depends on the inter-station distances (Extended Spatial Auto Correlation, ESAC). For every couple of stations the function $\phi(\omega)$ can be calculated in the frequency domain as follows:

$$\phi(\omega) = \frac{\frac{1}{M} \sum_{m=1}^M \text{Re}[{}_m S_{jn}(\omega)]}{\sqrt{\frac{1}{M} \sum_{m=1}^M [{}_m S_{jj}(\omega)] \sum_{m=1}^M [{}_m S_{nn}(\omega)]}} \quad (5.8)$$

where $\text{Re}[\text{arg}]$ is the real part of the complex argument, ${}_m S_{jn}$ is the cross-spectrum for the m th segment of the data, between the j th and the n th station, M is the total number of used segments, ${}_m S_{jj}$ and ${}_m S_{nn}$ are the power spectra of the m th segments at stations j and n .

An important application of these techniques regards the reconstruction of the sub-surface shear-wave velocity profile. Such studies started in the late '50s, but thanks to the technology evolution in the following decades (higher computing capability, 3-components seismometer, etc.) the quality and quantity of array surveys data recordings largely increased (Asten and Henstridge, 1984; Bache *et al.*, 1986; Tokimatsu *et al.*, 1992; 1996; Malagnini *et al.*, 1993; Arai *et al.*, 1996; Horike, 1985; Kagawa, 1996; Milana *et al.*, 1996; Miyakoshi and Okada, 1996; Friedrich *et al.*, 1998; Miyakoshi *et al.*, 1998; Maresca *et al.*, 1999; Scherbaum *et al.*, 1999; Kanno *et al.*, 2000; Liu *et al.*, 2000; Bettig *et al.*, 2001; Satoh *et al.*, 2001; Kudo

et al., 2002; Cornou *et al.*, 2003a; b; Ohori *et al.*, 2002; Flores Estrella and Aguirre Gonzalez, 2003; Scherbaum *et al.*, 2003).

5.2.1 Frequency-slowness analysis

The use of the frequency-slowness (ω - p) transform for the analysis of dispersive waves was proposed by McMechan and Yedlin (1981). It is based on the slant stack (τ - p) transform, one of the basic tools of seismic data processing. The τ - p transform allows the decomposition of a wave field into its plane wave linear components. In this case the τ - p transform is defined as:

$$\bar{u}(\tau, p) = \int_{-\infty}^{+\infty} u(\tau + px, x) dx \quad (5.9)$$

The transform gives the energy density as a function of τ (the time delay at zero offset) and p (the ray parameter, or slowness). The τ - p transform of a record in time-offset domain stacks the wave field along a straight line of slope p for each value of τ . A straight line in the time-offset domain is described by a constant τ and p ; a linear event in the x - t domain with a slope p and intercept τ would map into a single point in the τ - p plane.

On real discrete data, Eq. 5.9 is converted to the discrete slant stack transform where the integral is substituted by a sum:

$$\bar{u}(\tau_l, p_l) = \sum_{j=1}^N u(\tau_l + p_k x_j, x_j) \quad (5.10)$$

with $\tau_l = l\Delta\tau$ and $p_k = k\Delta p$. For the computation, the minimum and maximum values of p (p_{\min} and p_{\max}) and the step Δp must be set a priori; p_{\min} and p_{\max} are easily estimated on the basis of the inspection of the experimental seismogram; Δp depends on the frequency content of the signal. To avoid aliasing, the following sampling condition has to be satisfied:

$$\Delta p = \frac{1}{2\pi f_{\max} x_{\max}} \quad (5.11)$$

where f_{\max} and x_{\max} are the maximum frequency and the length of the transformed data in the x direction, respectively.

5.3 Horizontal-to-Vertical Spectral Ratio (HVSr or H/V)

The use of single-station noise recordings for the estimation of the local site effects have become increasingly popular, especially thanks to its simple approach which requires the use of a single three-component seismograph and its applicability also in areas of low or even no seismicity, which is nowadays enhanced by a wide range of low cost instruments. The best approach for understanding ground conditions is through direct observation of the seismic ground motion, but such studies are restricted to areas with relatively high seismicity. Because of these restrictions in other methods, such as only at high seismicity area and the availability of an adequate reference site, non-reference site methods have been applied to the site response studies. Noise is a very convenient tool to estimate the effect of surface geology on seismic motion without other geological information. The H/V technique (i.e. the ratio between the Fourier spectra of the horizontal and vertical components of noise) was firstly proposed by Nogoshi and Igarashi (1971), but becomes popular thanks to Nakamura (1989) which intended to achieve the amplification of the S-waves due to soft sediments by noise measurements, so arguing that this technique is capable of depicting the fundamental resonance frequency of a site.

5.3.1 The theoretical basis of the H/V method

Many observations and experiences on noise records show that it consists of both body and surface waves, but the theoretical basis of the H/V method still remains a matter of discussion and different explanations have been given.

The concept was introduced in the early seventies by Nogoshi and Igarashi (1971) and is based on the assumption that noise predominantly consists of surface waves. Under that hypothesis, many authors (Field and Jacob, 1993; Lachet and Bard, 1994; Ansary *et al.*, 1995; Horike, 1996; Tokimatsu *et al.*, 1996; Bard, 1998; Konno and Ohmachi, 1998) agreed on the following arguments:

- the H/V ratio is basically related to the ellipticity of Rayleigh waves, because of their predominance in the vertical component;
- the ellipticity is frequency-dependent and exhibits a sharp peak around the funda-

mental frequency for sites characterized by a high enough impedance contrast between the surface and the bedrock (and/or pseudo-bedrock).

Konno and Ohmachi (1998) simulated the particle motion of the fundamental mode of Rayleigh waves, in case of a single layer above the bedrock but with different impedance contrast. Fig. 5.1b shows three types of particle orbits during propagation of fundamental-mode Rayleigh waves in the models shown in Fig. 5.1a. Type 1 appears when a velocity contrast between the two layers is low ($V_{s2}/V_{s1} \leq 2.5$), in which the particle motion is retrograde at any period. Type 2 appears when the contrast is fairly high ($V_{s2}/V_{s1} \approx 2.5$). With an increase in the period, the motion changes in a variety, such as retrograde, vertical only, prograde, vertical only, and retrograde. Thus, at both periods T_1 and T_2 shown in Fig. 5.1b, the H/V ratio becomes 0, although T_1 and T_2 in type 2 are very close to each other. Type 3 appears when the velocity contrast is very high ($V_{s2}/V_{s1} \geq 2.5$). With the increasing period, the particle motion is, in order, retrograde, vertical only, prograde, horizontal only, and retrograde. Therefore, the H/V ratio becomes 0 at T_1 and infinite at T_2 . Fig. 5.1c illustrates the three types of the H/V ratio mentioned above: the curves for type 1 (thin solid line), type 2 (dotted line), and type 3 (thick solid line) correspond to S wave velocities of the surface layer of 250, 200, and 50 m/sec, respectively. Downward arrows indicate peak periods, while upward arrows trough periods. Sharp peaks do not appear in type 1 and type 2, while two deep troughs appear in type 2. Type 3 shows a sharp peak and a sharp trough, and the trough period is nearly half of the peak period.

Therefore, the ellipticity curves exhibit a pronounced trough at a half of the fundamental frequency peak, corresponding to a vanishing of the horizontal component (and a new inversion of the rotation sense, from clockwise to counterclockwise). This trough does exist even for lower impedance contrasts, so an unclear bump on the H/V curve, followed by a clear trough, may be used for the estimation of the fundamental frequency (Konno and Ohmachi, 1998).

On the contrary, Nakamura (1989) explained H/V peaks as caused by multiple refractions of vertical incident SH waves: assuming that the effect of surface waves can be either 'eliminated' or neglected, he claimed that this ratio is in direct relationship with the transfer

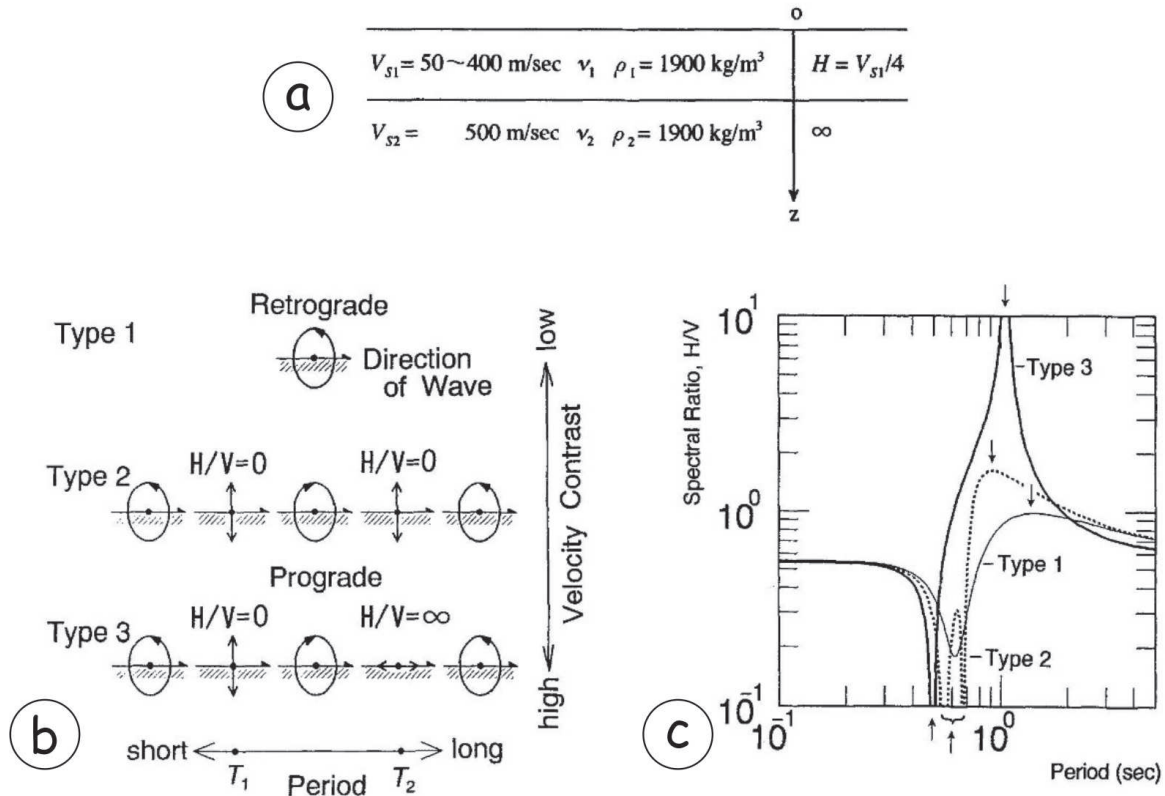


Figure 5.1: a) Model of an elastic layer over a half-space. Poisson's ratio (ν) were determined from V_S as follows: $\nu=0.499$ for $V_S < 150$ m/sec; $\nu=0.499-1.16 \cdot 10^{-4}$ for $V_S \geq 150$ m/sec. b) Particle motion of three types of fundamental Rayleigh waves for the above described models. c) Three types of H/V ratio of fundamental Rayleigh waves. Downward arrows show trough periods: type 1, $V_{S1} = 250$ m/sec; type 2, $V_{S1} = 200$ m/sec; type 3, $V_{S1} = 50$ m/sec (from Konno and Ohmachi, 1998).

function for S waves with respect to bedrock, because of the mainly body wave nature of the noise. In 1996 and 2000, Nakamura revised its first explanation recognizing the influence of surface waves. Noting the relation between horizontal and vertical earthquake motions obtained by strong motion seismometer (Nakamura and Saito, 1983), seismic characteristics of ground surface will be approximated with the spectral ratio of horizontal to vertical components of ground surface noise; this ratio is named as QTS (Quasi-Transfer Spectrum; Nakamura, 1996; 2000).

Applying this theory to a sedimentary basin (outlined in Fig. 5.2), horizontal and vertical spectra on the ground surface (H_f , V_f) can be written as follows:

$$H_f = A_h \cdot H_b + H_s \quad V_f = A_v \cdot V_b + V_s \quad (5.12)$$

$$T_h = \frac{H_f}{H_b} \quad T_v = \frac{V_f}{V_b} \quad (5.13)$$

where A_h and A_v are the amplification factors of horizontal and vertical motions of vertically incident body waves. H_b and V_b are the spectra of horizontal and vertical motions in the basement under the basin (outcropped basin). H_s and V_s are the spectra of horizontal and vertical motions of surface sedimentary ground based on seismic motion on the rock outcrop near the basin.

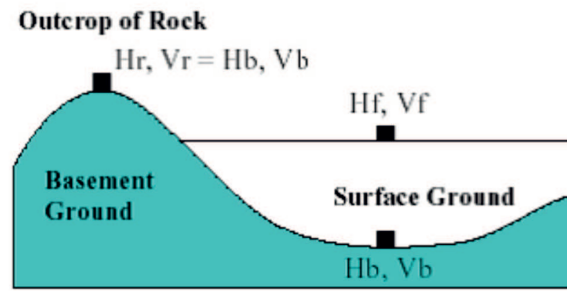


Figure 5.2: Simplified structure of a sedimentary basin (Nakamura, 2000).

Generally, Poisson ratio of sedimentary deposits exceeds 0.45, thus P-wave velocity is more than three-four times of the S-wave velocity. In such sedimentary layer, vertical component cannot be amplified ($A_v=1$) around the frequency range where horizontal receives large amplification. If there is no effect of Rayleigh waves, $V_f \approx V_b$. On the other hand, if V_f is larger than V_b , it is considered as the effect of surface waves. Then estimating the effect of Rayleigh waves by V_f/V_b ($=T_v$), horizontal amplification can be written as:

$$T_h^* = \frac{T_h}{T_v} = \frac{QTS}{\frac{H_b}{V_b}} = \frac{\left[\frac{A_h + \frac{H_s}{H_b}}{A_v + \frac{V_s}{V_b}} \right]}{\frac{H_b}{V_b}} \quad (5.14)$$

$$QTS = \frac{H_f}{V_f} = \frac{A_h \cdot H_b + H_s}{A_v \cdot V_b + V_s} = \frac{H_b}{V_b} \cdot \frac{\left[\frac{A_h + \frac{H_s}{H_b}}{A_v + \frac{V_s}{V_b}} \right]}{\frac{H_b}{V_b}} \quad (5.15)$$

In Eq. 5.15, $H_b/V_b \approx 1$. If there is no influence of Rayleigh waves, $QTS = A_h/A_v$. If the amount of Rayleigh waves is high, the second term in the above formulation gets dominant and $QTS = H_s/V_s$ and the lowest peak frequency of this ratio is nearly equal to the lowest proper frequency (f_0) of A_h . In the range of f_0 , $A_v = 1$. QTS shows stable

peak at frequency f_0 . Even when the influence of Rayleigh waves is important, V_S become small (which results in a peak of H_s/V_s) around the first order proper frequency due to the multiple reflection of SH-waves within the sedimentary filling and resulted amplification factor, regardless of the influence degree of Rayleigh waves.

For different wave-lengths, Ohta (1963) calculated H/V and phase velocity of Rayleigh waves for two layers model for various impedance ratio (varying between 1.2 and 4.5) and Poisson's ratio (varying between 0.25 and 0.49) both in sedimentary and basement layers. By using these calculated results, the relationship between the H/V of Rayleigh wave and the frequency is shown in Fig. 5.3a, and it shows the relations between impedance, peak and frequency. The frequency in this figure is normalized with the predominant frequency of surface layer, $f_0 = V_s/4h$. Group velocities calculated from phase velocities are normalized with S wave velocity and drawn with the frequency normalized with f_0 . Fig. 5.3b shows the distribution of group velocity versus frequency. Accordingly, if the impedance ratio is less than two, the energy of Rayleigh wave exists at the lower frequency range. Fig. 5.3c shows the change of impedance ratio for frequencies of trough and peak of H/V and minimum group velocity of Rayleigh waves. The frequencies corresponding to the trough and minimum group velocity (for almost all impedance ratio values), change between 1.5 and 2. The energy of the Rayleigh wave is almost zero at the peak frequency of H/V, and at the trough frequency of H/V the energy becomes to maximum. When the impedance ratio is greater than 2.5, the Rayleigh wave does not affect the H/V peak of ground motion. On the other hand, when the impedance ratio is less than 2.5, the Rayleigh wave affects the H/V peak of ground motion.

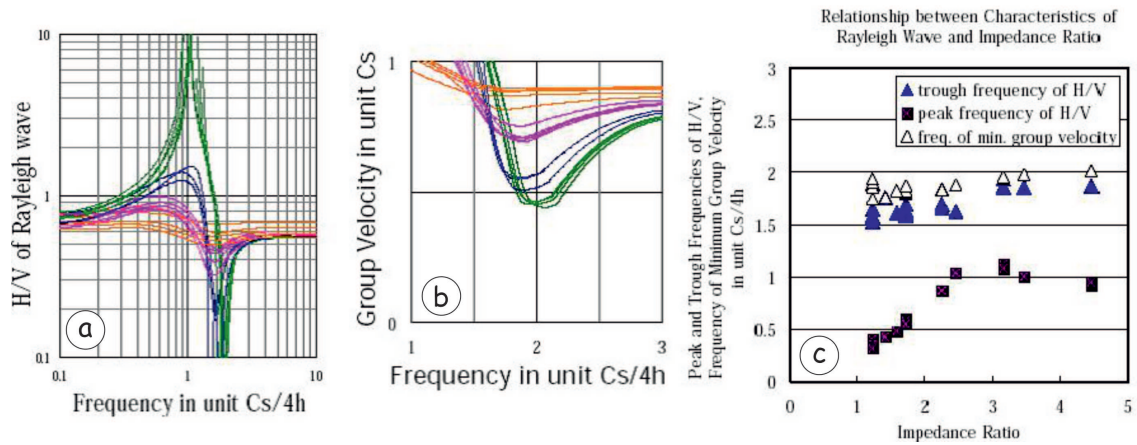


Figure 5.3: a) H/V of Rayleigh waves for two layered ground, with different impedance contrasts. b) Group velocity of Rayleigh waves. c) Relationship between characteristics of Rayleigh wave and impedance ratio (from Nakamura, 2000).

5.3.2 Applications of the H/V

The H/V technique is now widely used in site-response investigations and microzoning studies (Ansary *et al.*, 1995; Field *et al.*, 1995; Gaull *et al.*, 1995; Kudo, 1995; Theodulidis and Bard, 1995; Abeki *et al.*, 1996; Konno, 1996; Wakamatsu and Yasui, 1996; Alfaro *et al.*, 1997; Fäh, 1997; Bard, 1998; Duval *et al.*, 1998; Maruyama *et al.*, 2000; Ansal *et al.*, 2001; Duval *et al.*, 2001a; b; Lebrun *et al.*, 2001; Lombardo *et al.*, 2001; Mucciarelli and Gallipoli, 2001; Maresca *et al.*, 1999; 2003; Scherbaum *et al.*, 2003; Gallipoli *et al.*, 2004; Nguyen *et al.*, 2004; Talhaoui *et al.*, 2004; Tuladhar *et al.*, 2004; Dikmen and Mirzaoglu, 2005; Panou *et al.*, 2005; Havenith *et al.*, 2007; Gosar, 2007; Cara *et al.*, 2008; D'Amico *et al.*, 2008; Gosar and Martinec, 2009; Albarello *et al.*, 2011). Other applications of the H/V regard the study of sedimentary basins, in terms of variation of resonance frequency with depth, first-order estimations of the geometry of the main seismic reflectors and the mapping of the sediments thickness overlying the seismic bedrock (Ishida *et al.*, 1998; Mucciarelli and Gallipoli, 2001; Parolai *et al.*, 2002; Uebayashi, 2003; Hinzen *et al.*, 2004; Oliveto *et al.*, 2004; Garcia-Jerez *et al.*, 2006; Motamed *et al.*, 2007; D'Amico *et al.*, 2008; Herak *et al.*, 2010; Albarello *et al.*, 2011; Paolucci *et al.*, 2015). Another relevant use of noise is devoted to identify the fundamental frequencies of buildings and soil-structure resonance interaction (Mucciarelli and Gallipoli, 2001; Gallipoli *et al.*, 2004).

5.4 Data collection and processing

5.4.1 ESAC surveys: array configuration, measurements and processing

Array and single station noise measurements were performed along a profile running from Cento to Bondeno (western Ferrara Province; (Fig. 5.4), ca. 27 km-long and oriented SSW-NNE, almost perpendicular to the regional trend of the buried structures belonging to the Ferrara Arc.

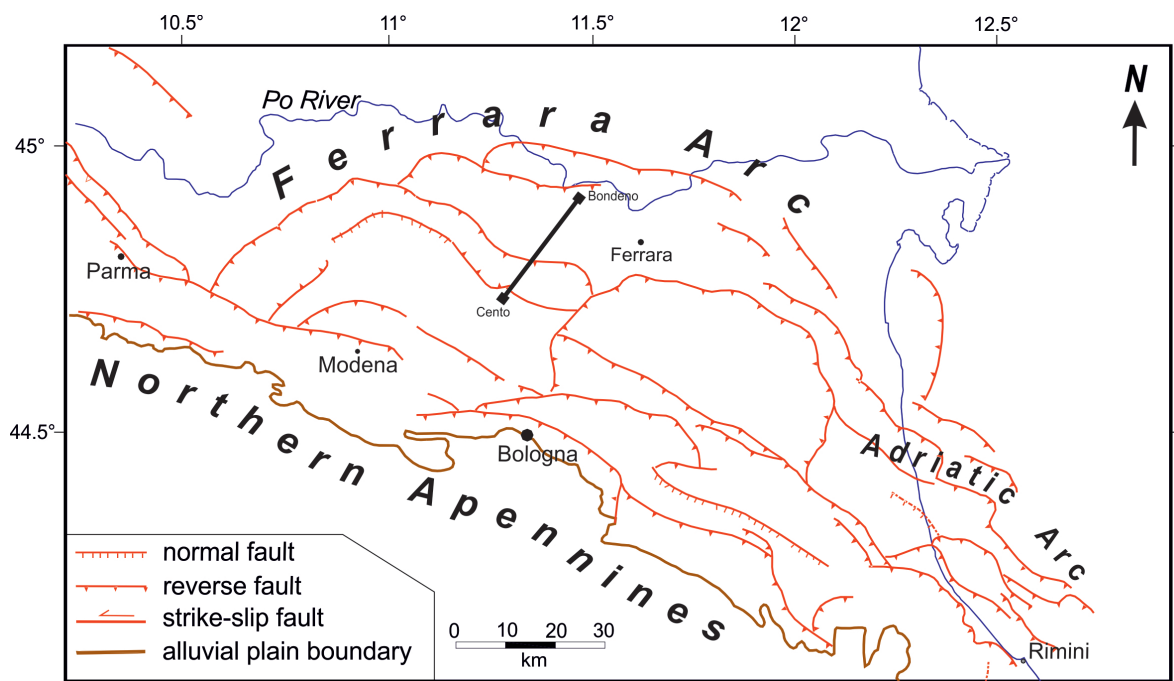


Figure 5.4: Tectonic sketch map of the Ferrara Arc (red lines; Pieri and Groppi, 1981) showing the location of the investigated profile (black line).

In order to carry out such surveys, L-shaped arrays, composed of 24 geophones, 8 m spaced, were laid out at each site (Fig. 5.5); geophones were of the type at 3-components and 4.5 Hz of proper frequency. A mean array aperture of about 130 m allows the investigation of the subsurface up to approximately 150 m depth. The minimum wavelength detected is twice the shortest distance between sensors deployed in the array (i.e. Nyquist wavenumber).



Figure 5.5: Particular of the array configuration for the acquisition of the experimental data.

Along the Cento-Bondeno profile, 13 ESAC surveys (see Fig. 5.6 for locations and Table 5.2 for detailed information) were performed from May to September 2013; in addition, 7 Re.Mi. surveys performed and processed by Abu-Zeid (2012) were exploited. The measurement sites were selected in order to highlight possible strong lateral lithological (i.e. elastic properties) variations at depth between 50 to 160 m below ground level; the mean distance between subsequent measurements is about 1.3 km.

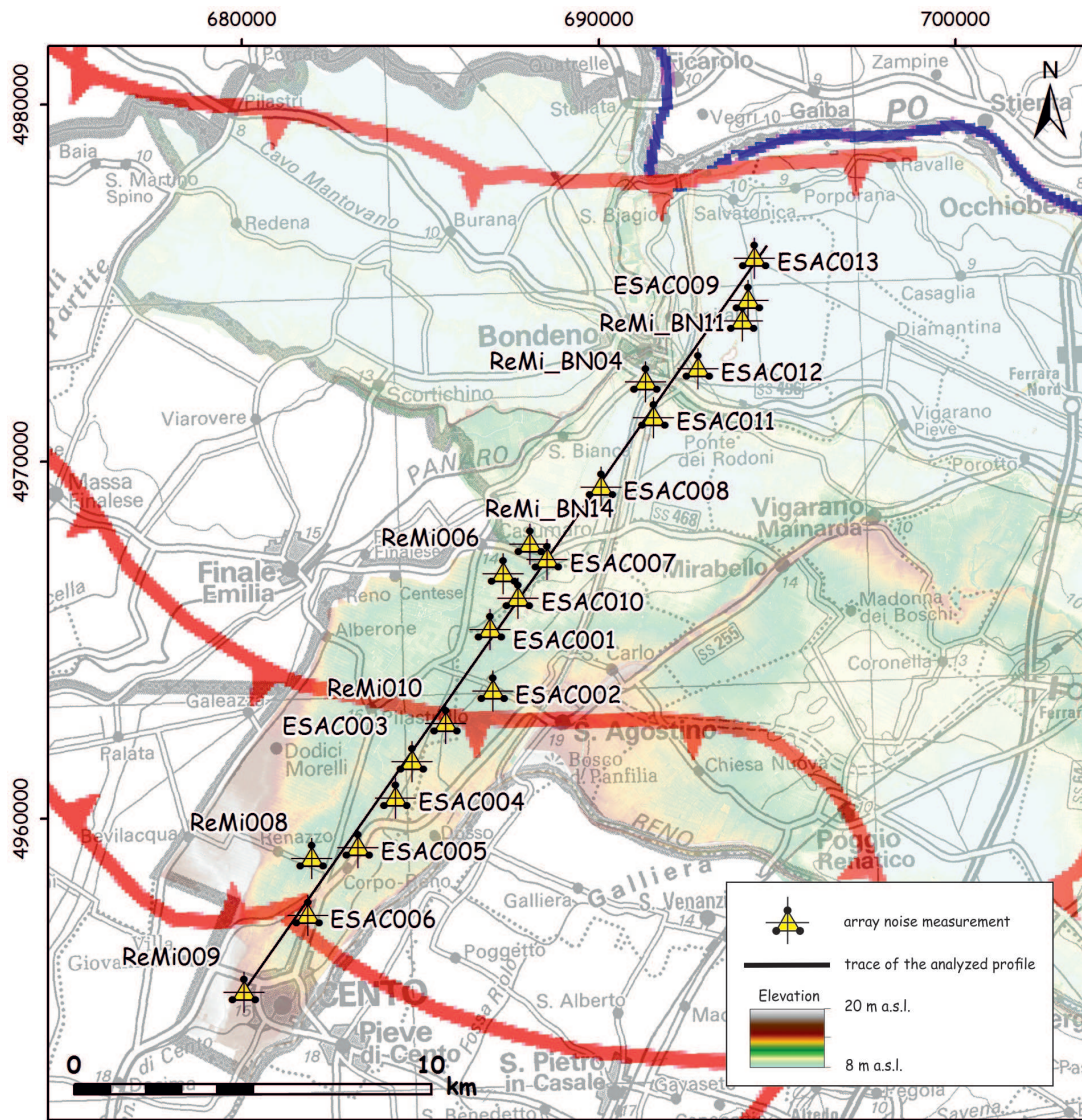


Figure 5.6: Location of the measured sites (yellow triangles) along the Cento-Bondeno profile (black line). In transparency is shown the DSM from LIDAR survey. A simplified outline of the main thrusts (red lines) of the buried Northern Apennines is also reported (from Pieri and Groppi, 1981).

Site name	Latitude (UTM, Zone 32N)	Longitude (UTM, Zone 32N)	Elevation (m)	Date (gg/mm/yy)	Time (hh:mm)	Δ (m) along trace profile	Δ (m) from trace profile	Δ (m) between subsequent measurements
ReMi009	4955137	680060	14.5	28/05/10	09:57	50	25	
ESAC006	4957327	681804	13.0	15/05/13	15:20	2845	195	2795
ReMi008	4958886	681953	11.3	28/05/10	13:18	4207	577	1362
ESAC005	4959220	683215	12.6	15/05/13	12:15	5205	264	998
ESAC004	4960593	684254	12.6	15/05/13	10:00	6925	326	1720
ESAC003	4961670	684477	12.5	13/05/13	14:45	7935	110	1010
ReMi010	4962672	685739	11.9	25/05/10	11:03	9480	348	1545
ESAC002	4963563	687038	12.0	13/05/13	12:50	10956	900	1476
ESAC001	4965344	686964	11.1	13/05/13	10:00	12371	183	1415
ESAC010	4966198	687706	10.0	02/09/13	09:40	13496	66	1125
ReMi006	4966903	687298	10.4	25/05/10	14:52	13839	805	343
ESAC007	4967237	688560	10.3	30/08/13	11:50	14837	36	998
ReMi_BN14	4967683	688077	10.7	09/04/10	16:20	14925	615	88
ESAC008	4969316	690045	8.9	30/08/13	14:15	17392	58	2467
ESAC011	4971209	691492	7.7	02/09/13	11:40	19773	155	2381
ReMi_BN04	4972286	691344	8.7	10/12/09	11:55	20570	583	797
ESAC012	4972657	692754	8.2	02/09/13	14:40	21683	357	1113
ESAC009	4973993	694016	7.6	30/08/13	16:50	23502	623	1819
ReMi_BN11	4974513	694165	8.1	12/04/10	10:20	24013	447	511
ESAC013	4975738	694350	7.1	02/09/13	16:40	25122	104	1109

Table 5.2: Detailed information about the ESAC and ReMi measurements performed along the Cento-Bondeno profile.

Seismic noise was recorded for the vertical component, obtaining time series of 15 minutes long sampled at 500 Hz. The processing of the array data were performed with the SeisOptR ReMi™ Software (<http://www.optimsoftware.com/index.php/seisopt-remi-by-optim-software>). The inversion of the dispersion curve allowed for 1D shear wave velocity estimation keeping layer thickness constant. Phase velocity data inversion was accomplished using a ‘regularization’ strategy, to stabilize the inversion process. Since a smoothing stabilizer was selected, the inverted models show smooth evolution of the shear wave velocities with depth maintain the capability to map high impedance contrasts.

As an example, the cumulative plot of the dispersion curves and the 1D shear wave velocity profiles obtained from the array surveys performed along the Cento-Bondeno profile are shown in Figs. 5.7 and 5.8, respectively.

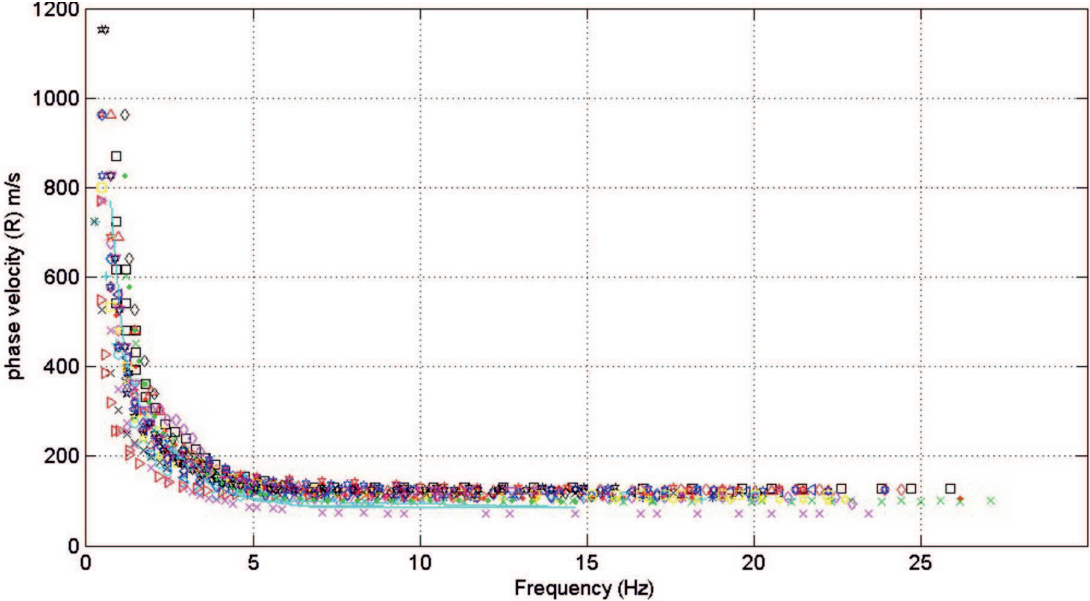


Figure 5.7: Fundamental mode dispersion curves calculated from the array surveys performed along the Cento-Bondeno profile.

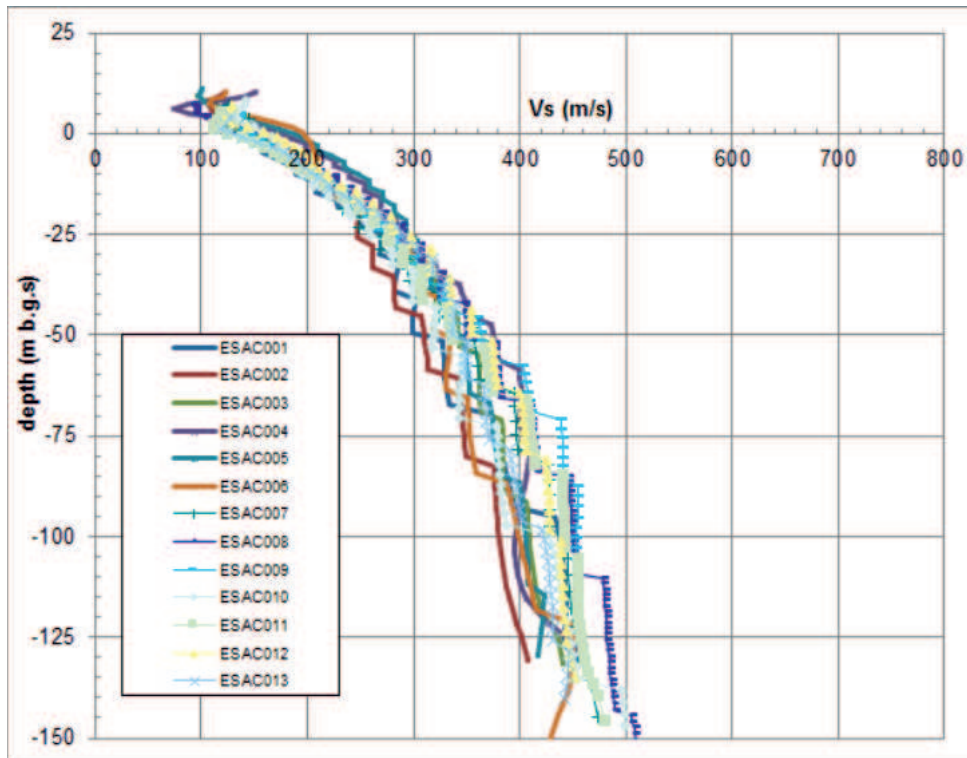


Figure 5.8: The 1D velocity profiles obtained by the array surveys performed along the Cento-Bondeno profile.

5.4.2 HVSR surveys: measurements and data processing

The single-station noise measurements were performed along the profile above mentioned, i.e. from Cento to Bondeno.

The acquisition of noise were performed with a 3-component short-period seismometer, with proper frequency equal to 2 Hz, connected via cable to the seismograph (distributed by MAE srl; Fig. 5.9).

The signal were acquired for at least 30, due to the expected low resonance frequency(ies) (< 1 Hz), as suggested by the SESAME Guidelines (SESAME, 2004); the sampling rate was set to 250 Hz.

The locations of the measured sites were carefully selected to avoid the influence of trees, sources of monochromatic noise, heavy traffic roads that can severely ‘distort’ and thus compromise the quality of the recordings. Additionally, the measurements were performed only on no-wind days, because it is known that the noise introduced by strong wind seriously affects the reliability of H/V analysis (SESAME, 2004; Mucciarelli et al., 2005). Moreover,

the seismometer were placed in a small hole filled with a mix of sand and gravel and coupled to the ground with a set of long spikes supplied by the manufacturer (Fig. 5.9): thus, this setup enables easy levelling and good soil coupling.

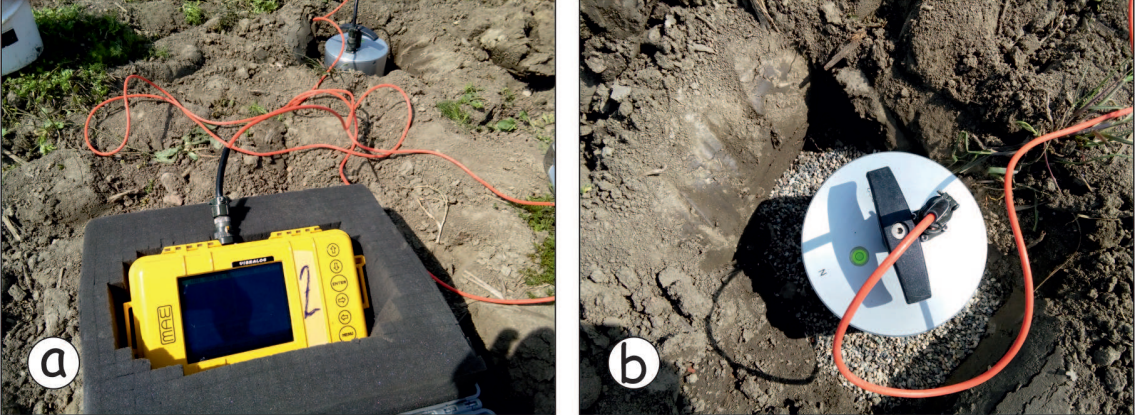


Figure 5.9: a) Seismograph and b) seismometer employed for the single-station noise measurements.

Along the Cento-Bondeno profile, 20 ambient noise measurements (see Fig. 5.10 for locations and Table 5.3 for detailed information) were performed from October 2014 to May 2015; the distance between subsequent measurements is variable among 0.4 to 3.4 km.

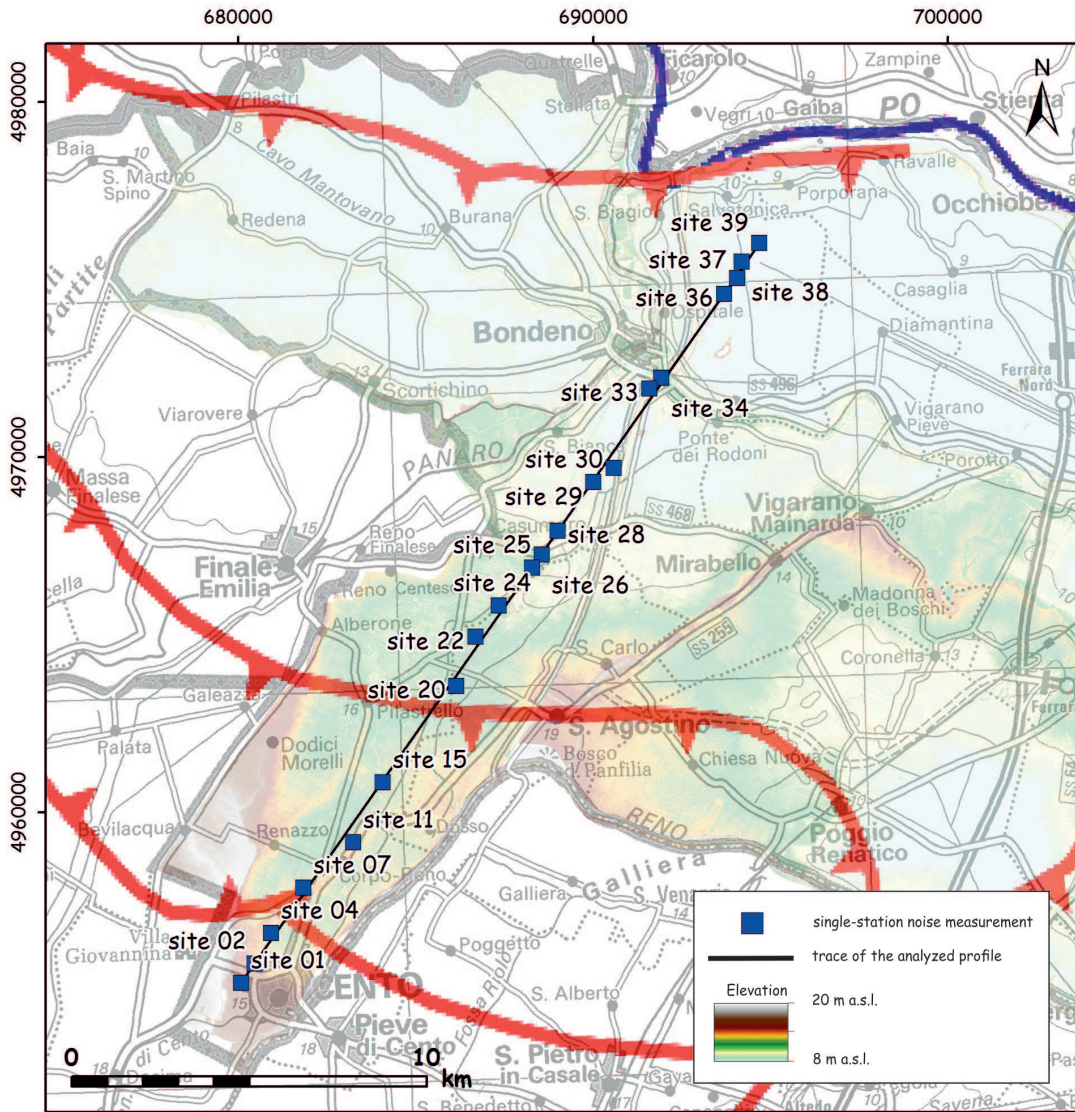


Figure 5.10: Location of the measured sites (blue squares) along the Cento-Bondeno profile (black line). In transparency is shown the DSM from LIDAR survey. A simplified outline of the main thrusts (red lines) of the buried Northern Apennines is also reported (from Pieri and Groppi, 1981).

Site name	Latitude (UTM, Zone 32N)	Longitude (UTM, Zone 32N)	Elevation (m)	Date (dd/mm/yy)	Start recording (hh:mm:ss)	Duration (m)	f ₀ (Hz)	A ₀	Δ(m) along trace profile	Δ(m) from trace profile	Δ(m) between subsequent measurements
site 01	4955190	680079	14.8	13/04/15	09:30:12	30	0.63 ± 0.08	2.5	105	10	
site 02	4955730	680459	13.6	10/04/15	10:25:37	30	0.66 ± 0.09	2.6	765	11	660
site 04	4956600	680921	12.5	13/04/15	12:04:07	30	0.58 ± 0.07	2.6	1742	110	977
site 07	4957870	681826	12.9	10/04/15	14:55:39	30	0.6 ± 0.01	2.4	3302	98	1560
site 11	4959140	683232	12.3	01/05/15	09:38:22	30	0.79±0.04	2.8	5149	323	1847
site 15	4960850	684062	11.7	01/05/15	12:10:07	30	0.69±0.03	3.1	7026	21	1877
site 20	4963560	686137	11.1	01/05/15	13:08:24	30	0.64±0.03	3	10436	164	3410
site 22	4964940	686688	11.2	24/04/15	10:53:44	30	0.64 ± 0.03	2.9	11882	177	1446
site 24	4965810	687340	10.2	17/04/15	13:23:48	30	0.75 ± 0.16	3.5	12969	143	1087
site 25	4966888	688273	11.2	24/04/15	12:49:03	30	0.73 ± 0.05	2.7	14387	2	1418
site 26	4967260	688551	10.0	24/10/14	17:23:11	30	0.73 ± 0.09	2.7	14851	15	464
site 28	4967920	689000	9.3	23/10/14	15:46:21	30	0.73 ± 0.05	2.9	15649	4	798
site 29	4969300	690001	9.0	24/04/15	14:30:47	30	0.67 ± 0.16	2.5	17354	31	1705
site 30	4969700	690579	7.8	24/04/15	15:35:32	30	0.66 ± 0.05	2.8	18013	275	659
site 33	4971930	691579	8.5	08/10/14	17:26:47	30	0.66 ± 0.04	2.9	20413	187	2400
site 34	4972230	691921	11.5	08/10/14	16:31:18	30	0.7 ± 0.07	2.9	20855	80	442
site 36	4974600	693686	8.3	08/10/14	11:31:16	30	0.76 ± 0.08	3.5	23809	5	2954
site 37	4975040	694046	6.5	08/10/14	10:28:43	30	0.72 ± 0.06	3.8	24376	47	567
site 38	4975510	694174	7.2	08/10/14	09:33:38	30	0.73 ± 0.11	3.7	24834	118	458
site 39	4976030	694673	6.1	08/10/14	08:45:23	30	0.78 ± 0.04	3.9	25547	8	713

Table 5.3: Detailed information about the HVSR measurements performed along the Cento-Bondeno profile.

Within the frame of the research project co-financed by the Municipality of Sant’Agostino (western Ferrara Province), aimed at realizing the seismic microzoning study as a fundamental support for the reconstruction phase after the Emilia 2012 sequence, several single-station noise measurements as shown in Fig. 5.11 were performed (see Table 5.4 for detailed information). The measurements were carried out with a seismometer with proper frequency equal to 4.5 Hz (distributed by Micromed; www.tromino.eu), acquiring the signal for 30 minutes.

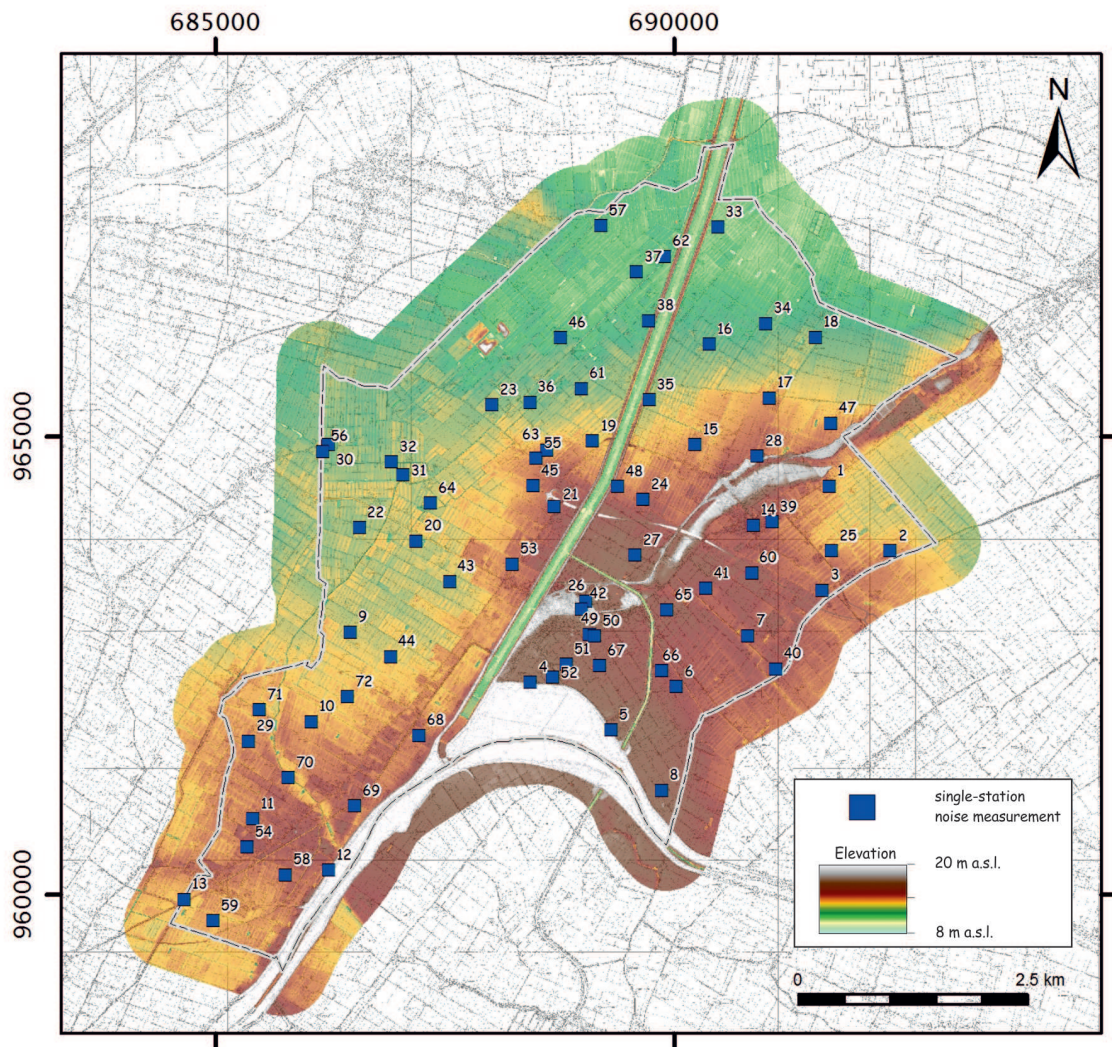


Figure 5.11: Location of the HVSr measurements performed for the seismic microzoning study of the Sant’Agostino Municipality. In transparency is shown the DSM from LIDAR survey.

Site name	Latitude (decimal degrees)	Longitude (decimal degrees)	Elevation (m)	Date (dd/mm/yy)	Start recording (hh:mm:ss)	Duration (min)	f ₀ (Hz)	A ₀
1	44.8069	11.4240	13	02/07/13	16:48:00	30	0.81	3.1
2	44.8004	11.4321	12.2	02/07/13	17:43:20	30	0.88	2.7
3	44.7968	11.4226	13.3	02/07/13	19:00:49	30	0.81	2.5
4	44.7886	11.3820	15.1	03/07/13	17:18:18	30	0.66	2.7
5	44.7837	11.3929	15.1	03/07/13	18:19:45	30	0.50	2.6
6	44.7862	11.4010	14.2	03/07/13	19:24:47	30	0.63	2.5
7	44.7914	11.4114	13.6	04/07/13	08:56:13	30	0.78	2.3
8	44.7776	11.3997	14.4	04/07/13	10:08:23	30	0.59	2.3
9	44.7940	11.3574	11.5	04/07/13	12:18:32	30	0.72	2.9
10	44.7854	11.3517	12.5	04/07/13	15:37:47	30	0.59	3.0
11	44.7760	11.3432	13.2	04/07/13	16:48:35	30	0.63	2.7
12	44.7707	11.3535	13.3	04/07/13	17:39:13	30	0.69	2.8
13	44.7683	11.3335	12.9	04/07/13	19:11:27	30	0.72	2.8
14	44.8033	11.4134	13.7	17/07/13	09:16:07	30	0.88	2.4
15	44.8114	11.4056	12.6	17/07/13	10:08:28	30	0.75	2.6
16	44.8212	11.4081	10.5	17/07/13	10:59:00	30	0.81	2.6
17	44.8157	11.4161	12	17/07/13	11:47:12	30	0.81	2.3
18	44.8216	11.4227	10.5	17/07/13	12:41:53	30	0.81	2.3
19	44.8121	11.3916	11.9	17/07/13	15:49:04	30	0.70	3.0
20	44.8027	11.3669	11.4	21/10/13	16:07:19	30	0.78	3.0
21	44.8057	11.3860	14	21/10/13	17:22:12	30	0.66	2.9
22	44.8042	11.3591	11.7	22/10/13	12:33:42	30	0.66	3.0
23	44.8159	11.3778	11.2	23/10/13	10:24:42	30	0.75	3.7
24	44.8062	11.3983	13.4	23/10/13	16:14:57	30	0.84	2.7
25	44.8006	11.4241	12.2	11/12/13	10:40:41	30	0.78	2.4
26	44.7964	11.3900	16	11/12/13	15:24:53	30	0.69	2.5
27	44.7997	11.3955	14.3	11/12/13	16:27:44	30	0.69	2.5
28	44.8101	11.4142	13.5	11/12/13	17:34:38	30	0.81	2.9
29	44.7836	11.3430	12.4	12/12/13	14:20:48	30	0.59	2.8
30	44.8125	11.3552	10.9	12/12/13	16:14:30	30	0.63	3.0
31	44.8093	11.3654	11.1	12/12/13	17:13:13	30	0.59	3.0
32	44.8106	11.3638	11.2	12/12/13	18:06:24	30	0.56	2.5
33	44.8327	11.4097	9.6	13/12/13	11:38:56	30	0.63	2.7
34	44.8231	11.4159	10.9	13/12/13	12:47:08	30	0.72	2.6
35	44.8159	11.3995	11.1	13/12/13	13:44:44	30	0.66	2.8
36	44.8160	11.3831	11	13/12/13	14:40:11	30	0.72	3.0
37	44.8285	11.3983	10	13/12/13	15:43:30	30	0.63	2.7
38	44.8237	11.3998	10	13/12/13	16:39:06	30	0.78	2.6
39	44.8036	11.4159	13.8	25/02/14	09:43:28	30	0.88	3.0
40	44.7892	11.4159	13.8	25/02/14	10:33:04	30	0.63	2.3
41	44.7973	11.4066	14	25/02/14	17:51:13	30	0.63	2.5
42	44.7956	11.3894	14.8	25/02/14	18:42:04	30	0.63	2.3
43	44.7987	11.3713	12.1	26/02/14	09:50:29	30	0.81	3.2
44	44.7915	11.3629	12.1	26/02/14	10:41:51	30	0.72	2.8
45	44.8069	11.3822	12.8	26/02/14	13:33:53	30	0.69	2.6
46	44.8223	11.3876	10.2	26/02/14	14:25:00	30	0.81	2.5
47	44.8131	11.4245	12.2	11/03/14	10:31:26	30	0.81	2.5
48	44.8066	11.3936	12.1	11/03/14	11:23:39	30	0.75	2.5
49	44.7931	11.3903	15	11/03/14	12:18:33	30	0.72	2.0
50	44.7929	11.3910	15	11/03/14	13:01:04	30	0.72	2.1
51	44.7888	11.3863	14.9	11/03/14	13:51:17	30	0.72	2.0
52	44.7890	11.3851	15.2	11/03/14	14:53:23	30	0.72	2.3
53	44.7991	11.3786	13.1	11/03/14	15:44:31	30	0.78	2.7
54	44.7732	11.3424	13.5	11/03/14	17:39:15	30	0.69	2.6
55	44.8088	11.3822	11.9	12/03/14	08:38:56	30	0.72	2.8
56	44.8118	11.3544	10.8	12/03/14	10:29:23	30	0.56	2.9

57	44.8331	11.3936	10	12/03/14	11:34:25	30	0.72	2.8
58	44.7704	11.3475	13.5	12/03/14	13:02:55	30	0.69	2.9
59	44.7661	11.3374	12.5	12/03/14	13:59:04	30	0.63	2.4
60	44.7987	11.4129	13.4	20/03/14	09:15:05	30	0.69	2.7
61	44.8172	11.3903	11	20/03/14	11:16:22	30	0.63	2.8
62	44.8299	11.4023	9.9	20/03/14	12:32:30	30	0.56	2.6
63	44.8113	11.3853	11.9	20/03/14	13:24:08	30	0.56	2.8
64	44.8064	11.3690	11.7	20/03/14	15:44:30	30	0.63	2.9
65	44.7953	11.4011	13.2	21/03/14	08:39:27	30	0.72	2.4
66	44.7893	11.4001	13.9	21/03/14	10:24:10	30	0.56	2.6
67	44.7900	11.3916	14.1	21/03/14	11:22:12	30	0.63	2.6
68	44.7837	11.3665	12.6	21/03/14	13:05:47	30	0.66	2.8
69	44.7755	11.3563	13.3	21/03/14	13:55:20	30	0.63	2.6
70	44.7799	11.3483	12.6	21/03/14	14:44:26	30	0.63	2.8
71	44.7867	11.3446	12.3	21/03/14	16:22:34	30	0.59	2.5
72	44.7877	11.3568	12.2	21/03/14	17:07:32	30	0.63	3.2

Table 5.4: Detailed information about the HVSR measurements performed for the seismic microzoning study of the Sant’Agostino Municipality.

The H/V curves were calculated using the Grilla software (www.tromino.eu). Considering the characteristics of the seismometer and the influence of weather-climate conditions for frequencies below 0.5 Hz (SESAME, 2004), the analysis was limited to the frequency band between 0.5 and 5 Hz. Recorded time series were visually inspected to identify possible erroneous measurements and stronger transients. Each record was then split into 60 s long non-overlapping windows, for which amplitude spectra (Fig.5.12c) were computed and then smoothed using the Konno and Ohmachi window (Konno and Ohmachi, 1998). The relation of Nakamura (1989) is applied for each individual window and the correspondent HVSR curve is obtained (Fig. 5.12a). From the color coded plot of the HVSR functions for all the time windows (Fig. 5.13b), those including strong transients were removed in order to be excluded from further processing. In addition, a directional analysis (Fig. 5.12d) was performed in 10° angular steps to identify possible directions of noise provenance.

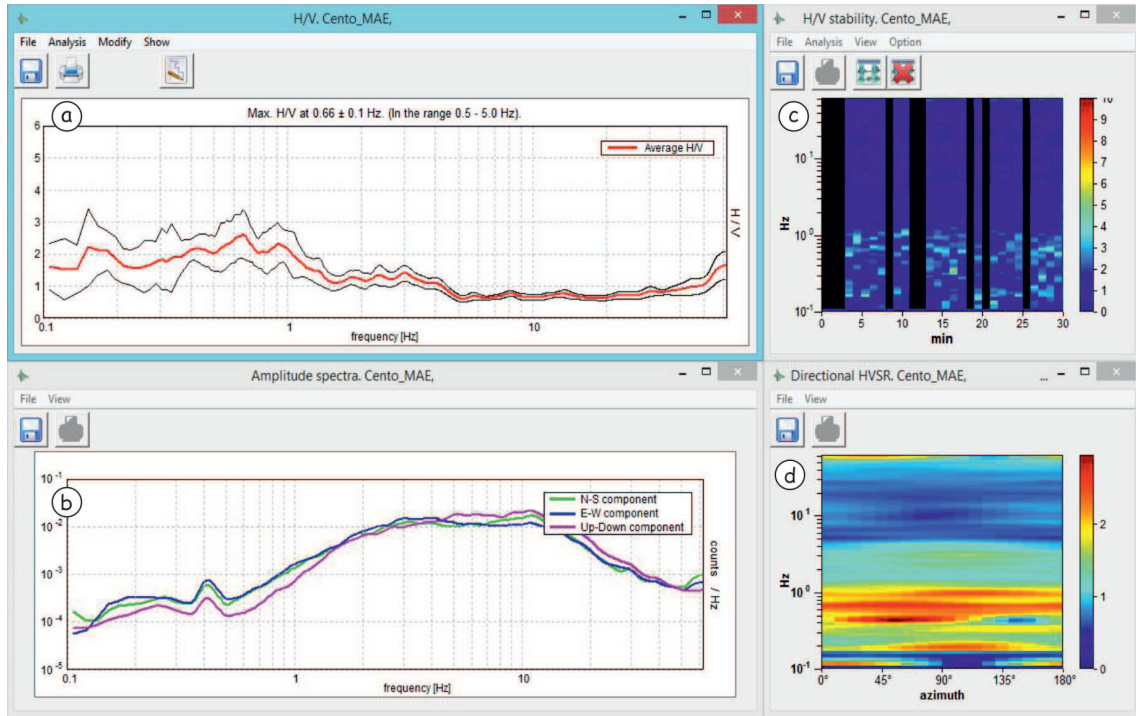


Figure 5.12: Example of H/VSR processing (site 2 along the Cento-Bondeno profile) with Grilla software (www.tromino.eu). a) H/VSR curve. b) amplitude spectra of the three ground motion components. c) H/VSR pattern as a function of time with transient removal and d) H/VSR as a function of the azimuth (i.e. directional analysis).

The analysis procedure could be summarized as follows:

- a cosine tapering with a length of 5% is applied on both side of the window signal of the Vertical (V), North-South (NS) and East-West (EW) components;
- a FFT is applied to the signal of the three components to obtain the three spectral amplitudes;
- a Konno and Ohmachi smoothing, with a bandwidth of 40 and arithmetical average, is applied to the three spectral amplitudes;
- H/V is computed by merging the horizontal (NS and EW) components with a quadratic mean:

$$H = \sqrt{\frac{NS^2 + EW^2}{2}} \quad (5.16)$$

Thus, in each windows the distribution of $\log_{10} (H/V)$ is obtained as a function of the frequency.

The geometric mean of H/V is calculated:

- H/V is averaged over all window results

$$H/V_{average} = \frac{\sum \log_{10}(H/V)}{n_{windows}} \quad (5.17)$$

- H/V standard deviation as follows

$$\sigma_{H/V} = \sqrt{\frac{\sum \log_{10}^2(H/V) - n \cdot \log_{10}^2(H/V_{average})}{(n_{windows} - 1)}} \quad (5.18)$$

- $H/V_{average}$ and $\sigma_{H/V}$ are set back to a linear scale by calculating $\overline{H/V} = 10^{H/V_{average}}$ and $\sigma_{\overline{H/V}} = 10^{\sigma_{H/V}}$.

5.4.3 Interpretation and inversion of the H/V curves

The interpretation of the H/V curve requires a preliminary careful evaluation of its characteristics. As a first criterion, the clarity of the peak can be used. When the peak is clear (and does not have an industrial origin), it indicates the presence of an impedance contrast at some depth and the peak frequency represents the natural frequency of the site. If the thickness is known, an estimation of the shear wave velocity can be obtained. On the contrary, if the curve is flat (H/V values around 1 or less), it is likely that the local velocity structure has no impedance contrasts (SESAME, 2004). A preliminary qualitative classification was proposed by Albarello *et al.* (2011), in order to provide an immediate indication about the quality of each H/V curve.

As previously mentioned, one of the most attractive applications of the H/V is the possibility to estimate the depth of the major impedance contrasts (i.e. the depth of the bedrock or pseudo-bedrock) through dedicated inversion procedures.

Originally based on a simple layer over half space subsurface, computational methods for the evaluation of the HVSR curve have recently become available for multi-layer systems where the subsurface is modeled as a stack of infinite parallel homogeneous layers and using different approaches such as computation of mechanical transfer functions (Ben-Menahem and Singh, 1981; Tsai, 1970; Tsai and Housner, 1970; Aki and Richards, 2002) or even exploiting a statistical approach (Sánchez-Sesma *et al.*, 2011; Lunedei and

Albarelo, 2010; 2015). These modeling strategies allowed for the investigation of the behavior of a more complex subsurface. Further, the availability of fast and efficient modeling strategies triggered the implementation of codes for the inversion of such curves, as for example the commercial software Grilla (www.tromino.eu) or the open source Geopsy (<http://geopsy.org>). Herak (2008) published a user friendly program in Matlab capable of obtaining the 1D distribution of the elastic properties of a subsurface consisting of a stack of layers by either inverting a HVSR curve or an average of a number of curves for the same specific location.

Although subsurface investigations based on multiple H/V measurements performed at different locations for 2D subsurface characterization were previously attempted (Oliveto *et al.*, 2004), H/V approach coupled with inversion became so popular and reliable after the introduction of such software for the construction of 2D subsurface images (Herak *et al.*, 2010). Nowadays, the strategy behind a 2D HVSR investigation is through “hvsr-profiling”, which consist of placing the different hvsr curves obtained along a linear profile, back to back and translating the frequency axis into “pseudo-depth” by means of some empirical relation (e.g. $f_0 = V_s/4h$ or using a functional where V_s increases with depth), which is usually based on a single and almost arbitrarily chosen average shear waves velocity value of the top sediments. The image obtained by hvsr-profiling is only an interpretation of the informative content of the data but it proved to be a very useful tool to depict the 2D nature of subsurface. The final link between this image and the true subsurface is usually provided by comparing the 2D pseudo-profile to the 1D models obtained by inverting the hvsr curves for few key locations.

Despite its usefulness, however, hvsr-profiling does not allow to retrieve an entire true 2D subsurface profile. This is because only a single value of V_s is used in the frequency-to-depth conversion.

Bignardi *et al.* (2015, submitted to Computers and Geosciences), developed an open source program, named OpenHVSR, for the simultaneous modeling and inversion of massive HVSR datasets. The forward modeling routine (FWD) implements the same modeling strategy present in ModelHVSR (Herak, 2008). The FWD calculates the theoretical transfer

function of a layered subsurface model based on Tsai's approach and enhanced to manage frequency-dependent attenuation and body-wave dispersion (Tsai, 1970, Tsai and Housner, 1970). The modeling algorithm assumes the subsurface as a stack of viscoelastic homogeneous layers over a half space. Each layer is described by its thickness h , and its mechanical behavior defined by the density (ρ), the compressive and shear wave velocities (V_p and V_s) and the corresponding attenuation factors (Q_p and Q_s) which are frequency dependent as follows:

$$Q = Q_0 f^k \quad (5.19)$$

where Q_0 is the attenuation factor at 1 Hz and k is a constant which is assumed to be fixed along the whole profile. Finally body waves dispersion, is considered through the logarithmic law (Aki and Richards, 2002):

$$v(f) = v(f_{ref}) \left[1 + (\pi Q_0)^{-1} \cdot \ln(f/f_{ref}) \right] \quad (5.20)$$

For each location, given a local subsurface the forward routine is used to calculate the amplification spectra for P and S waves and the HVSR curve (see Herak, 2008, for more details on the FWD).

The inversion strategy is based on the guided Monte Carlo method where at every iteration a randomly perturbed version of the best fitting model (i.e. the model which best reproduces the data) is produced and used to compute a set of simulated curves to be compared with the experimental hvsr curves.

Therefore, as a further step, all the H/V curves (for a total of 20 spectra) performed along the two above mentioned profiles, were inverted with such routine to infer the depth of the major impedance contrast(s). The input values of V_p and V_s were provided by the ESAC measurements, as they are assumed to be a sufficiently accurated approximation of the true subsurface. The ESAC and H/V inversion processes, however, are based on forward models with inherently different simulation approaches. The result is that while the ESAC inversion allows to retrieve a smooth model, such model is not suitable as it is to feed the

H/V inversion, because the latter requires well defined acoustic impedance contrasts in order to correctly reproduce the curve peaks. For this reason, the smooth V_s subsurface model obtained from the ESAC was piecewise averaged to obtain a blocky layered model (keeping in mind that for reproducing n H/V peaks $n+1$ layers are sufficient) to be used as starting guess for the H/V inversion. This allowed to start from a model already in the “basin attraction” of the H/V inversion global minima. Therefore, it was possible to optimize the local V_s profiles to both minimize the ESAC and the H/V objective functions. In order to optimize the subsurface starting model for each H/V curve, a 5% perturbation for the first 5000 generations and then successively a 15% perturbation for the next 25000 generations of the above mentioned parameters (i.e. V_p , V_s , ρ , h , Q_p and Q_s) were performed.

As an example, the inversion of one H/V curve performed along the Cento-Bondeno profile (i.e. site 39) is explained in the following. The starting blocky layered model (5.13a), in terms of thickness and body waves, was derived from the elaboration of the closest array survey (i.e. ESAC013); while, the density and attenuation factors were provided by the model proposed by Laurenzano *et al.* (2013) for the Casaglia site, about 5 kilometers to the east of the investigated site. The half space parameters were kept fixed. In particular, based on the V_s values provided by a crosshole survey, performed by the Regione Emilia-Romagna close to the Casaglia cemetery (Di Capua and Tarabusi, 2013) and several iterations with OpenHVSR routine (Bignardi *et al.*, 2015 submitted to Computers & Geosciences), a half space velocity of 850 m/s was chosen, as it better reproduce the amplification of the main resonance peak (i.e. $f_0 = 0.78 \pm 0.04$, $A_0 = 3.9$). The final subsoil blocky layered model is shown in Fig. 5.13b. The best fit between the experimental and theoretical H/V curves and the comparison between the smooth ESAC and the best H/V subsoil blocky layered inversion are shown in Fig. 5.13c and d, respectively.

The entire data and results collection is available under request.

a**Starting model**

Vp (m/s)	Vs (m/s)	ρ (g/cm ³)	Thickness (m)	Qp	Qs
1466.0	143.0	1.5	10.1	20.0	10.0
1543.0	211.0	1.5	9.4	40.0	10.0
1601.0	271.0	1.8	10.8	40.0	20.0
1650.0	324.0	1.9	19.7	40.0	20.0
1688.0	352.0	1.9	20.8	40.0	20.0
1715.0	382.0	1.9	21.1	40.0	20.0
1736.0	413.0	2.0	18.0	45.0	25.0
2000.0	850.0	2.1	999.0	999.0	999.0

b**Final model**

Vp (m/s)	Vs (m/s)	ρ (g/cm ³)	Thickness (m)	Qp	Qs
1456.2	159.9	1.5	12.7	8.4	5.0
1532.3	212.8	1.5	9.9	9.3	5.0
1628.2	222.2	1.7	12.1	8.3	5.0
1639.9	274.3	1.8	19.4	30.8	19.4
1697.6	324.0	2.0	21.9	36.9	15.7
1740.9	410.7	2.0	20.7	40.2	24.3
1776.9	433.4	2.1	19.9	32.6	16.5
2000.0	800.0	2.1	999.0	999.0	999.0

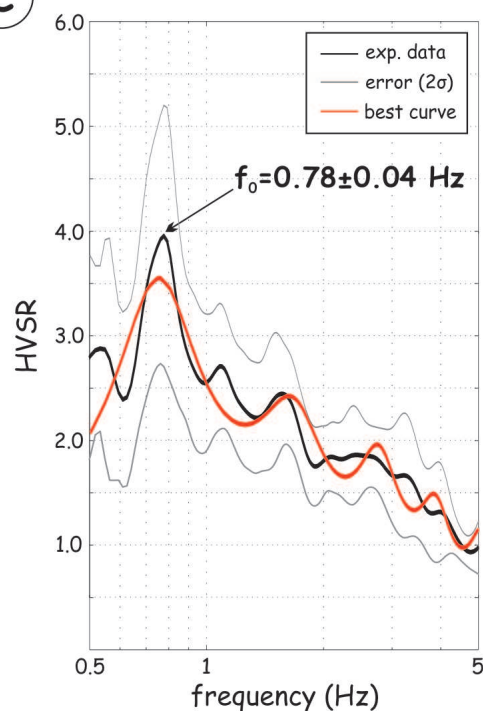
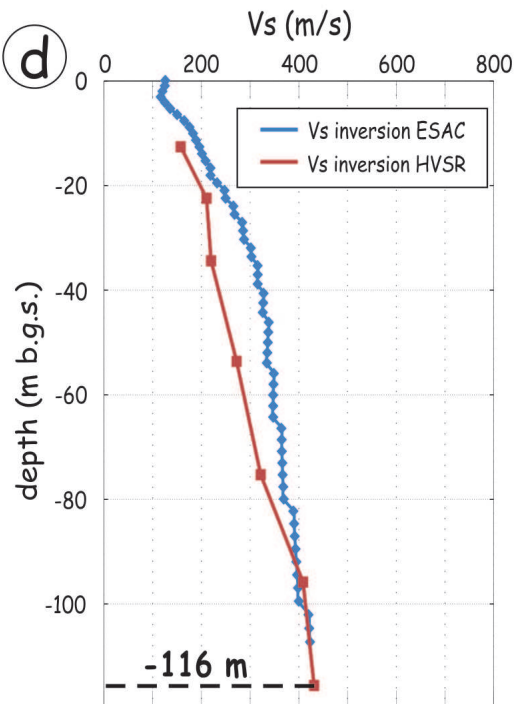
c**d**

Figure 5.13: Example of H/V inversion (site 39 along the Cento-Bondeno profile) with Open-HVSR routine (Bignardi *et al.*, 2015 submitted to Computers & Geosciences). a) Starting subsoil blocky layered model. b) Final subsoil blocky layered model. c) Best match between experimental and inverted data for the frequency band 0.5-5.0 Hz. d) Comparison between the smooth Vs model obtained by the ESAC survey and the best one from H/V subsoil blocky layered inversion.

Part III

Applications

Chapter 6

Case studies

6.1 Geophysical pseudo-2D sections

The architecture of the Po Plain foredeep filling, from Middle Pleistocene onward, is characterized by a generally “regressive” trend, interrupted by lesser fluctuations, evidenced by the transition from offshore Lower-Middle Peistocene deposits to marine-marginal and then to alluvial Quaternary sediments (Ricci Lucchi, 1986; Amorosi and Colalongo, 2005; Amorosi, 2008).

The great number of subsurface data collected during hydrocarbon explorations and water research (AGIP Mineraria, 1959; Aquater, 1976; 1978; Aquater-ENEL, 1981; Pieri and Groppi, 1975; 1981; RER & ENI-AGIP, 1998; Boccaletti *et al.*, 2004; 2011; Molinari *et al.*, 2007) allowed to map the main Quaternary unconformities: the most recent surface, at the regional scale, is the base of the Upper Emiliano-Romagnolo Synthem (AES; Boccaletti *et al.*, 2004) which is made up of a series of different depositional cycles whose limits are placed in correspondence of the bottom of the transgressive marine deposits. The transgressive portion of each cycle is characterized by the presence of fine materials (e.g. floodplain, marsh and coastal plain clays) with subordinated sandy intercalations. Instead, the ‘regressive’ sequence consists of alluvial plain deposits (e.g. fine sediments of overflowing river) where channel sands are subordinated in the form of isolated lenticular bodies. On the top of each cycle, the channel sands become abundant, thus forming laterally wider bodies (RER & ENI-AGIP, 1998; ISPRA, 2009).

The studies conducted by the RER & ENI-AGIP (1998), Boccaletti *et al.* (2004, 2011) and Molinari *et al.* (2007) revealed that the Quaternary succession is highly deformed and confirmed that the transitions between marine-continental sediments are the result of important tectonic phases followed by periods of strong subsidence. Therefore, the strong variable thickness of the Quaternary sequence from several hundreds to few tens of meters in correspondence of the growing anticlines; i.e. Mirandola, Casaglia, Argenta reflects the influence of the complex evolution of the blind thrusts belonging to the Ferrara Arc. Previous geophysical studies conducted by various authors (e.g. Priolo *et al.*, 2012; Paolucci *et al.*, 2015) focused the attention on mapping the fundamental resonance frequencies and the corresponding shear-wave velocity profiles in the area affected by the Emilia 2012 seismic sequence by independently interpret the HVSR curves (in the former case) or using a simplified power law to describe Vs variation with depth in the latter case. It was thus possible to establish a link between the main resonance peaks to known subsurface geological contacts.

With this premise, a geophysical surveys along a profile running from Cento to Bondeno (western Ferrara Province) were carried out, ca. 27 km-long and oriented SSW-NNE, almost perpendicular to the regional trend of the buried structures belonging to the central sector of the Ferrara Arc, which is one of the three arcs consisting of blind, north-verging thrusts and folds of the external Northern Apennines (Pieri and Groppi, 1981; Bigi *et al.*, 1992; Boccaletti *et al.*, 2004).

6.1.1 Cento-Bondeno profile

As described in the previous chapter, several geophysical surveys (i.e. ESAC and HVSR) exploiting the seismic ambient noise were carried out along a 27 km-long profile which runs from Cento to Bondeno (Figs. 5.6 and 5.10), in the western Ferrara Province.

The major outcomes of this survey are the reconstructions of two pseudo-2D sections, showing the shear-wave velocity pattern and the acoustic impedance variations along the investigated profile; additionally, through a ‘constrained’ inversion of the H/V curves starting from the Vs profiles provided by the ESAC measurements, it can be possible to retrieve the depth of the major impedance contrast(s).

The array surveys that were laid outside the investigated section, due to the local topographic conditions, have been projected onto the profile trace; their distance ranges between 10 and 900 m. The discrete information of all 1D Vs models (Fig. 6.1b and c) were interpolated with a minimum curvature algorithm in order to obtain the pseudo-2D velocity section. The resulting Vs profile is shown in Fig. 6.1a. Although 1D models locally reached higher depths, the reconstructed section reports the distribution of Vs down to an average depth of about 160 m b.g.l. (considering that the elevation of the sites ranges between 0 and 4.5 m a.s.l.). The shear wave velocity ranges between 100-150 m/s, just below ground surface, and in the central-northern portion of the profile it reaches 500 m/s at the maximum investigation depths. The vertical gradient of Vs is stronger between ReMi009 to ESAC003 and between ESAC010 to ESAC013, while in the central sector of the profile, between ReMi010 and ESAC001 the gradient is weaker and the Vs at 160 m b.g.s. is ca. 400 m/s. The comparison between the Vs profile with the Structural Model of Italy (Bigi *et al.*, 1992) shows that the greatest Vs gradients are located above the sets of thrust faults respectively pertaining to the Mirandola (i.e. periclinal termination) and Casaglia anticlines to the south and to the north, respectively; conversely, the sites where the gradient is smaller are located above a tectonically “depressed” area bounded by a reverse fault to the north (Fig. 6.1d).

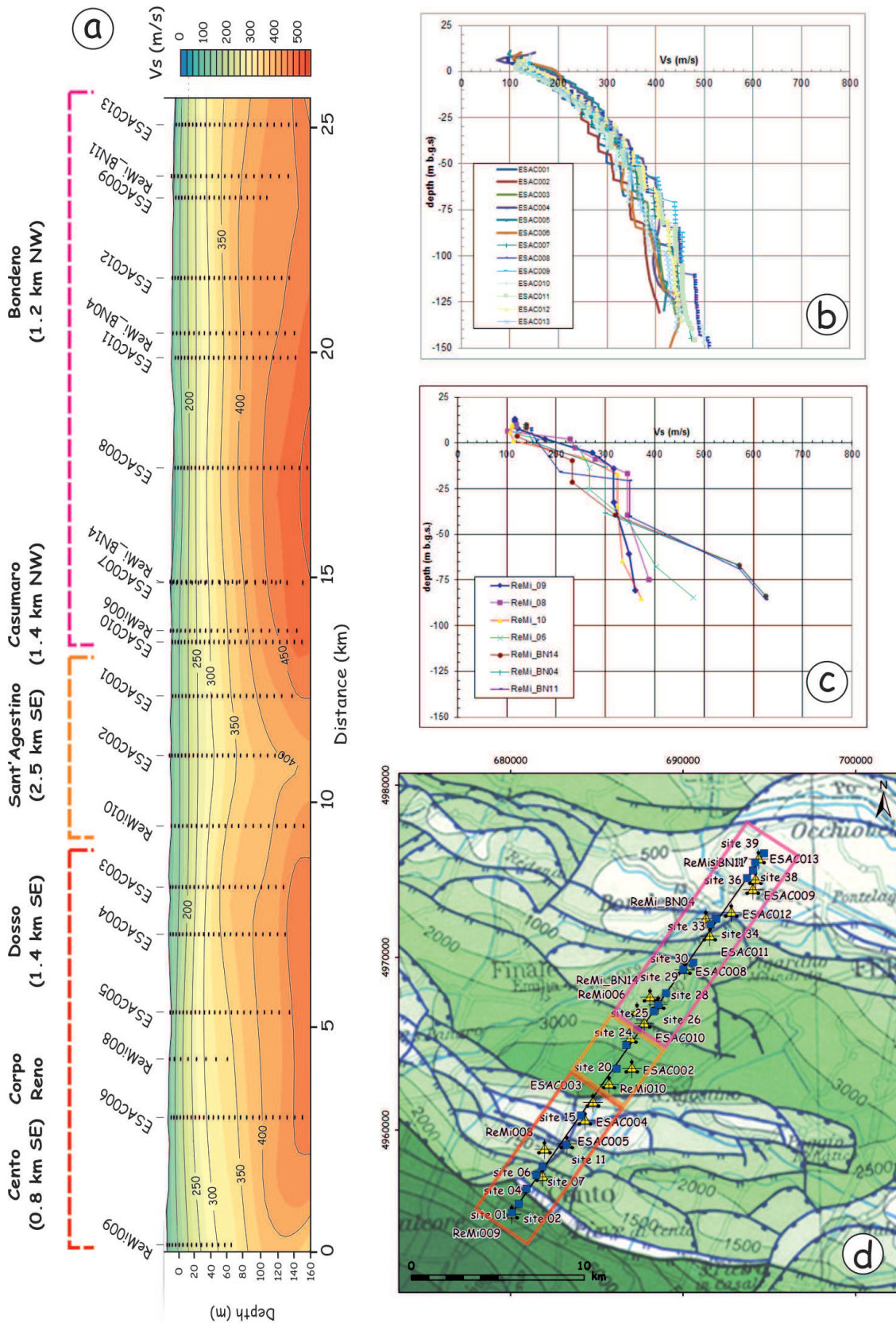


Figure 6.1: a) Shear-wave velocity section along the Cento-Bondeno profile. 1D velocity profiles from b) ESAC and c) Re.Mi. surveys. d) Location of the measured sites superimposed on the Structural Model of Italy (Bigi *et al.*, 1992)

The single-station surveys that were laid outside the investigated section, due to the local topographic conditions, have been projected onto the profile trace; their distance ranges between few meters and about 300 m. Using the HVSR profile routine (Herak *et al.*, 2010), which performs a side-by-side assembly of the observed spectra, the discrete information of the 21 HVSR curves were assembled in the frequency section shown in Fig.6.2. As described in Section 5.4.2, due to the characteristics of the seismometer and the influence of weather-climate conditions for frequencies below 0.5 Hz, the analysis was limited between 0.5 and 5 Hz.

The frequency section revealed the presence of an impedance contrast for frequencies ranging from a minimum of 0.58 Hz up to a maximum of 0.79 Hz (green dashed line in Fig. 6.2). Low fundamental resonance frequencies ($f_0 \leq 0.6$ Hz) characterized sites 4 and 7; while, for the other sites the f_0 is greater than 0.6 Hz. The HVSR amplitudes (A_0) in the reconstructed section (Fig. 6.2) are color-coded and are greater than 2.0. The larger values ($A_0 \geq 3.5$) were observed in the northern portion of the profile, between sites 36 to 39.

Assuming the V_s pattern, the fundamental resonance frequency and the impedance contrast variations to be determined by lateral lithological variations, especially in terms of differential compaction (i.e. age) of the sediments, the two pseudo-2D sections (Figs. 6.1a and 6.2) allow hypothesizing the occurrence of buried anticlinal structures in correspondence of the condensed stratigraphy and their recent tectonic evolution. This is further confirmed by the inversion of the HVSR curves (Fig. 6.3a), performed using the open source “Open-HVSR” routine (Bignardi *et al.*, 2015 submitted to Computers & Geosciences) to specifically invert large HVSR datasets.

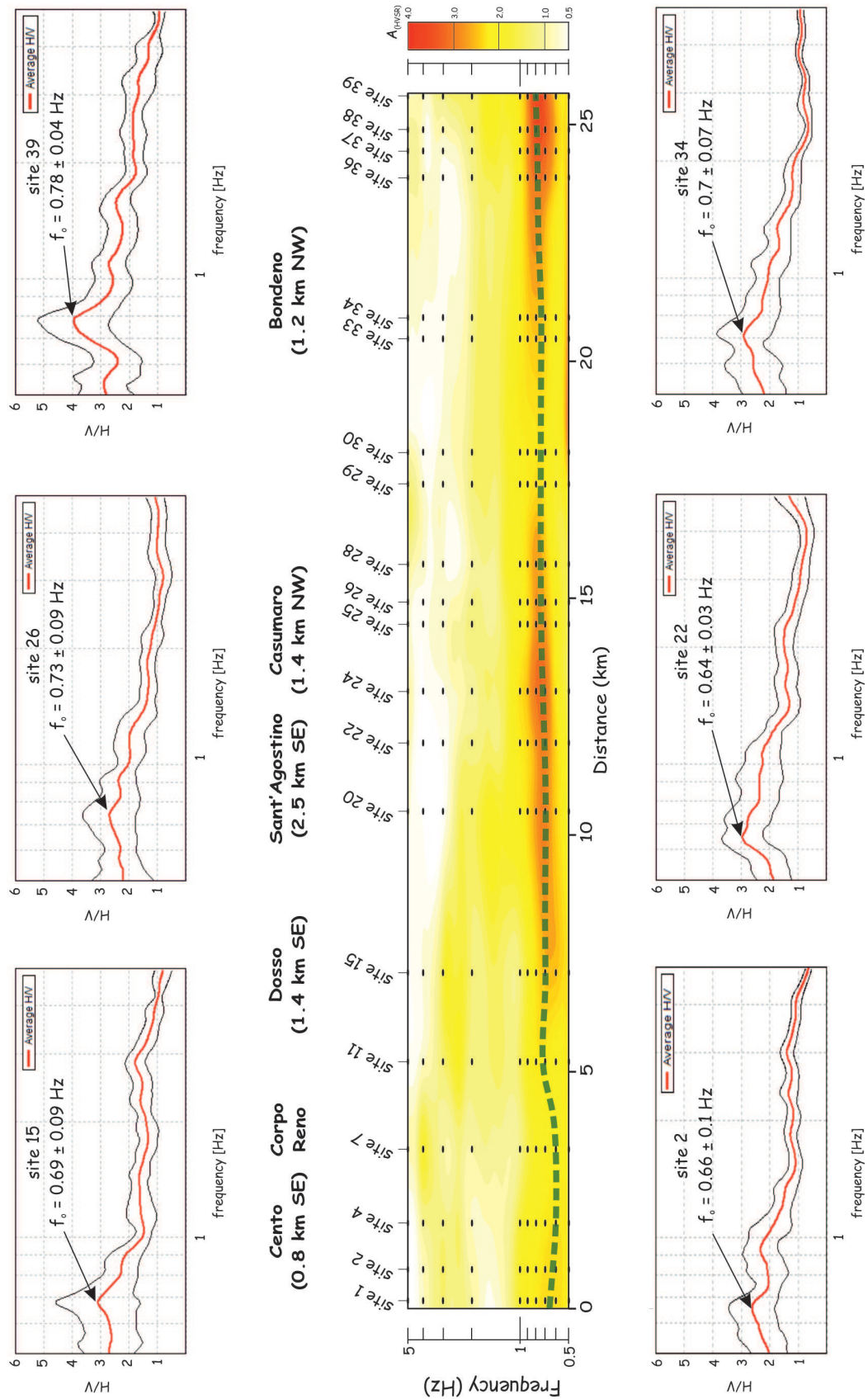


Figure 6.2: Smoothed HVSR profile obtained by gridding each average HVSR curve, between 0.5 and 5 Hz. Relative amplitudes are color-coded (see colorbar). Some examples of the HVSR curves are also shown.

The available geological information, in particular a map of the basal limit of the Complex Aquifer A2 (Fig. 6.3a; from Martelli Luca - RER, personal communication) and two geological sections, oriented NW-SE (Fig. 6.3a, b; from RER & ENI-AGIP, 1998) and SW-NE (Figs. 6.3a and 6.4c), clearly highlight how the development of anticline-syncline pairs deformed the overlying alluvial sequence, particularly influencing the depth of the basal limits and the thickness of the Lower and Undifferentiated Emiliano-Romagnolo Synthems (AEI and AESind, respectively; RER & ENI-AGIP, 1998). Additionally, due the occurrence of growing anticlines in the subsurface, the stratigraphic sequence may be not only ‘condensed’ but also incomplete, as in the case of the Casaglia anticline (between Diamantina and Occhiobello) where the Lower-Middle Pleistocene marine deposits lies directly above the Upper Miocene marls (Fig. 6.4c).

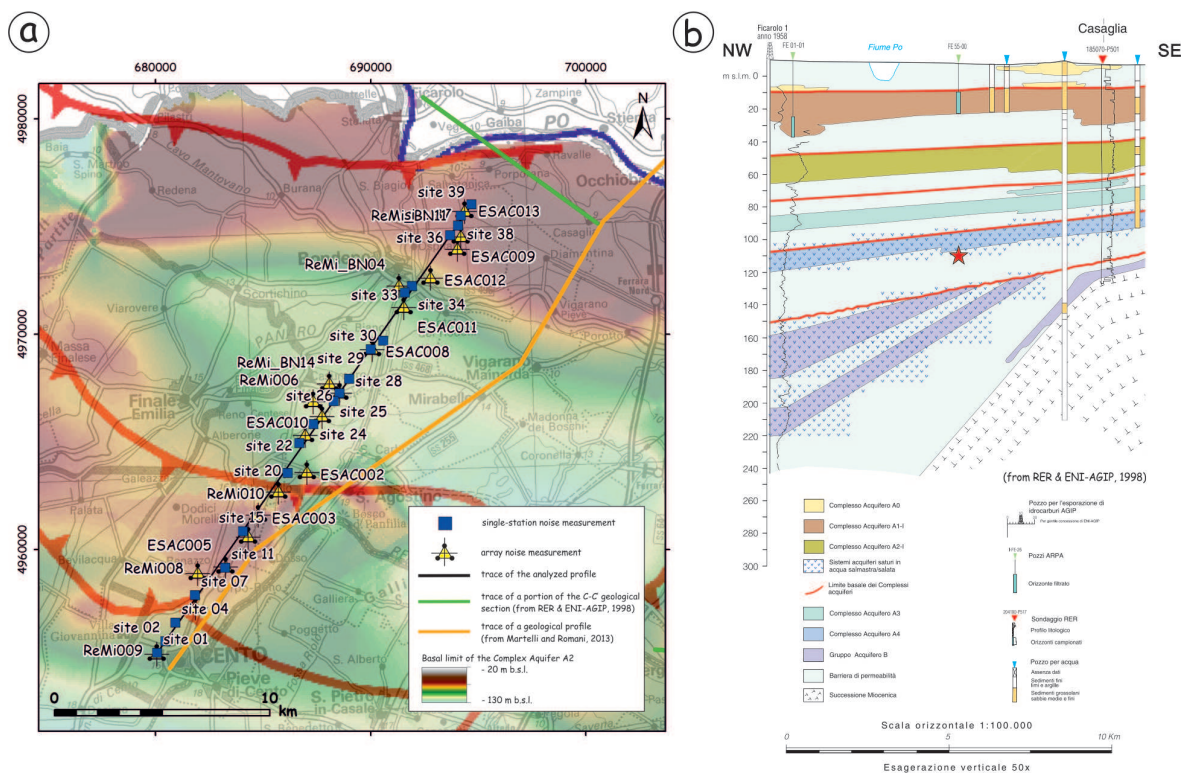


Figure 6.3: a) Map showing the basal limit of the Complex Aquifer A2 (from Martelli Luca - RER, personal communication) and the traces of the two available geological sections, oriented NW-SE and SW-NE; b) NW-SE section (portion of the C-C' geological profile from RER & ENI-AGIP, 1998). The red star represents the projection onto the section of the depth of the resonant interface for site 39 (see Fig. 6.4).

As described in Section 5.4.3, all the HVSR curves were inverted with OpenHVSR routine (Bignardi *et al.*, 2015 submitted to Computers & Geosciences). The smooth subsurface model provided by the closest array survey (i.e. ESAC and Re.Mi.) was piecewise averaged to obtain a blocky layered model to be used as starting guess for the inversion procedure.

The results provided by the inversion of the H/V curves with the available geological information indicates a good correspondence with the known main stratigraphic unconformities (Fig. 6.4a, b). In particular, the shallower resonant interface (green line in Fig. 6.4a) here detected could correspond to a surface located within one of the Middle Pleistocene sedimentary cycles (Figs. 6.3a, b and 6.4b), named AES6 (Complex Aquifer A2; RER & ENI-AGIP, 1998; Molinari *et al.*, 2007), belonging to higher rank sedimentary cycle represented by the Upper Emiliano-Romagnolo Synthem AES (RER & ENI-AGIP, 1998). Instead, the deeper one (blue line in Fig. 6.4a) could correspond to a surface located within another Middle Pleistocene sedimentary cycle (Figs. 6.3b and 6.4b), named AESind (Complex Aquifer A4, RER & ENI-AGIP, 1998; Molinari *et al.*, 2007) and can be considered as the seismic bedrock in accordance with the map of the bedrock depth proposed by Martelli and Romani (2013, see Fig. 6.14).

The geological section by Martelli and Romani (2013), documenting the occurrence of two buried anticline structures (i.e. periclinal termination of the Mirandola anticline to the south and Casaglia anticline to the north, respectively), allows hypothesizing that the shallow stratigraphic features here documented can be directly associated with the deep ongoing tectonic activity of the blind thrusts throughout the late Quaternary.

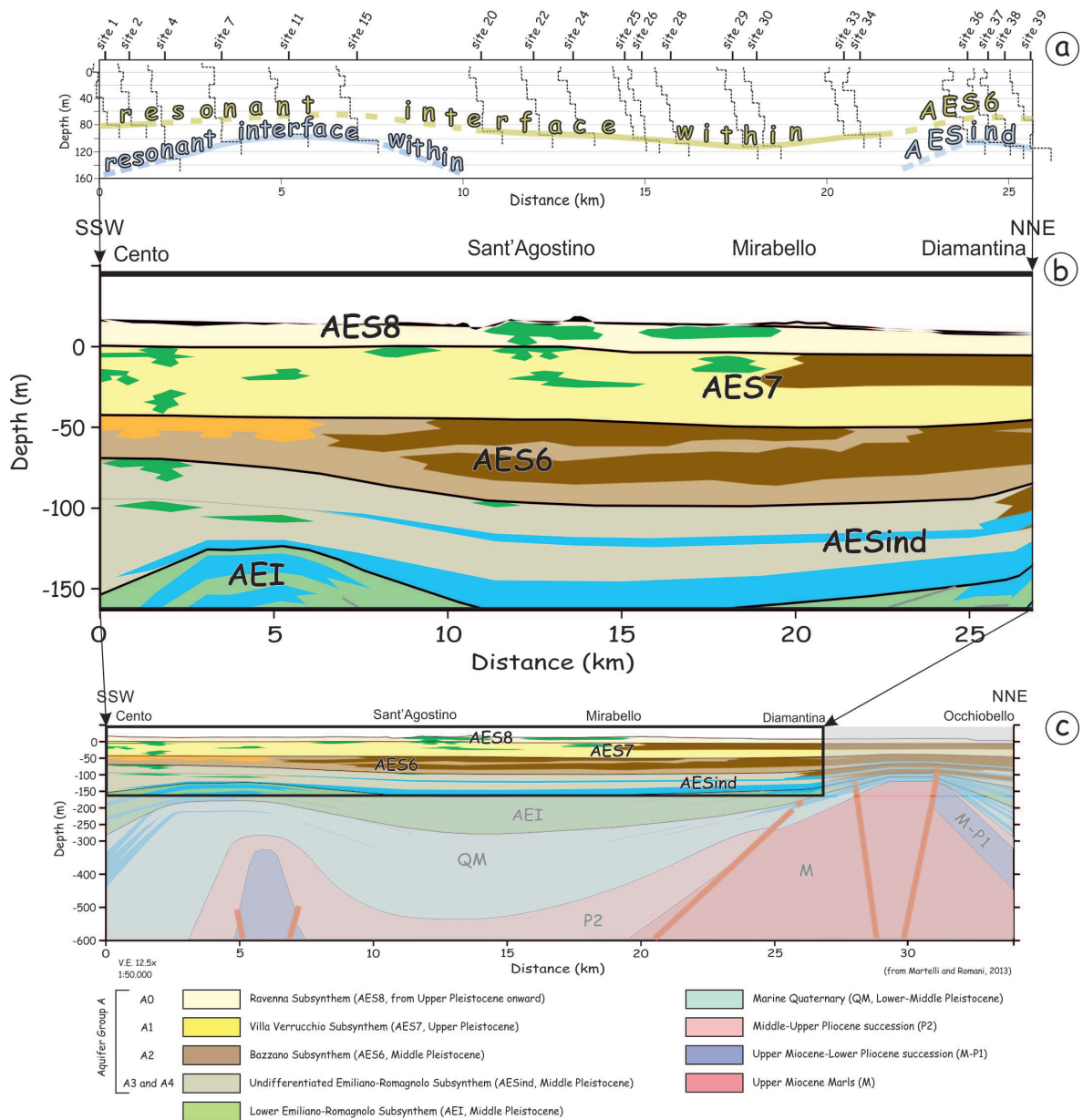


Figure 6.4: a) Vs profiles obtained by the inversion of the HVSr curves, in the frequency range 0.5-5 Hz. b) Particular of the c) geological profile made by Martelli and Romani (2013) (orange line in Fig. 6.3).

6.2 Tectonic deformation *versus* site effects

A relevant coseismic effect due to the reactivation of reverse blind faults, as in the case of the May 2012 Emilia seismic sequence, is the bending of the topographic surface and the consequent uplift of the broader epicentral area. The co-seismic areal uplift events are crucial for a better understanding of the seismotectonics of the broader area and thus for a better assessment of the seismic hazard in the region. The analysis based on DInSAR technique and on high precision levelling applied in the May 20 epicentral area revealed a marked uplift of the ground. The results of both techniques substantially agreed, although there were some considerable local discrepancies. For the purpose of this study, were analyzed in detail the geological site conditions, the distribution of liquefaction occurrences, the geomorphological map of the area and the structural model of the region in order to explain the observed discrepancies.

6.2.1 The May 2012 Emilia earthquakes imaged by geodetic approaches

To study the surface deformation caused by the May 20 and May 29 events, Caputo *et al.* (2015) applied the DInSAR technique to two pairs of SAR images. The first image pair was acquired by the Canadian satellite RADARSAT-1 (RS1). The pre-event RS1 image is dated May 12, 2012, few days before the first mainshock, while the second image was acquired on June 5. Hence the time span covered embraces the two main shocks and several after-shocks including five events with M_w greater than 5. The resulting deformation map (Fig. 6.5a) shows a region characterized by movement toward the satellite (an uplift), reaching a maximum displacement of about 20 cm in the LOS (Line of Sight) direction. Two connected and partially overlapping sectors within the study area show a marked displacement which is a clear effect of the (mainly) coseismic activity of the two causative faults associated with the May 20 (eastern sector, $M_w=6.1$) and May 29 (western sector, $M_w=5.9$) mainshocks. A relatively small subsidence, up to a peak value of about 3 cm, was also detected in the southern area close to the western sector.

A second SAR image pair was available from the Italian X-band SAR mission COSMO-SkyMed (CSK). The two images are dated May 19 and May 23, 2012, hence with four days

separation. This image pair encompasses only the first of the two main shocks. Fig. 6.5b shows the displacement map obtained from the DinSAR processing of the CSK images. As observed in the RS1 interferogram, we detected a region with a maximum positive movement (toward the satellite) in the LOS direction of about 12 cm. The lower displacement with respect to the RS1 interferogram is partly due to coverage of the CSK data frame only in the eastern sector of the epicentral area of the May 20 event, thus missing the sector with the largest values. However, because of the different time spans considered in the second interferogram, the larger surface displacement inferred from the RS1 is partly due to a prolonged post-seismic deformation effect.

The Ferrara Province is characterized by a low mean ground elevation a.s.l. and, for wide sectors, even below sea level; thus, accurate knowledge of the topography of the area is a crucial information. For this purpose, several permanent levelling networks were established through the territory many years ago. The creation of these networks and their repeated measurement are the principal ‘mission’ of the “Consorzio di Bonifica Pianura di Ferrara” (hereafter ‘Consortium’). The network provides a high accuracy local vertical datum and consists of about 1200 km of levelling lines across Ferrara Province with an average levelling section length of about 1 km. Since the first DInSAR results (Bignami *et al.*, 2012; Salvi *et al.*, 2012) concerning the two major Emilia 2012 earthquakes, a significant and broad uplift of the ground was recognised (Fig. 6.5). The eastern sector of the area affected by uplift is crossed by the levelling network of the Consortium; in the months following the seismic crisis, they carried out a dedicated survey along selected lines for a total length of about 120 km (Fig. 6.6). For the survey of the network, they applied the international standards for High-Precision geometric Levelling (HPL), which is an old method of geodetic surveying used to measure differences of elevation between two points at the Earth’s surface. The difference of height between two benchmarks (i.e. elevation reference point) is determined by differences of readings, made with a levelling instrument (optical level), measured on a graduated vertical staff placed on those points. The heights of the benchmarks were compared by obtaining the vertical movements of the ground during the time interval between the two HPL campaigns carried out before (March–September 2009) and after (September

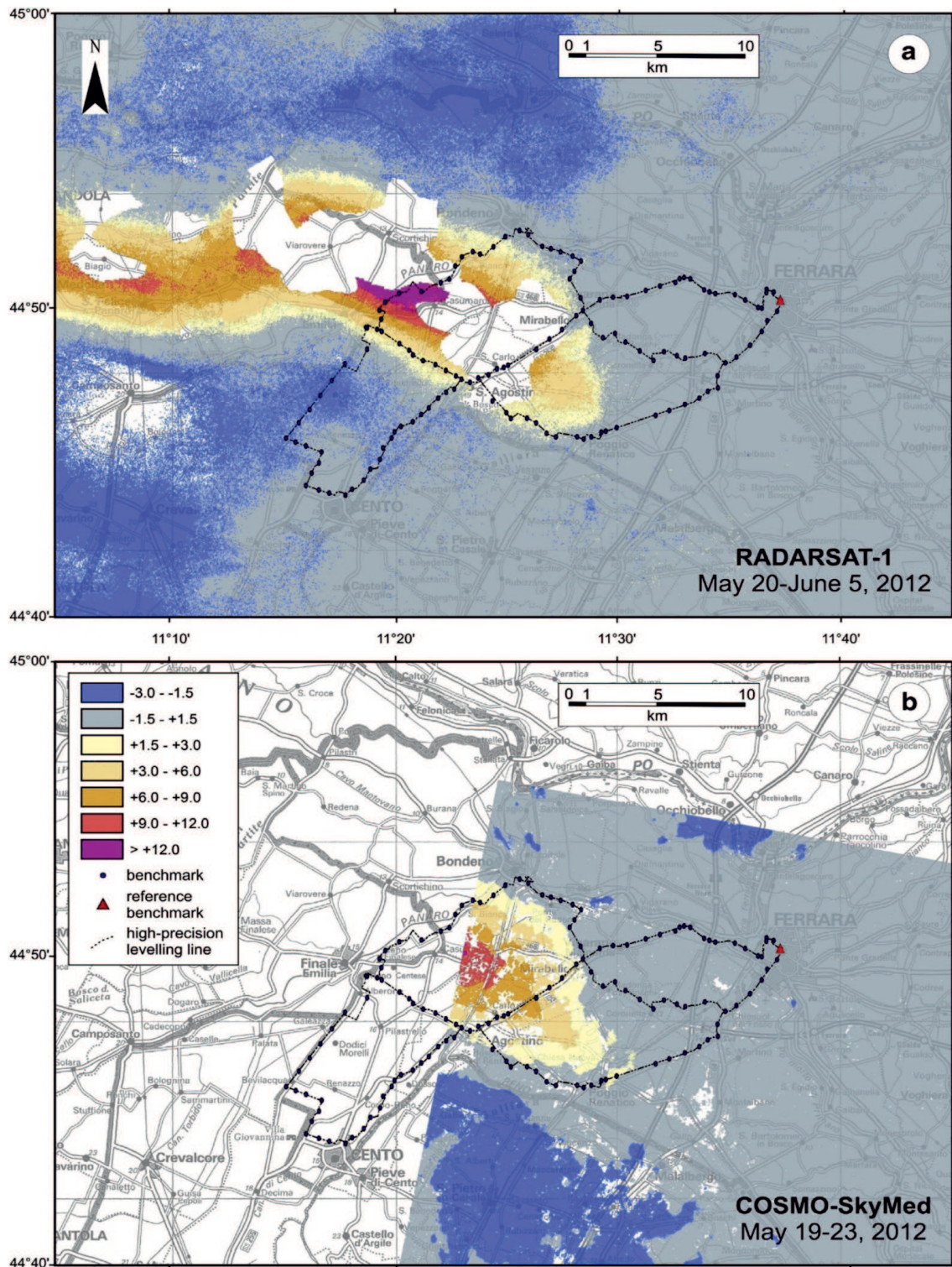


Figure 6.5: DInSAR results applied to a) Canadian RADARSAT-1 satellite data and b) European COSMO-SkyMed-1 satellite data. a) The paired images are dated May 12 and June 5, 2012 and thus document the deformation associated with both mainshocks (May 20 and 29). Note the distinct (though partially overlapping) effects of the two principal morphogenic earthquakes. b) The paired images are dated May 19 and May 23, 2012 and thus document the deformation associated only with the first mainshock (May 20). The High Precision Levelling (HPL) lines discussed later are also shown (from Caputo *et al.*, 2015).

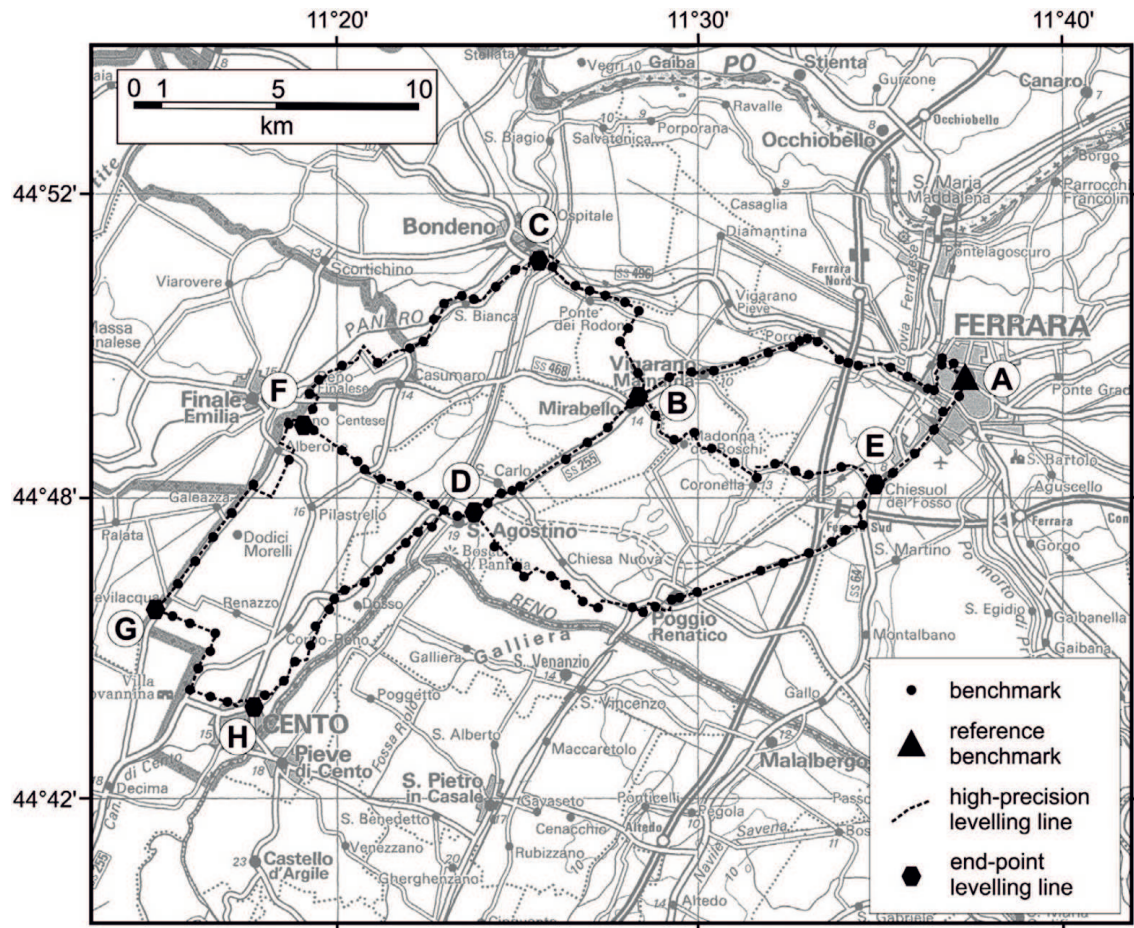


Figure 6.6: The first order levelling network belonging to the “Consorzio Pianura di Ferrara”, Ferrara Province, which was re-measured following the 2012 seismic sequence. Small dots represent the benchmarks of the Consortium, the hexagons represent the labelled benchmarks discriminating the levelling lines, while the triangle is the reference benchmark belonging to the Italian First Order Levelling Network, re-surveyed in 2005 by the IGM (Istituto Geografico Militare) (from Caputo *et al.*, 2015).

2012–June 2013) the seismic sequence.

The analysis of the vertical movements revealed both uplifted and subsided benchmarks. The three levelling lines closest to Ferrara (i.e. farthest from the epicentre), with a mean E–W orientation (Fig. 6.7) show remarkable temporal stability. A light but systematic uplift of 1–2 cm is suggested only in the western part of the D–E line, which is relatively close to the epicentral area (Fig. 6.7c). There are a few appreciable exceptions to this otherwise regular distribution of vertical movements near Mirabello (Fig. 6.7a, b) where a marked subsidence (up to ca. 10 cm) was measured.

Other levelling lines (Fig. 6.8), corresponding to the three paths closest to the epicentral area with a mean ESE–WNW orientation, run roughly parallel to the seismogenic fault’s

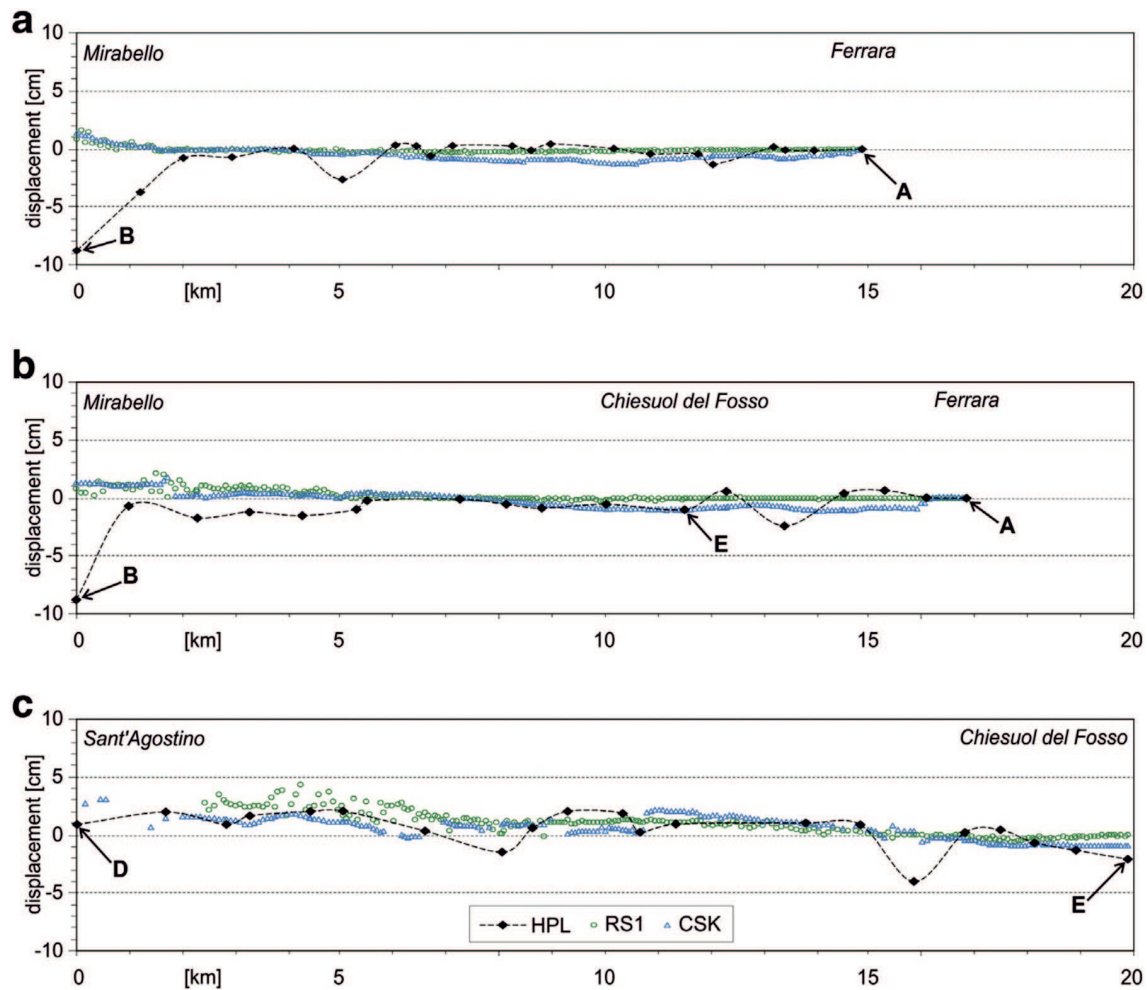


Figure 6.7: Vertical movements measured along the three levelling lines closest to Ferrara (i.e. farthest from the epicentre), with a mean E–W orientation and showing remarkable stability. The error bar at each benchmark calculated on the basis of the standard deviations of the differences in elevation (pre- to post-earthquake) is smaller than the symbol size. Capital letters refer to the benchmarks labelled in Fig. 6.6. HPL: high-precision levelling; RS1: RADARSAT-1; CSK: COSMO-SkyMed (from Caputo *et al.*, 2015).

strike associated with the morphogenic event of May 20th. The northern line (C–B in Fig. 6.8) shows no vertical movements, the southern one (6.8 in Fig. 6) a slight subsidence of ca. 2 cm all along its length, while the intermediate one (F–D in Fig. 6.8) clearly indicates a general uplift between 3 and 6 cm. This general picture, characterized by vertical stability in an ESE–WNW direction and lateral variations in a NNE–SSW direction is also clearly shown by the levelling line G–F–C (Fig. 6.9) where the maximum uplift values were observed. The vertical movement of the benchmarks gradually varies along this line: there is a slight subsidence in the southern sector (1–2 cm), which is smoothly inverted in the central sector south of Finale Emilia to become a positive vertical movement (i.e. uplift) that progressively

increases up to the maximum value reached at about 15 km (north of Finale Emilia). Farther northwards, the displacement of the benchmarks decreases to a few centimeters of uplift at Bondeno (Fig. 6.9a). Therefore, projecting the values along a NNE–SSW straight line, it is possible to estimate a wavelength of about 10 km for the fold deforming the topography.

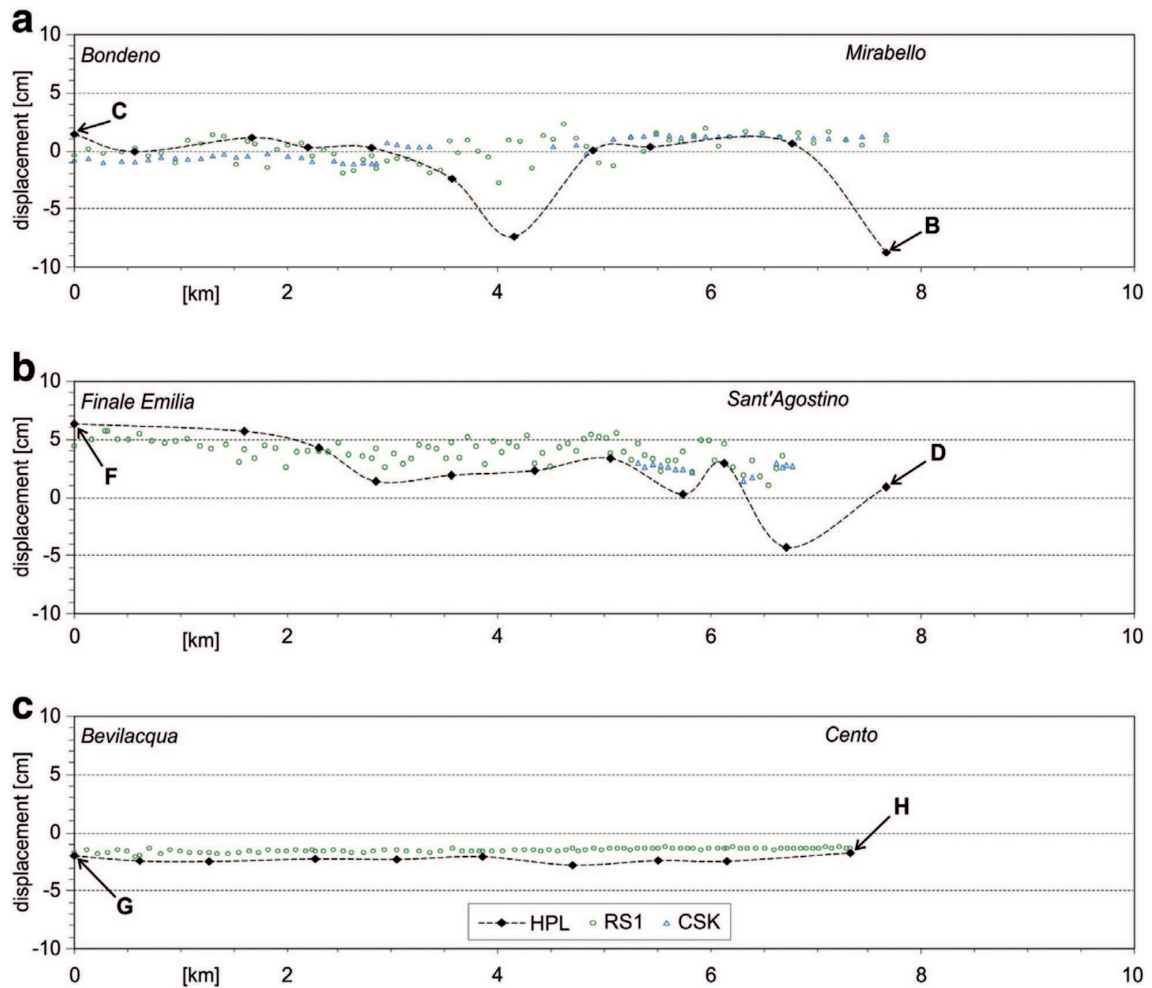


Figure 6.8: Vertical movements measured along the three levelling lines closest to the epicentral area with a mean ESE–WNW orientation showing a uniform behaviour of the single levelling lines, albeit variable from north to south. The error bar at each benchmark calculated on the basis of the standard deviations of the differences in elevation (pre- to post-earthquake) is smaller than the symbol size. Capital letters refer to the benchmarks labelled in Fig. 6.6. HPL: high-precision levelling; RS1: RADARSAT-1; CSK: COSMO-SkyMed (from Caputo *et al.*, 2015).

6.2.2 Major geomorphic effects: liquefaction and local subsidence

The May 2012 Emilia events were characterized by spectacular and locally very intense liquefaction phenomena (e.g. Caputo and Papathanassiou, 2012; Papathanassiou *et al.*, 2012) that possibly mobilized shallow, but in some places large, sedimentary volumes. As a consequence, ground deformations were induced at different scales involving areas from a few meters to several hundred meters in size; they caused horizontal movements up to several centimeters (i.e. lateral spreading), and both positive and negative vertical movements, the latter generally much more frequent and locally exceeding some tens of centimeters. These effects on the earth's surface occurred with a jeopardized pattern, thus influencing both terrestrial and satellite based techniques, albeit in different ways. For the HPL, this effect is particularly evident along the levelling line H–D–B (Fig. 6.9b). Indeed, it runs parallel to the previously described line G–F–C (Fig. 6.9a), showing both similarities and marked differences. For example, there are similarities in the southern and central sectors, where all the benchmarks from south to north show a quite constant subsidence value (ca. 2 cm) that progressively changes into positive vertical movements (up to 3 cm of uplift near Sant'Agostino). The G–F–C line continues to show regular uplifting northwards, as shown by the SAR displacements, In the H–D–B line instead the benchmarks deviate from a regular trend from San'Agostino (point D) onwards, showing highly variable vertical displacements with mainly negative values. Indeed, between San Carlo and Mirabello, the subsidence is locally as great as 11.4 cm (Fig. 6.9b).

The major aims of this study were the analysis of the possible causes in order to explain i) these discrepancies with respect to the relatively nearby and parallel profile (G–F–C), ii) the locally high subsidence values (up to –11.4 cm) and iii) the very short wavelength of the vertical variations.

It must be noted that the benchmark displacement could include the effect of long-term vertical movements during the period between the two campaigns (2005-2012). However, the available data (http://www.arpa.emr.it/dettaglio_notizia.asp?id=4801&idlivello=1-414), in Italian, last visited April 28, 2014) suggest that the 'regional' subsidence affecting the broader region of the lower Po Plain during this time span (and also recorded at the refer-

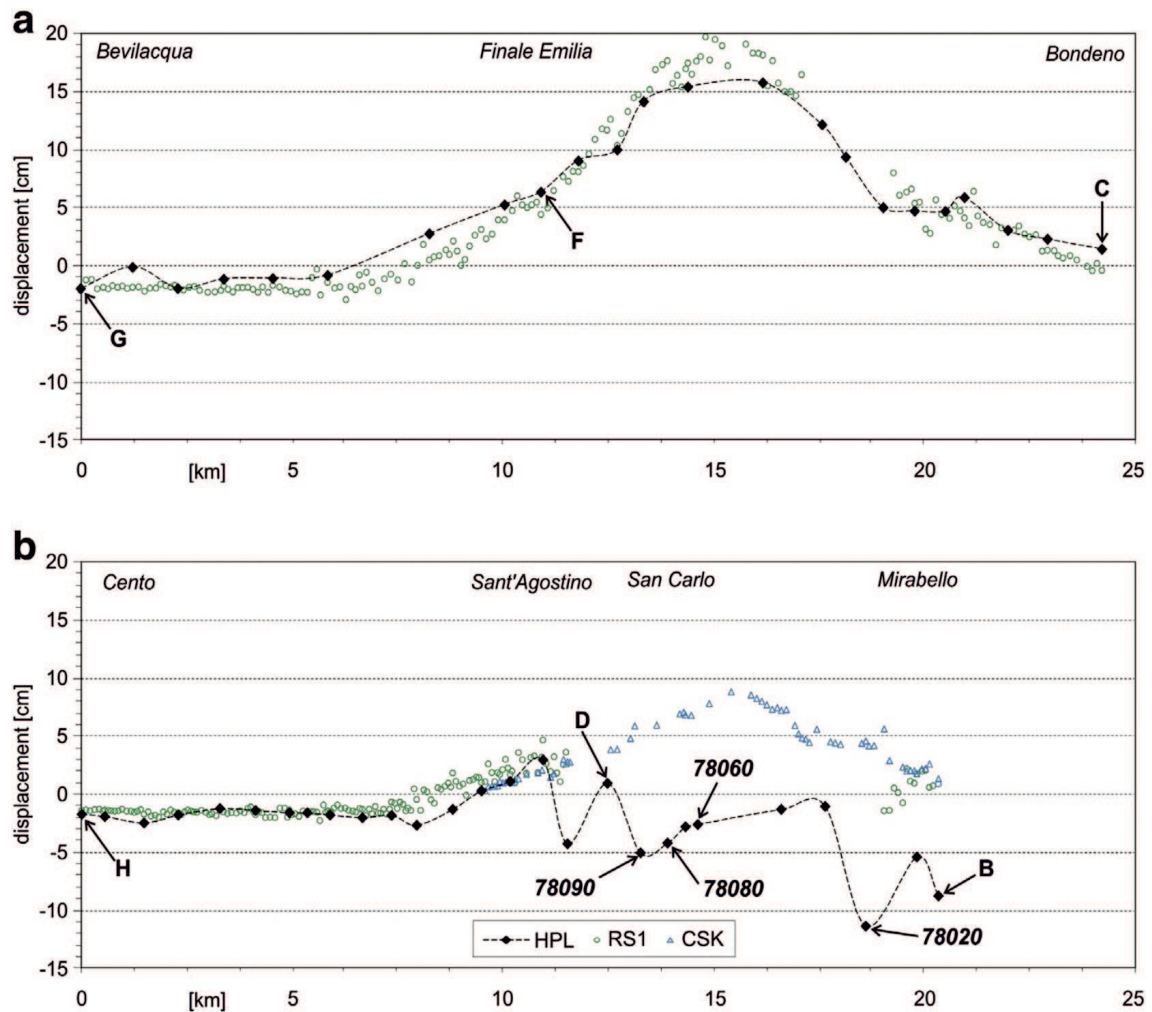


Figure 6.9: Vertical movements measured along the two levelling lines running perpendicular to the May 20 fault strike. Profile G–F–C (a) well reproduces the satellite results, while profile H–D–B shows some marked differences with strongly subsided benchmarks. The error bar at each benchmark calculated on the basis of the standard deviations of the differences in elevation (pre- to post-earthquake) is smaller than the symbol size. Capital letters refer to the benchmarks labelled in Fig. 6.6. HPL: high-precision levelling; RS1: RADARSAT-1; CSK: COSMO-SkyMed (from Caputo *et al.*, 2015).

ence benchmark of Ferrara) was less than 1 to 2 cm. Above all no significant gradients have been documented so far within the study area. Hence, it can be excluded a long-term effect as the cause of the local, albeit strongly, subsided benchmarks and the difference between the terrestrial levelling and satellite interferometry results. Therefore, the geological setting of the sites where the ‘anomalous’ benchmarks were installed, were analyzed in detail.

Information on the shallow subsoil close to each benchmark was derived from drill cores, penetration tests and water wells, as well as immediate post-event surveys following the May 20 earthquake (e.g. Papathanassiou *et al.*, 2012; Caputo and Papathanassiou, 2012).

For example, benchmark 78020 (yellow star in Fig. 6.10a), located at the entrance of the Mirabello cemetery, showed a subsidence of 11.4 cm (Fig. 6.9b). The cemetery area is located along a palaeo-reach of the Reno River and particularly at the base of the south-eastern slope of the left levee (Fig. 6.10a). The shallow stratigraphy observed in some drill cores around the benchmark (black stars in Fig. 6.10a) consists of alternating fine silty sand and saturated sandy silt in the first 5 to 6 m overlying a thick body of medium-grained sand. These are typical conditions prone to liquefaction in the case of seismic shaking. Indeed, during the May 20 event, the broader cemetery area was affected by several ground effects associated with, and induced by, widespread liquefaction phenomena. In particular, several ground deformations occurred co-seismically (red squares in Fig. 6.10a-d) a few meters from benchmark 78020, clearly documenting the local loss of shear resistance within the subsoil which certainly reacted differentially as a function of the vertical loads. The benchmark is cemented next to the heavy entrance pillar of the cemetery boundary wall, which very likely suffered some settling, thus also displacing the benchmark. Moreover, large amounts of liquefied sand were ejected within the broader area (blue dots in Fig. 6.10a) and this necessarily caused further subsidence due to the consequent compaction and volumetric reduction of the underlying sandy layer(s). In addition to the ‘local’ effects, the whole southeastern slope of the levee suffered large-scale lateral spreading (Fig. 6.10a,b); the sliding surface likely exploited gently dipping sandy foresets well documented within the same levee body a few kilometres to the south within a palaeo-seismological trench (Caputo *et al.*, 2012). Accordingly, the lateral spreading also induced a vertical component of motion (Fig. 6.10c), which certainly contributed to the subsidence of benchmark 78020 (-11.4 cm). Similar phenomena were documented by Pizzi and Scisciani (2012).

A second example is represented by benchmark 78060, located on the base of a tall lamp post in the centre of the roundabout at the northern entrance to San Carlo (Fig. 6.11a,b). Drill cores and CPT’s carried out a few tens of meters from the benchmark clearly show the presence of saturated fine silty sands at 4 to 6 m depth. Based on the CPT’s and the approach proposed by Idriss and Boulanger (2008), it was also possible to calculate a liquefaction potential index (LPI; Iwasaki *et al.*, 1978) of 10.5, which corresponds to a high liquefaction

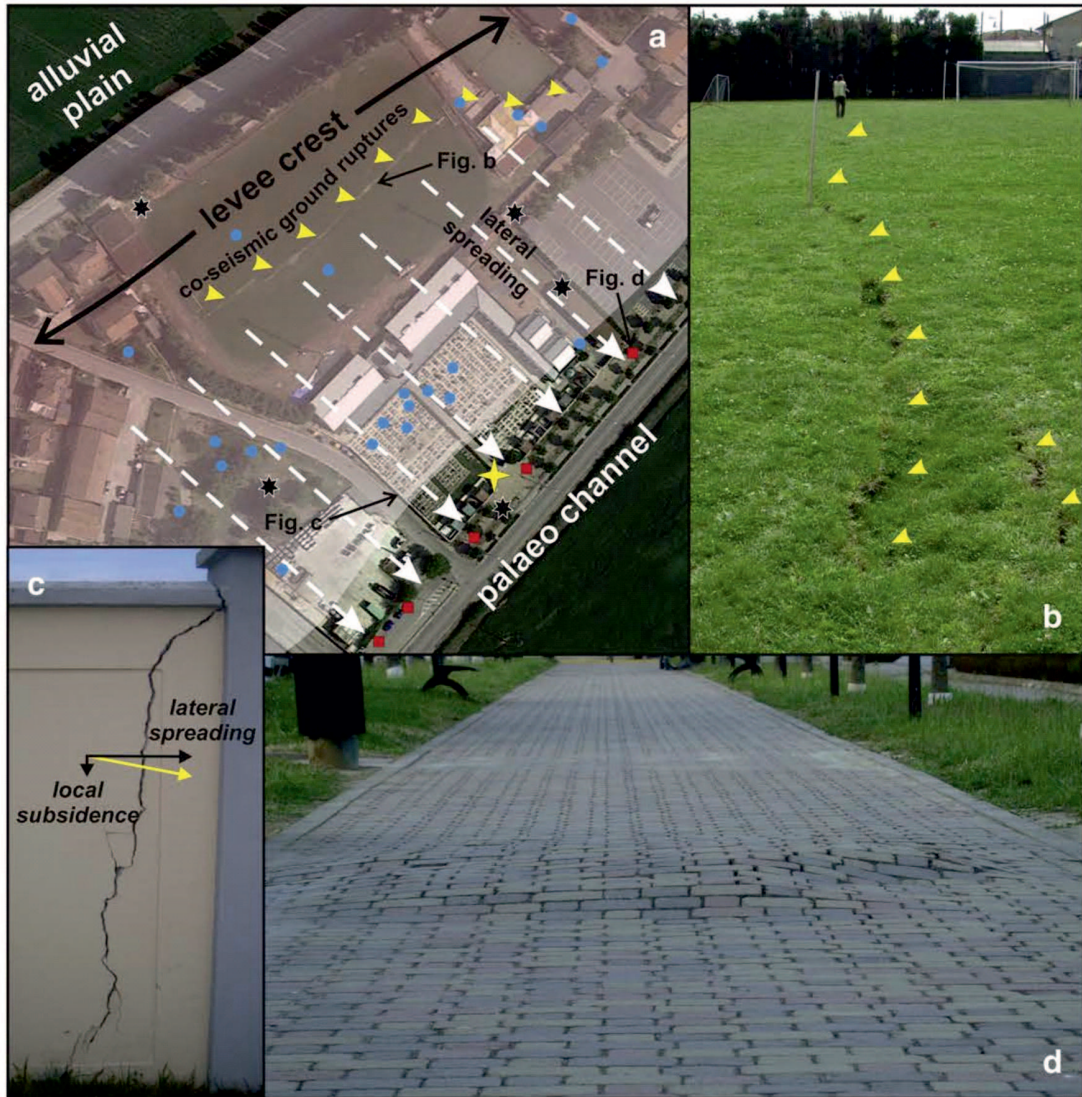


Figure 6.10: Geomorphological features observed in Mirabello the area. a) Google Earth frame of the cemetery area showing the distribution of secondary co-seismic effects, such as sand ejection points (blue dots), ground deformation sites (red squares), drill cores (black stars), ground ruptures (yellow arrows) and sliding direction due to lateral spreading (white arrows). The yellow star indicates the location of benchmark 78020 characterized by 11.4 cm of subsidence. b) Ground ruptures observed on top of the abandoned levee (see (a) for location). c) Effects of the lateral spreading on the lateral wall of the cemetery (see (a) for location). d) Example of ground deformation associated with shallow liquefaction (see (a) for location). 78080, which was apparently uplifted ca. 8 cm relative to the ground surface, thus coming out off its case.

potential risk (Sonmez, 2003). Moreover, widespread sand ejections were observed in the surroundings during the immediate post-event survey (Fig. 6.11c; Caputo and Papathanassiou, 2012). Considering the combined weight of the metal pole and its foundation (roughly 1 m³ of concrete), some amount of permanent settling induced by the coseismic liquefaction

would be expected and could reasonably explain the 2.8 cm of subsidence measured at this benchmark (Fig. 6.9b).

Benchmark 78080 located on the bike lane along the provincial road at San Carlo (Fig. 6.11a), showed a subsidence of 4.4 cm (Fig. 6.9b). CPTs carried out close to the benchmark clearly documented a saturated sandy silt layer at 4.5 to 5.5 m depth and a moderate LPI value. Interestingly, a few tens of meters away from the benchmark, a water well was apparently uplifted by ca. 8 cm, thus coming out of its case (Fig. 6.11e); the metal rod is rooted at 30 m-depth, suggesting that the nearby ground has permanently subsided as a consequence of the dewatering, sand ejection and hence compaction as observed in the surroundings.

Benchmark 78090 also showed a subsidence of 5.3 cm (Fig. 6.9b). As at Mirabello (Fig. 6.10a), this benchmark is fixed at the entrance of a cemetery located along the same palaeo-branch of the Reno River, although in this case at the base of the external slope of the right levee (Fig. 6.11a). Here lateral spreading and diffuse sand ejection also occurred in concomitance with the May 20 event (respectively white arrows and blue dots in Fig. 6.11a), while geotechnical results and palaeoseismological excavations (Caputo *et al.*, 2012) confirmed the presence of a thick layer of saturated fine-medium sands between 4 to 8-8.5 m depth. As a consequence, both horizontal and vertical movements were induced during the May 2012 major events (Figs. 6.9b and 6.11d), thus explaining the measured subsidence and allowing to classify this as a local effect.

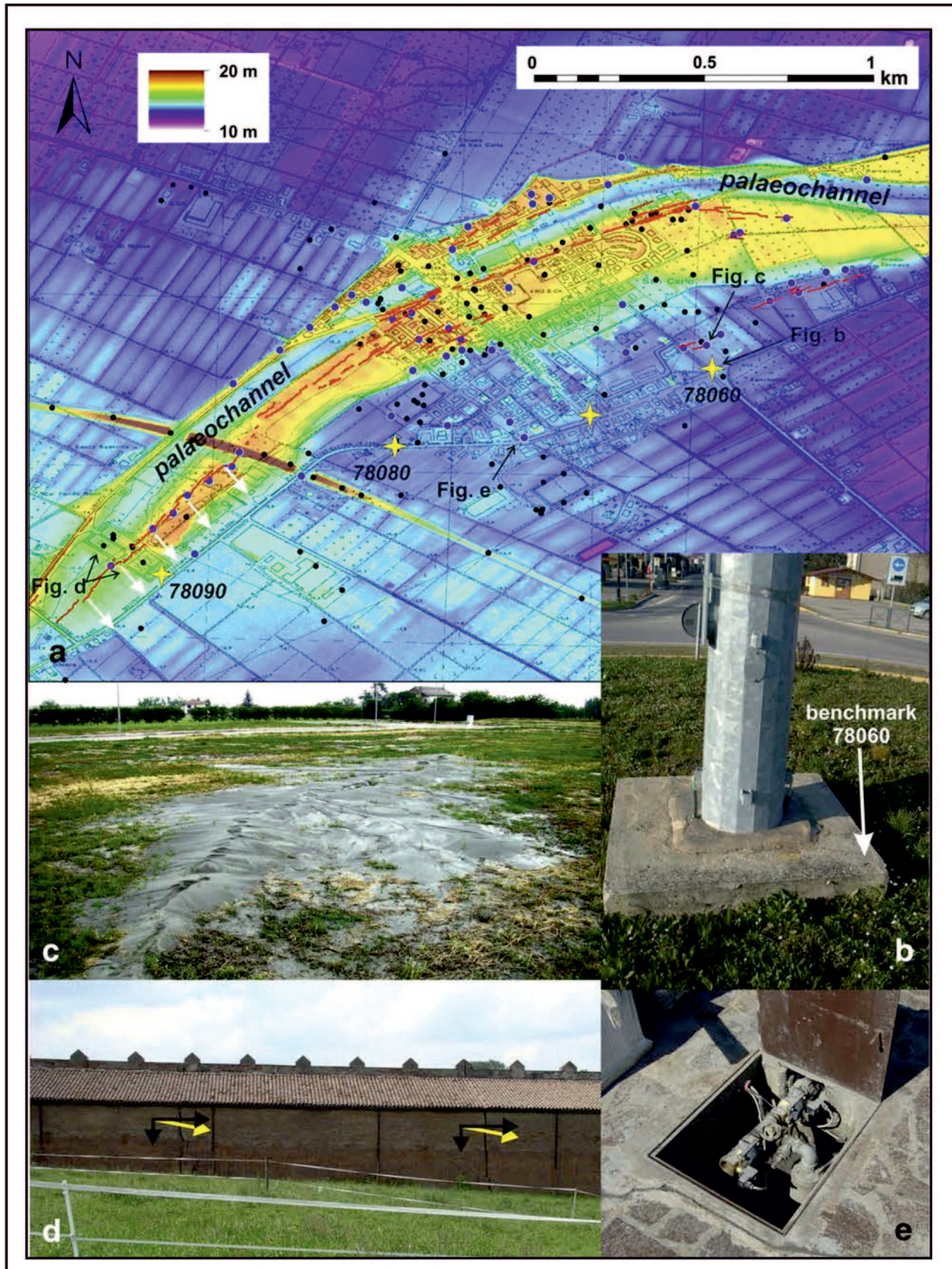


Figure 6.11: Geomorphological features observed in the San Carlo area. a) Digital elevation model clearly showing the two levees of the palaeo-Reno River. Red lines represent the major ground ruptures observed after the May 20 event (Caputo and Papathanassiou, 2012) generally associated with lateral spreading phenomena (white arrows). Blue dots are sand ejection points while black ones are penetration tests providing information about the shallow subsoil. Yellow stars are benchmarks of the HPL line. b) The foundation of the lamp post installed in the center of the roundabout at the northern entrance to San Carlo where diffuse liquefaction has occurred (c) (see (a) for locations). d) The southern wall of the cemetery built on the slope of the palaeolevee and affected by lateral spreading contributing to the subsidence of benchmark 78090. e) Example of a water well located close to benchmark.

6.3 Seismic Microzoning of the Sant'Agostino Municipality

The purpose of seismic microzoning studies is the characterization of a territory according to the seismic response, i.e. the behavior of the subsoil during a seismic event. In particular, the major aim is the distinction of the areas characterized by homogeneous behavior distinguishing between i) stable zones, ii) areas susceptible of amplification of the ground motion and iii) areas subject to instability, such as landslides, liquefaction, and surface fractures, thus can be identified and bounded.

The distinction between areas characterized by different seismic hazard represents a necessary information for the local administrations in order to prevent and reduce the risk, as well as a fundamental support to the local urban planning, so as to lead the choices to areas with a lower hazard and/or use of building constructions with a lower vulnerability to possible local effects.

6.3.1 Subsoil model and amplification estimation

Among the coseismic effects observed in occasion of the May 2012 Emilia seismic sequence, such great ground motion amplification was particularly unexpected. In fact, the horizontal acceleration locally exceeded 0.3 g, i.e. more than twice higher than that calculated for rock-site conditions, with a return period of 475 years (0.125 to 0.175 g; Stucchi *et al.*, 2011).

The analysis of local seismic response (Facciorusso *et al.*, 2012; Laurenzano *et al.*, 2013; Priolo *et al.*, 2012; Gallipoli *et al.*, 2014) have provided values of the amplification factors in agreement with those achieved by the regional charts (DAL 112/2007, Annex 2); therefore, in accordance with the Geological Survey of the Regione Emilia-Romagna, for the purpose of this research project and for microzoning studies carried out in the frame of the Ordinance 70/2012 ("Approvazione programma per gli studi microzonazione sismica"), the amplification factors were estimated based on the simplified procedures reported in the regional guidelines. For flat areas, these guidelines provided different charts based on the stratigraphy and depth of the bedrock (greater or less than 100 m \pm 20), yielding values in

terms of PGA (FA_{PGA}) and Housner Intensity, for different period intervals ($FA_{0.1-0.5s}$ and $FA_{0.5-1.0s}$).

In order to infer the bedrock depth, the Geological Survey of the Regione Emilia-Romagna performed several geophysical surveys (e.g. downhole, crosshole, SCPTu, HVSR). The results of these investigations showed that $V_{s30} < 225$ m/s and V_{s100} from 300 to 350 m/s; the fundamental frequency (f_0), indeed, varies from 0.8 to 1.1 Hz. By means of the empirical relation between f_0 and V_s (i.e. $f_0 = V_s/4h$), the depth of the first noticeable impedance contrasts (pseudo-bedrock) seems to be comprises between 70 and 150 m b.g.s. Thus, for sites characterized by $f_0 \geq 1$ Hz and amplitudes greater than 2.5, they estimated that the depth of the bedrock is less than $100 \text{ m} \pm 20$. By comparing this hypothesis with the available geological information, they suggested that the depth of the major impedance contrast (i.e. seismic bedrock) is located between the AES6 and AESind basal limits (Figs. 6.12a,d and Fig. 6.13; Martelli and Romani, 2013).

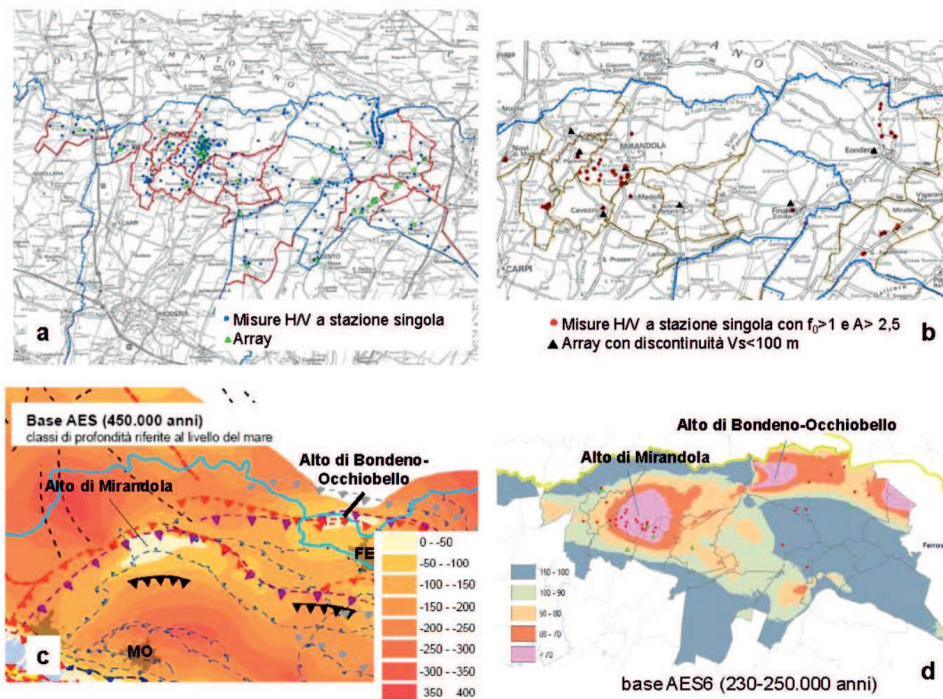


Figure 6.12: a) Locations of array and single-station noise measurements carried out by the Geological Survey of the Regione Emilia-Romagna. b) Location of array and single-station noise measurements suggesting the occurrence of an impedance contrast (i.e. bedrock) at depth lesser than 100 m. c) Bottom isobaths of AES and (d) AES6 (from Martelli and Romani, 2013).

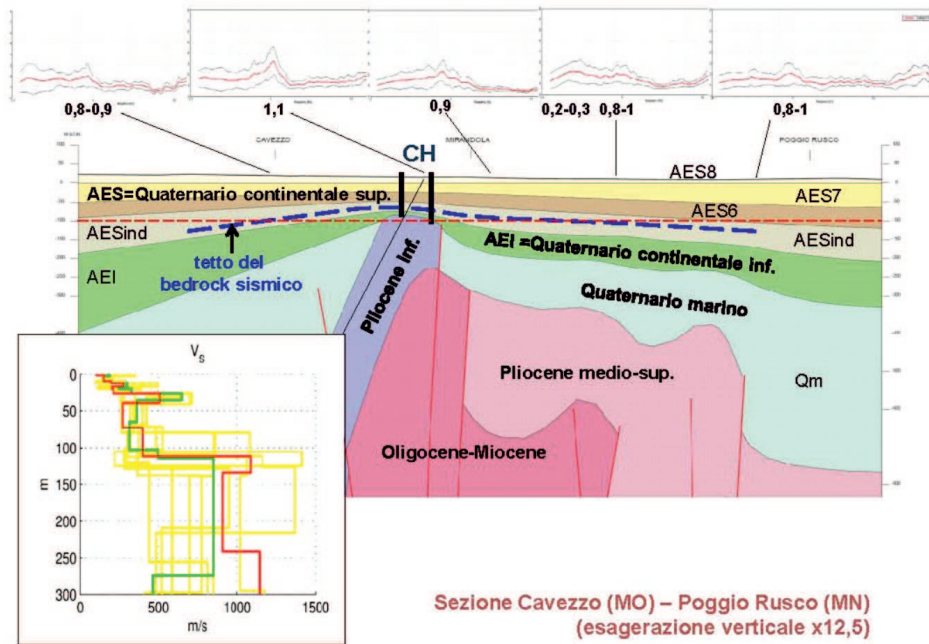


Figure 6.13: Bedrock depth estimation (blue line) through the comparison between H/V curves, Vs profile obtained by array surveys and stratigraphic constraints. CH: locations of crosshole investigations performed at Medolla and Mirandola (Modena Province) (from Martelli and Romani, 2013).

Subsequently, they distinguished two areas where the bedrock is located below and above 120 m, named A1 and A2, respectively (Fig. 6.14). Following the simplified procedure above mentioned (DAL 112/2007, Annex 2), the Geological Survey of the Regione Emilia-Romagna estimated the following amplification factors:

- A1 area: $FA_{PGA}=1.5$; $FA_{0.1-0.5s}=1.8$; $FA_{0.5-1.0s}=2.5$;
- A2 area: $FA_{PGA}=1.7$; $FA_{0.1-0.5s}=1.9$; $FA_{0.5-1.0s}=2.6$.

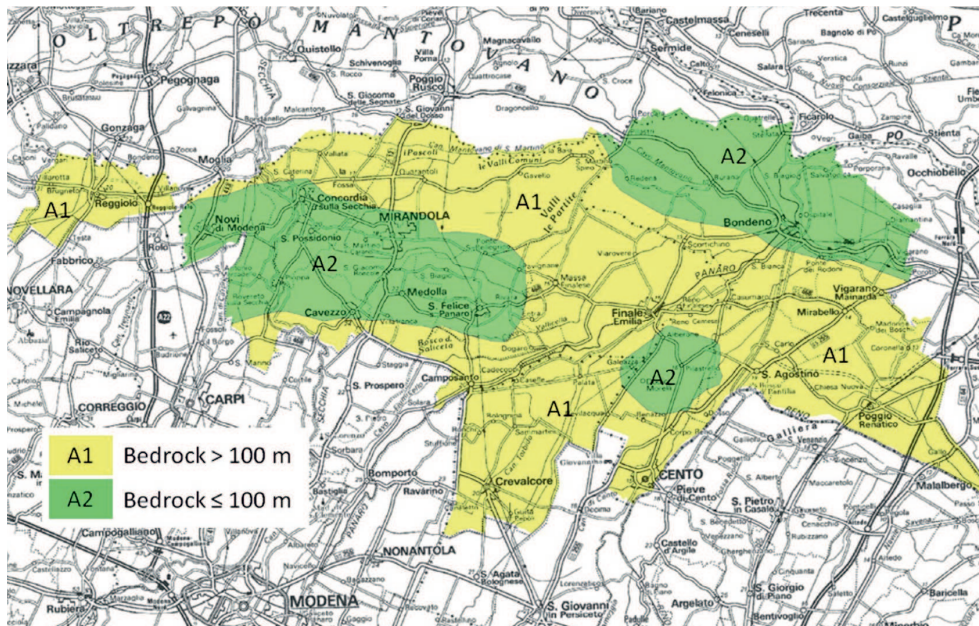


Figure 6.14: Map showing an approximate bedrock depth. A1: bedrock depth greater than 100 ± 20 m; A2: bedrock depth lower than 100 m (from Martelli and Romani, 2013).

6.3.2 Cartographic maps

In the Surveys Map (Fig. 6.15) the location of the geotechnical and geophysical surveys exploited for the seismic microzoning study are reported, including both the investigations archived in the Regione Emilia-Romagna database (339 surveys) and those added in the frame of this research (351 surveys). As recommended in the guidelines proposed by the Commissione Tecnica Nazionale for seismic microzoning studies (Seismic Microzoning Working Group, ICMS, 2008), each type of survey is codified by a different graphic symbol (standard representation).

Obviously, the majority of the investigations are clustered around the three villages within the municipality (San Carlo, Sant’Agostino and Dosso) and around a new urbanization area to the N-NE of Sant’Agostino, along the path of the provincial road SP70, between San Carlo and Sant’Agostino, and in correspondence of the municipal dump in the northern sector.

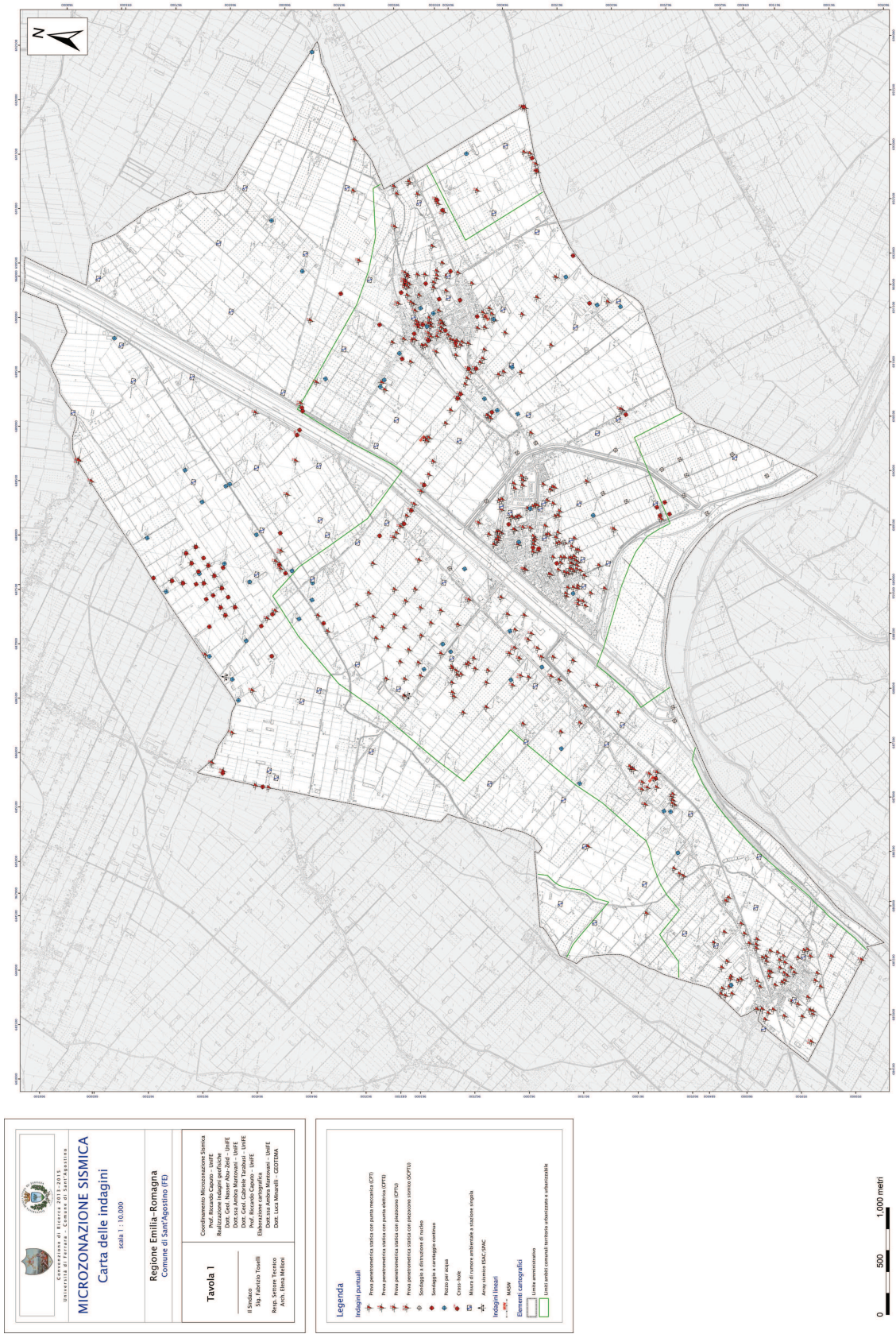


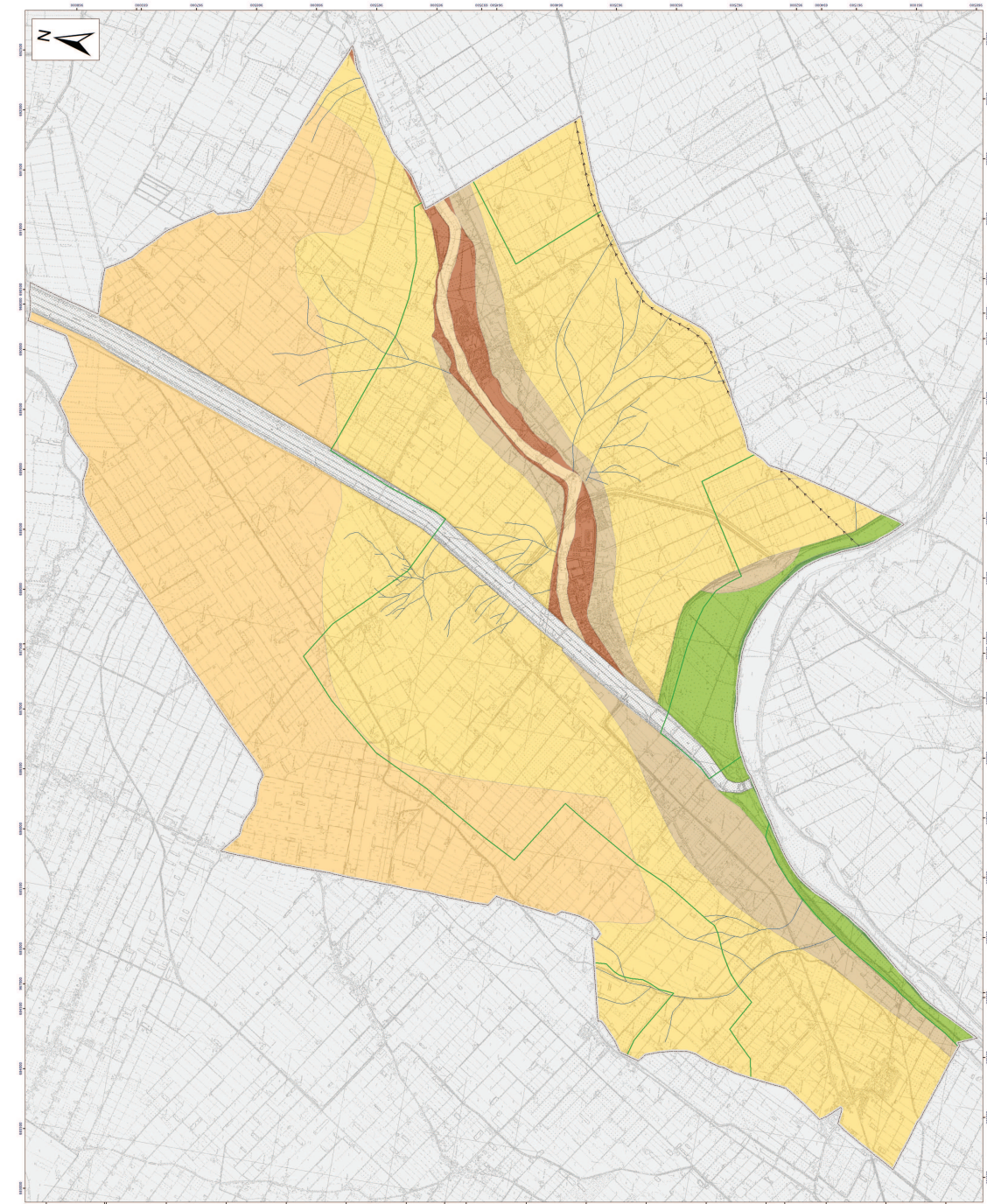
Figure 6.15: Surveys Map of the Sant'Agostino Municipality.



The Geologic Map (Fig. 6.16) shows the surface distribution of the Apennines alluvial sediments deposited in historical times by the Reno River. The absence of a previous detailed geological mapping has made necessary the reconstruction of the depositional geometries through an accurate interpretation of the surface stratigraphic relations. The interpretation of the relations between the surface sedimentary bodies was based on the analysis of satellite images and on the detailed digital elevation model (LIDAR). In addition, considering the recent age of the surface deposits (from 15th century onwards), the interpretation of the surface geomorphological features can be greatly supported by the numerous historical documents and accurate maps (Bondesan, 1986; M.U.R.S.T., 1997; Castiglioni *et al.*, 1999) concerning the evolution of the western sector of the present-day Ferrara Province and of the Reno River, which has been active since the end of the 18th century. Anyway, the depositional evolution of the Reno River in this area was greatly influenced by the anthropic activities, such as the construction of many embankment works and land reclamation, in order to impede further disastrous flooding events.

The whole set of surface data was compared with the geotechnical information derived from the available penetrometric tests, particularly of the first meters, which have confirmed the preliminary geomorphologic and stratigraphic interpretations based on remote sensing techniques.

The municipal area of Sant'Agostino is characterized by a largely flat morphology, with variable altitudes ranging from 8 m to 16 m a.s.l. The only relief is represented by the levees of an abandoned reach of the Reno River aligned in a NE-SW direction, and from that of the active Reno River delimiting the southern sector of the administrative boundary. From a lithologic point of view, the sedimentary body of the palaeo-Reno River channel consists of well drained sandy-silty soils, which can be subdivided into three different units, distinguished from chronological and sedimentological features. The first development phase of the palaeo-Reno River (15th century) is marked by the deposition of silty-sands sediments, while those related to the main depositional phase are characterized by coarser sands and silt. The sedimentary body deposited during the abandonment phase (18th century) are prevalently made of sandy-silts, which filled the last riverbed; so, the old course was grad-

ually dried up, while still maintaining its morphological evidence, only locally obliterated by human activities. Overall, the sandy body of the palaeo-Reno River channel is characterized by a variable thickness between 8 and 10 m. Apart from the channel sedimentary body, wide areas of the municipality are characterized by the presence of silty-sands, silts and clayey silts levee deposits originated by the overlapping of several flooding events of the palaeo-Reno River, which affected this area despite the repeated embankment works. The distribution of these crevasse splays and levee deposits respect to the axis of the river is quite symmetrical. The main crevasse channels, still very well preserved, are reported in the map as linear elements. Even further away from the palaeo-channel, the levee deposits are replaced by clays, silty-clays and organic clays bodies deposited in the damp environments characterizing the interchannels alluvial depressions, widely developed in the north-western sector of the municipality.



UNIVERSITÀ DI FERRARA - CENTRO DI SAN'AGOSTINO
MICROZONAZIONE SISMICA
Carta geologica
 scala 1:10.000

Regione Emilia-Romagna
Comune di Sant'Agostino (FE)

Tavola 2
 Il Sindaco
 Sig. Fabrizio Travelli
 Capo Settore Territorio
 Arch. Elena Melloni

Coordinamento Microzonazione Sismica
 di Area: Roberto Valentini
 Elaborazione carta geologica:
 Dott. Luca Marzocchi - GEOTIMA
 Direzione Ambito Montebianco - Unife
 Dott. Luca Marzocchi - Unife
 Dott. Luca Marzocchi - GEOTIMA

Legenda:

Tracce lineari
 ----- Canale naturale da zona di estrazione
 - - - - - Asse di drenaggio
 - - - - - Asse di alimentazione

Forme di superficie e spigoli
 - - - - - Asse di alimentazione

Faete deposizionali e litologie
 [Yellow] Terreni connessi tutti di area alluviale
 [Orange] Sabbie fluviato di riempimento di canale fluviato approssimativo
 [Brown] Sabbie e limi di riempimento di canale fluviato approssimativo
 [Light Green] Limi carbonati di riempimento di canale fluviato approssimativo
 [Dark Green] Argille oporistiche di deposito intracanal
 [Grey] Sabbie e limi di riempimento di canale fluviato (Bene alluviale)

Elementi Cartografici
 [Grey] Linea amministrativa
 [Green] Limiti attuali (canali) e storici (alluvioni) e urbanizzazione

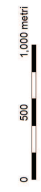


Figure 6.16: Geological Map of the Sant'Agostino Municipality.

In the Geological-Technical Map (Fig.6.17) is synthesized the basic information about geology, geomorphology, lithotechnical and geotechnical features, based on the critical review of all available data; therefore, the geological and geomorphological elements that, in case of an earthquake, can modify the seismic motion at the surface or determine any local effects are represented and shows the distribution of the shallow deposits.

Outcropping of depositional units attributable as bedrock are not present in the area, so will subsequently be described buried and surface geological forms, and the different types of shallow deposits.

The only buried geological form reported in the map is a palaeo-channel axis, which runs almost parallel to SE boundary of the Sant'Agostino municipality. This form marks the existence of an ancient palaeo-riverbed nowadays buried at shallow depth (about few meters).

The Holocene shallow alluvial deposits, shown in the Geologic Map, were distinguished into five different types, each of them associated with those proposed in the ICMS (2008). Such classes were defined through the Unified Soil Classification System (modified USCS, ASTM, 1985), which classifies the majority of the non-consolidated materials. For each of the identified units, different colors and letter codes corresponding to those of the USCS were reported in the map (Fig.6.17). The letter code, consisting of two capital letters followed by just as many small letters, refers to the lithotechnic characteristics of the shallow sediments and to their depositional environments, respectively.

In the following, the description of the units recognized within the investigated area:

- **interchannels depressions deposits** (*OLpl*) constituted by clays, silty-clays and clayey-silts, often organic and widely bioturbated, deposited in the floodplain damp environments which are subjected to consistent supplies of fine sediments during overbank flood episodes;

- **distal and proximal levees bodies** (*MLes*) deposited between the wide interchannels depressions and the fluvial channel bodies. These deposits consist of inorganic silts, fine silty-sands and silty-clays within which can be observed fining upward successions, abundant muddy intraclasts and organic materials;

- **fluvial channel body of the palaeo-Reno River** can be divided in two different units, whose limit marks a decrease of the flow rate and a consequent narrowing of the riverbed during the 18th century when, as a result of numerous flooding events, the fluvial sedimentary supply significantly changed. Therefore, poor sorted coarse to medium sands (*SPes*) characterize the older palaeo-Reno channel (since 15th century), while silty-sands to silts (*SMes*) identify the latest riverbed (18th century);

- **soils with anthropic remnants** (*RIzz*) are recognizable along narrow area, elongated in a NNE-SSW direction, from the southwest of Sant'Agostino village to the northern administrative boundary of the municipality. This unit corresponds to the Cavo Napoleonico, an artificial channel excavated since the 19th century as floodway of the Reno River in case of significant overflow episodes.

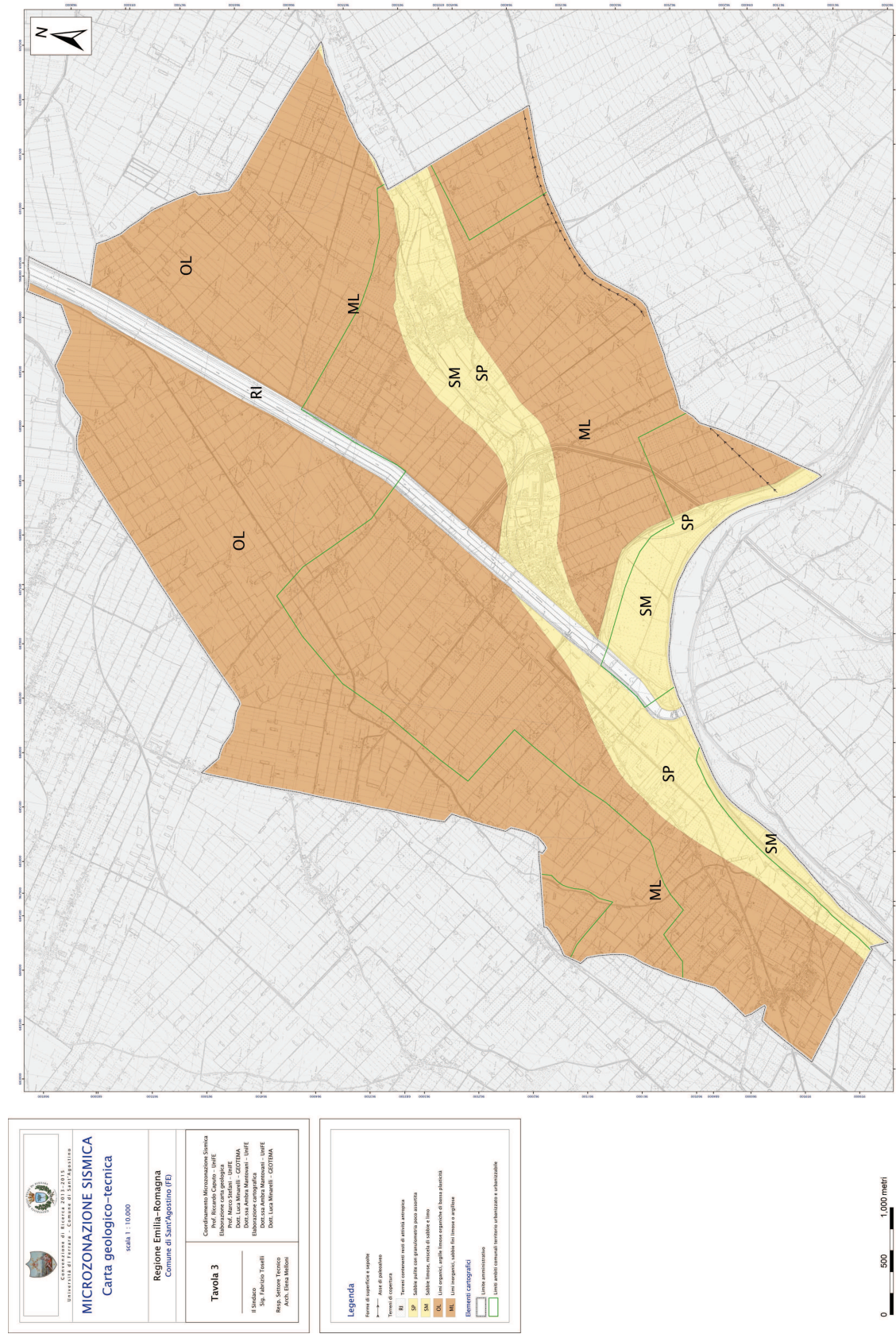


Figure 6.17: Geological-Technical Map of the Sant'Agostino Municipality.

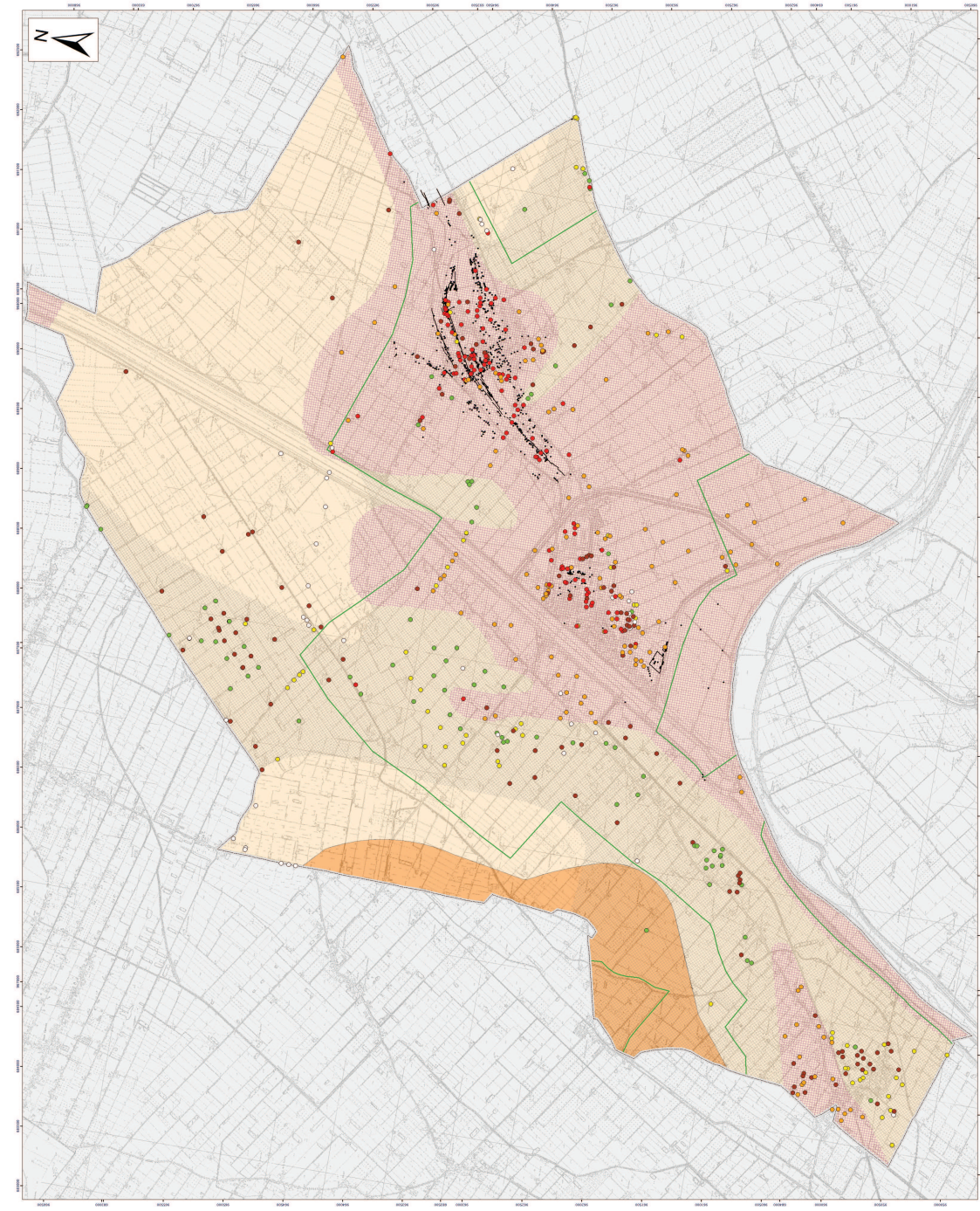
The MOPS Map (Homogeneous Microzones in Seismic Perspective; Fig. 6.18) represents the basic synthesis of the first level microzoning studies. In such maps, the areas subjected to ground motion amplification and/or to instability, such as liquefaction phenomena are classified.



As discussed in Section 6.3.1, the amplification factors were provided by the Geological Survey of the Regione Emilia-Romagna, based on the regional guidelines (DAL 112/2007). Most of the municipal territory is characterized by $FA_{PGA}=1.5$ (A1, pink area), while a very narrow area in the southwestern boundary is characterized by $FA_{PGA}=1.7$ (A2, orange area). Such 'lateral variation' can be justified with the occurrence in the subsurface of the periclinal termination of the Mirandola anticline, whose crest is oriented about ESE-WNW.

Each penetration tests were analyzed from a semi-quantitative point of view for detecting the presence of liquefiable horizons; in particular, the surveys were classified on the basis of the thickness and depth of the liquefiable layer(s) and represented by color-coded circles, as described in Section 4.3.2. Such classification provided punctual information. Moreover, as it is evident from the Surveys Map, the geognostic data are not homogeneously distributed over the municipal territory, but are clustered around the urbanized areas. In order to provide a simply graphical representation of the spatial distribution of the liquefiable layer(s) and take into account the partial subjectivity in the interpretation, in agreement with Geological Survey of the Regione Emilia-Romagna the following areas were distinguished:

- LQ1 area: occurrence of liquefiable layer(s) (at least 1 m thick) in the first 10 m b.g.s.;
- LQ2 area: occurrence of liquefiable layer(s) (at least 2 m thick) between 10 to 20 m b.g.s.;
- N area: absence of liquefiable layer(s) in the first 20 m b.g.s.

The first two areas are represented by purple and grey crossed grids, respectively, while, the last one is colorless.



MICRONAZIONE SISMICA
 Carta Microzone Omogenee
 in Prospettiva Sismica
 scala 1 : 10.000
 Regione Emilia-Romagna
 Comune di Sant'Agostino (FE)

Tavola 5
 Il Sindaco
 Sig. Fabrizio Toselli
 Resp. Settore Tecnico
 Arch. Elena Melloni

Coordinamento Microzonazione Sismica
 Prof. Riccardo Caputo - IURFE
 Sistema verificazione (verifica 2)
 Prof. Riccardo Caputo - IURFE
 Magnitudine sismica di riferimento
 Prof. Riccardo Caputo - IURFE
 Dott. Luca Marzulli - COTTIMA
 Cella di elaborazione dati (CDE)
 Dott.ssa Annalisa Mastromoni - IURFE
 Dott. Luca Marzulli - COTTIMA

Legenda

Integrare i particolari
 • Dispositivi sismologici 10 - 60 metri sesto fondo - 0,5 m dal p.c. (S1)
 • Dispositivi sismologici 10 - 1 m tra 10 e 15 m dal p.c. (S2)
 • Dispositivi sismologici 10 - 2 m tra 10 e 15 m dal p.c. (S3)
 • Dispositivi sismologici 10 - 2 m tra 15 e 20 m dal p.c. (S4)
 • Anziani ed anziani handicappati entro 20 m dal p.c. (S5)
 • Zone non interessate (S0)

Area di influenza di propagazione
 • Terreni incoerenti di risonanza con pareti 10 m dal p.c. (classico 1-4)
 • Terreni incoerenti di risonanza con pareti 10 m dal p.c. (classico 2-3)

Fattori di amplificazione
 • Fattore 1,5 (F1) - 1,5 m dal p.c. - 2,5 m dal p.c. (classico DAL 1,12 (2007))
 • Fattore 1,2 (F2) - 1,5 m dal p.c. - 2,5 m dal p.c. (classico DAL 1,12 (2007))

Siti occupazione regolamentati
 • Ispettorato paesati
 • Ispettorato forestali

Elementi cartografici
 Linea amministrativa
 Linea attività comuni territorio urbanizzato e urbanizzabile



Figure 6.18: Homogeneous Microzones in Seismic Perspective (MOPS) Map of the Sant'Agostino Municipality.

In the Amplification Factors and Liquefaction Hazard Map (Fig. 6.19) the areas susceptible to ground motion amplification and/or to liquefaction are identified.

Besides the amplification factors (discussed above), in this maps the calculated Liquefaction Potential Indexes (LPI), following the procedure described in Section 4.3.2, are also reported in correspondence of each penetrometric surveys. CPTu and SCPTu surveys are represented by colored squares. For completeness, notwithstanding the simplified procedure for the evaluation of the liquefaction potential are calibrated on piezocone tests, the LPI were calculated also for mechanical and electrical (CPT and CPTe) penetration survey. For this reason, these tests are reported in the maps with a different symbol (circle).

The symbols are color-coded, based on the LPI categories as proposed by Sonmez (2003):

- white symbol for null or low liquefaction hazard ($0 \leq LPI \leq 2$);
- yellow symbol for moderate liquefaction hazard ($2 < LPI \leq 5$); - red symbol for high liquefaction hazard ($5 < LPI \leq 15$).

Are also shown the LQ1-LQ2-N areas as above described.

In the Shear-wave velocity Map (Fig. 6.20) the fourteen Vs30 (i.e. mean Vs value in the first 30 m b.g.s.) values retrieved from both direct and indirect geophysical surveys are shown, in particular from:

- one crosshole;
- nine SCPTu;
- two MASW;
- two ESAC.

The values of Vs30 range from 162 to 218 m/s, thus belonging to the C soil category (NTC, 2008). This parameter is fundamental for the exploitation of the regional charts, as above described, in order to infer the value of the amplification factors.

In the Natural resonance frequencies Map (Fig. 6.21) the fundamental frequencies retrieved from 72 single-station noise measurements are shown.

Within the municipal territory, the fundamental frequency (f_0) ranges from 0.88 to 0.5 Hz, with amplitudes varying from 2.0 to 3.2.

Higher fundamental frequencies ($f_0 > 0.7$ Hz) were observed near San Carlo and in general in the northeastern sector; while, lower frequencies ($f_0 < 0.7$ Hz) were observed south of Sant'Agostino village and in general in the southern sector of the municipality.

Based on the observed fundamental frequencies (less than 1.0 Hz), as discussed in the previous paragraph, the depth of the main resonant surface (i.e. bedrock) within the entire territory can be hypothesized to be greater than 100 m.



Figure 6.20: Shear-wave velocity (V_{s30}) Map of the Sant'Agostino Municipality.



Figure 6.21: Natural resonance frequencies Map of the Sant'Agostino Municipality.

6.3.3 Stratigraphic architecture and depositional evolution

The lower portion of the investigated sedimentary bodies consists of sandy-silts and silty-sands deposits lying above a continuous horizon of medium-to-fine sand few meters thick (Fig. 6.22b). It lies at ca. 20 m depth below the palaeo-levees and about 16-17 m below the interfluvial areas. This succession, deposited during the late phase of the last glacial period (documented age of the top sediments of about 19.860 years; ISPRA, 2009) when the sea level was about 120 m lower (Trincardi *et al.*, 1994; Waelbroeck *et al.*, 2002), is attributable to the latest Pleistocene alluvial plain (Calabrese *et al.*, 2012).

Overlying this sedimentary unit the presence of a thick succession (at least 9-10 m), predominantly constituted of clays and silts with abundant organic fraction (Fig. 6.22b), proves the occurrence and persistence of swampy environments (documented age of the bottom sediments of about 4.440 years; ISPRA, 2009). About five thousands years ago, the sea water transgression reached its culmination. Notwithstanding the area of Sant'Agostino was not directly affected by this phenomena, the high eustatic level has made the water drainage particularly difficult, thus leading to the development of wider swampy areas. The upper limit of this unit lies from 6 to 8 m depth below the interchannels areas and from 11 to 13 m depth below the palaeo-levees.

The uppermost sedimentary unit develops from the surface down from 8 to 12 m depth. The geomorphological expression of this unit is an elongated topographic rise that stretched from the villages of Sant'Agostino to San Carlo, corresponds to a sedimentary body that had been accumulated by an abandoned reach of the Reno River that was active during Medieval and modern times (Fig. 6.22a). The levees consist of fine sands and sandy-silts close to old channel course, while moving away clayey- and sandy-silty become prevalent (Fig. 6.22b).

Moving away from the palaeo-levees, it can be found wide a sedimentary body constituted of silty-sands and sandy-silts, interpreted as crevasse splay deposits (Fig. 6.22b). Within the depression between the palaeo-levees, a few meters thick sandy body represents the most recent filling of the last Reno River, which had been active since the XVIII century. Below this deposits other sandy bodies can be found, reflecting an intense depositional

activity of ancient river systems since 1450-1481 A.D. onwards (Calabrese *et al.*, 2012).

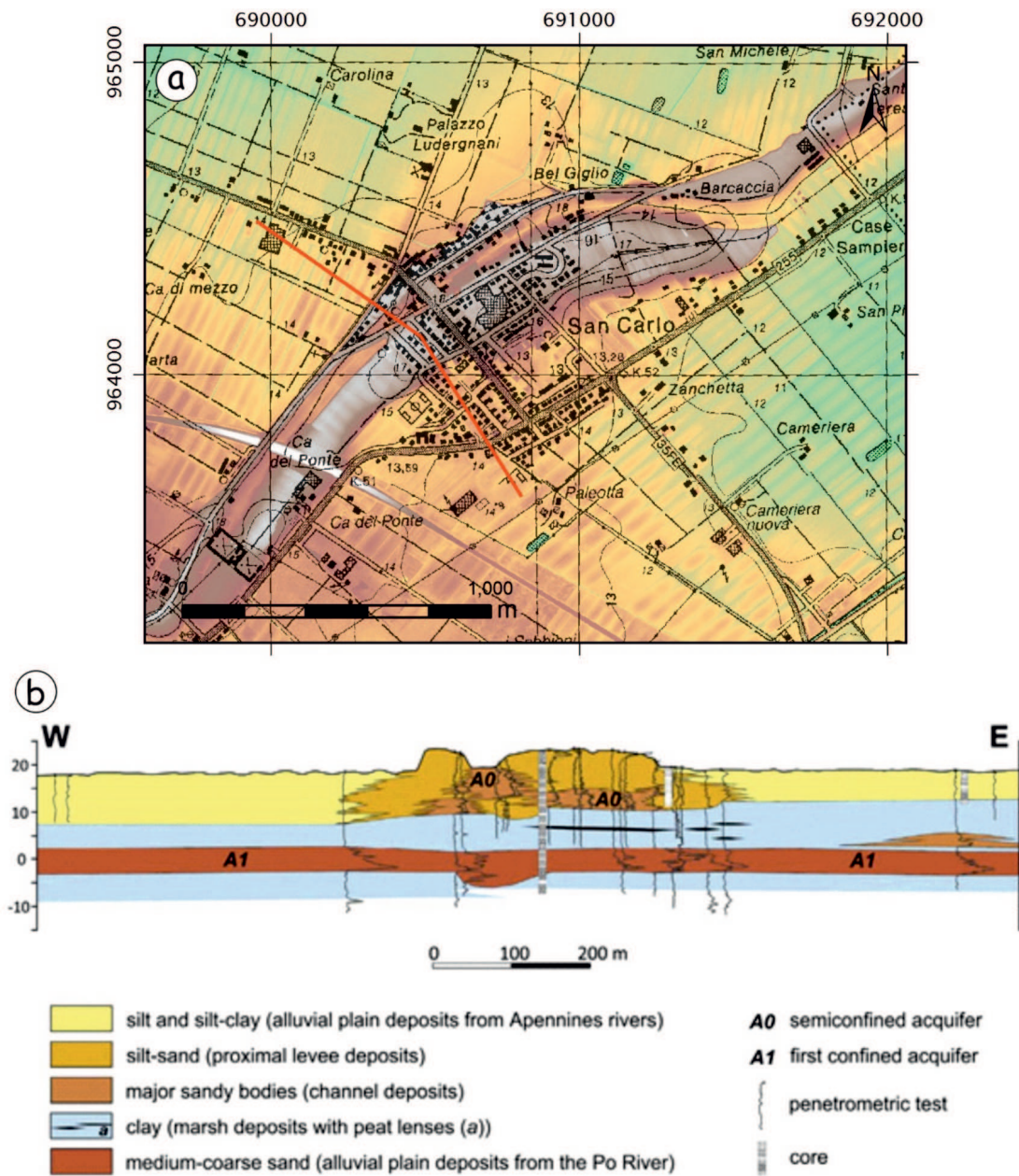


Figure 6.22: a) Trace of a geological profile across San Carlo area. b) Reconstructed geological section based on penetrometric tests and drill cores (from Papathanassiou *et al.*, 2015).

6.4 Quantitative assessment of liquefaction potential

The eastern sector of the Po Plain suffered diffuse and important liquefaction phenomena as a consequence of the May 20, and secondarily the May 29, 2012 earthquakes. The most impressive liquefaction manifestations were documented in a zone 3–4 km-long and 1 km-wide, where the villages of Sant' Agostino, San Carlo and Mirabello are located.

The existing post-earthquake reports and the availability of geotechnical data provided by in-situ tests consist the basic ingredients for a computation of the liquefaction potential parameters within this zone. In particular, the Liquefaction Potential Index (LPI) and Liquefaction Severity Number (LSN) indexes were evaluated and then correlated by considering liquefaction phenomena either observed on site or not. Thus, the existing classifications of the LPI and LSN were evaluated and compared with the observed liquefaction-induced deformations. The latter was applied and validated for the first time within a liquefiable area using post-earthquake data, after the development by Tonkin and Taylor (2013). In addition, a preliminary correlation of LPI and LSN indicates a trend that could be useful in future studies for delineating sites likely to liquefaction.

6.4.1 The May 20, 2012 Emilia earthquake: liquefaction-induced deformations

The Po Plain is characterized by the presence of palaeoriverbeds, out-flow channels and fans of the main Apennine streams crossing the area during the Holocene, which mostly controlled the distribution of the observed liquefaction phenomena, as widely discussed in Section 3.1. By taking into account the age and type of the deposits, following the criteria suggested by Youd and Perkins (1978), the susceptibility to liquefaction of the geological units within the investigated area is considered high. Similar scenarios have been generated in comparable alluvial settings, for example in concomitance of the 1990 Luzon Philippines, the 2007 Niigaten Chuetsu-oki Japan and the 2010 Darfield New Zealand (Wotherspoon *et al.*, 2012) earthquakes, showing that this type of geological and geomorphological settings is favorable to earthquake-induced surface ruptures and liquefaction phenomena.

The aims of this study was the computation of the liquefaction potential indexes (LPI and LSN) and the correlation with the concomitant occurrence, or not, of liquefaction phenomena and its observation at the surface, for two selected urban areas: Sant’Agostino and San Carlo, in the eastern epicentral sector, and Mirandola, on the western side (Fig. 6.23). Although the two areas have similar epicentral distances, the former experienced widespread liquefaction phenomena, like sand boils and ground fissures with ejection of silty sand–water mixtures and lateral spreading, while the western epicentral area generally did not, with only few exceptions.

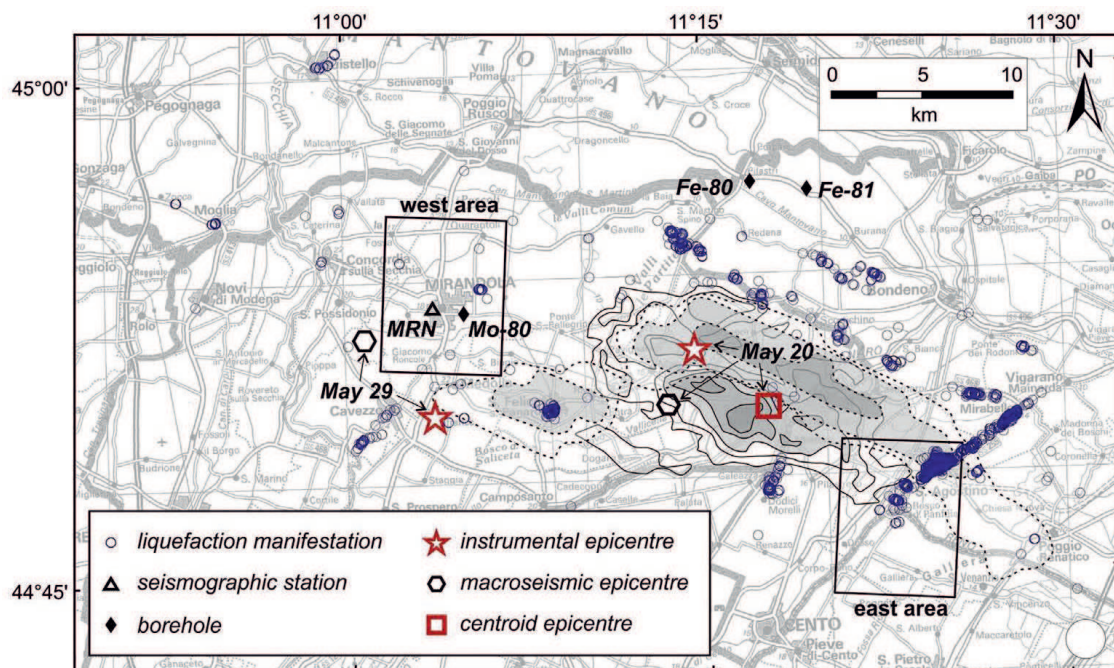


Figure 6.23: Epicentral area showing the liquefaction manifestations observed during post-event field surveys (Caputo and Papathanassiou, 2012; Papathanassiou *et al.*, 2012; Di Manna *et al.*, 2012; Emergeo Working Group, 2013). The stars indicate the instrumental epicenters of the May 20 ($M_w = 6.1$) and May 29 ($M_w = 6.0$) events (Pondrelli *et al.*, 2012; Massa *et al.*, 2013), the hexagons represent the corresponding macroseismic epicenters (Galli *et al.*, 2012), while the square is the surface projection of the slip plane centroid (Ganas *et al.*, 2012; Cesca *et al.*, 2013; Pezzo *et al.*, 2013). Continuous and dashed gray-scale contours represent the slip planes proposed by Ganas *et al.* (2012) and Pezzo *et al.* (2013), respectively. The triangle represents the Mirandola seismographic station (MRN) belonging to the national network, while the rhombs are the boreholes for the aquifers monitoring. The two black boxes indicate the investigated areas represented in Figs. 6.32 and 6.33.

For Sant’Agostino, San Carlo and Mirabello villages (western Ferrara Province), the May 20 main shock triggered locally important damages to lifelines (e.g. broken pipelines; Fig. 6.24a), paved roads (e.g. decametric long cracks with opening up to several cm; Fig.



Figure 6.24: Examples of damages produced by the May 20, 2012 earthquake. a) Broken pipelines. b) Paved roads. c) Buildings with cracking due to differential settlement. d) Lateral spreading (from Papathanassiou *et al.*, 2015).

6.24b) or buildings (e.g. cracking due to differential settlement; Fig. 6.24c) (e.g. Papathanassiou *et al.*, 2012; Emergeo Working Group, 2013). Furthermore, earthquake-induced lateral spreadings were reported in San Carlo and along the whole Sant'Agostino to Mirabello urban alignment (Fig. 6.23), inducing irrecoverable damages (Fig. 6.24d) to houses built at top of an abandoned natural levee. At this regard, the topography of the natural levees though only few meters-higher than the surrounding alluvial plain played a crucial role, synergic with the co-seismic shaking and the liquefaction, in generating the clustering of the observed damage (Di Manna *et al.*, 2012).



Figure 6.25: Examples of large-diameter water wells which locally enhanced the sand ejection during shaking and liquefaction of the sandy aquifer bodies (from Papathanassiou *et al.*, 2015).

A peculiarity of the region is also the presence of numerous large-diameter (ca. 1.5 m) water wells 5–10 m-deep generally connected with the first semi-confined aquifer (A0; Molinari *et al.*, 2007). Accordingly, during the main shock the ejection of large amounts of liquefied silty-sandy material was locally enhanced within courtyards of the residential buildings (Fig. 6.25). This phenomenon generally caused the complete loss of functionality of the wells that sometimes remained completely filled by sand (Papathanassiou *et al.*, 2012), but also induced small size settlement of the nearby residential buildings as a consequence of ground loss (Fig. 6.26).



Figure 6.26: Examples of ground loss due to liquefaction and consequent settlement of the buildings (from Papathanassiou *et al.*, 2015).

Along the Sant' Agostino, San Carlo and Mirabello urban alignment, important ground ruptures tens of meters-long, with opening up to 20–30 cm and vertical offsets between the two blocks of 15–20 cm were also observed in the free field (i.e. affecting ploughed or natural soil; Fig. 6.27a,b). Fractures were commonly aligned parallel to the levee and locally formed overstepping and overlapping sets with a cumulative length of several hundred meters. In most cases, sandy material was ejected through these cracks (Fig. 6.27b). Across one of such fracture systems a 50 m-long and 8 m-deep palaeoseismological trench has been excavated allowing to directly observe and log in detail the stratigraphy of the palaeo-levee as well as the several subvertical dikes and other liquefaction associated features, like palaeoslumps, graben structures and mixed-up sandy-silty layers (Caputo *et al.*, 2012; 2016). The

results of trenching document the occurrence of palaeoliquefaction phenomena likely associated with the 1570 Ferrara earthquake.

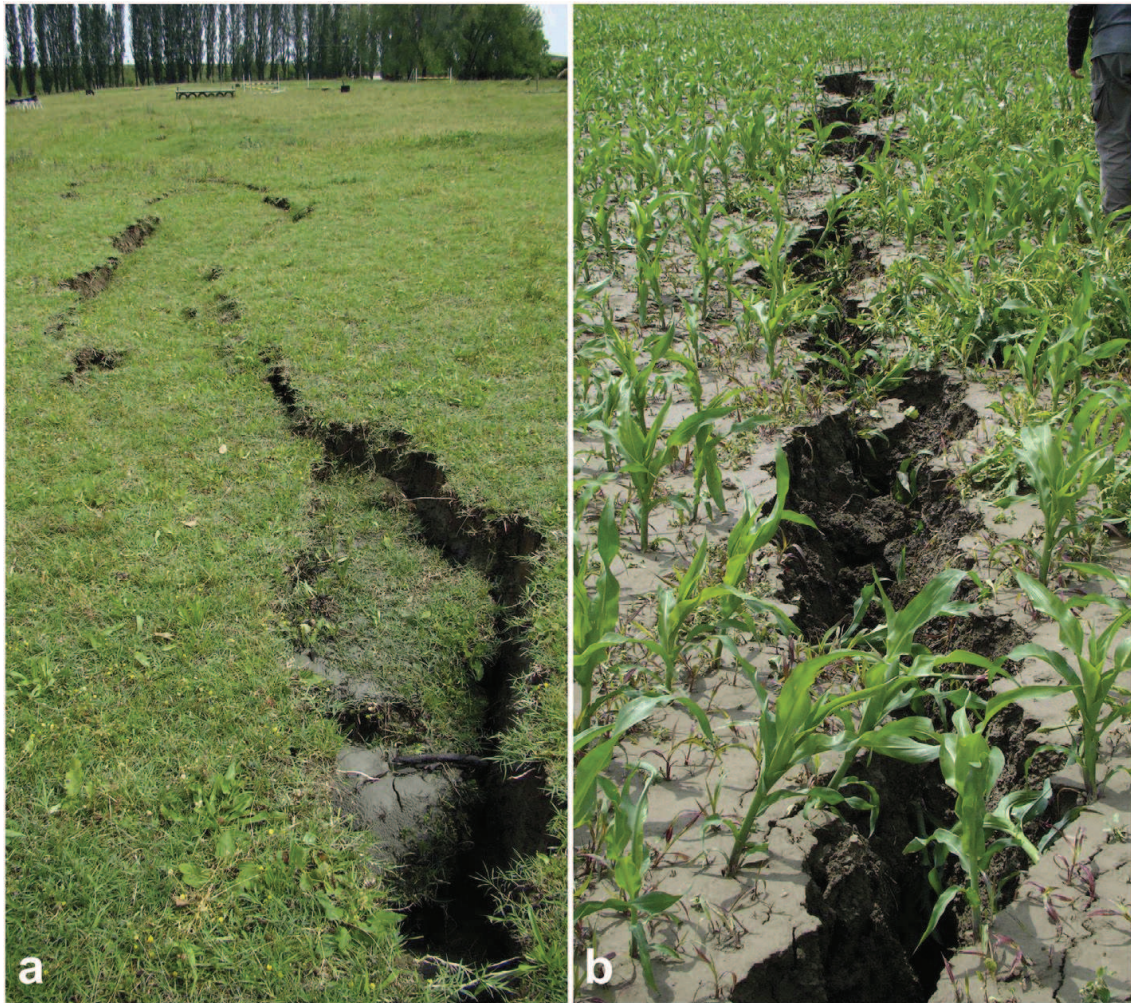


Figure 6.27: Examples of ground ruptures induced by lateral spreading phenomena occurring on top of an abandoned levee between San Carlo and Sant’Agostino. Fractures are several meters-long, arranged in complex overlapping and overstepping sets, characterized by horizontal opening up to 20 cm, sometimes by vertical displacements of 10–15 cm and locally by sand ejection (from Papathanassiou *et al.*, 2015).

Furthermore, buckling phenomena were locally observed in Mirabello at the base of the levee slope (Fig. 6.28), where contractional features formed due to the differential lateral sliding of building moving downslope on an inclined (even with few degrees) liquefied level (e.g. Pizzi *et al.*, 2012). Similar phenomena have also been documented after the Cephalonia, Greece 2014 (Valkaniotis *et al.*, 2014) and Great East Japan 2011 (e.g. Yasuda *et al.*, 2012) earthquakes. In some cases, when liquefied material during its upward migration encountered a top layer which was resistant enough to impede fracturing but not plastic



Figure 6.28: Example of an incipient buckling process affecting the top layer(s) and due to differential horizontal movements triggered by lateral spreading phenomena (from Papatthanassiou *et al.*, 2015).

deformation, say for example a pavement, local bulging structures formed (Fig. 6.29). For the area close to the town of Mirandola (eastern Modena Province), it is noteworthy that though at a similar epicentral distance, only few liquefaction manifestations were reported, including scattered water-sand ejections and liquefaction-induced ground disruptions (Fig. 6.23). Ground loss due to sand ejecta induced a settlement of about 6 cm in a residential house. As concerns the liquefaction surface manifestations that were reported outside of the eastern region of the meizoseismal zone (Sant'Agostino-San Carlo-Mirabello), Di Manna *et al.* (2012) report that in the area of San Felice sul Panaro the most common and frequently observed effects in urban areas were the ejection of sand from water wells. For example, these effects were mapped (e.g. Emergeo Working Group, 2013) in the area between the



Figure 6.29: Examples of bulging phenomena caused by the failed attempt of sand ejection due to the presence of a strong cap layer (from Papathanassiou *et al.*, 2015).

stadium and the railway station. Liquefaction-induced failures have also been reported in the Cavezzo village within and near the main canal while few isolated liquefaction surface evidences were mapped around the Medolla village (Emergeo Working Group, 2013). In addition, liquefaction manifestations were also reported by Di Manna *et al.* (2012) and Emergeo Working Group (2013) to the northwest of Mirabello and near Scortichino (Obici locality), Burana, San Martino Spino, Bondeno where the dominant type of liquefaction-induced ground disruption was reported to be fractures with sand ejection (Fig. 6.23).

6.4.2 Test sites

In order to correlate the liquefaction potential to the observation of liquefaction phenomena on ground surface triggered by the May 20, 2012 Emilia earthquake, the LPI and LSN values were determined for as many as possible in-situ tests carried out in drilling locations of two investigated areas Sant'Agostino and San Carlo, to the east, and Mirandola, to the west. For these two areas several tests were available and the locations of the manifestations were accurately documented by several post-earthquake field reports (Papathanassiou *et al.*, 2012; Crespellani *et al.*, 2012; Fioravante and Giretti, 2012; Emergeo Working Group, 2013; Regione Emilia-Romagna, personal communication).

Although in these post-earthquake reports liquefaction observations are commonly documented at a specific site and associated with point coordinates, the extent of liquefaction of the subsoil is obviously much wider. For this reason were realistically considered liquefaction zones around the observed manifestations following the procedure applied by O'Rourke *et al.* (2014): therefore, all in-situ tests falling within these zones were included in 'liquefied' subset. On the other hand, for the purpose of this analysis, were selected in-situ tests only from areas where effects of liquefaction were surely not observed on ground surface. Tests drilled within 'liquefied' and 'not-liquefied' zones are indicated in Tab. 6.1.

For the aim of this analysis only piezocone penetration (CPTu), seismic cones (SCPTu) and electrical cone penetration tests (CPTe) were considered due to several reasons: i) greater reliability in soil profile interpretation respect to the mechanical one (Lo Presti *et al.*, 2009); ii) guarantee the uniformity of the dataset in terms of measuring intervals of the geotechnical parameters (q_c and f_s , in addition u_2 only for piezocone tests); iii) all the methods devoted to evaluate soil liquefaction are based on piezocone and electrical cone penetration tests.

In order to correlate the numerical results with the observed or not effects of liquefaction on the ground surface in concomitance with the May 20 earthquake, only the test sites for which there were a sure evidence (either positive or negative) of liquefaction-induced ground disruption were selected. Accordingly, 2 CPTe and 47 CPTu and 11 SCPTu most of which were carried out in the months following the earthquake specifically for seismic microzoning purposes were included in the dataset. The selected test locations are shown in

Figs. 6.32 and 6.33, while in Tab. 6.1 relevant information are reported.

n	Area	RER code	Latitude	Longitude	Depth [m]	Water table [m]	PGA [g]	Liquefied zone	LPI	LSN
1	W	184090U053	44°52'02"	11°00'03"	15	4.9	0.19	N	0.2	0
2		184090U054	44°52'01"	11°00'03"	14	4.9	0.19	N	0.3	0
3		184090U055	44°51'35"	11°02'08"	15.5	3.4	0.23	N	1.2	0.6
4		184050U015	44°54'12"	11°02'38"	15	4.2	0.22	N	1.3	0.3
5		184050U016	44°54'13"	11°02'38"	15	4.2	0.22	N	2.7	1.5
6		184050U017	44°54'54"	11°02'39"	17	2.65	0.22	N	1.6	1.2
7		184050U018	44°54'54"	11°02'39"	17	3.45	0.22	N	2.4	1.5
8		184090B003	44°53'19"	11°03'19"	30.5	4.45	0.25	N	3.3	0.8
9		184090U052	44°53'55"	11°03'45"	16	2.5	0.25	N	4.9	2.3
10		184090U051	44°53'55"	11°02'47"	15	2.5	0.25	N	5.5	3.3
11		184090U046	44°53'39"	11°03'59"	18	4.3	0.26	N	5.5	0.4
12		184010E002	44°57'05"	11°04'02"	15	2.2	0.21	N	0.8	0.6
13		184010E001	44°57'06"	11°04'02"	15	2.2	0.21	N	1	0.5
14		184090U050	44°53'30"	11°04'14"	15	3.2	0.27	N	2	1.6
15		184090U049	44°53'31"	11°04'14"	15	3.25	0.27	N	2.4	1.4
16		184090U047	44°53'30"	11°04'15"	15	4.2	0.27	N	5.2	3.2
17		184090U048	44°53'30"	11°04'15"	15	3.7	0.27	N	6.3	3.2
18		184090B004	44°52'47"	11°04'44"	29.5	5.72	0.29	N	1.7	0.2
19		MI_01	44°57'33"	11°05'18"	30	1	0.22	N	16.1	4.8
20		CPTU2	44°53'47"	11°05'44"	16	1.4	0.31	Y	25.7	20.7
21		CPTU1	44°53'47"	11°05'46"	15.5	1.4	0.31	Y	18.9	14.4
22		MI_02	44°53'36"	11°06'44"	22.5	1	0.34	N	6.4	9.7
23		184060U001	44°54'14"	11°06'51"	15	3.8	0.31	N	10.6	5.5
24	E	203010U509	44°47'06"	11°21'06"	35	1.9	0.72	N	13.3	8.7
25		203010U013	44°47'30"	11°22'26"	20	2	0.69	N	18.9	11.7
26		203010U009	44°47'33"	11°22'29"	26	1	0.69	N	20	11.5
27		185130U006	44°48'52"	11°22'47"	40	3	0.73	N	1.5	2.1
28		203010U005	44°47'20"	11°22'47"	15	2.4	0.66	Y	19.1	9.6
29		203010U006	44°47'18"	11°22'49"	26	2.4	0.65	Y	12.6	7.5
30		203010U001	44°47'37"	11°23'16"	30	4	0.65	Y	13.9	16.9
31		203010U002	44°47'40"	11°23'16"	15	4.9	0.65	Y	15.5	17.1
32		185130U505	44°48'13"	11°24'25"	20	5	0.6	Y	9	12.2
33		185130U506	44°48'16"	11°24'29"	20	4.84	0.6	Y	16.6	18.1
34		185130B502	44°48'20"	11°24'29"	31	3	0.6	Y	25.4	25.7
35		185130B995	44°48'15"	11°24'31"	30	2	0.6	Y	8.4	15.1
36		185130U507	44°48'16"	11°24'32"	20	5.16	0.6	Y	13.5	15.2
37		185130B501	44°48'13"	11°24'33"	31	3	0.59	Y	15.6	15.9
38		185130U509	44°48'20"	11°24'36"	20	2.37	0.59	N	4.6	8.9
39		185130U508	44°48'17"	11°24'36"	20	4.22	0.59	Y	8.2	11.2
40		185130B503	44°48'18"	11°24'36"	30	3	0.59	Y	27.6	25.7
41		185130B996	44°48'13"	11°24'37"	30	1.4	0.59	Y	19.5	16.6
42		185130U510	44°48'21"	11°24'41"	20	5.23	0.59	N	6	8.6
43		185130B504	44°48'27"	11°24'43"	24	3	0.59	Y	25.8	23.4
44		185130U511	44°48'23"	11°24'44"	20	4.65	0.59	N	6.6	8.8
45		185130U512	44°48'25"	11°24'50"	20	4.4	0.58	Y	9.7	13.6
46		185130B999	44°48'25"	11°24'51"	30	5.4	0.58	Y	11.9	15.2

47	185130U513	44°48'26"	11°24'52"	20	4.18	0.58	Y	20.3	21
48	185130B998	44°48'26"	11°24'53"	30	4	0.58	Y	14.7	19.7
49	185130U514	44°48'26"	11°24'56"	20	4.55	0.58	Y	19.7	20.3
50	185130U022	44°48'40"	11°24'58"	30	1.8	0.58	N	10.7	7
51	185140U005	44°48'31"	11°25'15"	31	4.9	0.56	N	0	0
52	185140B001	44°48'17"	11°25'24"	32	2	0.54	N	8.9	16.5
53	185140U003	44°48'19"	11°25'27"	40	3.6	0.54	N	0.8	0.9
54	185140U004	44°48'20"	11°25'29"	40	3.3	0.54	N	0.2	0.8
55	185140U002	44°48'08"	11°25'35"	30	2.3	0.53	N	9.9	7.8
56	203020U099	44°47'51"	11°25'47"	36	1.8	0.51	N	7.9	6.9
57	203020U098	44°47'52"	11°25'50"	39.5	1.9	0.5	N	0.6	1.7
58	203020U097	44°47'54"	11°25'54"	39	2.05	0.5	N	4.6	10.5
59	203020U096	44°47'57"	11°26'13"	39	1.6	0.48	Y	6.9	13.9
60	203020U095	44°47'58"	11°26'13"	39	4.5	0.48	Y	9	13.6

Table 6.1: LPI and LSN calculated for the selected boreholes. W corresponds to Mirandola area, while E refers to San Carlo and Sant'Agostino villages. The test code, according to the Emilia-Romagna archival standards (<http://ambiente.re-gione.emilia-romagna.it/geologia/cartografia/webgis-banchedati/>), is reported in the second column. Water table is in meters below ground surface. Peak ground acceleration (PGA) as percentage of gravity. Test sites drilled within 'liquefied' (Y) and 'not-liquefied' (N) zones are indicated.

For each site, was obtained a simplified stratigraphy of the subsoil based on the interpretation of recorded values of tip resistance, sleeve friction ratio and pore pressure to a soil type behavior index (I_c) vertical profile. The classification of soil units follows the CPT soil behavior type chart, proposed by Robertson *et al.* (1986), while for boreholes deeper than 30 m was considered the normalized chart proposed by Robertson (1990). Therefore, rather than a purely lithological meaning, the obtained units bear a geotechnical information such as grain-size distribution. In particular, the units referred to as i) sands, ii) sand mixtures, iii) silt mixtures and vi) clays, respectively correspond to i) clean sand to silty sand, ii) silty sand to sandy silt, iii) clayey silt to silty clay and vi) silty clay to clay, soil units.

As concerns the water level depth necessary to calculate the pore pressure profile, the values measured during the drilling were taken into account. All these quantitative analyses were performed using the CLiq software (ver. 1.7.6.34; www.geologismiki.gr).

In Fig. 6.30, two representative lithostratigraphic profiles of the investigated areas documenting the lateral variability which characterizes the subsoil from the decameter to the kilometer scale are given. Indeed, sandy and/or silty sandy layers could vary both in depth

from the surface as well as in thickness, merging with other layers or laterally disappearing. Similar geological sections were presented by Calabrese *et al.* (2012).

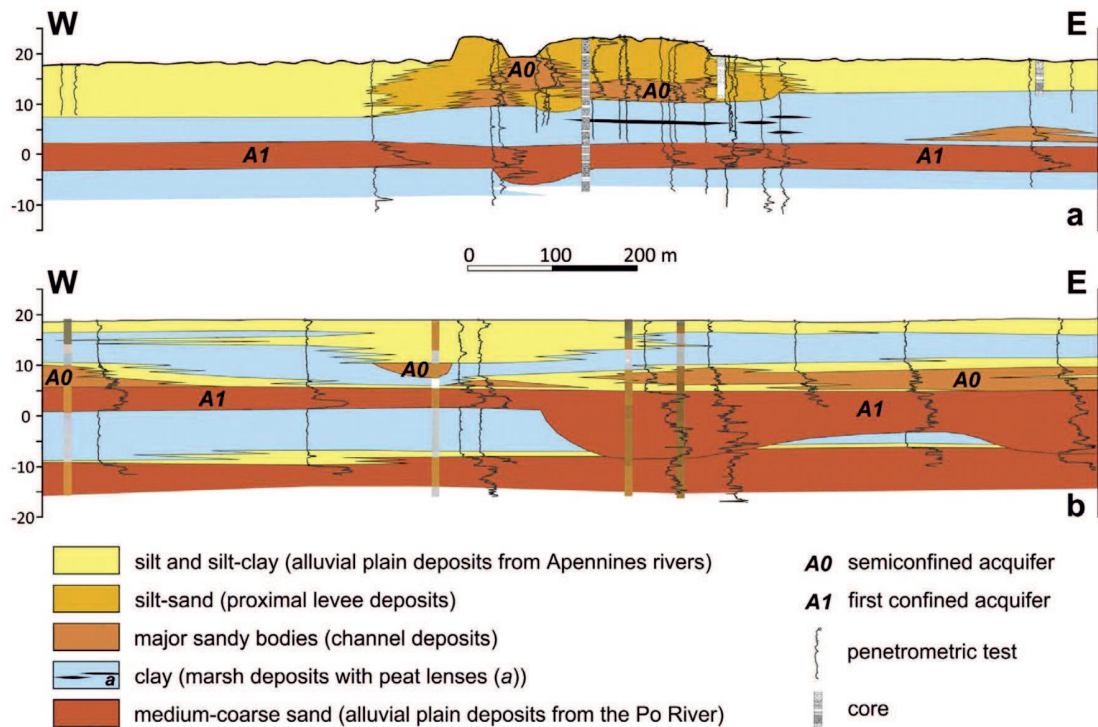


Figure 6.30: Representative sections across San Carlo (a) and Mirandola (b) areas based on penetrometric tests and cores. Note the strong lateral lithological variations occurring in the shallow subsoil and the different distribution of the sandy bodies in the two investigated areas. Legend: 1) silt and silt-clay (alluvial plain deposits from Apennine rivers); 2) silt-sand (proximal levee deposits); 3) major sandy bodies (channel deposits); 4) clay (marsh deposits) with peat lenses (a); 5) medium-coarse sand (alluvial plain deposits of Po River). A0 and A1 indicate the semi-confined and the first confined aquifers, respectively (Rapti-Caputo and Martinelli, 2009; Molinari *et al.*, 2007).

6.4.3 Site specific acceleration

For the quantitative assessment of the liquefaction potential, the ground acceleration at the site represents a fundamental parameter. As far as the two study areas fall within the epicentral zone (i.e. near field) where a strong gradient generally occurs due to geometric and anelastic attenuations, it would be not preferred to assume a unique acceleration value for all the dataset. Indeed, the distances for the selected locations from the instrumental epicenter fall in the range 10-17 km for the Mirandola area and 12-16 km for the Sant'Agostino area (Fig. 6.23).

In order to obtain ground acceleration value to be used in the analysis in correspondence of each geotechnical measurement at site, a ground motion probability equation (GMPE) was used. Among the several such empirical relations proposed in the literature, the empirical approach proposed by Bindi *et al.* (2011) was preferred because i) it is specifically based on the Italian strong motion database ITACA (Luzi *et al.*, 2008; Pacor *et al.*, 2011; <http://itaca.mi.ingv.it>), ii) it takes into account the style of faulting and iii) it is certainly the most updated one for Italy. The validity of the applied GMPE is in the moment magnitude range 4.0-6.9 and for distances up to 200 km, therefore including our dataset parameters.

The estimated PGA by the Bindi *et al.* (2011) GMPE represents the geometrical mean of the two horizontal components. In order to calculate the PGA values at each site, a scalar moment magnitude of 6.1 (Pondrelli *et al.*, 2012) was used and the hypocentral depth was selected at 7.0 km (Cesca *et al.*, 2013). To estimate the Joyner-Boore distance (RJB) required for calculating the PGA by GMPE, an empirical relationship between RJB and the epicentral distance was used (Montaldo *et al.*, 2005). Additionally, whereas all GMPEs including the one used for this analysis (Bindi *et al.*, 2011) assume a radial coseismic rupture and hence a radial distribution of seismic energy (i.e. ground acceleration). In contrast, the May 20 event was characterized by a strong directivity towards ESE of the rupture propagation (Ganas *et al.*, 2012; Pezzo *et al.*, 2013). Accordingly, for the epicentral location was used the vertical projection of the slip plane centroid (Cesca *et al.*, 2013; Cesca *et al.*, 2013; Ganas *et al.*, 2012; Pezzo *et al.*, 2013), which assured a more realistic distribution of the acceleration especially in the near-field.

Based on the information on the shear wave velocity in the first 30 m obtained from the available SCPTus and following the EC8 (CEN, 2003), all sites were characterized as class C soil (i.e. with a V_{S30} in the range 180-360 m/s). The calculated acceleration values for each site by Bindi *et al.*'s (2011) GMPE are listed in Tab. 6.1 and plotted in Fig. 6.31.

The two horizontal accelerations recorded at the Mirandola station (MRN) during the May 20 event, which represents the only available value in the epicentral area, perfectly fit the value estimated by using the Bindi *et al.* (2011) GMPE (Fig. 6.31). This measurement is the only one carried out in the near-field (i.e. within a distance comparable to the fault's

dimensions); nevertheless, several other stations located in the far-field, which have recorded the May 20 event show PGA values falling within the standard deviation curves of the used GMPE for class C. At this regard, it should also be noted that a systematic revision of the soil classification in correspondence of the stations of the Italian accelerometric network is in progress and possible minor mismatches between predicted and measured PGA values could disappear if considering, for example, a class B GMPE curve.

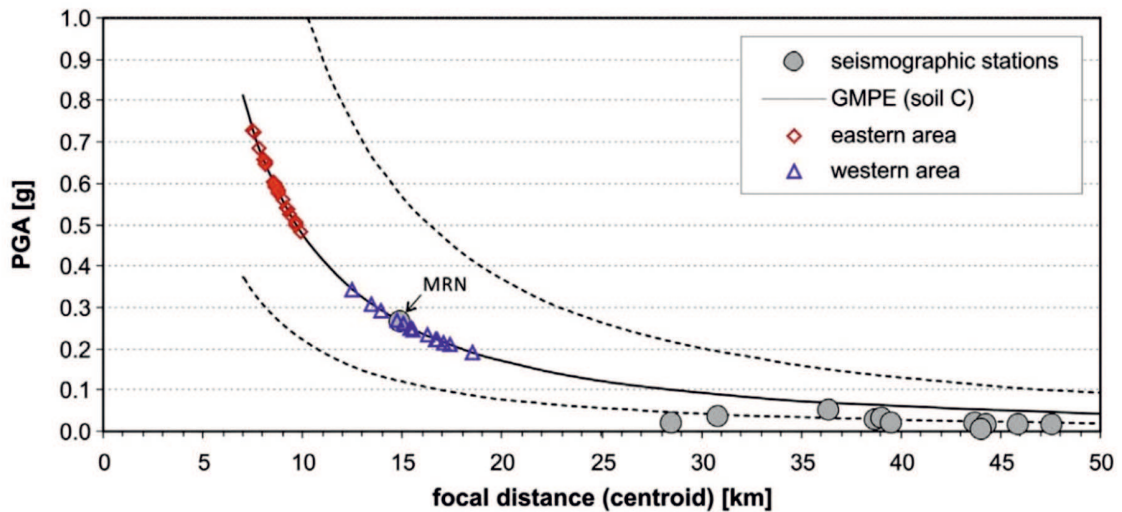


Figure 6.31: The PGA calculated as a function of the focal distance based on the GMPE proposed by Bindi *et al.* (2011); dashed curves are the $\pm \sigma$. Rhombs and triangles represent the test sites of the eastern and western epicentral areas, respectively. The circles indicate the PGA value measured during the May 20 main shock at the several stations belonging to the Italian seismographic network (itaca.mi.ingv.it). The record at the Mirandola station (MRN), which is the only one in the seismic near-field, is in perfect agreement with the predicted value.

6.4.4 Evaluating the liquefaction potential

In order to evaluate the liquefaction potential of a soil, the factor of safety against liquefaction (F_s) should be computed by using the widely applied stress-based approach, the so called ‘simplified procedure’, as widely described in Section 4.2.3. For the purpose of this study, for the evaluation of factor of safety, was applied the Idriss and Boulanger (2008) stress-based approach, which compares the earthquake-induced cyclic stress ratio (CSR) with the cyclic resistance ratio of the soil (CRR). Additionally in order to take into account the fines content in the absence of site-specific laboratory test data, the Robertson and Wride (1998) approach

was followed. Both approaches were applied in order to maintain the consistency with the procedure followed by Tonkin and Taylor (2013) for the development of LSN methodology (see Section 4.2.4). As above mentioned, the depth groundwater level as input for the calculation of the factor of safety was obtained from the drilling studies and is listed in Tab. 6.1.

For the computation of the liquefaction potential on the vertical soil column composed of multiple layers, the Liquefaction Potential Index (LPI) proposed by Iwasaki et al. (1978) was used (see Section 4.2.4). The LPI value has the capability of characterizing liquefaction potential of a soil column of 20 m from the ground surface. In addition, according to Toprak and Holzer (2003) the ‘simplified procedure’ predicts what will happen to a soil element whereas the LPI predicts the performance of the whole soil column and the consequences of liquefaction at the ground surface.

Papathanassiou (2008) stated that the advantage of LPI is that it quantifies the likelihood of liquefaction at the site, by providing a unique value for the entire soil column instead of several factors of safety (one for each layer) and accordingly, assesses the spatial probability of liquefaction potential through the compilation of liquefaction hazard maps. Several similar thematic maps were published, e.g. among others by Ansary and Rashid (2000), Holzer *et al.* (2002), Sonmez (2003), Sonmez and Gokceoglu (2005), Koyuncu and Ulusay (2004), Ulusay and Kuru (2004), Papathanassiou *et al.* (2005), Hayati and Andrus (2008), Juang and Li (2007), Lenz and Baise (2007), Chung and Rogers (2011) and Dixit *et al.* (2012). Furthermore, as mentioned above, Tonkin and Taylor (2013) have recently developed a new approach for assessing the type of damaging effects of shallow liquefaction on structures (LSN). It is worth mentioning that both methods require numerical information provided by insitu tests, though the former method (LPI) was formulated based on values obtained from SPT (Standard Penetration Test), while the latter (LSN) by data provided by CPT. Both LPI and LSN methods were used for mapping the liquefaction potential for a comparison.

6.4.5 Comparison of LPI and LSN values

In order to correlate the liquefaction potential to the observation of liquefaction phenomena on ground surface triggered by the May 20, 2012 Emilia earthquake, the LPI and LSN values were determined for as many as possible in-situ tests carried out in drilling locations of two investigated areas Sant'Agostino and San Carlo, to the east, and Mirandola, to the west. For these two areas several tests were available and the locations of the manifestations were accurately documented by several post-earthquake field reports (Papathanassiou *et al.*, 2012; Emergeo Working Group, 2013; Regione Emilia-Romagna, personal communication).

Although in these post-earthquake reports liquefaction observations are commonly documented at a specific site and associated with point coordinates, the extent of liquefaction of the subsoil is obviously much wider. For this reason were realistically considered liquefaction zones around the observed manifestations following the procedure applied by O'Rourke *et al.* (2014): therefore, all in-situ tests falling within these zones were included in 'liquefied' subset. On the other hand, for the purpose of this analysis, were selected in-situ tests only from areas where effects of liquefaction were surely not observed on ground surface. Tests drilled within 'liquefied' and 'not-liquefied' zones are indicated in Tab. 6.1.

In summary, a total of 60 in-situ were selected (23 and 37 in the western and eastern study areas, respectively) of which 23 drilled in 'liquefied' zones and 37 in 'non-liquefied' zones (Tab. 6.1). In Figs. 6.32 and 6.33 are represented the maps of the two investigated areas with the obtained LPI and LSN values, respectively, as well as the 'liquefied' zones.

For the 'liquefied' zones, the values of the LPI range from 6.9 to 27.6 and the values of the LSN from 7.5 to 25.7 (Tab. 6.1). In contrast, for the 'non-liquefied' zones the values are commonly smaller than 10 for both LPI and LSN, with only few exceptions.

As above mentioned, the obtained values of the LSN were separated in two subsets based on their correlation with 'liquefied' or 'not-liquefied' zones as observed in the field after the earthquake. Their statistical distribution is graphically shown in Fig. 6.34a. The obtained results are in good agreement with the classification proposed by Tonkin and Taylor (2013), which propose a threshold value of 10. Indeed, in the 'liquefied' and 'non-liquefied' subsets the 77.3% and 83.3% of the data have a value respectively greater and smaller than

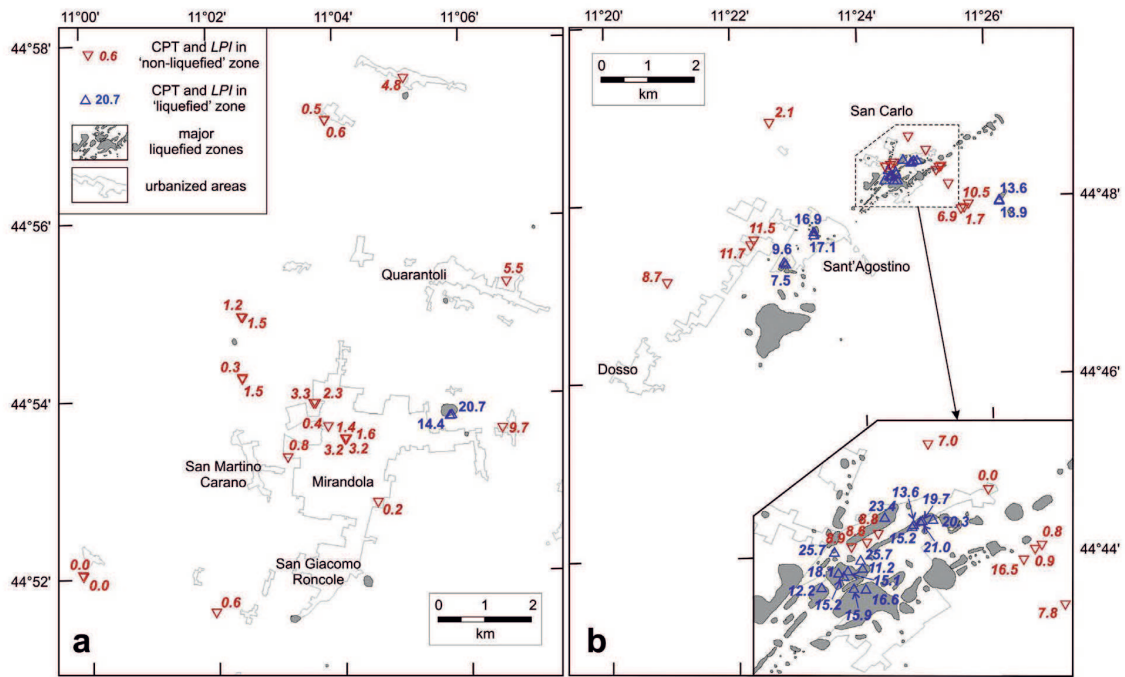


Figure 6.32: The LPI values calculated for the two investigated epicentral areas of Mirandola (a) and Sant'Agostino (b). See Fig. 6.23 for locations.

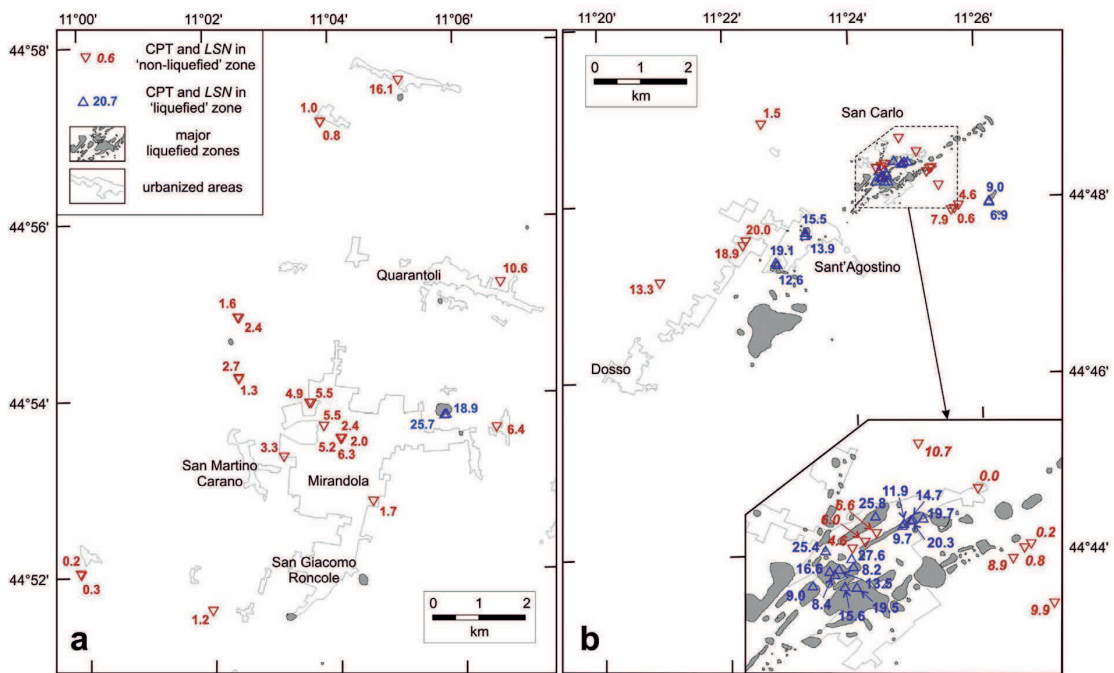


Figure 6.33: The LSN values calculated for the two investigated epicentral areas of Mirandola (a) and Sant'Agostino (b). See Fig. 6.23 for locations.

the threshold of 10 (Fig. 6.34a).

As concerns the statistical distribution of LPI (Fig. 6.34b), several threshold values have been proposed in the literature for separating potentially liquefiable conditions from not

liquefiable ones. For example the value of 5 as proposed by Iwasaki *et al.* (1978), Toprak and Holzer (2003) and Sonmez (2003) does not justify the observed results as far as 36.2% of the ‘non-liquefied’ sites have an LPI greater than 5. In contrast, assuming a threshold of LPI = 13 or 14 as proposed by Lee *et al.* (2004) and Papathanassiou (2008), respectively, almost all ‘non-liquefied’ sites are characterized by smaller calculated values (97.3%). Moreover, 86.4% and 72.8% of the in-situ tests drilled where liquefaction-induced surface evidences were reported provides and LPI value which is higher than the threshold of Lee *et al.* (2004) and Papathanassiou (2008), respectively.

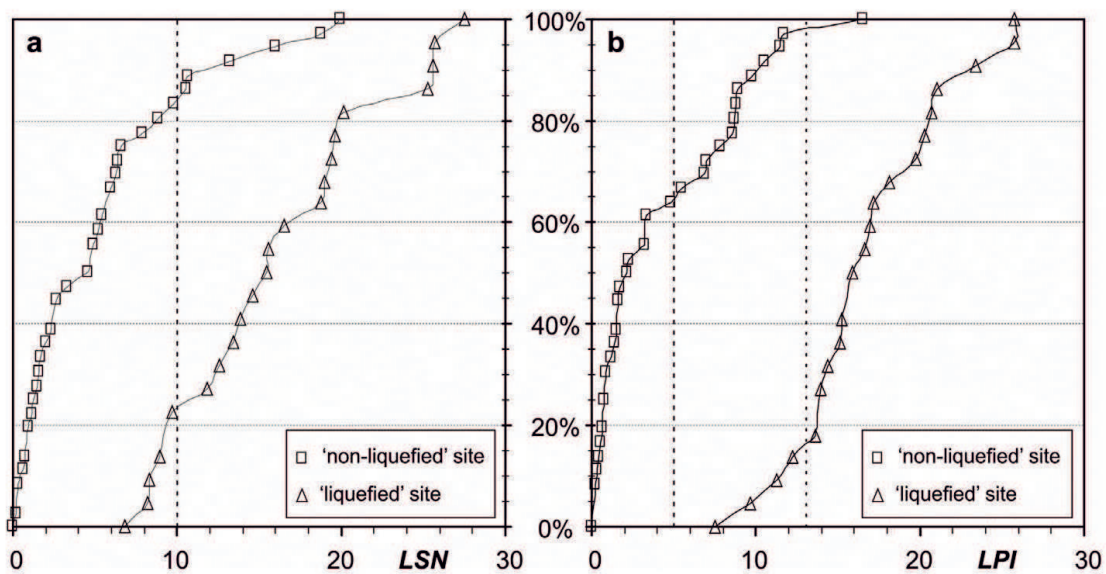


Figure 6.34: Cumulative distribution of the LSN (a) and LPI (b) within the investigated areas. Squares and triangles correspond to penetration tests drilled in ‘non-liquefied’ and ‘liquefied’ zones, respectively, as observed in the field after the earthquake. The vertical dashed lines represent the different thresholds discussed in the text.

Moreover, by plotting the computed values of LPI versus LSN for each site, were also analyzed their correlation with evidence or not of liquefaction-induced ground disruptions (Fig. 6.35). For reference, in the figure are also reported the LPI threshold values equal to 5 (proposed by Iwasaki *et al.*, 1978; Toprak and Holzer, 2003; Sonmez, 2003), 13 (proposed by Lee *et al.*, 2004) and 14 (proposed by Papathanassiou, 2008), as well as the LSN threshold value equal to 10 as it was proposed by Tonkin and Taylor (2013). Based on the observed field evidence of liquefaction-induced phenomena on ground surface and by taking into account the combinations of LPI-LSN values, four classes could be recognized in the

graph (Fig. 6.35): ‘almost no liquefaction effects are observed on ground surface’ (class-I), ‘few liquefaction effects are observed on ground surface’ (class-II), ‘effects of liquefaction are likely observed on ground surface’ (class-III) and ‘effects of liquefaction are very likely observed on ground surface’ (class-IV). The proposed classification, arising from the combination of LPI and LSN values, could be interpreted as the tendency of a soil in terms of co-seismic behavior instead of applying LPI or LSN approaches alone.

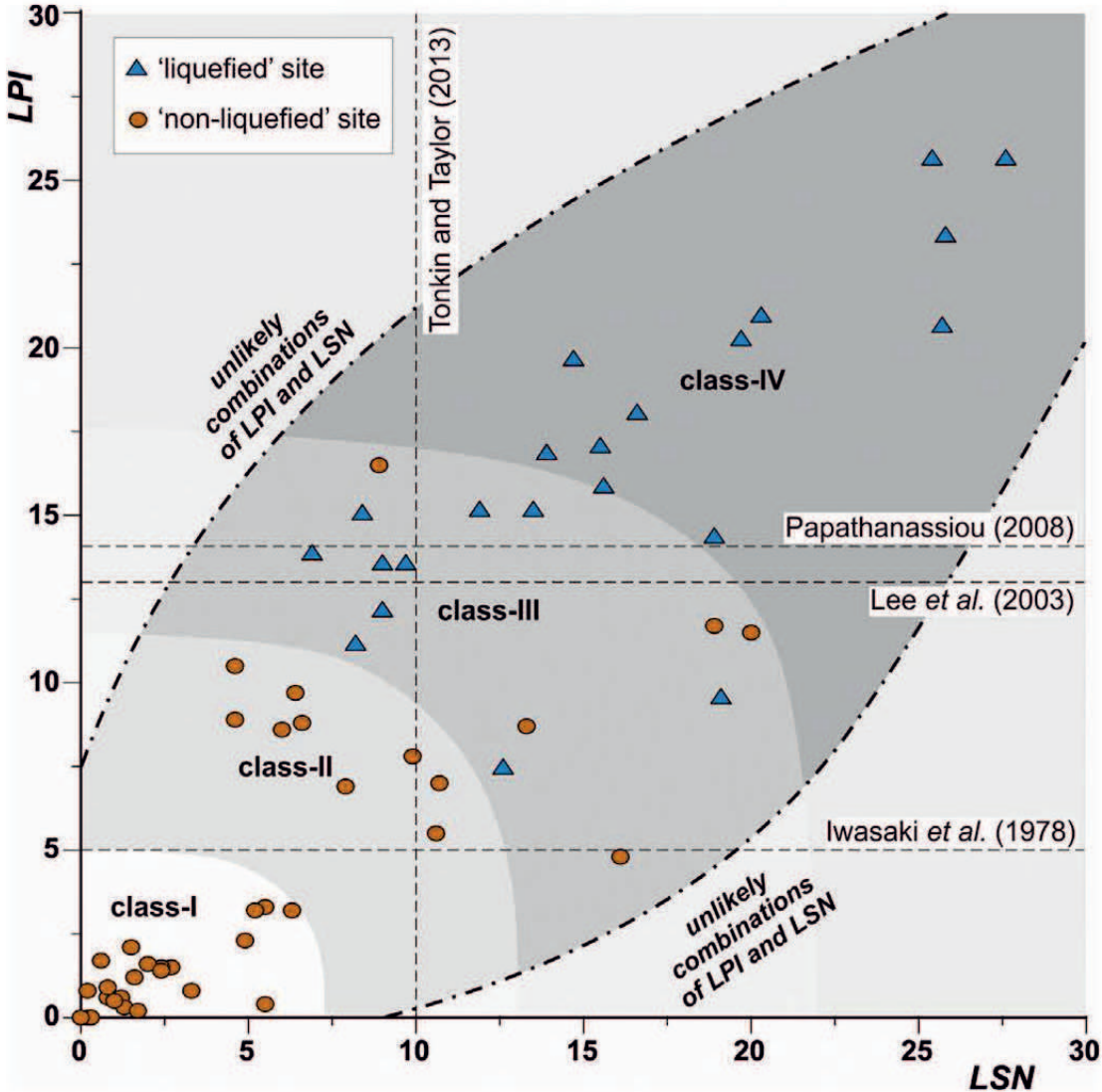


Figure 6.35: Correlation between LPI and LSN values for all the investigated sites. The dashed lines indicate the threshold criteria proposed by the different authors as discussed in the text. The four gray scale areas tentatively separate LPI–LSN conditions associated with liquefaction evidence observed on ground surface: class-I: ‘almost no’, class-II: ‘few’, class-III: ‘likely’ and class-IV: ‘very likely’.

Part IV

Summary

Chapter 7

Conclusions

The major aim of this research project was the study of the shallow subsurface of the central sector of the Ferrara Arc through a multidisciplinary approach, in order to emphasize its recent tectonic activity. Improve the knowledge of the geological and geophysical properties of the shallow subsoil is fundamental for mitigate the seismic hazard, as they play a key role in controlling the occurrence of coseismic effects and consequently the earthquake damage pattern. This issue was addressed through the application of different geological, geotechnical and geophysical strategies, thus concretising in the four case studies discussed in Chapter 6. In the following are summarized the major outcomes for each of the above mentioned case studies. Additionally, some considerations about the improvements and possible future works are reported.

7.1 Geophysical pseudo-2D sections

The investigated area for this study is the eastern sector of the Po Plain and in particular the central sector of the Ferrara Arc, which is one of the major arcs, consisting of blind, north-verging thrusts and folds, which represent the external Northern Apennines front. Due to the combination of fast subsidence-sedimentary rates and conversely low tectonic ones, the thrusts below the Po Plain are blind. Moreover, the strong variable thickness of the Quaternary sequence from several hundreds to few tens of meters in correspondence of the growing anticlines; e.g. Mirandola, Casaglia, Argenta reflects the influence of the complex evolution

of the blind thrusts belonging to the Ferrara Arc. In order to investigate the shallow subsurface and emphasized possible lateral changes, in terms of lithological and thus geophysical properties variations, a geophysical surveys along a profile running from Cento to Bondeno (western Ferrara Province), ca. 27 km-long and oriented SSW-NNE almost perpendicular to the regional trend of the buried structures, were carried out. The investigation was based on seismic techniques, exploiting the ambient seismic noise (i.e. ESAC and HVSR).

Based on numerous 1D measurements carried out along the profiles it was possible to reconstruct pseudo-2D sections. It was thus possible to highlight the recent tectonic activity of buried structures underlying this sector of the Po Plain by means of low-cost geophysical surveys (no expensive equipment nor large teams). In fact, assuming that the Vs pattern and the fundamental resonance frequency variations are determined by lateral lithological variations, the reconstructed pseudo-2D sections document the occurrence of buried anticline structures in correspondence of the condensed stratigraphic sections. This is confirmed by the 'constrained' inversion of the HVSR curves, which allows to correlate the observed frequency(ies) peaks to some major stratigraphic unconformities.

In particular, it was recognized a shallow resonant interface located between 90-120 m b.g.s. that can be considered as a pseudo-bedrock (i.e. Vs between 500 to 600 m/s), while in correspondance of two growing anticlinal structures (i.e. Mirandola and Casaglia anticlines), where the stratigraphic sequence is 'condensed', the fundamental resonance frequency peak pertains to a resonance interface located between 100 to 130 m b.g.s., that in this case can be considered as the seismic bedrock in its strict definition (i.e. Vs \geq 800 m/s).

From the geological point of view, the inferred depth of the major impedance contrast(s) is consistent with that of the other geophysical tests and the available information about the subsurface stratigraphy. As a final consideration, the comparison between the results described and discussed in Sections 6.1.1 and the available geological information suggests that the documented shallow stratigraphic features can be directly associated with the deep ongoing tectonic activity of the blind thrusts throughout the Quaternary.

7.2 Tectonic deformation *versus* site effects

In this work was documented how widespread liquefaction phenomena, induced by seismic shaking affecting recent clastic and saturated deposits, can strongly influence the local elevations even completely reverse the large-scale tectonic signal (i.e. from uplift to absolute subsidence). The importance of this result resides in the fact that geological and seismotectonic conditions characterizing the Emilia 2012 epicentral area occur in many other regions worldwide. Indeed, the outcomes of this work highlight how important is a good knowledge of the geological and geotechnical characteristics, and thus of the criticalities, of the shallow subsurface. For practical reasons the benchmarks for high precision levelling (HPL) are located along major road axes, that in alluvial plains, commonly run on top of artificial embankments or natural levees. In case of moderate-to-strong seismic shaking, such earthworks and sedimentary bodies easily undergo diffuse settling and liquefaction. If no alternative siting is available for HPL lines, network planners should be aware of the intrinsic risk of ‘loosening’ some of the benchmarks. Strategic precautions could be the positioning of a (much) denser network or the use of more stable installation techniques, such as connecting the benchmark to a rod driven below the liquefaction depth. In the former case, the chance of preserving correct measurements along the line increases, while using a deeper foundation of selected benchmarks could avoid the effects of liquefaction which are potentially devastating for HPL networks, but are largely limited to the first 10-15 m-depth.

7.3 Seismic microzoning of the Sant’Agostino Municipality

In order to better address the reconstruction after the May 2012 seismic sequence, and to favor a correct urban planning by the local administrations, the seismic microzoning study realized in the frame of this research project is of utmost importance.

The new insights provided by the seismic microzoning study, allow to subdivide the municipal territory into three areas characterized by different hazard in case of future seismic events, according to the liquefaction susceptibility of the shallow deposits (down to the first 20 m-depth), which obviously reflects the 3D distribution of the fluvial sandy bodies.

The central-southern sector of the municipality, over an area elongated in a NNE-SSW direction including almost all the urbanized areas, is characterized by saturated channel sediments deposited by the old Reno River from ca. 1450 to 1795. This sandy bodies show high LPI values, in some cases greater than 10, thus reflecting a high liquefaction hazard. In the Amplification Factors and Liquefaction Hazard Map this area are classified as LQ1. Moving away from palaeo-riverbed, the liquefaction hazard is slightly lower in the crevasse splays deposits due to reduced thickness of the liquefiable sandy bodies and to the lower topographic gradients.

The analysis of the available geognostic surveys revealed that the central-western and southern portions of the municipality are characterized by the presence of thick sandy bodies at depth greater than 20 m b.g.s. These sediments were deposited by old apenninic riverbeds active during the late phase of the last glacial maximum (i.e. < 15-18 ka). These areas are characterized by low LPI values, reflecting an insignificant to low liquefaction hazard mainly due to a great lithostatic load, which prevent the occurrence of surface liquefaction manifestations but does not inhibit the occurrence of liquefaction in the subsurface. This occurrence should be however carefully considered in case of tall buildings and/or deep foundations.

The northern and western sectors are topographically depressed with respect to the surroundings and are characterized by the absence of important sandy bodies in the first 20 m depth. Therefore, these areas show an insignificant liquefaction hazard but, as the above described areas, are susceptible to ground motion amplification.

As a final comment, some consideration between urban development and liquefaction susceptibility. Within the study area, the urban development and the occurrence of saturated sandy bodies prone to liquefaction seems to be strictly connected. This relation is not by chance and it affects most of the villages and historical centers of the Po Plain, whereas the environmental conditions had influenced both the distribution of the liquefiable sandy bodies and the urban development. The low morphological gradients and the evolution of 'suspended' riverbeds, characterizing the alluvial plain, make the water drainage very difficult, particularly in correspondence of the most subsiding areas. The morphologically depressed

areas, characterized by fine sediments (i.e., clay and peats), have poor geotechnical properties, therefore, the historical distribution of wetlands and marshes had impeded the urban and agricultural development. Conversely, the palaeo-levees are raised with respect to the surrounding flat countryside, thus avoiding flooding due to overflowing of the rivers or heavy rainfalls, and these sandy bodies are characterized by excellent geotechnical properties (in static conditions) for the construction of buildings and roads. The combination of these factors thus favored the development of urban centers above the levees sandy bodies, whereby modern settlements evolved around the old ones and most of the existing roads run through the historical paths of the palaeo-rivers. Therefore, this critical condition persists even today representing a serious problem as highlighted in occasion of the 20 May 2012 earthquake, that triggered extensive liquefaction induced surface manifestations and structural damages. Moreover, since the crests of the palaeo-levees are up to 5 m higher than the surrounding interfluvial areas, high topographic gradients locally exist and, in case of widespread liquefaction, this setting may play a key role in the lateral spreading phenomena.

7.4 Quantitative assessment of liquefaction potential

The 20th May, 2012 earthquake that occurred in Emilia Romagna, northern Italy triggered widespread liquefaction phenomena in the epicentral area. The most impressive liquefaction surface evidences were documented in a zone including the urban areas of Sant'Agostino, San Carlo and Mirabello. Few weeks after the event, several boreholes with in-situ tests were drilled in the epicentral area providing crucial information regarding the geotechnical characteristics of the subsoil layers. This information has been systematically collected and analyzed in order to evaluate the liquefaction potential in these sites by computing the LPI and LSN values. Initially, the liquefaction potential of the soil layers encountered in these boreholes, defined as factor of safety, was evaluated using the Idriss and Boulanger (2008) stress-based approach, while the estimation of fines content was achieved by applying Robertson and Wride (1998) method. Afterwards, since field observations of liquefaction-induced failures exist and data provided by CPTu and SCPTu are available, the outcome of the evaluation of liquefaction potential parameters, e.g. LPI and LSN, has been correlated

to the observation or not of effects of liquefaction on ground surface and compared with the existing relevant classifications. It is thus believed that the outcome of this comparison could provide a useful feedback regarding the LPI and, for the first time, of the LSN approaches. From the comparison, it is possible to conclude that the computed LSN values are in agreement with the proposed classification of Tonkin and Taylor (2013). However, taking into account the amount of ejecta observed, it would be expected that the LSN values in ‘liquefied’ zones should be higher. This apparent discrepancy may be explained by the fact that the upward moving of liquefied sandy material was facilitated by the presence of wells in almost every courtyard of San Carlo. Without the existence of these wells it is not sure that the same amount of sand material would have been able to penetrate the crust layer and reach the surface. Another possible cause of the large number of liquefaction-induced ground disruption in the eastern investigated area of San Carlo–Sant’Agostino, could be correlated to the fact that the potentially liquefiable sand bodies in the first 5–30 m-depth generally represent semiconfined-to-confined aquifers. The correlation of the computed LPI values with the existing classifications is in agreement with LPI classifications and the relevant threshold values proposed by Lee *et al.* (2004) and Papathanassiou (2008) (13 and 14, respectively). The outcome of this research shows that a threshold value of LPI around 13 or 14 is better to be taken into account instead of 5 for discriminating sites where liquefaction surface evidences should be expected from the ‘non-liquefied’ ones. Moreover, from the correlation of the LSN values with the case of liquefaction-induced ground disruption it is possible to observe that the proposed threshold of 10 fits statistically well the used dataset. In addition, a preliminary correlation of LPI and LSN indicates a trend that could likely improve the outcomes of microzoning studies allowing to better characterize the liquefaction hazard of urban areas.

7.5 Improvements and future works

The seismic passive methods give the opportunity to collect a massive dataset in a short period of time, which in turn, allow to obtain a large number of local 1D shear wave velocity profiles capable of exploring the subsurface down to few hundreds of meters depth. Further,

the fundamental resonance frequencies and the depth to the major impedance contrast of the investigated sites can be obtained. Accordingly, it is possible to carry out a sufficient number of such measurements in order to derive reliable pseudo-2D sections, several kilometers-long, so emphasizing the possible occurrence of lateral shear wave velocity (and amplitude) variations, which will likely reflect the stratigraphic changes and, in the geological context of the Po Plain, provide information about the recent tectonic activity of the blind faults.

As an additional benefit result, the subsurface characterization beyond the traditional 30 m represents a very useful information toward a better urban planning and to a more realistic evaluation of the local site response, especially in view of anticipating new laws that may in the future prescribe to extend this kind of investigations to higher depths.

Among the major coseismic effect induced by the May 2012 Emilia seismic sequence, particularly impressive were the extensive liquefaction manifestations at the surface that caused severe damages to unreinforced masonry and precast industrial buildings within the broader epicentral area; thus, a correct evaluation of the susceptibility to liquefaction is of utmost importance. The results presented in this research project show that the use of both LPI and LSN could likely improve the outcomes of microzoning studies allowing to better characterize the liquefaction hazard of urban areas. In fact, the combination of these values, rather than applying LPI (or LSN) approach alone, could be used for discriminating the tendency of different geological and geotechnical subsoil conditions to generate or not liquefaction surface manifestations.

Part V

References

Bibliography

- Abbate, E., Bortolotti, V., Conti, M., Marcucci, M., Principi, G., Passerini, P., and Treves, B. (1986). Apennines and Alps ophiolites and the evolution of the western Tethys. *Mem. Soc. Geol. It.*, 31:23–44.
- Abeki, N., Punongbayan, R. S., Garcia, D. C., Narag, I. C., Bautista, B. C., Bautista, M. L. P., Banganan, E. L., Tabanlar, R. A., Soneja, D. S., Masaki, K., Maeda, N., and Watanabe, K. (1996). Site response evaluation of metro Manila using microtremor observation. In *Proceedings of the 11th World Conference on Earthquake Engineering*, Acapulco, Mexico.
- Abu-Zeid, N. (2012). Contributo delle indagini geofisiche per la microzonazione sismica del settore occidentale della Provincia di Ferrara. *Il Geologo dell'Emilia Romagna*, 45:13–25.
- Abu-Zeid, N., Bignardi, S., Caputo, R., Mantovani, A., Tarabusi, G., and Santarato, G. (2013). Acquisition of vs profiles across the Casaglia anticline (Ferrara Arc). DPC-INGV-S1 Project, Final Report, pp. 42-46.
- Abu-Zeid, N., Bignardi, S., Caputo, R., Mantovani, A., Tarabusi, G., and Santarato, G. (2014). Shear-wave velocity profiles across the Ferrara Arc: a contribution for assessing the recent activity of blind tectonic structures. In *Proceedings of the 33th Conference of the National Group of Solid Earth Geophysics*, volume 1, pages 117–122.
- AGIP-MINERARIA (1959). Campi gassiferi padani. In *Atti Convegno 'Giacimenti Gassiferi dell'Europa Occidentale'*. Accademia Nazionale dei Lincei.
- Akamatsu, J., Fujita, M., and Nishimura, K. (1992). Vibrational characteristics of microseisms and their applicability to microzoning. *J. Phys. Earth*, 40:137–150.
- Aki, K. (1957). Space and time spectra of stationary stochastic waves, with special reference to microtremors. *Bull. Earth. Res Inst.*, 35:415–456.
- Aki, K. (1964). A note on the use of microseisms in determining the shallow structures of the earth's crust. *Geophys.*, 29:665–666.

- Aki, K. and Richards, P. (2002). *Quantitative Seismology, 2 ed.* University Science Books, 700pp. Sausalito, CA.
- Albarelo, D., Cesi, C., Eulili, V., Guerrini, F., Lunedei, E., Paolucci, E., Pileggi, D., and Puzzilli, L. (2011). The contribution of the ambient vibration prospecting in seismic microzoning: an example from the area damaged by the 26th April 2009 l Aquila (Italy) earthquake. *BGTA*, 52(3):513–538.
- Albarelo, D. and Lunedei, E. (2011). Structure of ambient vibration wavefield in the frequency range of engineering interest ([0.5, 20] hz): insights from numerical modelling. *Near Surface Geophysics*, 9(6):543–599.
- Alfaro, A. F., Gutierrez, T., Sugagna, S., Figueras, X., Goula, L., PujadesAlfaro, A., Gutierrez, F., Sugagna, T., Figueras, S., Goula, X., and Pujades, L. (1997). Measurements of microtremors in Barcelona: A tool for seismic microzonation. In *Proceedings of IAMG1997*. Barcelona, Spain.
- Alvarez, W. (1972). Rotation of the Corsica-Sardinia Microplate. *Nat. phys. sc.*, 235:103–105.
- Amorosi, A. (2008). Delineating aquifer geometry within sequence stratigraphic framework: evidence from Quaternary of the Po River Basin Northern Italy. *GeoActa Special Publication*, 1:1–14. Bologna.
- Amorosi, A., Bruno, L., Rossi, V., Severi, P., and Hajdas, I. (2014). Paleosol architecture of a late Quaternary basin-margin sequence and its implications for high resolution, non-marine sequence stratigraphy. *Glob. Planet. Ch.*, 111:12–25.
- Amorosi, A. and Colalongo, M. (2005). The linkage between alluvial and coeval nearshore marine succession: evidence from the Late Quaternary record of the Po River Plain, Italy. In: *M. Blum and S. Marriott (Eds.) Fluvial Sedimentology, IAS Special Publication*.
- Amorosi, A., Colalongo, M., Fiorini, F., Fusco, F., Pasini, G., Vaiani, S., and Sarti, G. (2004). Palaeogeographic and palaeo-climatic evolution of the Po Plain from 150-ky core records. *Glob. Planet. Ch.*, 40(1-2):55–78.
- Amorosi, A., Colalongo, M., Fusco, F., Pasini, G., and Fiorini, F. (1999). Glacio-eustatic control of continental-shallow marine cyclicity from Late Quaternary deposits of the southeastern Po Plain (Northern Italy). *Quat. Res.*, 52:1–13.
- Amorosi, A. and Farina, M. (1995). Large-scale architecture of a thrust-related alluvial complex from subsurface data: the Quaternary succession of the Po Basin in the Bologna area (northern Italy). *Giornale di Geologia*, 57:3–16.
- Ansal, A., Iyisan, R., and Güllü, H. (2001). Microtremor measurements for the microzonation of Dinar. *Pure Appl. Geophys.*, 158:2525–2541.

- Ansary, M. and Rashid, M. (2000). Generation of liquefaction potential map for Dhaka, Bangladesh. In *Proceedings of the 8th ASCE Specialty Conference On Probabilistic Mechanics and Structural Reliability*. University of Notre Dame, Indiana (USA), July 24-26. Paper n. PMC200-061.
- Ansary, M. A., Yamazaki, F., Fuse, M., and Katayama, T. (1995). Use of microtremors for the estimation of ground vibration characteristics. In *Third international conferences on recent advances in geotechnical earthquake engineering and soil dynamics.*, volume 2. St. Louis, Missouri.
- AQUATER (1976). Elaborazione dei dati geofisici relativi alla Dorsale Ferrarese. Rapporto inedito per ENEL.
- AQUATER (1978). Interpretazione dei dati geofisici delle strutture plioceniche e Quaternarie della Pianura Padana e Veneta. Rapporto inedito per ENEL.
- AQUATER-ENEL (1981). *Elementi di neotettonica del territorio italiano*. Volume speciale, Roma.
- Arai, H., Tokimatsu, K., and Abe, A. (1996). Comparison of local amplifications estimated from microtremor F-K spectrum analysis with earthquake records. In *Proceedings of the 11th World Conference on Earthquake Engineering*. Acapulco, Mexico.
- Argnani, A., Barbacini, G., Bernini, M., Camurri, F., Ghielmi, M., Papani, G., Rizzini, F., Rogledi, S., and Torelli, L. (2003). Gravity tectonics driven by Quaternary uplift in the Northern Apennines: insights from the La Spezia-Reggio Emilia Geo-Transect. *Quat. Int.*, 101(102):13–26.
- Argnani, A. and Frugoni, F. (1997). Foreland deformation in the Central Adriatic and its bearing on the evolution of the Northern Apennines. *Ann. Geophys.*
- Asten, M. W. (1978). Geological control of the three-component spectra of Rayleigh-wave microseisms. *BSSA*, 68(6):1623–1636.
- Asten, M. W. and Henstridge, J. D. (1984). Arrays estimators and the use of microseisms for reconnaissance of sedimentary basins. *Geophys.*, 49(11):1828–1837.
- ASTM (1985). *Classification of Soils for Engineering Purposes: Annual Book of ASTM Standards*. D 2487-83, 04.08, American Society for Testing and Materials, pp. 395- 408.
- Astori, A., Castaldini, D., Burrato, P., and Valensise, G. (2002). Where the Alps meet the Apennines, active tectonics and seismicity of central Po Plain. Progetto SAFE, semestrer meeting, Mantova, 20-23 September.
- Bache, T., Marshall, P., and Young, J. (1986). High-frequency seismic noise characteristics at the four United Kingdom-type arrays. *BSSA*, 76(3):601–616.

- Barchi, M., Landuzzi, A., Minelli, G., and Piali, G. (2001). *Outer Northern Apennines*. In Vai G.B. and Martini I.P. (Eds): *Anatomy of an Orogen: Northern Apennines and Adjacent Mediterranean Basins*. Kluwer Academic Publ., Dordrecht, 215-254.
- Bard, P. (1998). Microtremor measurements: A tool for site effect estimation? In *Proceeding of the Second International Symposium on the Effects of Surface Geology on Seismic Motion*, volume 3, pages 1251–1279. Yokohama, Japan.
- Bartolini, C., Bernini, M., Carloni, G., Costantini, A., Federici, P., Gasperi, G., Lazzarotto, A., Marchetti, G., Mazzanti, R., Rapani, G., Panzini, G., Rau, A., Sandrelli, F., Vercesi, P., Castaldini, D., and Francavilla, F. (1982). Carta neotettonica Appennino Settentrionale. Note illustrative. *Boll. Soc. Geol. It.*, 101:523–549. Roma.
- Begemann, H. K. S. (1965). The friction jacket cone as an aid in determining the soil profile. In *Proceedings of the 6th International Conference on Soil Mechanics and Foundation Engineering*, volume 2, pages 17–20. ICSMFE, Montreal, September 8 - 15.
- Ben-Menahem, A. and Singh, S. (1981). *Seismic Waves and Sources*. Springer-Verlag, New York.
- Bertelli, T. (1872). Osservazioni sui piccolo movimenti dei pendoli in relazione ad alcuni fenomeni meteorologiche. *Bullettino Meteorologico dell'Osservatorio del Collegio Romano*, 101. Roma, Italy.
- Bertotti, G., Capozzi, R., and Picotti, V. (1998). Extension controls Quaternary tectonics, geomorphology and sedimentation of the N-Apennines foothills and adjacent Po Plain (Italy). *Tectonophys.*, 282:291–301.
- Bettig, B., Bard, P., Scherbaum, F., Riepl, J., Cotton, F., Cornou, C., and Hatzfeld, D. (2001). Analysis of dense array noise measurements using the modified spatial auto-correlation method (SPAC). Application to the Grenoble area. *BGTA*, 42(3-4):281–304.
- Bigi, G., Cosentino, D., Parotto, M., Sartori, R., and Scandone, P. (1992). Structural Model of Italy, scale 1:500.000. 114(3). *Prog. Fin. Geodinamica, Quad. 'La Ricerca Scientifica'*, C.N.R., Roma.
- Bignami, C., Burrato, P., Cannelli, V., Chini, M., Falcucci, E., Ferretti, A., Gori, S., Kyriakopoulos, C., Melini, D., Moro, M., Novali, F., Saroli, M., Stramondo, S., Valensise, G., and Vannoli, P. (2012). Coseismic deformation pattern of the emilia 2012 seismic sequence imaged by radarsat-1 interferometry. *Ann. Geophys.*, 55(4):788–795.
- Bindi, D., Pacor, F., Luzi, L., Puglia, R., Massa, M., Ameri, G., and Paolucci, R. (2011). Ground motion prediction equations derived from the Italian strong motion database. *Bull. Earthq. Eng.*, 9:1899–1930.

- Bindi, D., Parolai, S., Cara, F., Di Giulio, G., Ferretti, G., Luzi, L., Monachesi, G., Pacor, F., and Rovelli, A. (2009). Site Amplifications Observed in the Gubbio Basin, Central Italy: Hints for Lateral Propagation Effects. *BSSA*, 99:741–760.
- Boatwright, J., Fletcher, J., and Fumal, T. (1991). A general inversion scheme for source, site and propagation characteristics using multiply recorded sets of moderate-sized earthquakes. *BSSA*, 81:1754–1782.
- Boccaletti, M., Bonini, M., Corti, M., Gasperini, G., Martelli, L., Piccardi, L., Severi, P., and Vannucci, G. (2004). *Carta sismotettonica della Regione Emilia-Romagna scala 1:250000. Note illustrative*. A cura di M. Boccaletti e L. Martelli. S.EL.C.A, Firenze.
- Boccaletti, M., Calamita, F., Centamore, E., Deiana, G., Dondi, L., Gelati, R., Massari, F., Moratti, G., and Ricci Lucchi, F. (1987). Neogene tectonic phases of the Northern Apennines-South Alpine system; their significance in relation to the foredeep sedimentation. In *Proceedings of the 8th Congress of Regional Committee on Mediterranean Neogene Stratigraphy*, pages 201–208. Budapest, 15-22 September.
- Boccaletti, M., Calamita, F., Deiana, G., Gelati, R., Massari, F., Moratti, G., and Ricci Lucchi, F. (1990). Migrating foredeep-thrust belt system in the northern Apennines and southern Alps. *Paleogeography, Paleoclimatology, Paleocology*, 77:3–14.
- Boccaletti, M., Corti, G., and Martelli, L. (2011). Recent and active tectonics of the external zone of the Northern Apennines (Italy). *Int. J. Earth Sci.*, 100:1331–1348.
- Bondesan, M. (1986). Lineamenti di geomorfologia del Basso Ferrarese. In *La civiltà comacchiese e pomposiana dalle origini preistoriche al tardo medioevo*. (Comacchio, 1984), Bologna, Nuova Alfa Ed., pp.17-28.
- Bondesan, M., Ferri, R., and Graziani, S. (1992). Aspetti geomorfologici e problemi paleogeografici della zona fra Bondeno, Finale Emilia e Mirabello nel quadro degli antichi domini idrografici del Secchia, del Panaro e del Reno. In *Gelichi, S. (Ed.), Un mito e un territorio: Ansalaregina e l'Alto Ferrarese nel Medioevo. Ed. All'insegna del Giglio*. Firenze, pp. 13-44.
- Bonnefoy-Claudet, S. and Bard, P. (2006). The nature of noise wavefield and its application for site effects studies. A literature review. *Earth-Sci. Rev.*, 79:205–227.
- Bonnefoy-Claudet, S., Cornou, C., Bard, P., Cotton, F., Moczo, P., Kristek, J., and Fäh, D. (2006). H/V ratio: a tool for site effects evaluation. Results from 1-D noise simulations. *Geophys. J. Int.*, 167:827–837.
- Bonnefoy-Claudet, S., Cornou, C., Bard, P.-Y., and Cotton, F. (2004). Nature of noise wavefield. SESAME report, D13.08 (<http://sesame-fp5.obs.ujf-grenoble.fr>).

- Bordoni, P., Azzara, R., Cara, F., Cogliano, R., Cultrera, G., Di Giulio, G., Fodarella, A., Milana, G., Pucillo, S., Riccio, G., Rovelli, A., Augliera, P., Luzi, L., Lovati, S., Massa, M., Pacor, F., Puglia, R., and Ameri, G. (2012). Preliminary results from EMERSITO, a rapid response network for site-effect studies. *Ann. Geophys.*, 55(4):599–607.
- Bordoni, P., Cultrera, G., Margheriti, L., Augliera, P., Caielli, G., Cattaneo, M., de Franco, R., Michelini, A., and Spallarossa, D. (2003). A microseismic study in a low seismicity area: the 2001 site-response experiment in the Città di Castello (Italy) basin. *Ann. Geophys.*, 46(6).
- Bottoni, A. (1873). *Appunti storici sulle rotte del basso Po dai tempi romani a tutto il 1839*. Tip. Sociale, Ferrara.
- Boulanger, R., Idriss, I., and Mejia, L. (1995). Investigation and evaluation of liquefaction related ground displacements at Moss Landing during the 1989 Loma Prieta earthquake. *Report No. UCD/CGM-95/02*. Center for Geotechnical Modeling, Department of Civil and Environmental Engineering, University of California, Davis, 231 pp.
- Boulanger, R., Mejia, L., and Idriss, I. (1997). Liquefaction at Moss landing during Loma Prieta earthquake. *J. Geotech. Geoenviron. Eng.*, 123(5):453–467.
- Boulanger, R. W. (2003). High overburden stress effects in liquefaction analyses. *J. Geotech. Geoenviron. Eng.*, 129(12):1071–1082.
- Boulanger, R. W. and Idriss, I. M. (2004). State normalization of penetration resistances and the effect of overburden stress on liquefaction resistance. In *Proceedings of the 11th International Conference on Soil Dynamics and Earthquake Engineering*.
- Brune, J. and Oliver, J. (1959). The seismic noise of the Earth s surface. *BSSA*, 49:349–353.
- Burrato, P., Ciucci, F., and Valensise, G. (2003). An inventory of river anomalies in the Po Plain, northern Italy: evidence for active blind thrust faulting. *Ann. Geophys.*, 46(5):865–882.
- Burrato, P., Vannoli, P., Fracassi, U., Basili, R., and Valensise, G. (2012). Is blind faulting truly invisible? Tectonic-controlled drainage evolution in the epicentral area of the May 2012, Emilia-Romagna earthquake sequence (northern Italy). *Ann. Geophys.*, 55(4):525–531.
- Butler, R., Lickorish, W., Grasso, M., Pedley, H., and Ramberti, L. (1995). Tectonics and sequence stratigraphy in Messinian basins, Sicily: constraints on the initiation and termination of the Mediterranean salinity crisis. *Geol. Soc. Am. Bull.*, 107:425–439.

- Calabrese, L., Martelli, L., and Severi, P. (2012). Stratigrafia dell'area interessata dai fenomeni di liquefazione durante il terremoto dell'Emilia (maggio 2012). In *Proceedings of the 31th Conference of the National Group of Solid Earth Geophysics*, volume 2, pages 119–126. Potenza, November 20-22.
- Campanella, R. and Robertson, P. (1988). Current status of the piezocone test. In 1, editor, *Proceedings of First International Symposium on Penetrating Testing, ISOPT-1*, pages 93–116. Orlando, March 22-24.
- Capon, J. (1969). High-resolution frequency-wavenumber spectrum analysis. *IEEE*, 57:1408–1419.
- Capon, J., Greenfield, R. J., and Kolker, R. J. (1967). Multidimensional maximum-likelihood processing of a large-aperture seismic array. *IEEE*, 55:192–211.
- Caputo, R., Iordanidou, K., Minarelli, L., Papathanassiou, G., Poli, M., Rapti-Caputo, D., Sboras, S., Stefani, M., and Zanferrari, A. (2012). Geological evidence of pre-2012 seismic events, Emilia-Romagna, Italy. *Ann. Geophys.*, 55(4):743–749.
- Caputo, R. and Papathanassiou, G. (2012). Ground failure and liquefaction phenomena triggered by the 20 May, 2012 Emilia-Romagna (Northern Italy) earthquake: case study of Sant'Agostino-San Carlo-Mirabello zone. *Nat. Hazards Earth Syst. Sci.*, 12(11):3177–3180.
- Caputo, R., Pellegrinelli, A., Bignami, C., Bondesan, A., Mantovani, A., Stramondo, S., and Russo, P. (2015). High-precision levelling, DInSAR and geomorphological effects in the Emilia 2012 epicentral area. *Geomorphology*, 235:106–117.
- Caputo, R., Poli, M. E., Minarelli, L., Rapti, D., Sboras, S., Stefani, M., and Zanferrari, A. (2016). Trench investigation of the 2012 coseismic environmental effects at San Carlo (N Italy), and evidence for the 1570 Ferrara earthquake liquefaction. *Tectonics (submitted)*.
- Cara, F., Cultrera, G., Azzara, R. M., De Rubeis, V., Di Giulio, G., Giammarinaro, M. S., Tosi, P., Vallone, P., and Rovelli, A. (2008). Microtremor Measurements in the City of Palermo, Italy: Analysis of the Correlation with Local Geology and Damage. *BSSA*, 98(3):1354–1372.
- Cara, F., Di Giulio, G., Cavinato, G. P., Famiani, D., and G., M. (2011). Seismic characterization and monitoring of Fucino Basin (Central Italy). *Bull. Earthq. Eng.*, 9:1961–1985.
- Carannante, S., Argnani, A., Massa, M., D'Alema, E., Lovati, S., Moretti, M., Cattaneo, M., and Augliera, P. (2015). The May 20 (Mw 6.1) and 29 (Mw 6.0), 2012, Emilia (Po Plain, northern Italy) earthquakes: New seismotectonic implications from subsurface geology and high-quality hypocenter location. *Tectonophys.*, 655:107–123.
- Carminati, E., Lustrino, M., and Doglioni, C. (2012). Geodynamic evolution of the central and western Mediterranean: Tectonics vs. igneous petrology constraints. *Tectonophys.*, 579:179–192.

- Caserta, A., Zahradnik, J., and Plicka, V. (1999). Ground motion modeling with a stochastically perturbed excitation. *J. Seismol.*, 3:45–59.
- Castellarin, A. (2001). Alps-Apennines and Po Plain-Frontal Apennines Relationships. In *G.B. Vai e I.P. Martini (Eds.), Anatomy of an Orogen: Northern Apennines and Adjacent Mediterranean Basins*. Kluwer Academic Publ. Dordrecht, 177-197.
- Castellarin, A., Eva, C., Giglia, G., Vai, G., Rabbi, E., Pini, G., and Crestana, G. (1985). Analisi strutturale del Fronte Appenninico Padano. *Giornale di Geologia*, 47:47–75.
- Castellarin, A. and Vai, G. (1986). Southalpine versus Po Plain appenninic arcs. In *F. C. WEZEL (Ed.), The Origin of the Arcs, Development in Geotectonics*, volume 21, pages 253–280. Elsevier, Amsterdam.
- Castiglioni, G., Biancotti, A., Bondesan, M., Cortemiglia, G. C., Elmi, C., Favero, V., Gasperi, G., Marchetti, G., Orombelli, G., Pellegrini, G. B., and Tellini, C. (1999). Geomorphologic map of the Po Plain, Italy, at a scale of 1:250 000. *Earth Surf. Proc. Land.*, 24:1115–1120.
- Castiglioni, G. and Pellegrini, G. (2001). *Illustrative notes of the geomorphological map of the Po Plain*, volume IV. Suppl. Geogr. Fis. Dinam. Quat.
- Cavazza, W. and Wezel, F. (2003). The Mediterranean region - A geological primer. *Episodes*, 26(3).
- CEN (2003). prEN 1998-1 - eurocode 8: design of structures for earthquake resistance. Part 1: General rules, seismic actions and rules for buildings. Draft No 6, Doc CEN/TC250/SC8/N335, January, Brussels.
- Centamore, E., Deiana, G., Micarella, A., and Potetti, M. (1986). Il Trias-Paleogene delle Marche. In *La geologia delle Marche*, pages 9–27. Studi Geologici Camerti.
- Centamore, E., Fumanti, F., and Nisio, S. (2002). The Central Northern Apennines geological evolution from Triassic to Neogene time. *Boll. Soc. Geol. It.*, 1:181–197.
- Cesca, S., Braun, T., Maccaferri, F., Passarelli, L., E., R., and Dahm, T. (2013). Source modelling of the M5-6 Emilia-Romagna, Italy, earthquakes (2012 May 20-29). *Geophys. J. Int.*, 193(3):1658–1672.
- Cestari, F. (2009). *Prove geotecniche in sito*. Ed. Segrate Geo-Impianti, 415 pp.
- Champel, B., van der Beek, P., Mugnier, J., and Leturmy, P. (2002). Growth and lateral propagation of fault-related folds in the Siwaliks of western Nepal: Rates, mechanisms, and geomorphic signature. *J. Geophys. Res.*, 107.
- Channell, J., D'Argenio, B., and Horvath, F. (1979). Adria, the African promontory, in Mesozoic Mediterranean paleogeography. *Earth-Sci. Rev.*, 15:213–292.

- Chouet, B., De Luca, G., Milana, G., Dawson, P., Martini, M., and Scarpa, R. (1998). Shallow velocity of Stromboli volcano, Italy, derived from small-aperture array measurements of Strombolian tremor. *BSSA*, 88(3):653–666.
- Chung, J.-W. and Rogers, J. (2011). Simplified method for spatial evaluation of liquefaction potential in the St. Louis area. *J. Geotech. Geoenviron. Eng.*, 137(5):505–515.
- Ciabatti, M. and Veggiani, A. (1990). Caratteri ed evoluzione del litorale emiliano-romagnolo. In *Il mondo della natura in Emilia-Romagna. La pianura e la costa*, pages 77–94. Cinisello Balsamo.
- Cornou, C. (2002). *Traitement d'antenne et imagerie sismique dans l'agglomération grenobloise (Alpes françaises): implications pour les effets de site*. PhD thesis, Université Joseph Fourier. 260 pp.
- Cornou, C., Bard, P.-Y., and Dietrich, M. (2003a). Contribution of dense array analysis to identification and quantification of basin-edge induced waves. part i: Methodology. *BSSA*, 93(6):2604–2623.
- Cornou, C., Bard, P.-Y., and Dietrich, M. (2003b). Contribution of dense array analysis to identification and quantification of basin-edge induced waves. part ii: Application to Grenoble basin (french Alps). *BSSA*, 93(6):2624–2648.
- Costa, M. (2003). The Buried, Apenninic Arcs of the Po Plain and Northern Adriatic Sea (Italy): A New Model. *Boll. Soc. Geol. It.*, 122:3–23.
- CPTI11, a cura di Rovida, A., Camassi, R., Gasperini, P., and Stucchi, M. (2011). CPTI11, la versione 2011 del Catalogo Parametrico dei Terremoti Italiani. Milano, Bologna, <http://emidius.mi.ingv.it/CPTI>.
- Cremonini, G. and Ricci Lucchi, F. (1982). *Guida alla Geologia del margine appenninico-padano*. Società Geologica Italiana, Guide geologiche regionali, Pitagora Tecnoprint, Bologna.
- Crespellani, T., Facciorusso, J., Ghinelli, A., Madaia, C., Renzi, S., and Vannucchi, G. (2012). Rapporto preliminare sui diffusi fenomeni di liquefazione verificatisi durante il terremoto in pianura padana emiliana del maggio 2012. Rapporto 31 maggio 2012. <http://ambiente.regione.emiliaromagna.it/geologia/temi/sismica/liquefazione-gruppo-di-lavoro>.
- Cresta, S., Monechi, S., and Parisi, G. (1989). *Stratigrafia del Mesozoico e Cenozoico nell'area umbro-marchigiana. Itinerari geologici sull'appennino umbro-marchigiano (Italia)*, volume 39. Memorie descrittive Carta Geologica d'Italia, 182 pp.
- Cubrinovski, M., Bray, J., Taylor, M., Giorgini, S., Bradley, B., Wotherspoon, L., and Zupan, J. (2011). Soil liquefaction effects in the central business district during the February 2011 Christchurch earthquake. *Seismol. Res. Lett.*, 82(6):893–904.

- DAL (112/2007). Atto di indirizzo e coordinamento tecnico ai sensi dell'art. 16, c. 1, della L. R. 20/2000 per "Indirizzi per gli studi di microzonazione sismica in Emilia-Romagna per la pianificazione territoriale e urbanistica". Deliberazione dell'Assemblea Legislativa della Regione Emilia-Romagna n. 112 del 02/05/2007, Bollettino Ufficiale della Regione Emilia-Romagna n. 64 del 17/05/2007.
- Dalla, S., Rossi, M., Orlando, M., Visentin, C., Gelati, R., Gnaccolini, M., Papani, G., Belli, A., Biffi, U., and Citrullo, D. (1992). Late Eocene-Tortonian tectono-sedimentary evolution in the western part of the Padan basin (northern Italy). *Paleontol. Evol.*, (24-25):341–362.
- D'Amico, V., Picozzi, M., Baliva, F., and Albarello, D. (2008). Ambient noise measurements for preliminary site-effects characterization in the urban area of Florence, Italy. *BSSA*, 98:1373–1388.
- DBMI11, a cura di Locati, M., Camassi, R., and Stucchi, M. (2011). DBMI11, la versione 2011 del Database Macrosismico Italiano. Milano, Bologna, <http://emidius.mi.ingv.it/DBMI11>.
- Devoti, R., Esposito, A., Pietrantonio, G., Pisani, A., and Riguzzi, F. (2011). Evidence of large-scale deformation patterns from GPS data in the Italian subduction boundary. *Earth Planet. Sci. Lett.*, 311:1–12.
- Di Capua, G. and Tarabusi, G. (2013). Site specific hazard assessment in priority areas. DPC-INGV-S2 Project, Annex 3 to Deliverable 4.1.
- Di Manna, P., Guerrieri, L., Piccardi, L., Vittori, E., Castaldini, D., Berlusconi, A., Bonadeo, L., Comerci, V., Ferrario, F., Gambillara, R., Livio, F., Lucarini, M., and Michetti, A. M. (2012). Ground effects induced by the 2012 seismic sequence in Emilia: implications for seismic hazard assessment in the Po plain. *Ann. Geophys.*, 55(4):696–703.
- Dikmen, U. and Mirzaoglu, M. (2005). The seismic microzonation map of Yenisehir-Bursa, NW of Turkey by means of ambient noise measurements. *J. Balkan Geophys. Soc.*, 8(2):53–62.
- Dixit, J., Dewaikar, D., and Jangid, R. (2012). Assessment of liquefaction potential index for Mumbai City. *Nat. Hazards Earth Syst. Sci.*, 12(9):2759–2768.
- Dobry, R. (1989). Some Basic Aspects of Soil Liquefaction During Earthquakes. In *Proceedings of the Conference on Earthquake Hazards and the Design of Constructed Facilities in the Eastern United States*. Academy of Sciences, New York, Feb. 24-26.
- Doglioni, C. (1993). Some remarks on the origin of foredeeps. *Tectonophys.*, 228(1-2):1–20.
- Dondi, L. and D'Andrea, M. (1986). La Pianura Padana e Veneta dall'Oligocene superiore al Pleistocene. *Giornale di Geologia*, 48:197–225.

- Dondi, L., Mostardini, F., and Rizzini, A. (1982). Evoluzione sedimentaria e paleogeografia nella Pianura Padana. In *G. Cremonini and F. Ricci Lucchi (Eds.), Guida alla Geologia del margine appenninico-padano*, pages 47–58. Guida Geol. Reg., S.G.I.
- Douglas, B. J. and Olsen, R. S. (1981). Soil classification using electric cone penetrometer. In *Proceedings of Conference on Cone Penetration Testing and Experience*, pages 209 – 227. St. Louis, October 26 - 30.
- Douze, E. J. (1964). Rayleigh waves in short-period seismic noise. *BSSA*, 54(4):1197–1212.
- Douze, E. J. (1967). Short-period seismic noise. *BSSA*, 57(1):55–81.
- Duval, A.-M., Bard, P.-Y., Lebrun, B., Lacave-Lachet, C., Riepl, J., and Hatzfeld, D. (2001a). H/V technique for site response analysis. Synthesis of data from various surveys. *BGTA*, 42(3-4):267–280.
- Duval, A.-M., Méneroud, J.-P., Vidal, S., and Singer, A. (1998). Relation between curves obtained from microtremor and site effects observed after Caracas 1967 earthquake. In *Proceedings of the 11th European Conference on Earthquake Engineering*. Paris, France.
- Duval, A.-M., Vidal, S., Méneroud, J.-P., Singer, A., De Santis, V., Ramos, C., Romero, G., Rodriguez, R., Pernia, A., Reyes, N., and Griman, C. (2001b). Caracas, Venezuela, site effect determination with microtremor. *Pure Appl. Geophys.*, 158(12):2513–2523.
- EmergeoWorkingGroup (2013). Liquefaction phenomena associated with the Emilia earthquake sequence of May-June 2012 (Northern Italy). *Nat. Hazards Earth Syst. Sci.*, 13:935–947.
- Eslami, A. and Fellenius, B. (1997). Pile Capacity by direct CPT and CPTu methods applied to 102 case histories. *Can. Geotech. J.*, 34(6):886–898.
- Eslami, A. and Fellenius, B. (2004). CPT and CPTu Data for Soil Profile Interpretation: Review of Methods and a Proposed New Approach. *Iranian J. Sci. Tech.*, 28(B1):69–86.
- Facciorusso, J. (2008). Calcolo del potenziale di liquefazione su vasta scala: approccio deterministico e approccio probabilistico.
- Facciorusso, J., Madiari, C., and Vannucchi, G. (2012). Risposta sismica locale e pericolosità di liquefazione a S. carlo e Mirabello.
- Facciorusso, J., Madiari, C., and Vannucchi, G. (2013). Confronto tra metodi semplificati di stima del rischio di liquefazione da prove Cpt e CPTu. Università degli Studi di Firenze. Facoltà di Ingegneria - Sezione Geotecnica.

- Fantoni, R. and Franciosi, R. (2008). 8 geological sections crossing po plain and adriatic foreland. *ROL Soc. Geol. It.*, 3(1):367–368.
- Fantoni, R. and Franciosi, R. (2010). Tectono-sedimentary setting of the Po Plain and Adriatic foreland. *Rend. Fis. Acc. Lincei*, 21 (Suppl.1):197–209.
- Fellenius, H. and Eslami, A. (2000). Soil Profile Interpreted from CPTu Data. Year 2000 Geotechnics, Geotechnical Engineering Conference, Asian Institute of Technology, Bangkok.
- Field, E. and Jacob, K. (1993). The theoretical response of sedimentary layers to ambient seismic noise. *Geophys. Res. Lett.*, 20(24):2925–2928.
- Field, E. H., Clement, A. C., Jacob, K. H., Aharonian, V., Hough, S. E., Friberg, P. A., Babaian, T. O., Karapetian, S. S., Hovanessian, S. M., and Abramian, H. A. (1995). Earthquake site-response study in Giumri (formely Leninakan), Armenia, using ambient noise observations. *BSSA*, 85(1):349–353.
- Finn, W. D. L., Brandy, P. L., and Pickering, D. L. (1970). Effect of Strain History on Liquefaction of Sand. *J. Geotech. Eng. Div.*, 96(6):1917–1934.
- Fioravante, V. and Giretti, D. (2012). Il caso di Sant’Agostino-San Carlo. <http://ambiente.regione.emilia-romagna.it/geologia/temi/sismica/speciale-terremoto>.
- Flores Estrella, H. and Aguirre Gonzalez, J. (2003). SPAC: An alternative method to estimate earthquake site effects in Mexico city. *Geofisica Internacional*, 42(2):227–236.
- Franceschini, A. (1983). Una storia di acque. In *Sitti, R. (Ed.), Vigarano, Storia/Attualità*, pages 21–50. ArtStudio C, Ferrara.
- Frepoli, A. and Amato, A. (1997). Contemporaneous extension and compression in the Northern Apennines from earthquake fault plane solutions. *Geophys. J. Int.*, 129:368–388.
- Friedrich, A., Krüger, F., and Klinge, K. (1998). Ocean-generated microseismic noise located with the Gräfenberg array. *J. Seismol.*, 2:47–64.
- Frizzi, A. (1848). *Memorie per la storia di Ferrara*. Ferrara.
- Fäh, D. (1997). Microzonation of the city of basel. *J. Seismol.*, 1(1):87–102.
- Galli, P. (2000). New empirical relationships between magnitude and distance for liquefaction. *Tectonophysics*, 324:169–187.

- Gallipoli, M., Mucciarelli, M., Castro, R., Mochavesi, G., and Contri, P. (2004a). Structure, soil-structure response and effects of damage based on observations of horizontal-to-vertical spectral ratios of microtremors. *Soil Dyn. Earthq. Eng.*, 24:487–495.
- Gallipoli, M., Mucciarelli, M., Eeri, M., Gallicchio, S., Tropeano, M., and Lizza, C. (2004b). Horizontal to Vertical Spectral Ratio (HVSR) measurements in the area damaged by the 2002 Molise, Italy, earthquake. *Earthq. Spec.*, 20(1):81–93.
- Gallipoli, M. R., Chiauzzi, L., Stabile, T. A., Mucciarelli, M., Masi, A., Lizza, C., and Vignola, L. (2014). The role of site effects in the comparison between code provision and near field strong motion of the Emilia 2012 earthquakes. *Bull. Earthq. Eng.*, 12(5):2211–2230.
- Ganas, A., Roumelioti, Z., and Chousianitis, K. (2012). Static stress transfer from the May 20, 2012, M 6.1 Emilia-Romagna (northern Italy) earthquake using a co-seismic slip distribution model. *Ann. Geophys.*, 55(4).
- García-Jerez, A., Luzón, F., Navarro, M., and Pérez-Ruiz, J. (2006). Characterization of the sedimentary cover of the Zafarraya basin (Southern Spain) by means of ambient noise. *BSSA*, 96:957–967.
- Gasperi, G., Gelati, R., and Papani, G. (1984). Neogene evolution of the Northern Apennines on the Po Valley side. *Giorn. Geol.*, 3(48):187–195.
- Gaull, B. A., Kagami, H., Eeri, M., M., and Taniguchi, H. (1995). The microzonation of Perth, western Australia, using microtremor spectral ratio. *Earthq. Spec.*, 11(2):173–191.
- Gelati, R., Rogledi, S., and Rossi, M. (1989). Significance of the Messinian unconformity-bounded sequences in the Apenninic margin of the Padan foreland basin, Northern Italy. *Mem. Soc. Geol. It.*, 39:319–323.
- Ghielmi, M., Minervini, M., Nini, C., Rogledi, S., Rossi, M., and Vignolo, A. (2010). Sedimentary and tectonic evolution in the eastern Po-Plain and northern Adriatic Sea area from Messinian to Middle Pleistocene (Italy). *Rend. Lincei-Sci. Fis. Nat.*, 21 (Suppl. 1):131–166.
- Golesorkhi, R. (1989). *Factors Influencing the Computational Determination of Earthquake-Induced Shear Stresses in Sandy Soils*. PhD thesis, University of California, Berkeley. 395 pp.
- Gosar, A. (2007). Microtremor HVSR study for assessing site effects in the Bovec basin (NW slovenia) related to 1998 Mw5.6 and 2004 Mw5.2 earthquakes. *Eng. Geol.*, 91:178–193.
- Gosar, A. and Martinec, M. (2009). Microtremor HVSR study of site effects in the ilirska Bistrica Town Area (S. Slovenia). *J. Earthq. Eng.*, 13:50–67.

- Guidoboni, E. (2006). *Libro di diversi terremoti, di Pirro Ligorio*. Edizione nazionale delle opere di Pirro Ligorio edition. Codice 28, Ja II 15 dell'Archivio di Stato di Torino, Edizione critica, Introduzione e Apparato storico a cura di E. Guidoboni.
- Guidoboni, E., Ferrari, G., Mariotti, D., Comastri, A., G., T., and Valensise, G. (2007). CFTI4Med, Catalogue of Strong Earthquakes in Italy from 461 B.C. to 2000 and in the Mediterranean area, from 760 B.C. to 1500, An Advanced Laboratory of Historical Seismology. <http://storing.ingv.it/cfti4med/>.
- Gutenberg, B. (1958). Microseisms. *Adv. Geophys.*, 5:53–92.
- Hanks, T. (1975). Strong ground motion of the San Fernando, California, earthquake: ground displacements. *BSSA*, 65:193–225.
- Haubrich, R. A., Munk, W. H., and Snodgrass, F. E. (1963). Comparative spectra of microseisms and swell. *BSSA*, 53(1):27–37.
- Havenith, H., Faeh, D., Polom, U., and Roulè, A. (2007). S-wave velocity measurements applied to the microzonation of Basel, Upper Rhine Graben. *Geophys. J. Int.*, 170:346–358.
- Hayati, H. and Andrus, R. (2008). Liquefaction potential map of Charleston, South Carolina based on the 1886 earthquake. *J. Geotech. Geoenviron. Eng.*, 134(6):815–828.
- Herak, M. (2008). ModelHVSR-a Matlab tool to model horizontal-to-vertical spectral ratio of ambient noise. *Comput. Geosci.*, 35:1514–1526.
- Herak, M., Allegretti, I., Herak, D., Kuk, K., Kuk, V., Maric, K., Markusic, S., and Stipcevic, J. (2010). HVSR of ambient noise in Ston (Croatia): comparison with theoretical spectra and with the damage distribution after the 1996 Ston-Slano earthquake. *Bull. Earthq. Eng.*, 8:483–499.
- Hinzen, K., Scherbaum, F., and Weber, B. (2004). On the resolution of H/V measurements to determine sediment thickness, a case study across a normal fault in the Lower Rhine embayment, Germany. *J. Earthq. Eng.*, 8:909–926.
- Hisada, Y., Aki, K., and Teng, T.-L. (1993). 3-D simulations of the surface wave propagation in the Kanto sedimentary basin, Japan (part 2: application of the surface wave BEM). *BSSA*, 83:1700–1720.
- Holbrook, J. and Schumm, S. (1999). Geomorphic and sedimentary response of rivers to tectonic deformation: a brief review and critique of a tool for recognizing subtle epeirogenic deformation in modern and ancient settings. *Tectonophys.*, 305:287–306.
- Holzer, T., Bennett, M., Noce, T., Padovani, A., and Tinsley, I. J. (2006a). Liquefaction hazard mapping with LPI in the Greater Oakland, California, Area. *Earthq. Spec.*, 22(3):693–708.

- Holzer, T., Bennett, M., Noce, T., Padovani, A., and Tinsley III, J. (2002). Liquefaction hazard and shaking amplification maps of Alameda, Berkeley, Emeryville, Oakland and Piedmont: a digital database. U.S. Geological Survey 02-296 (<http://geopubs.wr.usgs.gov/open-file/of02-296>).
- Holzer, T., Blair, J., Noce, T., and Bennett, M. (2006b). Predicted liquefaction of east bay fills during a repeat of the 1906 San Francisco earthquake. *Earthq. Spec.*, 22(2):261–277.
- Holzer, T., Noce, T., Bennett, M., Tinsley, I. J., and Rosenburg, L. (2005). Liquefaction at Oceano, California, during the 2003 San Simeon earthquake. *BSSA*, 95(6):2396–2411.
- Horike, M. (1985). Inversion of phase velocity of long-period microtremors to the S-wave-velocity structure down to the basement in urbanized areas. *J. Phys. Earth*, 33:59–96.
- Horike, M. (1996). Geophysical exploration using microtremor measurements. In *Proceedings of the 11th World Conference on Earthquake Engineering*. Acapulco, Mexico.
- Idriss, I. and Boulanger, R. (2008). *Soil liquefaction during earthquakes*. MNO 12, 242 pp. Earthquake Engineering Research Institute, Oakland, USA.
- Idriss, I. M. (1999). An update to the Seed-Idriss simplified procedure for evaluating liquefaction potential. In *Proceedings of the TRB Workshop on New Approaches to Liquefaction*, number FHWA-RD-99-165. Federal Highway Administration, January.
- Idriss, I. M. and Boulanger, R. W. (2003). Relating K_v and K_h to SPT blow count and to CPT tip resistance for use in evaluating liquefaction potential. In *Proceedings of the Dam Safety Conference (ASDSO)*. September 7-10, Minneapolis, MN.
- Idriss, I. M. and Boulanger, R. W. (2004). Semi-empirical procedures for evaluating liquefaction potential during earthquakes. In *Proceedings of the 11th International Conference on Soil Dynamics and Earthquake Engineering*, volume 26, pages 115–130.
- Ishida, H., Nozawa, T., and Niwa, M. (1998). Estimation of deep surface structure based on phase velocities and spectral ratios of long-period microtremors. In *Proceeding of the Second International Symposium on the Effects of Surface Geology on Seismic Motion*, volume 2, pages 697–704. Yokohama, Japan.
- Ishihara, K. (1985). Stability of natural deposits during earthquakes. In *Proceedings, 11th International Conference on Soil Mechanics and Foundation Engineering*, pages 321–376. A. A. Balkema, Rotterdam.
- ISPRA (2009). *Carta Geologica d'Italia alla scala 1:50.000, Foglio 203 Poggio Renatico*. Coord. Scient.: U. Cibin, Regione Emilia-Romagna. ISPRA, Servizio Geologico d'Italia - Regione Emilia-Romagna, SGSS.

- Iwasaki, T., Tatsuoka, F., Tokida, K., and Yasuda, S. (1978). A practical method for assessing soil liquefaction potential based on case studies at various sites in Japan. In *Proceedings of the 2nd International Conference on Microzonation*, pages 885–896. San Francisco.
- JapanRoadAssociation (1980). *Specifications for highway bridges, Part V. Earthquake Resistant Design*, Tokyo, Japan.
- Jefferies, M. and Davies, M. (1991). Soil classification by the cone penetration tests: Discussion. *Can. Geotech. J.*, 28(1):173–176.
- Jefferies, M. and Davies, M. (1993). Use of CPTU to estimate equivalent SPT N60. *Geotech. Testing J.*, 16(4):458–468.
- Joyner, W. (2000). Strong motion from surface waves in deep sedimentary basins. *BSSA*, 95:95–112.
- Juang, C., Jiang, T., and Andrus, R. (2002). Assessing probability-based methods for liquefaction evaluation. *J. Geotech. Geoenviron. Eng.*, 128(7):580–589.
- Juang, C. and Li, D. (2007). Assessment of liquefaction hazard in Charleston Quadrangle, South Carolina. *Eng. Geol.*, 92:59–72.
- Juang, C. H., Liu, C.-N., Chen, C.-H., Hwang, J.-H., and Lu, C.-C. (2008). Calibration of liquefaction potential index: a re-visit focusing on a new cptu model. *Eng. Geol.*, 102(1-2):19–30.
- Kagawa, T. (1996). Estimation of velocity structures beneath Mexico city using microtremor array data. In *Proceedings of the 11th World Conference on Earthquake Engineering*. Acapulco, Mexico.
- Kagawa, T., Zhao, B., Miyakoshi, K., and Irikura, K. (2004). Modeling of 3-D basin structures for seismic wave simulations based on available information on the target area: case study of the Osaka Basin, Japan. *BSSA*, 94:1353–1368.
- Kanai, K., Osada, T., and Tanaka, T. (1954). Measurement of the microtremors. *Bull. Earthq. Res Inst.*, 32:199–209.
- Kanai, K. and Tanaka, T. (1961). On microtremors. *Bull. Earthq. Res Inst.*, 39:97–114.
- Kanno, T., Kudo, K., Takahashi, M., Sasatani, T., Ling, S., and Okada, H. (2000). Spatial evaluation of site effects in Ashigara valley based on S-wave velocity structures determined by array observations of microtremors. In *Proceedings of the 12th World Conference on Earthquake Engineering*. Auckland, New Zealand.

- Kayen, R. E., Mitchell, J. K., Seed, R. B., and Nishio, S. (1998). *Soil liquefaction in the east bay during the earthquake. The Loma Prieta, California, Earthquake of October 17, 1989 - Liquefaction*. Thomas L. Holzer (Eds.), U.S. Geological Survey Professional Paper 1551-B, B61-B86.
- Konno, K. (1996). Amplification factors estimated from spectral ratio between horizontal and vertical components of microtremor. In *Proceedings of the 11th World Conference on Earthquake Engineering*. Acapulco, Mexico.
- Konno, K. and Ohmachi, T. (1998). Ground-motion characteristics estimated from spectral ratio between horizontal and vertical components of microtremor. *BSSA*, 88(1):228–241.
- Koyuncu, N. and Ulusay, R. (2004). Geo-engineering evaluation with prime consideration to liquefaction potential for Eskisehir city (Turkey). In *Proceedings of the Int. Symp. Eng. Geol. for Infrastructure Planning in Europe, A European Perspective*, pages 125–132. Liege, Belgium.
- Ku, C. S., Juang, C. H., and Ou, C. Y. (2010). Reliability of CPT I_c as an index for mechanical behaviour classification of soils. *Geotech.*, 60(11):861–875.
- Kudo, K. (1995). Practical estimates of site response. State-of-art report. In *Proceedings of the 5th International Conference on Seismic Zonation*. Nice, France.
- Kudo, K., Kanno, T., Sasatani, T., Morikawa, N., Apostolidis, P., Pitilakis, K., Raptakis, D., Takahashi, M., Ling, S., Nagumo, H., Irikura, K., Higashi, S., and Yoshida, K. (2002). S-wave velocity structure at EURO-SESITES, Volvi, Greece determined by the spatial auto-correlation method applied for array records of microtremors. In *Proceedings of the Mini-Symposium on Site Effects Evaluation for Strong Motion Prediction*. Tokio, Japan.
- Lachet, C. and Bard, P.-Y. (1994). Numerical and theoretical investigations on the possibilities and limitations of Nakamura's technique. *J. Phys. Earth*, 42:377–397.
- Lacoss, R. T., Kelly, E. J., and Nafi, T. M. (1969). Estimation of seismic noise structure using arrays. *Geophys.*, 34(1):21–38.
- Lai, C. G., Foti, S., Godio, A., Rix, G. J., Sambuelli, L., and Socco, L. V. (2000). Caratterizzazione geotecnica dei terreni mediante l'uso di tecniche geofisiche. *Rivista Italiana di Geotecnica*, 34(3):99–118.
- Laurenzano, G., Priolo, E., Barnaba, C., Gallipoli, M. R., Klin, P., Mucciarelli, M., and Romanelli, M. (2013). Studio sismologico per la caratterizzazione della risposta sismica di sito ai fini della microzonazione sismica di alcuni comuni della regione Emilia-Romagna - Relazione sulla attività svolta. Rel. OGS 2013/74 Sez. CRS 26, 31 luglio.

- Lebrun, B., Hatzfeld, D., and Bard, P.-Y. (2001). Site effect study in urban area: Experimental results in Grenoble (France). *Pure Appl. Geophys.*, 158(12):2543–2557.
- Lee, D., Ku, C., and Yuan, H. (2004). A study of the liquefaction risk potential at Yuanlin, Taiwan. *Eng. Geol.*, 71(1-2):97–117.
- Lenz, J. and Baise, L. (2007). Spatial variability of liquefaction potential in regional mapping using CPT and SPT data. *Soil Dyn. Earthq. Eng.*, 27:690–702.
- Li, T. M. C., Ferguson, J. F., Herrin, E., and Durman, H. B. (1984). High-frequency seismic noise at Lajitas, Texas. *BSSA*, 74(5):2015–2033.
- Liu, H.-P., Boore, D. M., Joyner, W. B., Oppenheimer, D. H., Warrick, R. E., Zhang, W., Hamilton, J. C., and Brown, L. T. (2000). Comparison of phase velocities from array measurements of rayleigh waves associated with microtremor and results calculated from borehole shear-wave velocity profiles. *BSSA*, 90(3):666–679.
- Lo Presti, D., Meisina, C., and Squeglia, N. (2009). Applicabilità di prove penetrometriche statiche nella ricostruzione del profilo stratigrafico. *Rivista Italiana di Geotecnica*, 2:9–33.
- Lombardo, G., Coco, G., Corrao, M., Imposa, S., Azzara, R., Cara, F., and Rovelli, A. (2001). Results of microtremor measurements in the urban area of Catania, Italy. *BGTA*, 42(3-4):317–334.
- Longuet-Higgins, M. S. (1950). A theory of the origin of microseisms. *Phil. Trans. Royal Soc. London*, 243:1–35.
- Lunedei, E. and Albarello, D. (2010). Theoretical HVSR curves from full wavefield modelling of ambient vibrations in a weakly dissipative layered earth. *Geophys. J. Int.*, 181:1093–1108.
- Lunedei, E. and Albarello, D. (2015). HVSR curve by a full-wavefield model of ambient vibrations generated by a distribution of correlated surface sources. *Geophys. J. Int.*, 201:1140–1153.
- Lunne, T., Robertson, P. K., and Powell, J. J. J. (1997). *Cone penetration testing in geotechnical practice*. Blackie Academic and Professional, London.
- Luzi, L., Hailemichael, S., Bindi, D., Pacor, F., Mele, F., and Sabetta, F. (2008). ITACA (ITalian ACcelometric Archive): a web portal for the dissemination of Italian strong motion data. *Seismol. Res. Lett.*, 79(5):716–722.
- Luzi, L., Pacor, F., Ameri, G., Puglia, R., Burrato, P., Massa, M., Augliera, P., Franceschina, G., Lovati, S., and Castro, R. (2013). Overview on the strong-motion data recorded during the May-June 2012 Emilia seismic sequence. *Seismol. Res. Lett.*, 84(4):629–644.

- Malagnini, L., Rovelli, A., Hough, S. E., and Seeber, L. (1993). Site amplification estimates in the Garigliano valley, Central Italy, based on dense arrays measurements of ambient noise. *BSSA*, 83(6):1744–1755.
- Mantovani, A., Abu-Zeid, N., Bignardi, S., and Santarato, G. (2015). A geophysical transect across the central sector of the Ferrara Arc: passive seismic investigations - part ii. In *Proceedings of the 34th Conference of the National Group of Solid Earth Geophysics*, volume 1, pages 114–120.
- Marcuson, W. I. (1978). Definition of Terms Related to Liquefaction. *J. Geotech. Eng. Div.*, 104(9):1197–1200.
- Maresca, R., Castellano, M., De Matteis, R., Saccorotti, G., and Vaccariello, P. (2003). Local site effects in the town of Benevento (Italy) from noise measurements. *Pure Appl. Geophys.*, 160:1745–1764.
- Maresca, R., Del Pezzo, E., La Rocca, M., Liguori, G., Milana, G., and Sabbarese, C. (1999). Site response obtained from array techniques applied to the seismic noise: Two examples in Italy. *J. Seismol.*, 3:31–43.
- Margheriti, L., Azzara, R., Cocco, M., Delladio, A., and Nardi, A. (2000). Analyses of borehole broadband recordings: test site in the Po basin, Northern Italy. *BSSA*, 90:1454–1463.
- Margheriti, L., Lucente, F. P., and Pondrelli, S. (2003). SKS splitting measurements in the Apenninic-Tyrrhenian domain (Italy) and their relation with lithospheric subduction and mantle convection. *J. Geophys. Res.*, 108(B4).
- Martelli, L. and Romani, M. (2013). Microzonazione Sismica e analisi della Condizione Limite per l’Emergenza delle aree epicentrali dei terremoti della pianura emiliana di maggio-giugno 2012 (Ordinanza del Commissario Delegato - Presidente della Regione Emilia-Romagna n. 70/2012) - Relazione illustrativa. <http://ambiente.regione.emilia-romagna.it/geologia/temi/sismica/speciale-terremoto/sisma-2012-ordinanza-70-13-11-2012-cartografia>.
- Martin, G. R., Finn, W., and Seed, H. (1975). Fundamentals of Liquefaction under Cyclic Loading. *J. Geotech. Eng. Div.*, 101(5):423–438.
- Maruyama, Y., Yamazaki, F., and Hamada, T. (2000). Microtremor measurements for the estimation of seismic motion along expressway. In *Proceedings of the 6th International Conference of Seismic Zonation*, pages 1361–1366.
- Massa, M. and Augliera, P. (2013). Teleseisms as estimator of experimental long period site amplifications: example in the Po Plain (Italy) from the 2011, Mw 9.0, Tohoku-Oki (Japan) earthquake. *BSSA*, 103(5):2541–2556.
- Massa, M., Augliera, P., Carannante, S., Cattaneo, M., D’Alema, E., Lovati, S., Monachesi, G., Moretti, M., and Piccinini, D. (2013). Relocated seismicity in the Po Plain. DPC-INGV-S1 Project, Final Report, pp. 213-222.

- Maurer, B., Green, R., Cubrinovski, M., and Bradley, B. (2014). Evaluation of the liquefaction potential index for assessing liquefaction hazard in Christchurch, New Zealand. *J. Geotech. Geoenviron. Eng.*, 140(7).
- Mayne, P. W. (2007). *Cone penetration testing: state of practice*. Number 20-05. NCHRP Report, Transportation Research Board., Washington, D.C.
- McMechan, G. A. and Yedlin, M. J. (1981). Analysis of dispersive waves by wave field transformation. *Geophys.*, 46:869–874.
- Meletti, C. and Valensise, G. (2004). Zonazione sismogenetica ZS9 - app.2 al Rapporto Conclusivo. In *Gruppo di Lavoro MPS (2004). Redazione della mappa di pericolosità sismica prevista dall'Ordinanza PCM 3274 del 20 marzo 2003*. Rapporto Conclusivo per il Dipartimento della Protezione Civile, INGV, Milano-Roma, aprile 2004, 65 pp. + 5 allegati.
- Milana, G., Azzara, R., Bertrand, E., Bordoni, P., Cara, F., Cogliano, R., Cultrera, G., Di Giulio, G., Duval, A., and Foderella, A. (2011). The contribution of seismic data in microzonation studies for downtown L'Aquila. *Bull. Earthq. Eng.*, 9(3):741–759.
- Milana, G., Barba, S., Del Pezzo, E., and Zambonelli, E. (1996). Site response from ambient noise measurements: New perspectives from an array study in central Italy. *BSSA*, 86(2):320–328.
- Miyakoshi, K., Kagawa, T., and Kinoshita, S. (1998). Estimation of geological structures under the Kobe area using the array recordings of microtremors. In *Proceeding of the Second International Symposium on the Effects of Surface Geology on Seismic Motion*, volume 2, pages 691–696. Yokohama, Japan.
- Miyakoshi, K. and Okada, H. (1996). Estimation of the site response in the Kushiro city, Hokkaido, Japan, using microtremors with seismometer arrays. In *Proceedings of the 11th World Conference on Earthquake Engineering*. Acapulco, Mexico.
- Molinari, F., Boldrini, G., Severi, P., Duroni, G., Rapti-Caputo, D., and Martinelli, G. (2007). *Risorse idriche sotterranee della Provincia di Ferrara. Regione Emilia-Romagna (DB MAP Eds.)*. Florence, 61 pp.
- Montaldo, V., Faccioli, E., Zonno, G., Akinci, A., and Malagnini, L. (2005). Treatment of ground-motion predictive relationships for the reference seismic hazard map of Italy. *J. Seismol.*, 9(3):295–316.
- Montevocchi, G. and Novara, P. (2000). *In Agro Decumano. Per un catalogo del patrimonio storico archeologico del territorio a sud di Ravenna*. 222 pp.
- Moss, R. (2003). *CPT-Based Probabilistic Assessment of Seismic Soil Liquefaction Initiation*. PhD thesis, University of California, Berkeley.

- Moss, R., Seed, R., Kayen, R., Stewart, J., Der Kiureghian, A., and Cetin, K. (2006). Cpt-based probabilistic and deterministic assessment of in situ seismic soil liquefaction potential. *J. Geotech. Geoenviron. Eng.*, 132(8):1032–1051.
- Motamed, R., Ghalandarzadeh, A., Tawhata, I., and Tabtabaei, S. (2007). Seismic microzonation and damage assessment of Bam City, Southeastern Iran. *J. Earthq. Eng.*, 11:110–132.
- Mucciarelli, M. and Gallipoli, M. (2001). A critical review of 10 years of microtremor HVSr technique. *BGTA*, 42:255–266.
- Mucciarelli, M., Gallipoli, M., Di Giacomo, D., Di Nota, F., and Nino, E. (2005). The influence of wind on measurements of seismic noise. *Geophys. J. Int.*, 161:303–308.
- M.U.R.S.T. (1997). *Carta Geomorfologica della Pianura Padana alla scala 1:250.000*. coord. Castiglioni G.B., S.EL.CA., Firenze.
- Nakamura, Y. (1989). A method for dynamic characteristics estimation of subsurface using microtremor on the ground surface. *Quarterly Report of RTRI*, 30:25–33.
- Nakamura, Y. (1996). Real Time Information Systems for Seismic Hazards Mitigation UrEDAS, HERAS and PIC. *Quarterly Report of RTRI*, 37(3):112–127.
- Nakamura, Y. (2000). Clear identification of fundamental idea of Nakamura's technique and its applications. In *Proceedings of the 12th World Conference on Earthquake Engineering*. 8 pp., New Zealand.
- Nakamura, Y. and Saito, A. (1983). Amplification characteristics Estimation of Surface Ground based on Strong Motion Records. In *Proceedings of 17th Earthquake Engineering Symposium of Japan Society of Civil Engineers*, pages 25–28.
- Nardon, S., Marzorati, D., Bernasconi, A., Cornini, S., Gonfalini, M., Romano, A., and Terdich, P. (1991). Fractured carbonate reservoir characterisation and modelling: a multidisciplinary case study from the Cavone oil field. Italy, *First Break*, 9, 12, 553-565.
- NationalCenterforEarthquakeEngineeringResearch (1997). Technical Report NCEER-97-022. In *Proceedings of the NCEER Workshop on Evaluation of Liquefaction Resistance of Soils*, pages 41–88. T. L. Youd and I. M. Idriss editors.
- NationalResearchCouncil (1985). *Liquefaction of Soils During Earthquakes*. Committee on Earthquake Engineering, National Research Council, National Academy Press, Washington, D.C.

- Nguyen, F., Van Rompaey, G., Teerlynck, H., Van Camp, M., Jongmans, D., and Camelbeeck, T. (2004). Use of microtremor measurement for assessing site effects in Northern Belgium - interpretation of the observed intensity during the Ms = 5.0 June 11 1938 earthquake. *8(1):41–56.*
- Nogoshi, M. and Igarashi, T. (1971). On the amplitude characteristics of microtremor (Part 2). *J. Seismol. Soc. Japan, 24:26–40.*
- Ohmachi, T. and Umezono, T. (1998). Rate of Rayleigh waves in microtremors. In *Proceeding of the Second International Symposium on the Effects of Surface Geology on Seismic Motion*, volume 2, pages 587–592. Yokohama, Japan.
- Ohori, M., Nobata, A., and Wakamatsu, K. (2002). A comparison of ESAC and FK methods of estimating phase velocity using arbitrarily shaped microtremor arrays. *BSSA, 92(6):2323–2332.*
- Ohta, Y. (1963). On the Phase Velocity and Amplitude Distribution of Rayleigh Type Waves in Stratified Double Layer. *J. Seismol. Soc. Japan, 2(16):12–25.*
- Okada, H. (1986). A research on long period microtremor array observations and their time and spatial characteristics as probabilistic process. Report of a Grant-in-Aid for Co-operative Research (A) No. 59340026 supported by the Scientific Research Fund in 1985.
- Okada, H. (2003). *The Microtremor Survey Method*. Geophys. Monograph Series, SEG, 129 pp.
- Oliveto, A., Mucciarelli, M., and Caputo, R. (2004). HVSR prospections in multi-layered environments: an example from the Tyrnavos Basin (Greece). *J. Seismol., 8:395–406.*
- Olsen, R. and Mitchell, J. (1995). Cpt stress normalization and prediction of soil classification. In *Proceedings of the International Symposium on Cone Penetration Testing*, volume 2, pages 257–262. Swedish Geotechnical Society, Linköping, Sweden.
- Olsen, R. S. (1997). Cyclic liquefaction based on the cone penetrometer test. In *Proceedings of the NCEER Workshop on Evaluation of Liquefaction Resistance of Soils*. National Center for Earthquake Engineering Research, State University of New York at Buffalo, Report No. NCEER-97-0022, pp. 225-76.
- Orense, R., Kiyota, T., Yamada, S., Cubrinovski, M., Hosono, Y., Okamura, M., and Yasuda, S. (2011). Comparison of liquefaction Features observed during the 2010 and 2011 Canterbury earthquakes. *Seismol. Res. Lett., 82(6):905–918.*
- Ori, G. (1993). Continental depositional systems of the Quaternary of the Po Plain (northern Italy). *Sedim. Geol., 83:1–14.*

- O'Rourke, T., Jeon, S.-S., Toprak, S., Cubrinovski, M., Hughes, M., van Ballegooy, S., and Bouziou, D. (2014). Earthquake response of underground pipeline networks in Christchurch, NZ. *Earthq. Spec.*, 30(1):183–204.
- Pacor, F., Paolucci, R., Ameri, G., Massa, M., and Puglia, R. (2011). Italian strong motion records in ITACA: overview and record processing. *Bull. Earthq. Eng.*, 9(6):1741–1759.
- Panou, A., Theodulidis, N., Hatzidimitriou, P., Stylianidis, K., and Papazachos, C. (2005). Ambient noise horizontal-to-vertical spectral ratio for assessing site effects estimation and correlation with seismic damage distribution in urban environment: the case of city of Thessaloniki (Northern Greece). *Soil Dyn. Earthq. Eng.*, 25(4):261–274.
- Panza, G., Romanelli, F., Vaccari, F., Decanini, L., and Mollaioli, F. (2001). Contribution of the deterministic approach to the characterization of the seismic input. OECD-NEA Workshop on Engineering characterization of Seismic Input, BNL, Upton, New York, 15-17 November, 1999, NEA/CSNI/R(2000)2, pp. 655-715.
- Paolucci, E., Albarello, D., D'Amico, S., Lunedei, E., Martelli, L., Mucciarelli, M., and Pileggi, D. (2015). A large scale ambient vibration survey in the area damaged by May-June 2012 seismic sequence in Emilia Romagna, Italy. *Bull. Earthq. Eng.*, 13(11):3187–3206.
- Papathanassiou, G. (2008). LPI-based approach for calibrating the severity of liquefaction-induced failures and for assessing the probability of liquefaction surface evidence. *Eng. Geol.*, 96:94–104.
- Papathanassiou, G., Pavlides, S., and Ganas, A. (2005). The 2003 Lefkada earthquake: Field observations and preliminary microzonation map based on liquefaction potential index for the town of Lefkada. *Eng. Geol.*, 82(1):12–31.
- Parolai, S., Bormann, P., and Milkereit, C. (2002). New relationships between Vs, thickness of sediments, and resonance frequency calculated by the H/V ratio of seismic noise for the Cologne area (Germany). *BSSA*, 92(6):2521–2527.
- Passeri, L. (1994). *Appennino umbro-marchigiano*. Guide Geologiche Regionali 7, SGI, BE-MA, Milano, 301 pp.
- Pezzo, G., Merryman Boncori, J., Tolomei, C., Salvi, S., Atzori, S., Antonioli, A., Trasatti, E., Novali, F., Serpelloni, E., Candela, L., and Giuliani, R. (2013). Coseismic deformation and source modeling of the May 2012 Emilia (Northern Italy) earthquakes. *Seismol. Res. Lett.*, 84(4):645–655.
- Picotti, V. and Pazzaglia, F. (2008). A new active tectonic model for the construction of the Northern Apennines mountain front near Bologna (Italy). *J. Geophys. Res.*, 113(B8).

- Pieri, M. (1983). Three seismic profiles through the Po Plain. In A.W. Bally (Ed) *Seismic Expression of Structural Styles. A Picture and Work Atlas*. The American Association of Petroleum Geologists, Studies in Geology 15: 3.4.1/8-3.4/26.
- Pieri, M. and Groppi, G. (1975). The structure of the Pliocene-Quaternary sequence in the subsurface of the Po and Veneto plains, the pedepenninic Basin and the Adriatic sea. In L. Ogniben, M. Parotto and A. Pratlurion (Eds.), *Structural Model of Italy*, pages 409–415. CNR, Rome.
- Pieri, M. and Groppi, G. (1981). Subsurface geological structure of the Po Plain, Italy. CNR, Prog. Final. Geodin., pubbl. n. 414, Napoli.
- Pizzi, A. and Scisciani, V. (2012). The May 2012 Emilia (Italy) earthquakes: preliminary interpretations on the seismogenic source and the origin of the coseismic ground effects. *Ann. Geophys.*, 55(4):751–757.
- Pondrelli, S., Salimbeni, S., Perfetti, P., and Danecek, P. (2012). Quick regional centroid moment tensor solutions for the Emilia 2012 (northern Italy) seismic sequence. *Ann. Geophys.*, 55(4):615–621.
- Priolo, E., Romanelli, M., Barnaba, C., Mucciarelli, M., Laurenzano, G., Dall’Olio, L., Abu-Zeid, N., Caputo, R., Santarato, G., Vignola, L., Lizza, C., and Di Bartolomeo, P. (2012). The Ferrara Thrust Earthquakes of May-June 2012 - Preliminary Site Response Analysis at the Sites of the OGS Temporary Network. *Ann. Geophys.*, 55(4):591–597.
- Rapti-Caputo, D. and Martinelli, G. (2009). The geochemical and isotopic composition of aquifer systems in the deltaic region of the Po River (northern Italy). *Hydrogeol. J.*, 17(2):467–480.
- RER and ENI-AGIP (1998). *Riserve idriche sotterranee della Regione Emilia-Romagna*. A cura di G. Di Dio. S.EL.CA. (Firenze).
- Reutter, K., Giese, P., and Closs, H. (1980). Lithospheric split in the descending plate: observations from the Northern Apennines. *Tectonophys.*, 64(1-2):T1–T9.
- Ricci Lucchi, F. (1986). Oligocene to Recent foreland basins of northern Apennines. In Allen and P. Homewood (Eds.), *Foreland Basins*, volume 8, pages 105–139. IAS, Special Publication.
- Ricci Lucchi, F., Colalongo, M., Cremonini, G., Gasperi, G., Iaccarino, S., Papani, G., Raffi, S., and Rio, D. (1982). Evoluzione sedimentaria e paleogeografia nel margine appenninico. In G. Cremonini and F. Ricci Lucchi (Eds.), *Guida alla Geologia del margine appenninico-padano*, pages 17–46. Guida Geol. Reg., S.G.I.
- Rizzini, A. and Dondi, L. (1979). Messinian evolution of the Po Basin and its economic implication (hydrocarbons). *Palaeogeogr. Palaeoclimatol. Palaeoecol.*, 29:41–74.
- Robertson, P. (1990). Soil classification using the cone penetration test. *Can. Geotech. J.*, 27(1):151–158.

- Robertson, P. (2009). CPT interpretation - a unified approach. *Can. Geotech. J.*, 46:1–19.
- Robertson, P. and Cabal, K. (2010). Estimating soil unit weight from CPT. In *Proceedings of the 2nd Int. Symposium on Cone Penetration Testing*, volume 2, pages 447–454. Huntington Beach, CA.
- Robertson, P. and Campanella, R. (1985). Liquefaction Potential of Sands Using the Cone Penetration Test. *J. Geotech. Div.*, 111(3):298–307.
- Robertson, P., Campanella, R., Gillespie, D., and Rice, A. (1986). Seismic CPT to Measure In-situ Shear Wave Velocity. *J. Geotech. Eng.*, 112(8):791–803.
- Robertson, P. and Fear, C. (1995). Liquefaction of Sands and Its Evaluation. In *Proceedings of the 1st International Conference on Earthquake Geotechnical Engineering*. Keynote Lecture, Tokyo, Japan.
- Robertson, P. and Wride, C. (1998). Evaluating cyclic liquefaction potential using the cone penetration tests. *Can. Geotech. J.*, 35(3):442–459.
- Robertson, P. K. (2010). Soil behaviour type from the CPT: an update. In *2nd International Symposium on Cone Penetration Testing*, volume 2, pages 575–583. Huntington Beach, CA.
- Robertson, P. K. and Wride, C. E. (1997). Cyclic liquefaction and its evaluation based on SPT and CPT. In *Proceedings of the NCEER Workshop on Evaluation of Liquefaction Resistance of Soils*.
- Rosenbaum, G. and Lister, G. (2005). The Western Alps from the Jurassic to Oligocene: spatio-temporal constraints and evolutionary reconstructions. *Earth-Sci. Rev.*, 69:281–306.
- Roveri, M., Bassetti, M., and Ricci Lucchi, F. (2001). Mediterranean messinian salinity crisis: an apennine foredeep perspective. *Sedim. Geol.*, 140:201–214.
- Roversi, R. (1989). Assetto idraulico del territorio ferrarese. In *Corbo (Ed.), Terre e acqua*.
- Rovida, A., Camassi, R., Gasperini, P., and Stucchi, M. (2011). CPTI11, la versione 2011 del Catalogo Parametrico dei Terremoti Italiani. <http://emidius.mi.ingv.it/CPTI11>.
- Sakaji, K. (1998). Temporal variation of the power spectra of microtremors observed at soil and rock sites. Graduation thesis, Hokkaido University.
- Salvi, S., Tolomei, C., Merryman Boncori, J., Pezzo, G., Atzori, S., Antonioli, A., Trasatti, E., Giuliani, R., Zoffoli, S., and Coletta, A. (2012). Activation of the SIGRIS monitoring system for ground deformation mapping during the Emilia 2012 seismic sequence, using COSMO-SkyMed inSAR data. *Ann. Geophys.*, 55(4):796–802.

- Santarato, G., Mantovani, A., Abu-Zeid, N., Bignardi, S., Marchini, G., Valenti, C., Tarabusi, G., and Palmieri, F. (2015). A geophysical transect across the central sector of the Ferrara Arc for highlighting its recent activity. DPC-INGV-S1 Project, Final Report.
- Saraò, A. and Peruzza, L. (2012). Fault-plane solutions from moment-tensor inversion and preliminary Coulomb stress analysis for the Emilia Plain. *Ann. Geophys.*, 55(4):647–654.
- Sato, T., Graves, R., and Somerville, P. (1999). Three-dimensional finite-difference simulations of long-period strong motions in the Tokyo metropolitan area during the 1990 Odawara earthquake (Mj 5.1) and the great 1923 Kanto earthquake (Ms 8.2) in Japan. *BSSA*, 89:579–607.
- Satoh, T., Kawase, H., and Shinichi, M. (2001). Estimation of S-wave velocity structures in and around the Sendai Basin, Japan, using arrays records of microtremors. *BSSA*, 91(2):206–218.
- Scardia, G., Muttoni, G., and Sciunnach, D. (2006). Subsurface magnetostratigraphy of Pleistocene sediments from the Po Plain (Italy): Constraints on rates of sedimentation and rock uplift. *Geol. Soc. Am. Bull.*, 118(11-12):1299–1312.
- Scherbaum, F., Hinzen, K.-G., and Ohrnberger, M. (2003). Determination of shallow shear wave velocity profiles in the Cologne/Germany area using ambient vibrations. *Geophys. J. Int.*, 152:597–612.
- Scherbaum, F., Riepl, J., Bettig, B., Ohrnberger, M., Cornou, C., Cotton, F., and Bard, P.-Y. (1999). Dense array measurements of ambient vibrations in the Grenoble basin to study local site effects.
- Schmertmann, J. H. (1978). Guidelines for cone test, performance, and design.
- Schumm, S., Dumont, J., and Holbrook, J. (2000). *Active Tectonics and Alluvial Rivers*. Cambridge University Press, 290 pp.
- Scognamiglio, L., Margheriti, L., Mele, F., Tinti, E., Bono, A., De Gori, P., Lauciani, V., Lucente, F., Mandiello, A., Marcocci, C., Mazza, S., Pintore, S., and Quintiliani, M. (2012). The 2012 Pianura Padana Emiliana seismic sequence: locations, moment tensors and magnitudes. *Ann. Geophys.*, 55(4):549–556.
- Scrocca, D., Carminati, E., Doglioni, C., and Marcantoni, D. (2007). Slab retreat and active shortening along the Central-Northern Apennines. In *Lacombe, O., Lavq, J., Roure, F., Verges, J. (Eds.), Thrust Belts and Foreland Basins: From Fold Kinematics to Hydrocarbon Systems*, pages 471–487.
- Seed, H. B. (1979). Soil Liquefaction and Cyclic Mobility Evaluation for Level Ground During Earthquakes. *J. Geotech. Eng. Div.*, 105(2).
- Seed, H. B. and Idriss, I. M. (1971). Simplified procedure for evaluating soil liquefaction potential. *J. Geotech. Eng. Div.*, 97(9):1249–1273.

- Seed, H. B. and Idriss, I. M. (1982). Ground motions and soil liquefaction during earthquakes. Earthquake Engineering Research Institute Monograph, Oakland, Calif.
- Seed, H. B., Mori, K., Chan, C. K., Seed, H. B., Mori, K., and Chan, C. K. (1977). Influence of Seismic History on Liquefaction of Sand. *J. Geotech. Eng. Div.*, 103(4).
- Seed, R. B., Cetin, K. O., Moss, R. E. S., Kammerer, A., Wu, J., Pestana, J., and Riemer, M. (2001). Recent advances in soil liquefaction engineering and seismic site response evaluation. In *Proceedings, 4th International Conference and Symposium on Recent Advances in Geotechnical Earthquake Engineering and Soil Dynamics*. University of Missouri, Rolla, MO, Paper SPL-2.
- Seed, R. B., Cetin, K. O., Moss, R. E. S., Kammerer, A., Wu, J., Pestana, J., Riemer, M., Sancio, R. B., Bray, J. D., Kayen, R. E., and Faris, A. (2003). Recent Advances in Soil Liquefaction Engineering: a Unified and Consistent Framework. In *26th Annual ASCE Los Angeles Geotechnical Spring Seminar*. Keynote presentation, Long Beach, CA.
- Seo, K. (1997). *Comparison of measured microtremors with damage distribution*. JICA, Research and Development Project on Earthquake Disaster Prevention.
- Serpelloni, E., Anzidei, M., Baldi, P., Casula, G., and Galvani, A. (2005). Crustal velocity and strain-rate fields in Italy and surrounding regions: New results from the analysis of permanent and non-permanent GPS networks. *Geophys. J. Int.*, 161(3):861–880.
- Serva, L. (1990). Il ruolo delle scienze della terra nelle analisi di sicurezza di un sito per alcune tipologie di impianti industriali: il terremoto di riferimento per il sito di Viadana (mn). *Boll. Soc. Geol. It.*, 109:375–411.
- Sherif, M. A., Ishibashi, I., and Tsuchiya, C. (1977). Saturation Effects on Initial Soil Liquefaction. *J. Geotech. Eng. Div.*, 103(8):914–917.
- Shibata, T. and Teparaksa, W. (1988). Evaluation of liquefaction potentials of soils using cone penetration tests. *Soils and Foundations*, 28(2):49–60.
- Shuttle, D. A. and Cuning, J. (2007). Liquefaction potential of silts from CPTu. *Can. Geotech. J.*, 44(1):1–19.
- Singh, S., Donovan, N. C., and Park, F. (1980). A Re-examination of the effect of Prior Loadings on the Liquefaction Resistance of Sands. In *Proceedings of the 8th World Conference on Earthquake Engineering*, volume 3. Istanbul, Turkey.
- Somerville, P., Collins, N., Graves, R., and Pitarka, A. (2004). An engineering ground motion model for basin generated surface waves. In *Proceedings 13th World Conference on Earthquake Engineering*. Vancouver, Canada.

- Sonmez, H. (2003). Modification of the liquefaction potential index and liquefaction susceptibility mapping for a liquefaction-prone area (Inegol, Turkey). *Environ. Geol.*, 44(7):862–871.
- Sonmez, H. and Gokceoglu, C. (2005). A liquefaction severity index for engineering practice. *Environ. Geol.*, 48(1):81–91.
- Stark, T. D. and Olson, S. M. (1995). Liquefaction resistance using CPT and field case histories. *J. Geotech. Eng.*, 121(12):856–869.
- Stein, R. S. and Yeats, R. S. (1989). Hidden Earthquakes. *Sci. Am.*, 260:48–57.
- Stephenson, W. (2003). Factors bounding prograde Rayleigh-wave particle motion in a soft-soil layer. In *Pacific Conference on Earthquake Engineering*.
- Stucchi, M., Meletti, C., Montaldo, V., Crowley, H., Calvi, G., and Boschi, E. (2011). Seismic hazard assessment (2003-2009) for the italian building code. *BSSA*, 101(4):1885–1911.
- Suzuki, Y., Koyamada, K., and Tokimatsu, K. (1997). Prediction of liquefaction resistance based on CPT tip resistance and sleeve friction. In *Proceedings, 14th International Conference on Soil Mechanics and Foundation Engineering*, volume 1, pages 603–606. Hamburg, Germany.
- Suzuki, Y., Tokimatsu, K., Taya, Y., and Kubota, Y. (1995). Correlation between CPT data and dynamic properties of in situ frozen samples. In *Proceedings, 3rd International Conference on Recent Advances in Geotechnical Earthquake Engineering and Soil Dynamics*, volume I. St. Louis, MO.
- Sánchez-Sesma, F. J., Rodríguez, M., Iturrarán-Viveros, U., Luzón, F., Campillo, M., Margerin, L., García-Jerez, A., Suarez, M., Santoyo, M. A., and Rodríguez-Castellanos, A. (2011). A theory for microtremor H/V spectral ratio: application for a layered medium. *Geophys. J. Int.*, 186:221–225.
- Talhaoui, A., Iben Brahim, A., Aberkan, M., Kasmi, M., and El Mouraouah, A. (2004). Seismic microzonation and site effects at al Hoceima city, Morocco. *J. Earthq. Eng.*, 8(4):585–596.
- Theodulidis, N. P. and Bard, P.-Y. (1995). Horizontal to vertical spectral ratio and geological conditions: An analysis of strong motion data from Greece and Taiwan (SMART-1). *Soil Dyn. Earthq. Eng.*, 14:177–197.
- Tizzani, R., Castaldo, R., Solaro, G., Pepe, S., Bonano, M., Casu, F., Manunta, M., Manzo, M., Pepe, A., Samsonov, S., Lanari, R., and Sansosti, E. (2013). New insights into the 2012 Emilia (Italy) seismic sequence through advanced numerical modeling of ground deformation inSAR measurements. *Geophys. Res. Lett.*, 40(10):1971–1977.
- Tokimatsu, K. (1997). Geotechnical site characterization using surface waves. In *Proceedings of the First International Conference on Earthquake Geotechnical Engineering*, volume 3, pages 1333–1368.

- Tokimatsu, K., Arai, H., and Asaka, Y. (1996). Three-dimensional soil profiling in Kobe area using microtremors. In *Proceedings of the 11th World Conference on Earthquake Engineering*. Acapulco, Mexico.
- Tokimatsu, K., Shinzawa, K., and Kuwayama, S. (1992). Use of short-period microtremors for Vs profiling. *J. Geotech. Eng.*, 118(10):1544–1558.
- Toksöz, M. N. and Lacoss, R. T. (1968). Microseisms: mode structure and sources. *Science*, 159:872–873.
- Tonkin and Taylor (2010a). Darfield earthquake 4 september 2010 geotechnical land damage assessment & reinstatement. Stage 1 report. Technical report, Earthquake Commission. 38 pp. (<http://www.tonkin.co.nz/canterbury-land-information/docs/T&T-Stage>)
- Tonkin and Taylor (2010b). Darfield earthquake 4 september 2010 geotechnical land damage assessment & reinstatement. Stage 2 report. Technical report, Earthquake Commission. 72 pp. (<http://www.tonkin.co.nz/canterbury-land-information/docs/T&T-Stage>)
- Tonkin and Taylor (2013). Canterbury earthquakes 2010 and 2011. Land Report as at 29 February 2012. Technical report, Earthquake Commission. 108 pp. (<http://www.tonkin.co.nz/canterbury-land-information/docs/downloads2592013/T&T-Stage-3-Report.pdf>).
- Toprak, S. and Holzer, T. (2003). Liquefaction potential index: field assessment. *J. Geotech. Geoenviron. Eng.*, 129(4):315–322.
- Treves, B. (1992). Inquadramento geodinamico. In *Guida n° 4, Appennino tosco-emiliano*. A cura della Società Geologica Italiana Be-Ma, Milano.
- Trincardi, F., Correggiari, A., and Roveri, M. (1994). Late Quaternary transgressive erosion and deposition in a modern epicontinental shelf: The Adriatic Semienclosed Basin. *Geo-Mar. Lett.*, 14:41–51.
- Tsai, N. (1970). A note on the steady-state response of an elastic half-space. *BSSA*, 60:795–808.
- Tsai, N. and Housner, G. (1970). Calculation of surface motions of a layered half-space. *BSSA*, 60:1625–1651.
- Tsuchida, H. (1970). Prediction and Countermeasure Against the Liquefaction in Sand Deposits. In *Abstract of the Seminar in the Port and Harbor Research Institute*. (in Japanese).
- Tuan, T. T., Scherbaum, F., and Malischewsky, P. G. (2011). On the relationship of peaks and troughs of the ellipticity (H/V) of Rayleigh waves and the transmission response of single layer over half-space models. *Geophys. J. Int.*, 184:793–800.
- Tuladhar, R., Yamazaki, F., Warnitchai, P., and Saita, J. (2004). Seismic microzonation of the greater Bangkok area using microtremor observations. *Earthq. Eng. Struc. Dyn.*, 33(2):211–225.

- Uebayashi, H. (2003). Extrapolation of irregular subsurface structures using the horizontal-to-vertical spectral ratio of long-period microtremors. *BSSA*, 93(2):570–582.
- Ulusay, R. and Kuru, T. (2004). Adana-Ceyhan (Turkey) earthquake and a preliminary microzonation based on liquefaction potential for Ceyhan town. *Nat. Hazards*, 32(1):59–88.
- Vai, G. (1997). Cyclostratigraphic estimate of the Messinian stage duration. In A. Montanari, G. S. Odin and R. Coccioni (Eds.), *Miocene Stratigraphy: An Integrated Approach*, pages 463–476. Elsevier, Amsterdam.
- Valkaniotis, S., Ganas, A., Papathanasiou, G., and Papanikolaou, M. (2014). Field observations of geological effects triggered by the January-February 2014 Cephalonia (Ionian Sea, Greece) earthquakes. *Tectonophys.*, 630:150–157.
- van Ballegooy, S., Malan, P., Jacka, M., Lacrosse, V., Leeves, J., and Lyth, J. (2012). Methods for characterizing effects of liquefaction in terms of damage severity. In *Proceedings of the 15th World Conferences on Earthquake Engineering*. Portugal, Lisbon.
- Vannoli, P., Basili, R., and Valensise, G. (2004). New geomorphic evidence for anticlinal growth driven by blind-thrust faulting along the northern Marche coastal belt (central Italy). *J. Seismol.*, 8:297–312.
- Veggiani, A. (1987). Territorio, ambiente, clima. Le trasformazioni nei tempi protostorici. Emilia-Romagna: parte orientale. In *Studi e documenti di archeologia, numero speciale dedicato alla XI Biennale di Arte Antica*, volume 3, pages 73–80. Bologna.
- Vittori, E. and Ventura, G. (1995). Grain size of fluvial deposits and late Quaternary climate: A case study in the Po River valley (Italy). *Geology*, 23(8):735–738.
- Waelbroeck, C., Labeyrie, L., Michel, E., Duplessy, J., McManus, J., Lambeck, K., Balbon, E., and Labracherie, M. (2002). Sea-level and deep water temperature changes derived from benthic foraminifera isotopic records. *Quat. Sci. Rev.*, 21:295–305.
- Wakamatsu, K. and Yasui, Y. (1996). Possibility of estimation for amplification characteristics of soil deposits based on ratio of horizontal to vertical spectra of microtremors. In *Proceedings of the 11th World Conference on Earthquake Engineering*. Acapulco, Mexico.
- Walker, A. and Steward, H. (1989). Cyclic Undrained Behavior of Nonplastic and Low Plasticity Silts. In *Technical Report NCEER-89-0035*. National Center for Earthquake Engineering Research, SUNY at Buffalo, July 26.
- Whitman, R. V. (1985). On Liquefaction. In *Proceedings of the Eleventh International Conference on Soil Mechanics and Foundation Engineering*. San Francisco.

- Wotherspoon, L., Pender, M., and Orense, R. (2012). Relationship between observed liquefaction at Kaiapoi following the 2010 Darfield earthquake and former channels of the Waimakariri River. *Eng. Geol.*, 125:45–55.
- Yamamoto, H. (2000). Estimation of shallow S-wave velocity structures from phase velocities of love- and rayleigh- waves in microtremors. In *Proceedings of the 12th World Conference on Earthquake Engineering*. Auckland, New Zealand.
- Yamanaka, H., M., D., and Kagami, H. (1993). Continuous measurements of microtremors on sediments and basement in Los Angeles, California. *BSSA*, 83(5):1595–1609.
- Yamanaka, H., Takemura, M., H., I., and Niwa, M. (1994). Characteristics of long-period microtremors and their applicability in exploration of deep sedimentary layers. *BSSA*, 84(6):1831–1841.
- Yasuda, S., Harada, K., Ishikawa, K., and Kanemaru, Y. (2012). Characteristics of liquefaction in Tokyo Bay area by the 2011 Great East Japan Earthquake. *Soils Found.*, 52(5):793–810.
- Youd, T., Perkins, D., and Brachman, R. (1978). Mapping liquefaction-induced ground failure potential. *J. Geotech. Eng. Div.*, 104 (No. GT4):433–446.
- Youd, T. L. and Hoose, S. N. (1977). Liquefaction Susceptibility and Geologic Setting. In *Proceedings of the Sixth World Conference on Earthquake Engineering*, volume 3. Prentice-Hall, Inc., Englewood Cliffs, New Jersey.
- Youd, T. L., Idriss, I. M., Andrus, R. D., Arango, I., Castro, G., Christian, J. T., Dobry, R., Liam Finn, W. D., Harder, L. F. J., Hynes, M. E., Ishihara, K., Koester, J. P., Laio, S. S. C., Marcuson, I. W. F., Martin, G. R., Mitchell, J. K., Moriwaki, Y., Power, M. S., Robertson, P. K., Seed, R. B., and Stokoe, I. K. H. (2001). Liquefaction resistance of soils: Summary report from the 1996 NCEER and 1998 NCEER/NSF workshops on evaluation of liquefaction resistance of soils. *J. Geotech. Geoenviron. Eng.*, 127(10):817–833.
- Zhang, G., Robertson, P., and Brachman, R. (2002). Estimating liquefaction-induced ground settlements from the CPT for level ground. *Can. Geotech. J.*, 39(5):1168–1180.
- Zhou, S. (1980). Evaluation of the liquefaction of sand by static cone penetration test. In *Proceedings, 7th World Conference on Earthquake Engineering*, volume 3, pages 156–162. Istanbul, Turkey.

Acknowledgements

I warmly thank the Administration of the Sant'Agostino Municipality (Ferrara Province), and in particular its major Fabrizio Toselli, for the farsightedness shown in deciding to adopt an important study such as the seismic microzoning prior to the Ordinance 70/2012, thus financially supporting my research project.

This research also represents a contribution to the Ph.D. Spinner Project EGEST ('Effetti geologici superficiali del terremoto emiliano 2012: studi finalizzati al miglioramento della sicurezza e sostenibilità dello sviluppo territoriale'; coord. R. Caputo) that co-financed this project.

The DPC-INGV Seismological Project S1 (local responsables Prof. Riccardo Caputo and Prof. Giovanni Santarato; Director Andrea Argnani) contributed to this research. This study does not necessarily represent the official opinion and policies of the Italian Presidenza del Consiglio dei Ministri - Dipartimento di Protezione Civile (DPC).

I am very grateful to Prof. Giovanni Santarato for having made available the geophysical instrumentation, for the useful recommendations and suggestions in management, processing and interpretation of the geophysical data and for the valuable critical reviews that helped improve some sections of my thesis.

I am more than thankful to Dr. Nasser Abu-Zeid and Dr. Samuel Bignardi for their scientific advices and suggestions, for the encouragement and the continuous moral support during the most difficulties moments, but also for the laughs and the funny moments and so much more.

I am particularly grateful to Dr. Luca Martelli (Geological Survey of the Regione Emilia-Romagna) for providing several geotechnical, hydrological and field data and for his willingness in the frame of the Seismic Microzoning study of the Sant'Agostino Municipality, which was carried out in a complementary and synergistic way in order to provide the local Administration a refined survey of the entire territory.

I thank John Th. Ioannides, founder of the Geologismiki, for providing the academic license of the CLiq software.

I also thank Dr. Marco Marcaccio (ARPA - Regione Emilia-Romagna) for providing

several geotechnical, hydrological and field data and the several professional geologists (Dr. Enrico Taddia, Dr. Emanuele Stevanin, Dr. Corrado Ballotta, Dr. Stefano Vincenzi, Dr. Biagio Tranquillo, Dr. Massimiliano Plazzi and Dr.ssa geol. Raffaella Maurizzi) that have made available their archives.

I thank Luca Minarelli for the recommendations and suggestions in collecting and managing the geotechnical data, in the frame of the activity carried out for the Seismic Microzoning study of the Sant'Agostino Municipality.

A special thank to my family because despite many difficulties they gave me their support and encouragement. Thanks to my partner Salvatore, because he patiently and lovingly supported me during these years.

I thank all the colleagues of the Department and in particular the CazzenGEO group for supporting me even when I've been really unbearable.